Alkali-activated slag-based concrete incorporating single and multiple hooked-end steel fibres: New developments and challenges

Zur Erlangung des akademischen Grades eines

Doktors der Ingenieurwissenschaften (Dr.-Ing.)

von der KIT-Fakultät für Bauingenieur-, Geo- und Umweltwissenschaften
des Karlsruher Instituts für Technologie (KIT)

genehmigte

Dissertation

von

Laura Rossi

aus Brescia, Italien

Erster Gutachter: Prof. Dr.-Ing. Frank Dehn
Zweiter Gutachter: Prof. Dr. Guang Ye

Tag der mündlichen Prüfung: 03.04.2025

Karlsruhe (2025)

Abstract

The pursuit of carbon neutrality within the construction sector has resulted in a growing interest in alternative sustainable construction materials to decrease the reliance on cement and cement-based concrete, thereby mitigating the environmental impact intrinsically associated with their production processes.

Alkali-activated slag-based concrete (AASC) has become the subject of increasing research studies, presenting itself as a viable alternative to conventional Portland cement-based concrete (PCC) from an environmental and mechanical point of view. However, the variability and versatility of AASC are among the key barriers to its widespread manufacturing and commercialisation. The variability of mechanical and durability performance depending on the chemical characteristics and proportions of its components, combined with the lack of design codes and building regulations, hinder the uptake of this technology on a larger scale. Being able to correlate the mechanical performance of alkali-activated slag-based concrete to its mix design and predict such performance through analytical and numerical models represents the first step towards promoting the use of AASC and steel fibre-reinforced AASC (SFRAASC) in the construction industry, and it is the main focus of this research work.

Firstly, experimental data available from the literature for different types of alkali-activated concrete, *i.e.* fly ash-based, slag-based and blended systems, were collected. These data have been used to assess the applicability to the main classes of plain and steel fibre-reinforced AAC (SFRAAC) of current code-based empirical models and analytical correlations between mechanical properties developed for plain and steel fibre-reinforced PCC (SFRPCC), respectively. New empirical equations have been proposed to describe the mechanical behaviour of different alkali-activated concretes with and without the incorporation of steel fibres.

After narrowing the research focus to alkali-activated slag-based concrete (AASC), single (3D) and novel multiple (4D and 5D) hooked-end steel fibres were added in different volume fractions up to 0.75% to the concrete matrix. Their effect on the composite compressive and tensile behaviours was then evaluated experimentally. Compressive strength, modulus of elasticity, stress-strain response under uniaxial compression, splitting tensile strength and residual flexural tensile strength have been evaluated for each fibre type (3D, 4D and 5D) and volume fraction (0%, 0.25%, 0.50%, and 0.75%). Furthermore, the fibre-matrix bond strength has been evaluated by performing single fibre pull-out tests. The performance of single and multiple hooked-end steel fibres has also been investigated on a reference cement-based concrete of similar strength grade to evaluate the effect of the concrete matrix performance on the composite mechanical behaviour.

Finally, Finite Element Modelling (FEM) was used to derive the compressive and tensile constitutive models for SFRAAC to foster the implementation of new design codes and building regulations as well as the upscaling transition from laboratory research to real-scale applications. A new design tool based on the empirical correlations derived from the experimental data collected in this research work is proposed to facilitate the design of SFRAASC for use in practice.

Zusammenfassung

Das Streben nach Kohlenstoffneutralität im Bausektor hat zu einem wachsenden Interesse an alternativen, nachhaltigen Baumaterialien geführt, um die Abhängigkeit von Zement und Beton sowie die Umweltauswirkungen ihrer Produktionsprozessen zu reduzieren.

Alkalisch aktivierter Hüttensandbeton (AASC) ist Gegenstand zunehmender Forschungsarbeiten, da er aus ökologischer und mechanischer Sicht eine echte Alternative zu herkömmlichem Portlandzementbeton (PCC) darstellt. Die Variabilität und Vielseitigkeit in Abhängigkeit von den chemischen Eigenschaften und den jeweiligen Anteilen der Komponenten von AASC sowie das Fehlen von Normen und Bauvorschriften gehören jedoch zu den Haupthindernissen für die Einführung dieser Technologie in größerem Maßstab. Die Möglichkeit, die mechanischen Eigenschaften von alkalisch aktiviertem Hüttensandbeton mit der Rezeptur zu korrelieren und diese Eigenschaften mit Hilfe analytischer und numerischer Modelle vorherzusagen, stellt den ersten Schritt zur Förderung der Verwendung von AASC und stahlfaserverstärktem AASC (SFRAAC) in der Bauindustrie dar und ist der Hauptschwerpunkt dieser Forschungsarbeit.

Zunächst wurden in der Literatur verfügbare experimentelle Daten für verschiedene Arten von alkalisch aktivierten Betone, d. h. auf Flugasche-basierte, Hüttensand-basierte und gemischte Systeme, gesammelt. Diese Daten wurden verwendet, um die Anwendbarkeit der derzeitigen normativen, empirischen Modelle und analytischen Korrelationen zwischen den mechanischen Eigenschaften, die für normalen und stahlfaserverstärkten PCC (SFRPCC) entwickelt wurden, auf die Hauptklassen von normalen und stahlfaserverstärkten AAC (SFRAAC) zu bewerten. Es wurden neue empirische Gleichungen vorgeschlagen, um das mechanische Verhalten von alkalisch aktivierten Betonen mit und ohne Stahlfasereinlage zu beschreiben.

Nach der Eingrenzung des Forschungsschwerpunkts auf alkalisch aktivierte Betone auf Hüttensand-basis (AASC) wurden der Betonmatrix einzelne (3D) und neuartige Stahlfasern mit mehreren Haken (4D und 5D) in unterschiedlichen Volumenanteilen zugesetzt. Ihre Auswirkungen auf das Druck- und Zugverhalten der Verbundwerkstoffe wurden anschließend experimentell untersucht. Druckfestigkeit, Elastizitätsmodul, Spannungs-Dehnungs-Verhalten bei einachsiger Druckbelastung, Spaltzugfestigkeit und Restbiegezugfestigkeit wurden für jeden Fasertyp (3D, 4D und 5D) und jeden Volumenanteil (0%, 0,25%, 0,50% und 0,75%) evaluiert. Die Festigkeit der Faser-Matrix-Verbindung wurde durch Auszugsversuche an einzelnen Fasern bewertet. Die Leistung von 3D, 4D, und 5D Stahlfasern wurde auch an einem zementbasierten Referenzbeton ähnlicher Festigkeitsklasse untersucht, um die Auswirkungen der Betonmatrix auf das mechanische Verhalten des Materials zu bewerten.

Schließlich werden mit Hilfe der Finite-Elemente-Methode (FEM), die Druck- und Zugmodelle für SFRAAC abgeleitet, um die Umsetzung neuer Konstruktionsnormen und Bauvorschriften sowie den Übergang von der Laborforschung zu realen Anwendungen zu fördern. Ein neues *design tool*, das auf den empirischen Korrelationen basiert, die aus den in dieser Forschungsarbeit gesammelten experimentellen Daten abgeleitet wurden, wird vorgeschlagen, um die Bemessung von SFRAASC für den Einsatz in der Praxis zu erleichtern.

Acknowledgement

This research work is the result of years of work, scientific experiments, multiple failed attempts, hundreds of specimens tested, and countless read articles. But above all, it is the result of human relationships, exchange of ideas and mutual help. Thus, I would like to thank all the people who crossed my path and helped me with their support, their knowledge, their physical work, or simply their presence in the last four years.

First of all, I would like to express my deepest gratitude to my supervisor, Prof. Dr.-Ing. Frank Dehn, for his constant encouragement, critical feedback, enlightening and constructive discussions, which contribute significantly to this research work.

I would like to express my deepest appreciation to the committee members, Dr. Guang Ye, Prof. Dr. Frank Schilling, Prof. Dr. Katja Emmerich, and Prof. Dr.-Ing. Lothar Stempniewski for their support.

Additionally, this research work would not have been possible without the support from all the members of the PhD Training Network on Durable, Reliable and Sustainable Structures with Alkali-Activated Materials (DuRSAAM), from renowned professors to industrial partners and fellow PhD students who provided motivation, knowledge and expertise in the last 5 years.

I am extremely grateful to Dr Ravi Patel, who helped me find order into the chaos of my experimental results and to transform them into the publications of which this thesis consists.

I would like to extend my sincere thanks to all the colleagues, lab technicians, and students who helped me intellectually and physically during my years of research work. Special thanks to Richard, my office and PhD-adventure partner, with whom I shared the achievements and challenges of the PhD life, but also a friend and an inspiration, who motivated me to continue moving forward every single day. My experimental work would have not been possible without the help and patience of Marcel and Patrick, who helped me despite the initial language barrier and my daily questions, becoming a fundamental support for my research work and my professional growth.

I am also grateful to my long-distance best friend, Denny, who has been my emotional support through every single professional and personal challenge faced in the last 5 years. She was there for me in the hardest moments and she never gave up on me even when I was giving up on myself.

Many thanks to Lars, who entered my life unexpectedly but purposely decided to stay by my side during every single step of this journey. His knowledge, support and encouragement, but above all his presence, calmness and patience have been my strength in the hardest moments.

Lastly, I would like to thank my parents for always supporting me and encouraging me, although my decisions often made no sense to them. Every single choice led to this moment and I could not be more proud.

Karlsruhe, in January 2025

Contents

List of Figures

List of Tables

List of Abbreviations and Symbols

AAC	Alkali-Activated Concrete
AASC	Alkali-Activated Slag-based Concrete
AFm	Monosulfoaluminate
AFt	Tri-sulfoaluminate (ettringite)
Al_2O_3	Aluminum Oxide
C_2S	Dicalcium silicate (belite)
C_3A	Tricalcium aluminate (celite)
C_3S	Tricalcium silicate (alite)
C_4AF	Tetracalcium aluminoferrite
CaO	Calcium Oxide
$CaCO_3$	Calcium Carbonate (Calcite)
$Ca(OH)_2$	Calcium hydroxide
C-A-S-H	Calcium Aluminium Silicate Hydrate
CDPM	Concrete Damage Plasticity Model
CEM	Cement type
CH	Calcium hydroxide (portlandite)
CS	Compressive Strength
CZM	Cohesive Zone Model
CMOD	Crack Mouth Opening Displacement
$CMOD_j$	CMOD corresponding to 0.5 mm (j = 1), 1.5 mm (j = 2), 2.5 mm (j = 3) and 3.5 mm (j = 4)
CO_2	Carbon dioxide
CO_{2eq}	CO_2 equivalent
COD	Crack Opening Displacement
C-S-H	Calcium Silicate Hydrate

$C\bar{S}H_2$	Calcium sulfate dihydrate (gypsum)
e.g.	*Exempli gratia* (for example)
EN	*Europäische Norm* (German) – European Standard
FA	Fly Ash
FA-C	Class-C Fly Ash
FA-F	Class-F Fly Ash
FEM	Finite Element Method
Fe_2O_3	Iron (III) Oxide (hematite)
Fe_3O_4	Iron (II, III) Oxide (magnetite)
fib	*Fédération Internationale du Béton* (French) – International Federation for Structural Concrete
FH	Iron hydroxide
FMUF	Fibre Material Utilisation Factor
FPZ	Fracture Process Zone
GGBFS	Ground Granulated Blast Furnace Slag
GHG	GreenHouse Gas
GWP	Global Warming Potential
H_2CO_3	Carbonic acid
HM	Hydration Modulus of GGBFS
i.e.	*Id est* (Latin) – that is
IAE	Integral Absolute Error
ITZ	Interfacial Transition Zone
K	Potassium oxide (K_2O)
L	Load
LOP	Limit of Proportionality
MgO	Magnesium oxide
MK	Metakaolin

M_s	Silicate modulus (SiO_2/Na_2O [mol/mol])
N	Sodium oxide (Na_2O)
Na_2SiO_3	Sodium Silicate (SS)
NaOH	Sodium hydroxide (SH)
N-A-S-H	Sodium Alumino-Silicate Hydrate
P_2O_5	Phosphorus pentoxide
PC	Portland Cement
PCC	Portland Cement Concrete
PE	Polyethylen (fibres)
POFA	Palm Oil Fuel Ash
PP	Polypropylene (fibres)
PVA	Polyvinyl Alcohol (fibres)
REF	Reference concrete
RILEM	*Réunion Internationale des Laboratories et Expertes des Matériaux, systèmes de construction et ouvrages* (French) – International Union of Laboratories and Experts in Construction Materials, Systems and Structures
RH	Relative Humidity
RHA	Rice Husk Ash
RPCC	Reinforced PCC
SCMs	Supplementary Cementitious Materials
SF	Silica Fume
SFRAAC	Steel Fibre-Reinforced Alkali-Activated Concrete
SFRAASC	Steel Fibre-Reinforced Alkali-Activated Slag-based Concrete
SFRC	Steel Fibre-Reinforced Concrete
SFRPCC	Steel Fibre-Reinforced Portland Cement Concrete
SH	Sodium Hydroxide
SiO_2	Silicon dioxide (silica)
SLS	Serviceability Limit State

SS	Sodium Silicate (*waterglass*)
ULS	Ultimate Limit State
d_c	Compressive damage parameter (CDP model)
d_f	Fibre diameter [mm]
d_t	Tensile damage parameter (CDP model)
d_f/l_f	Fibre aspect ratio (fibre diameter/fibre length)
E_c	Modulus of elasticity of the reference concrete (without fibres) [GPa]
E_{cm}	Secant elastic modulus of the compressive stress-strain curve [GPa]
E_{cyf}	Modulus of elasticity of steel fibre-reinforced concrete [GPa]
e	Flow potential eccentricity
$f_{ck,cyl}$	Characteristic cylindrical compressive strength [MPa]
$f_{ck,cube}$	Characteristic cubic compressive strength [MPa]
f_{cm}	Mean compressive strength [MPa]
$f_{cm,cube(REF)}$	Mean cubic compressive strength of the reference concrete [MPa]
$f_{cm,cyl(REF)}$	Mean cylindrical compressive strength of the reference concrete [MPa]
$f_{ctk,min}$	Minimum characteristic tensile strength (5% fractile)
$f_{ctk,max}$	Maximum characteristic tensile strength (95% fractile)
f_{ctm}	Mean tensile strength [MPa]
f_{Fts}	Residual flexural strength at the SLS
f_{Ftu}	Residual flexural strength at the ULS
f_{LOP}	Flexural strength corresponding to the LOP
f_{Rj}	Residual flexural strength corresponding to $CMOD_j$ (j = 1, 2, 3, 4) [MPa]
f_{Rjk}	Characteristic residual flexural strength corresponding to $CMOD_j$ (j = 1, 3) [MPa]
f'_{cu}	Cubic compressive strength of the reference concrete (without fibres) [MPa]
f'_{cuf}	Cubic compressive strength of steel fibre-reinforced concrete [MPa]
f'_{cylf}	Cylindrical compressive strength of steel fibre-reinforced concrete [MPa]

f'_{lf}	Flexural strength of steel fibre-reinforced concrete [MPa]
f'_{sptf}	Splitting tensile strength of steel fibre-reinforced concrete [MPa]
f'_t	Tensile strength [MPa]
G_F	Fracture energy [N/mm]
K_b	Basicity coefficient of GGBFS
K_c	Ratio of the second stress invariant on the tensile meridian to that on the compressive meridian at the initial yield
k	Parameter defining the compressive stress-strain relationship of PCC and SFRPCC according to the *fib* Model Code 2020
L_e	Fibre embedded length [mm]
l_f	Fibre length [mm]
N_f	Number of fibre at the beam cross-section
P_{max}	Maximum Pull-out load [N]
RI_v	Fibre volumetric Reinforcing Index [$(d_f/l_f) \cdot v_f$]
t_i	Initiation period
t_p	Propagation period
v_f	Fibre volume fraction [%]
w	Crack opening [mm]
W_P	Pull-out work [Nmm]
δ	Displacement [mm]
ε_c	Generic compressive strain [‰]
ε_{c1}	Strain corresponding to the peak compressive stress [‰]
ε_{cu1}	Ultimate strain [‰]
ε_c^{el}	Compressive elastic strain [‰]
ε_c^{in}	Compressive inelastic strain [‰]
ε_c^{pl}	Compressive plastic strain [‰]
$\varepsilon_{c,max(FRC)}$	Strain corresponding to $\sigma_{c,max(FRC)}$ of fibre-reinforced concrete [‰]

$\varepsilon_{c,max(REF)}$	Strain corresponding to $\sigma_{c,max(REF)}$ of the reference concrete [‰]
ε_t^{ck}	Tensile cracking strain [‰]
ε_t	Generic tensile strain [‰]
μ	Viscosity parameter
η	Variable respresenting the ratio between the generic compressive strain ε_c and the strain corresponding to the peak compressive stress ε_{c1}
σ	Standard deviation
σ_c	Generic compressive stress [MPa]
σ_{b0}	Biaxial compressive yield stress [MPa]
σ_{c0}	Uniaxial compressive yield stress [MPa]
$\sigma_{c,max(FRC)}$	Peak compressive stress of fibre-reinforced concrete [MPa]
$\sigma_{c,max(REF)}$	Peak compressive stress of the reference concrete (without steel fibres) [MPa]
σ_t	Generic tensile stress [MPa]
σ_{tf}	Maximum tensile strength of the fibre [MPa]
$\sigma_{t,max}$	Tensile stress corresponding to the maximum pull-out load [MPa]
τ_{avg}	Average bond strength [MPa]
τ_{eqv}	Equivalent bond strength [MPa]
Ψ	Dilation angle [°]

List of Publications

Sections of this dissertation have been published in the following peer-reviewed journal articles:

- **Rossi, L.**; de Lima, L.M.; Sun, Y.; Dehn, F.; Provis, J.L.; Ye, G.; De Schutter, G. Future perspectives for alkali-activated materials: From existing standards to structural applications. *RILEM Technical Letters* ***7***: 159-177 (2022)
  DOI: 10.21809/rilemtechlett.2022.160

- **Rossi, L.**; Patel, R.A.; Dehn, F. Compressive behaviour of alkali-activated slag-based concrete and Portland cement concrete incorporating novel multiple hooked-end steel fibres. *Materials and Structures*, 56-96 (2023).
  DOI: 10.1617/s11527-023-02180-2

- **Rossi, L.**; Patel, R.A.; Dehn, F. New analytical models to predict the mechanical performance of steel fibre-reinforced alkali-activated concrete. *Structural Concrete* (2024).
  DOI: 10.1002/suco.202301104

- **Rossi, L.**; Zappitelli, M.P.; Patel, R.A.; Dehn, F. Flexural tensile behaviour of alkali-activated slag-based concrete and Portland cement-based concrete incorporating single and multiple hooked-end steel fibres. *Journal of Building Engineering* ***98***, 111090 (2024)
  DOI: 10.1016/j.jobe.2024.111090

- **Rossi, L.**; Zappitelli, M.P.; Patel, R.A.; Dehn, F. Pull-out behaviour of single and multiple hooked-end steel fibres embedded in alkali-activated slag-based concrete and Portland cement concrete (***to be submitted to the Journal of Building Engineering***)

Additional publications on alkali-activated concretes (AACs) and steel fibre-reinforced alkali-activated concretes (SFRAACs) can be found in:

Peer-reviewed journal articles:

- Sun, Y.; de Lima, L.M.; **Rossi, L.**; Jiao, D.; Li, Z.; Ye, G.; De Schutter, G.; Interpretation of the early stiffening process in alkali-activated slag pastes, *Cement and Concrete Research* ***167***, 107118 (2023).
  DOI: 10.1016/j.cemconres.2023.107118
- Koenig, A.; Wuestemann, A.; Gatti, F.; **Rossi, L.**; Fuchs, F.; Fessel, D.; Dathe, F.; Dehn, F.; Minelli, F.; Flexural behaviour of steel and macro-PP fibre reinforced concretes based on alkali-activated binders, *Construction and Building Materials* ***211***, pp. 583-589 (2019).
  DOI: 10.1016/j.conbuildmat.2019.03.227

Conference papers:

- **Rossi, L.**; Patel, R.A.; Dehn, F.; Compressive and tensile behaviour of alkali-activated slag-based concrete incorporating single and multiple hooked-end steel fibres. In: *Proceedings of the 21st International Conference on Building Materials (Ibausil 2023)*, 13.-15. September 2023, Weimar, Germany, pp. 335-341
  DOI: 10.1002/cepa.2773
- **Rossi, L.**; Dehn, F.; Alkali-activated slag-based concrete incorporating single and multiple hooked-end steel fibres: mechanical behaviour and limitations to field applications. In: *Proceedings of the DuRSAAM 2023 Symposium: Advancing alkali-activated materials*, 8.-10. February 2023 – Gent, Belgium, pp. 164 – 167
  DOI: 10.5281/zenodo.7747121
- **Rossi, L.**; Patel, R.A.; Dehn, F.; Fibre-reinforced alkali-activated slag concrete: from mechanical properties characterisation to structural design. In: *Proceedings of the 14th fib PhD Symposium in Civil Engineering*, 5.-7. September 2022 – Rome, Italy, pp. 737 – 743

E-book:

- Matthys, S.; Tavasoli, S. and Bouwheer, K. (Eds.); The Urban Concrete Innovation, URBCON/DuRSAAM (**contributor**)
  DOI: 10.5281/zenodo.8040421

Committee work:

- **Member** of the RILEM TC 294-MPA: Mechanical properties of alkali-activated concrete and **contributor** in Chapter 7 – *Hardened AAM properties* – Chapter 9 – *Properties of fibre-reinforced alkali-activated concrete (FRAAC)* – and Chapter 15 – *Applications* of the State-of-the-Art Report (***to be published***)

In German:

- **Rossi, L.**; Lamparter, S.; Alós Shepherd, D.; Dehn, F. Technologie der alkalisch-aktivierten Betone – ein Überblick. *Beton* **12,** 484-491 (2024)

1 Introduction

1.1 Towards decarbonisation of cement and concrete production

According to the World Meteorological Organisation (WMO), greenhouse gas emissions (GHG) derived from human activities have driven an alarming increase in the climate change rate over the last decade (2011-2020), resulting in an exponential increase in global mean temperature, rising sea level, accelerating glacial melting, increasing ocean warming and acidification, and intensifying catastrophic natural events, all of which having devastating effects on the global economy [1 – 2] The main factor driving the growing rate of climate change is the constant population growth resulting in new urban settlements and built environments, increasing demand for globally available, affordable, versatile, and durable construction materials, such as ordinary Portland Cement Concrete (PCC) [3]. As shown in Figure 1.1, the global population increased at a constant rate (almost doubling between 1950 and 2015), and cement production increased steadily from 1950 to 2000, with the growth rate accelerating from 2000 to 2015, nearly tripling in just 15 years, achieving a production of 4.6 billion tonnes in 2015 [4].

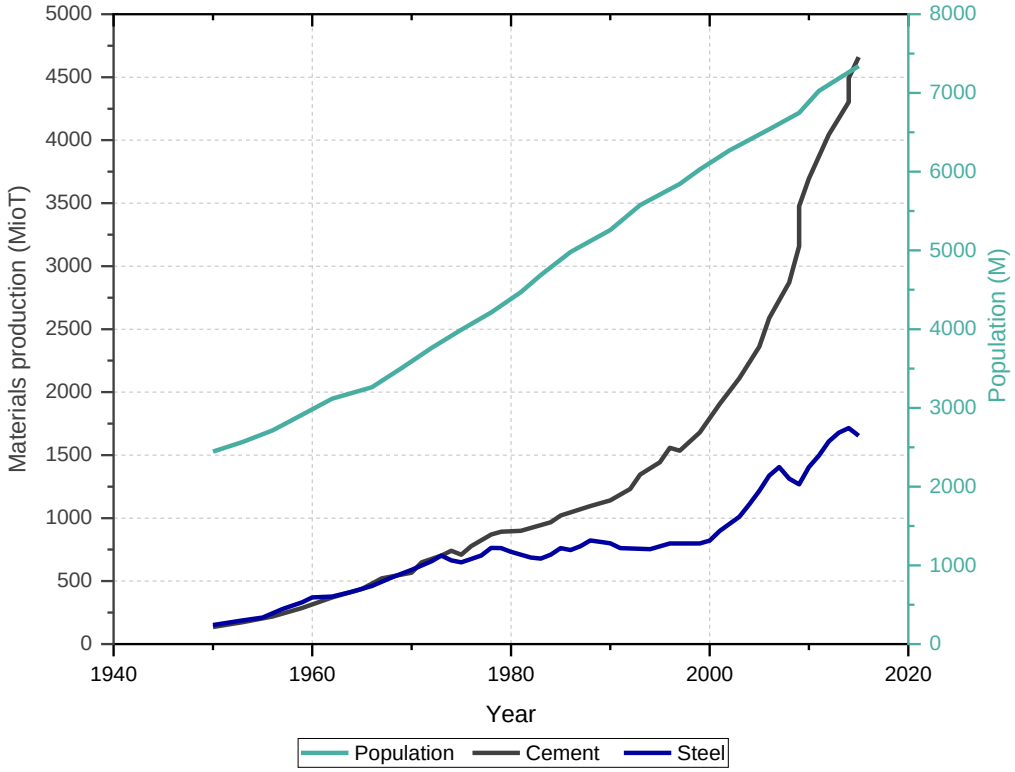

Figure 1.1: Comparison of the cement and crude steel productions with the population growth [Modified from: [4]]

To counteract the decline of the current global condition, the European Union committed to achieving resource efficiency and carbon neutrality by 2050 through a legislative framework (the European Green Deal) tackling all global economic sectors, including the construction industry. Portland cement-based concrete (PCC) is the most used human-made construction material due to its ease of sourcing and production, affordability, and extensively validated performance reliability [3]. Concrete is an inorganic heterogeneous material consisting of a specific proportioned mix of Portland cement (PC), which hardens and sets in contact with water, as well as fine and coarse aggregates, which has been widely used in a diversified range of uses in architecture, engineering, and construction [5 – 6]. Due to its versatility and large-scale use, cement-based concrete represents the most suitable solution for addressing the needs of the growing population and built environment. However, the construction industry is one of the main contributors to global energy consumption, natural resources exploitation, and CO_2 emissions, with Portland cement production responsible for up to 8-9% of annual global anthropogenic carbon dioxide (CO_2) emissions [3, 7 – 9] and concrete accounting for 40% of the CO_2 emissions attributed to building construction [5], as shown in Figure 1.2.

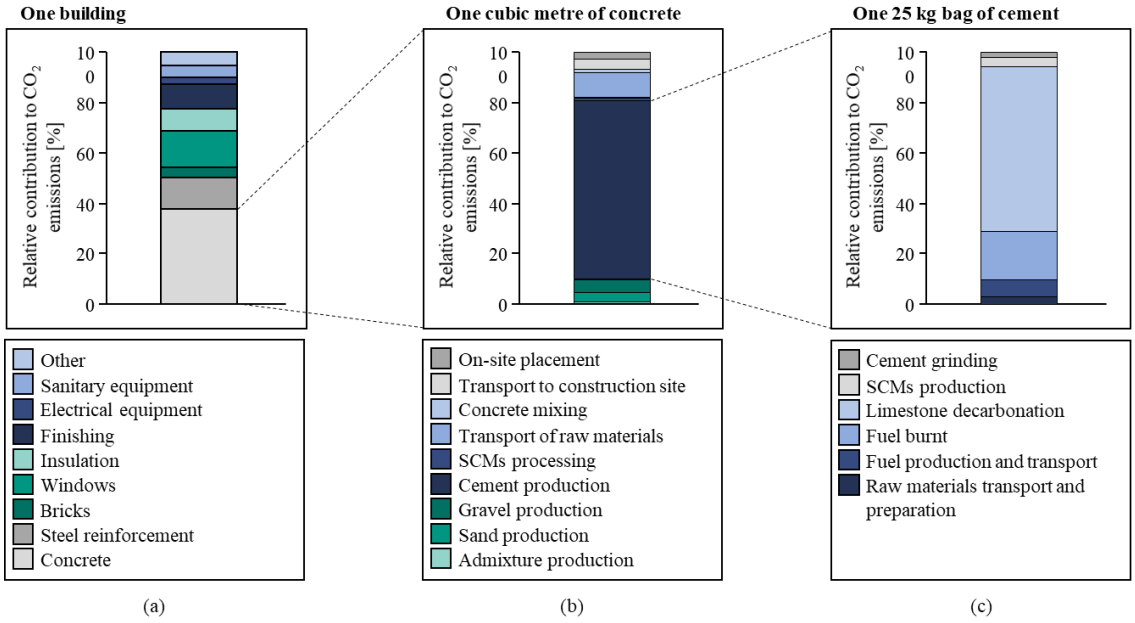

Figure 1.2: Relative contribution to CO2 emission of building materials in (a) one building, (b) one cubic metre of concrete, and (c) one bag of cement to the construction and maintenance of a typical multifamily residential building [Modified from: [5]]

With an expected 50% increase in annual cement production by 2050 [8], the environmental impact of the construction industry is bound to increase without targeted actions. Thus, decarbonisation of the cement and concrete sectors is fundamental in achieving carbon neutrality and economic growth decoupled from resource use. Although around 40% of cement production-induced CO_2 emissions are caused by the combustion of fossil fuels, which can be easily contained by employing renewable energy sources and implementing energy-efficient production plants, more than 60% of emissions are intrinsically related to the chemical process required to transform raw materials into clinker, *i.e.* the cement main constituent [2, 7]. Cement is obtained by thermal treatment of calcium- and aluminosilicate-rich raw materials, such as limestone, clay, iron ore, and

sand, at high temperatures (up to 1450 °C) in a rotary kiln, where limestone ($CaCO_3$) is decomposed into calcium oxide (CaO) and carbon dioxide (CO_2), and calcium silicates and aluminates are formed [5]. The resulting melted materials (*clinker*) are then rapidly cooled and finely ground with gypsum into Portland cement [5]. As a result, calcination-related CO_2 emissions cannot be eliminated, making complete decarbonisation challenging in the cement and concrete sectors. Among all the possible mitigation strategies, partial or total replacement of clinker with supplementary cementitious materials (SCMs) is the most promising route to a large-scale reduction of greenhouse gas emissions and towards sustainability in the cement and concrete industry [5, 10].

Supplementary cementitious materials are finely ground inorganic silicate-, aluminosilicate-, or calcium-aluminosilicate-rich compounds (Figure 1.3), generally natural pozzolans, thermally treated clay minerals or industrial by-products, such as silica fume (from the ferrosilicon industry), fly ash (from coal-powered power plants), and blast furnace slag (from pig iron production), exhibiting either *latent hydraulic* or *pozzolanic* properties when in contact with water. Contrary to hydraulic binders, such as Portland cement, which chemically react with water to set and harden into a cementitious matrix, latent hydraulic binders react slowly with water and require an alkaline environment to accelerate the hardening process, whereas pozzolanic materials, despite not spontaneously reacting with water, develop hydraulic properties when calcium hydroxide is present, both producing reaction products similar to those obtained in Portland cement [11 – 13].

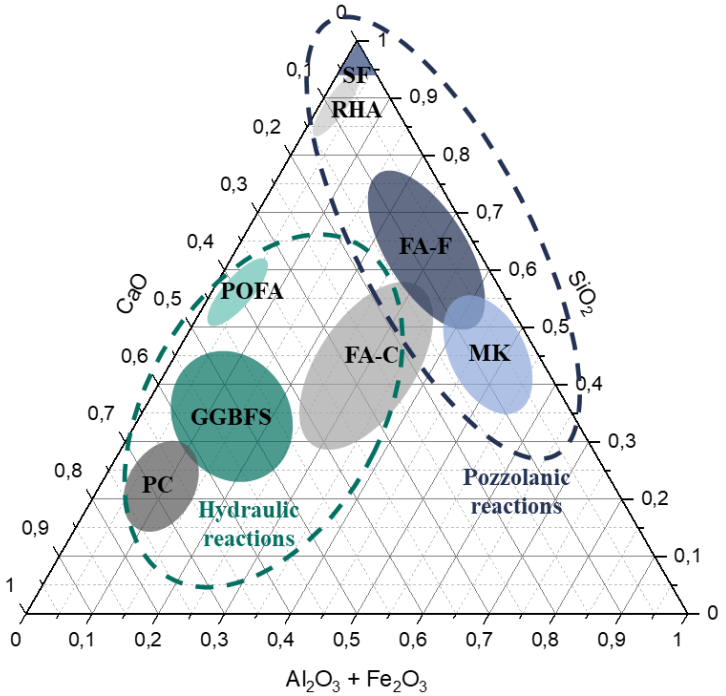

Figure 1.3: Ternary phase diagram showing the chemical composition of the most commonly used supplementary cementitious materials as partial cement clinker replacement [Modified from [14]]

The partial replacement of Portland cement with SCMs has been widely adopted in the construction industry, as it represents the most favourable and cost-effective strategy to reduce the carbon dioxide emissions associated with concrete production while enhancing the concrete short- and long-term performance [10 – 12]. Depending on the type of supplementary cementitious material

and the clinker substitution rate, six standard types of cement have been developed and commercialised based on the composition, specifications and conformity criteria provided by the European Standard EN 197-1 [15], as summarised in Table 1.1.

Table 1.1: Notation, designation and composition of standard cements according to EN 197-1

Notation	Cement type	Composition [%, by mass]	
		Clinker	Other constituents
CEM I	Portland cement	95 – 100	-
CEM II	Portland composite cement	65 – 94	Up to 35% of additional SCMs
CEM III	Blast furnace cement	5 – 64	35 – 95 % blast furnace slag
CEM IV	Pozzolanic cement	45 – 89	11 – 55 % pozzolanic materials[a]
CEM V	Blast furnace slag pozzolanic cement	20 – 64	18 – 49 % blast furnace slag + 18 – 49% pozzolanic materials[a]
CEM VI	Composite cement	35 – 49	31 – 59 % blast furnace slag + 6 – 20 % pozzolanic materials[a] / 6 – 20 % limestone

[a] Pozzolanic materials = natural pozzolans and/or fly ash

However, physical (e.g., fineness) or chemical (e.g., chemical composition and reactivity) incompatibilities between Portland cement and SCMs in blended cement can result in unacceptable undesired properties (e.g., excessive water demand, reduced short- and long-term performance) at high cement replacement levels (> 30%), constituting a significant technical limitation to their widespread use [16]. To overcome these incompatibilities and further minimise the CO_2 emissions related to cement production, SCMs can be used as the only binders in alternative cement-free concrete, such as alkali-activated concrete.

Alkali-activated concrete (AAC) is manufactured through the chemical reaction of solid calcium silicates or aluminosilicate-rich precursors with a solid or dissolved alkali metal source [17]. Given their chemical composition and latent hydraulic or pozzolanic nature (Figure 1.3), supplementary cementitious materials (SCMs) are an ideal source of calcium and aluminosilicates. These require a soluble alkali source supplying metal cations, raising the pH of the reacting system, and accelerating the dissolution process of the solid precursor [17]. Although alkali-activated concrete is obtained through a reaction mechanism differing from the hydration process of conventional Portland cement-based concrete (PCC), such a mixture of precursors, activators, fine and coarse aggregates sets and hardens developing short- and long-term mechanical and durability properties comparable or even superior to those of conventional concrete [18].

Despite its development and use as a construction material since the early 1900s, alkali-activated concrete has gained widespread interest in recent years as an environmentally friendly cement-free alternative to traditional concrete [19]. The industrial by-product nature of the majority of suitable binders for the alkaline activation, *i.e.* the high variability of their chemical composition, combined with the vast number of possible metal alkali sources, results in endless mix design formulations yielding materials with a wide range of short-and long-term performance and CO_2 savings up to 97% in comparison to traditional concrete [20]. On the other hand, the variability and versatility of alkali-activated concrete result in conflicting results in assessing its environmental impact over its lifetime cycle [21, 22]. The significant reductions in the CO_2 emissions

associated with alkali-activated concrete in comparison to traditional concrete are not intrinsic to the entire class of alternative cement-free materials, as they are highly dependent on material composition (e.g., precursors, activators, aggregates), processes (e.g., materials production energy and transportation), end-use applications and their variations with the geographic location [22]. However, alkali-activated concrete can meet the design performance requirements and achieve a significantly lower carbon footprint through tailored design as fit-for-purpose materials for desired applications, resulting in an appealing alternative to traditional cement-based concrete [23].

The local variability, availability and cost of the precursors and the technical limitations related to the novelty level of alkali-activated concrete hinder its implementation, preventing them from reaching large-scale operational maturity and market acceptance by 2050 [5]. Furthermore, the global availability of industrial by-products, such as fly ash and blast furnace slag, is expected to decrease over the future decades as coal-fired power plants are gradually being decommissioned worldwide and more efficient steel-making technologies are being introduced [11, 12, 24], resulting in a shortage of supplementary cementitious materials to be employed as clinker replacement in blended cement (Table 1.1) or in alkali-activated systems. Alkali-activated concrete (AAC) must therefore replace PCC only in applications where AAC has been demonstrated to perform more effectively than traditional concrete, particularly in terms of high early-age strength development, resistance to aggressive environments, and elevated temperatures [20, 23].

Alkali-activated concrete, like traditional cement-based concrete, can endure uniaxial compressive loadings but exhibits brittle behaviour under uniaxial tension, *i.e.* sudden failure without warning of collapse, necessitating the addition of reinforcing steel bars capable of withstanding such stresses in structural reinforced concrete members. Under loading conditions or external restraints, the unavoidable microcracks present in the concrete member due to material intrinsic phenomena, such as drying shrinkage or thermal gradients [25], grow in size, providing a preferential pathway for the ingress of external agents, promoting steel corrosion and shortening the concrete structure service life. As a result, design codes provide a minimum concrete cover depth and a maximum allowable crack width to minimise the risk of corrosion. However, these stringent requirements can result in a congested reinforcement layout, making fibre reinforcement a suitable alternative to conventional reinforcement [25].

The incorporation of randomly distributed steel fibres into the concrete matrix enhances the material load-bearing capacity and ductility, *i.e.* the ability to undergo irreversible deformation before fracture under applied tensile stresses, by bridging the microcracks and transferring the stresses to the concrete matrix at the crack surfaces [18, 26]. The effect of steel fibres with the improved resistance to aggressive environments observed in alkali-activated concretes makes these cement-free construction materials a viable competitive alternative to traditional cement-based concrete in terms of performance and environmental impact. Thus, to further validate the potential of steel fibre-reinforced alkali-activated concrete (SFRAAC), an in-depth investigation of the effect of different commercially available hooked-end steel fibres, *i.e.* single (3D), double (4D) and triple (5D) hooked-end steel fibres, added to the alkali-activated concrete matrix in different dosages is necessary.

1.2 Portland cement and concrete

1.2.1 Portland cement production

Portland cement (PC) is obtained from the calcination, *i.e.* high-temperature thermal treatment, in a rotary kiln of limestone (about 75%), as a source of calcium oxide (CaO) and clay (about 25%), which contains silica (SiO_2), aluminium oxide (Al_2O_3) and iron oxide (Fe_2O_3) [6, 13]. Additional corrective elements, such as sand, iron ore, or bauxite, can be added to the initial raw materials to ensure the appropriate chemical composition of the final product, which determines its hydraulic behaviour and the performance of the resulting hydrated hardened matrix (see Section 1.2.2) [5, 13]. The raw materials are crushed, homogenised, and finely ground into powder before being calcined up to 1450 °C in a rotary kiln [5, 13]. The raw material mixture enters the kiln at a temperature of 700 – 800 °C and, throughout the kiln length, the decarbonation of limestone occurs, *i.e.* calcium carbonate ($CaCO_3$) decomposes into calcium oxide (CaO) and carbon dioxide (CO_2), and the newly formed CaO reacts with silica, alumina, and ferrite obtained from clay decomposition. As the materials move along the kiln, the temperature rises to 1250 °C causing the previously formed calcium silicates (belite or C_2S) and aluminates to create tricalcium aluminate (C_3A) and tetracalcium aluminoferrite (C_4AF) [5, 13]. At 1330 °C, belite, aluminate, and ferrite start melting into alite (C_3S). At the end of the kiln, at around 1450 °C, the resulting material, known as *clinker*, is cooled rapidly and ground with gypsum (calcium sulfate dihydrate or $C\bar{S}H_2$) to obtain Portland cement. The main components of Portland cement are summarised in Table 1.2 [27].

Table 1.2: Portland cement main compounds

Compound	Chemical formula	Common notation	Content [wt. %]
Alite – tricalcium silicate	Ca_3SiO_5	C_3S	55
Belite – dicalcium silicate	Ca_2SiO_4	C_2S	20
Celite – tricalcium aluminate	$Ca_3Al_2O_6$	C_3A	10
Brownmillerite – tetracalcium aluminoferrite	$Ca_4Al_2Fe_2O_{10}$	C_4AF	8
Gypsum – calcium sulfate dihydrate	$CaSO_4 \cdot 2H_2O$	$C\bar{S}H_2$	5
Sodium oxide Potassium oxide	Na_2O K_2O	N K	≤ 2

1.2.2 Cement hydration

Cement hydration consists of a series of coupled chemical reactions occurring at different rates between cement and water, inducing the setting and hardening of the water-cement system into a solid matrix, which acts as the binder in cement-based concrete [13, 28]. The hydration reactions of the cement constituents (Table 1.2) are exothermic. As a result, the progression of the hydration can be observed in the calorimetry plot of the rate of heat evolution over time, as shown in Figure 1.4. Since the hydration of tricalcium silicate (C_3S) controls the setting and early-age strength development of the hydrated cement-based materials, it has been extensively investigated by isothermal calorimetry and used as a model to describe the hydration of Portland cement [29].

Portland cement hydration is a more intricate process where the different cement components react simultaneously at different rates, influencing each other [29]. Figure 1.4 shows the rate of heat evolution over time for cement, which can be divided into five distinct regions, each corresponding to a specific period (or stage) of its hydration mechanism.

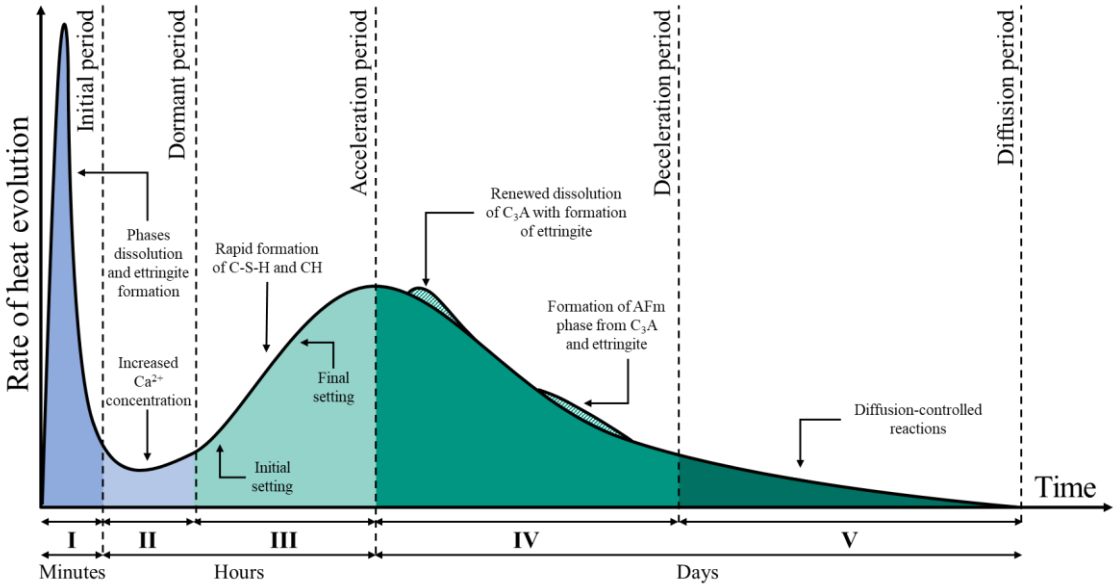

Figure 1.4: Schematic representation of the cement hydration stages based on the rate of heat evolution over time [Modified from [28, 30 – 31]]

I. *Initial period*. The initial period is characterised by a series of rapid reactions between the main Portland cement constituents with water upon wetting, with the aluminate phases (in particular C_3A) reacting very quickly and exothermically, resulting in a significant exothermic signal in the calorimetry curve. In the presence of calcium sulfate (gypsum), the rapid reaction of C_3A leads to the formation of tri-sulfoaluminate (AFt) or ettringite ($C_3A{\cdot}3CaSO_4{\cdot}32H_2O$), followed by a low-heat period governed by the amount of calcium sulfate (gypsum) in the system, which persists until the main rate peak of C_3S hydration. After the calcium sulfate total consumption, the reaction progresses into forming calcium-alumino-mono sulfate phases. Although C_3S should theoretically continue to dissolve until equilibrium concentrations of calcium and silicates in the solution are achieved, the dissolution rate of C_3S decelerates rapidly while the solution is still undersaturated [32]. Among the several theories proposed to explain the early deceleration of the C_3S dissolution rate [28, 32], the *protective membrane theory* and the *dissolution theory* appear to be the most widely accepted [32 – 33].

According to the *protective membrane theory*, the alite dissolution rate decelerates due to the formation of a continuous and thin metastable layer of a calcium silicate hydrate phase (C-S-H) [34] or a "superficially hydroxylated layer" [35] around the C_3S surface, inhibiting its further reaction with water [28, 32]. According to the *dissolution theory*, the rate of dissolution of C_3S decreases as the system approaches equilibrium, *i.e.* undersaturation decreases [33]. As a result, hydration can only proceed via water diffusion through the thin layer or by interaction with the outer hydrated products, initiating the dormant or slow dissolution period [28, 32].

II. *Dormant (or induction) period.* During this transition period, the initially rapid rate of hydration reaches its minimum, in which small-scale chemical reactions generate negligible heat release [13, 32]. Free lime (CaO) also dissolves rapidly and exothermically, and depending on its amount, it can lead to portlandite (CH) supersaturation and nucleation.

III. *Acceleration (or post-induction) period.* At the end of the induction period, the hydration of C_3S accelerates resulting in progressive nucleation and growth of clusters of needle-shaped C-S-H (outer C-S-H) [13] on the cement particles, which govern the reaction kinetics up to the heat evolution peak [32 – 33], with the hydration rate directly proportional to the number of active C-S-H growth sites, *i.e.* its surface area [32].

IV. *Deceleration period.* Once the heat evolution peak is achieved, the hydration rate decreases with a progressive reduction of the heat release. The progress of the calcium silicates and aluminates hydration results in the formation of C-S-H inside the hydration shell formed in the previous period (inner C-S-H), and ettringite crystals and alumina-ferrite-mono phases (AFm), respectively [13, 29].

V. *Diffusion period.* The limited diffusion capacity of the hydration products in the solid state causes the post-peak hydration rate to decrease at later ages (1 – 3 days) [13]. The overall volume of the hydration products is generally 5 – 10 % lower than the combined volume of cement and water initially reacting. This volume loss, also known as chemical shrinkage, leads to the formation of pores and a drop in the internal relative humidity with a consequent decrease in the hydration rate [32].

Thermodynamic modelling can be used to predict the phase assemblages formed during cement hydration. Assuming thermodynamic equilibrium between the liquid and the solid phases, *i.e.* the pore solution and the precipitating hydrates, respectively, their evolution over time can be predicted given the cement chemical composition and the dissolution rate of its main constituents as a function of time as input parameters [36]. Figure 1.5 shows an example of the phase assemblage obtained through thermodynamic modelling during the hydration of Portland cement [37].

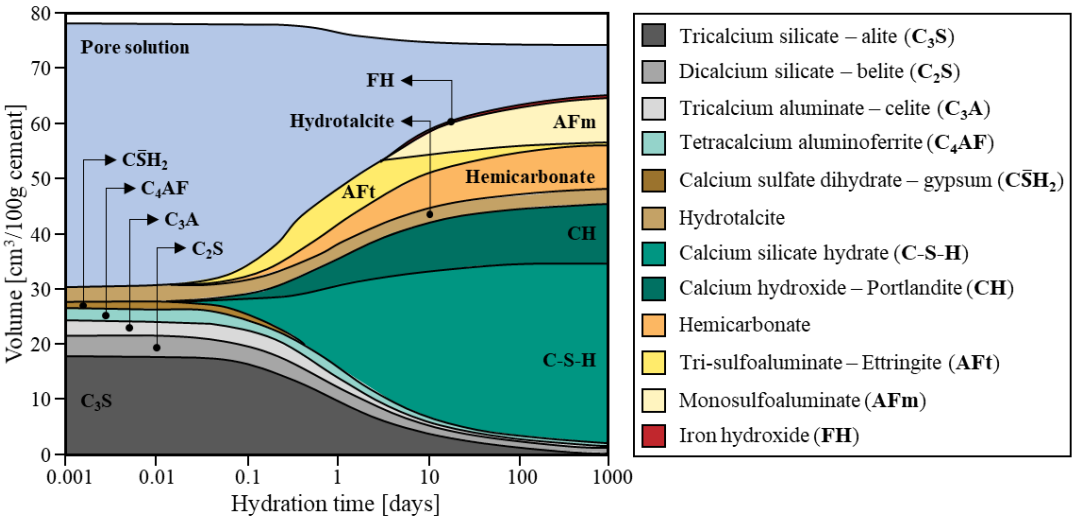

Figure 1.5: Phase assemblage during cement hydration obtained by thermodynamic modelling (w/c = 0.50) [Modified from [37]]

The type and amount of reaction products formed during the cement hydration, together with the resulting porosity and water content, directly affect the hardened cement paste microstructure and performance, as summarised in Table 1.3.

Table 1.3: Effect of the microstructure on the performance of cement-based concrete [13]

Constituent	Content [wt. %][a]	Compressive strength	Dimensional stability	Durability
C-S-H	48.7	Mainly responsible for the mechanical strength	It induces creep and shrinkage	Its intrinsic porosity affects the diffusion of both endogenous and exogenous substances
CH	13.9	It fills the pores, reducing porosity and increasing the strength	Dimensionally stable – it restricts the volumetric changes associated with C-S-H	Decreasing the porosity, it decreases diffusion of both endogenous and exogenous substances, but it decreases the resistance to ASR, carbonation and acid attack
AFt AFm	3.6 11.1	They fill the pores, reducing porosity and increasing the strength	AFt swelling contributes to expansion	Decrease the sulfate resistance
Porosity	16.0	Indirectly affects the strength (*i.e.* higher porosity corresponds to lower strength)	Porosity, pore size and distributions directly affect the creep and shrinkage behaviours	Directly affects diffusion of both endogenous and exogenous substances
Water	4.1	Higher water/cement (w/c) ratios result in higher porosity and lower strength	Water in the pore system directly affects shrinkage	Higher w/c results in higher porosity and higher permeability (lower durability)

[a] The estimated volume percentages refers to a 14-month-old saturated Portland cement-based paste obtained with a w/c = 0.5. Unreacted cement particles accounts for the 2.6%

1.2.2.1 Effect of SCMs on cement hydration

The partial replacement of Portland cement with supplementary cementitious materials (SCMs) in blended cement directly affects the hydration kinetics and products and the resulting hardened material microstructure and performance [38]. Although SCMs have varying effects on the hydration mechanism and products depending on their chemical composition and physical properties, they decrease the total volume of hydrates formed. As a result, blended cement-based matrices have a higher total porosity than pure PC-based hardened paste but a more refined pore structure, which provides higher strength and lower permeability [38]. Table 1.4 summarises the effect of the most used SCMs, namely silica fume, fly ash, and blast furnace slag, on the hydration mechanism and products in Portland cement-SCMs blended cement. Isolating the effect of SCMs on the hydration kinetics of PC-SCMs cement compared to pure Portland cement is challenging, as the hydration of the Portland cement phases and the reaction mechanisms of the SCMs are simultaneous and influence one another [38].

Table 1.4: Effect of different SCMs on the hydration mechanism and products in blended PC-SCMs cements

SCMs	Main characteristics	Reaction mechanism	Effect on cement hydration products
Silica fume	High SiO_2 content Very fine particle size High pozzolanic reactivity	SiO_2 reacts with high calcium C-S-H to form low calcium C-S-H, which can incorporate more aluminium (C-A-S-H)	↓ portlandite ↑ C-S-H with ↓ C/S ratio ↓ alkali concentration ↓ pH pore solution
Fly ash	High SiO_2 and Al_2O_3 content Limited reactivity	Destabilisation of portlandite and formation of additional C-(A)-S-H with low C/S and AFm phases	↓ portlandite ↑ C-S-H with ↓ C/S ratio ↓ Ettringite ↑ AFm phases Strätlingite may form
Blast furnace slag	High CaO content 7 – 15 % MgO content	Destabilisation of portlandite only at high replacement levels Disappearance of monocarbonate	Portlandite ↑ C-S-H with ↓ C/S ratio and ↑ Al/Si ratio ↓ AFm phases Ettringite Strätlingite formation depends on the Al_2O_3 content Hydrotalcite-like products

SCMs can alter the hydration process by acting as fillers or actively participating in the chemical reaction [12]. The reactivity of SCMs depends on the alkalinity of the pore solution, which gradually increases over the first few days of hydration [12, 38]. Thus, SCMs do not actively react to produce hydrates but rather act as fillers, providing additional space and surface for the hydration products generated by the hydration of the cement phases [38]. As a result, a steeper acceleration and a higher maximum rate of heat evolution, indicating a higher number of C-S-H nucleation sites, can be observed in the calorimetry curve. As the solubility of silica varies significantly with the pH of the pore solution, the higher the pH, the faster the reaction rate [38]. However, with higher PC replacement rates with SCMs, the rapid early rates of reaction cause a reduction in the pH, limiting the solubility of amorphous silicates and slowing the reaction rate.

1.2.3 Portland cement concrete

Portland cement-based concrete (PCC) is a two-phase system consisting of a hydrated cement matrix formed by the hydration of Portland cement with water and fine and coarse aggregates, which act as fillers and account for around 70% of the total concrete volume. As a result, the hardened concrete's short- and long-term performance depends on the properties of the matrix, the aggregates, and their interface [39]. Table 1.5 summarises the main factors affecting the characteristics of the concrete matrix and aggregates and the resulting fresh and hardened concrete properties, particularly its compressive strength.

Table 1.5: Main factors affecting the properties of the two phases of concrete and their interface

Concrete matrix	Aggregates	Fresh concrete properties	Hardened concrete properties
Type of cement (CEM I – CEM VI) Cement fineness Cement content (c) Water content (w) w/c ratio Mineral admixtures Chemical admixtures (type and dosage) Curing conditions Voids	Rock type (basalt, limestone, quartzite, sandstone) Shape (rounded, angular, irregular, elongated) Dimension (fine aggregates: 0 – 2 mm, coarse aggregates: 2 – 63 mm) Porosity, permeability, and water absorption Grading curve (amount of aggregates of a specific dimension in the total volume) Content	Water content Aggregate type and grading Aggregate/cement ration Cement fineness Mixing time Temperature Porosity ↓ aggregate/cement ratio ↑ workability ↑ coarse/fine aggregate ↓ workability	Fresh concrete properties Water/cement ratio Curing conditions Curing time Aggregate/cement ratio Porosity Pore size distribution (gel pores 0.5 – 10 nm, capillary pores 5-5000 nm, macropores) Microcracking ↑ w/c ↓ compressive strength (CS); ↑ aggregate/cement ↑ CS

The mechanical and durability performance of hardened concrete has been extensively investigated over the last century, and design codes (*fib* Model Code 2020) and standards (Eurocode 2, EN 206) have been developed to assist in the proper design of concrete to meet the performance requirements of a specific application in practice. The mechanical performance of concrete under compression, *i.e.* compressive strength (f_{cm}), modulus of elasticity (E_{cm}), stress-strain under uniaxial load, and tension, *i.e.* direct (f_{ctm}) or indirect (splitting and flexural) tensile strength, can be correlated to the material compressive strength through empirical code-based equations. As a result, for each class of concrete, which is defined by the characteristic values of the compressive strength determined on both cylindrical ($f_{ck,cyl}$) and cubic samples ($f_{ck,cube}$), the main mechanical performance can be predicted through analytical correlations without additional experimental verifications, as shown in Table 1.6.

Table 1.6: Mechanical performance of each concrete grade according to design codes (*fib* Model Code 2020) and standards (EN 1992-1-1: Eurocode 2)

	Concrete grade														Analytical correlations
	C12	C16	C20	C25	C30	C35	C40	C45	C50	C55	C60	C70	C80	C90	
$f_{ck,cyl}$ [MPa]	12	16	20	25	30	35	40	45	50	55	60	70	80	90	$f_{ck} = f_{cm} - 8$
$f_{ck,cube}$ MPa]	15	20	25	30	37	45	50	55	60	67	75	85	95	105	
E_{ci} [GPa] [a]	27.1	28.8	30.3	32.0	33.6	35.0	36.3	37.5	38.6	39.7	40.7	42.6	44.4	46.0	$E_{ci} = E_{c0} \cdot \alpha_E \cdot \left(\frac{f_{cm}}{10}\right)^{1/3}$
E_{cm} [GPa] [b]	27.0	29.0	30.0	31.0	33.0	34.0	35.0	36.0	37.0	38.0	39.0	41.0	42.0	44.0	$E_{cm} = 22 \cdot \left(\frac{f_{cm}}{10}\right)^{0.3}$
E_{c1} [GPa] [a]	11.1	12.2	13.3	14.9	16.5	18.2	20.0	21.6	23.2	24.7	26.2	28.9	31.4	33.8	$E_{c1} = \frac{E_{ci}}{k}$
ε_{c1} [‰] [a]	1.9	2.0	2.1	2.2	2.3	2.3	2.4	2.5	2.6	2.6	2.7	2.7	2.8	2.9	-
ε_{c1} [‰] [b]	1.8	1.9	2.0	2.1	2.2	2.25	2.3	2.4	2.45	2.5	2.6	2.7	2.8	2.8	-
f_{ctm} [MPa] [a]	1.4	1.9	2.3	2.7	3.0	3.3	3.5	3.8	3.9	4.1	4.3	4.5	4.8	5.0	$f_{ctm} = 1.8 \cdot \ln(f_{ck}) - 3.1$
f_{ctm} [MPa] [b]	1.6	1.9	2.2	2.6	2.9	3.2	3.5	3.8	4.1	4.2	4.4	4.6	4.8	5.0	$f_{ctm} = \begin{cases} 0.3 \cdot (f_{ck})^{2/3}, & \leq C50/60 \\ 2.2 \cdot \ln\left(1 + \left(\frac{f_{cm}}{10}\right)\right) & > C50/60 \end{cases}$
$f_{ctk,min}$ [MPa] [a]	1.0	1.3	1.6	1.9	2.1	2.3	2.5	2.6	2.8	2.9	3.0	3.2	3.4	3.5	$f_{ctk,min} = 0.7 \cdot f_{ctm}$
$f_{ctk,min}$ [MPa] [b]	1.1	1.3	1.5	1.8	2.0	2.2	2.5	2.7	2.9	3.0	3.1	3.2	3.4	3.5	
$f_{ctk,max}$ MPa] [a]	1.8	2.5	3.0	3.5	3.9	4.3	4.6	4.9	5.1	5.3	5.6	5.9	6.2	6.5	$f_{ctk,min} = 1.3 \cdot f_{ctm}$
$f_{ctk,max}$ MPa] [b]	2.0	2.5	2.9	3.3	3.8	4.2	4.6	4.9	5.3	5.5	5.7	6.0	6.3	6.6	

[a] *fib* Model Code 2020, [b] EN 1992-1-1: Eurocode 2, E_{ci} = tangen modulus of elasticity, $E_{c0} \cdot \alpha_E = 21.5 \cdot \alpha_E$, with α_E depending on the type of aggregate, E_{c1} = secant modulus of elasticity (the slope of the line connecting the origin and the peak of a stress-strain curve), ε_{c1} = strain corresponding to the peak stress, k = plasticity number

1.2.4 Reinforced Portland cement concrete

Although Portland cement-based concrete (PCC) can easily withstand significantly high compressive loading and stresses, it exhibits brittle behaviour under tension and bending, failing without collapse warning, and tensile strength values up to 10 times lower than compressive strength values [39]. Thus, steel reinforcement, such as steel rebars and stirrups, is added to the plain concrete to enhance its tensile strength and durability, hindering crack formation and propagation under tension and bending loads. However, corrosion of the concrete-embedded steel reinforcement is the leading cause of premature deterioration in reinforced concrete structures [40].

1.2.4.1 Corrosion resistance of reinforced concrete

Steel corrosion involves the anodic dissolution (oxidation) of iron and the reduction of oxygen to hydroxide ions, as the degradation process of steel reinforcement in concrete strongly depends on the pH of the pore solution [40]. Depending on the pH of the aqueous environment, iron oxidation results in numerous soluble and insoluble compounds (Fe_2O_3 and Fe_3O_4), the latter forming a dense, stable oxide film protecting the underlying metallic iron from further dissolution (passivation) [40]. In cement-based concrete (PCC), the alkalinity of the pore solution (pH = 12.5 – 13.8) allows the embedded steel reinforcement to passivate, hindering its corrosion. However, chloride ions and carbon dioxide can dissolve the passivation film once they penetrate the concrete matrix, breaking down the passive layer locally or lowering the alkalinity of the pore solution, respectively [40]. Chloride-induced and carbonation-induced corrosion significantly impact the service life of conventional or steel fibre-reinforced concrete (SFRC) structures, which comprises two main stages, as shown in Figure 1.6: the initiation and the propagation period [40].

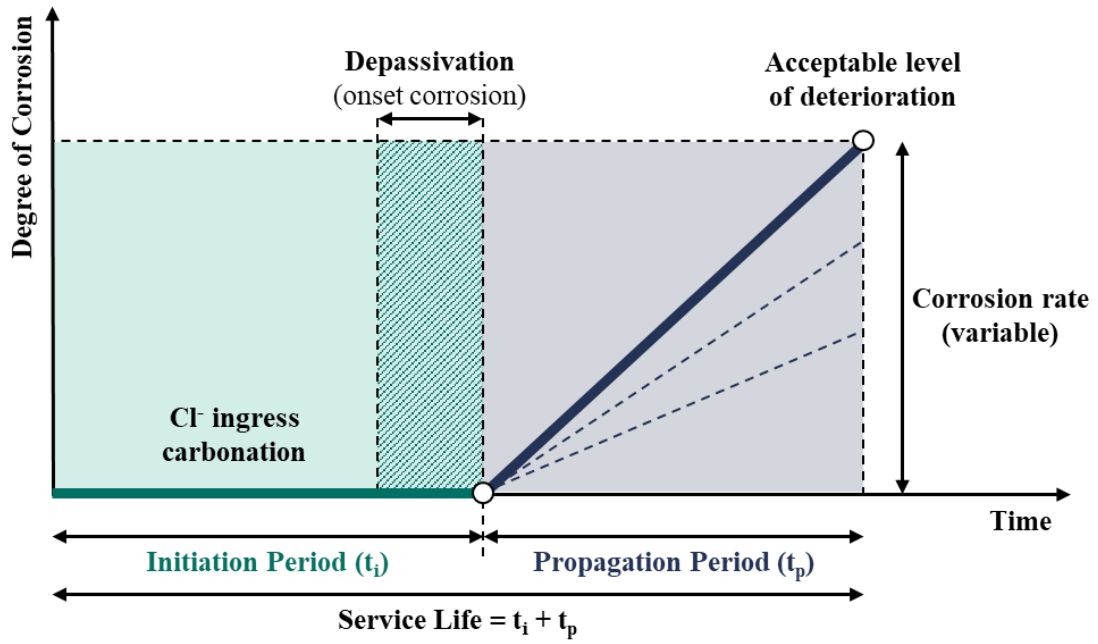

Figure 1.6. Schematic representation of the effect of corrosion on the service life of reinforced concrete structures [Modified from: [40 – 41]]

The *initiation period* (t_i) can be defined as the time required for the aggressive species to penetrate the concrete cover and reach the embedded reinforcement, resulting in steel depassivation and onset corrosion. This stage depends mainly on the concrete cover depth and the concrete intrinsic properties governing the transport of aggressive species [40]. The *propagation period* (t_p) represents the time between corrosion initiation and corrosion-induced cracking, spalling or structural failure [40 – 41].

1.2.4.1.1 Chloride-induced corrosion

Chloride-induced corrosion initiates when chloride ions penetrating the concrete cover reach the embedded steel reinforcement in the critical concentration required for steel depassivation. As chloride ingress into traditional PCC mainly occurs primarily by capillary suction near the surface and diffusion beneath it, the composition of the concrete pore solution, the concrete porosity, *i.e.* the number of capillary pores and their interconnectivity, and its permeability play a fundamental role [40].

1.2.4.1.2 Carbonation-induced corrosion

Carbonation-induced corrosion occurs when the gaseous carbon dioxide in the environment penetrates the concrete through its pores and dissolves in the pore solution forming weak carbonic acid, reducing the alkalinity of the pore solution and causing the dissolution of the hydration products and the precipitation of $CaCO_3$. The lower pH of the pore solution promotes the depassivation of the steel embedded in concrete [40].

1.3 Steel fibre-reinforced concrete

To reduce the risk of corrosion in reinforced concrete structures, design codes and standards specify a minimum concrete cover depth and a maximum admissible crack width to prevent external aggressive agents from coming into contact with the steel reinforcement and initiating corrosion [25]. However, for engineering structures exposed to maritime environments, such as harbour piers, or de-icing salts, such as bridges, adhering to the requirements outlined in design standards can result in congested reinforcement schemes or over-dimensioned concrete members, which are expensive and difficult to handle [25]. Thus, partial or total replacement of the traditional steel reinforcement with randomly distributed steel fibres represents the most viable alternative.

1.3.1 The technology

Single or hybrid combinations of steel fibres can minimise and prevent microcracking formation and propagation, enhancing the ductility and durability of traditional Portland cement-based concrete (PCC) [42 – 43]. Figure 1.7 describes schematically the effect of steel fibres on the fracture process of concrete under uniaxial tension.

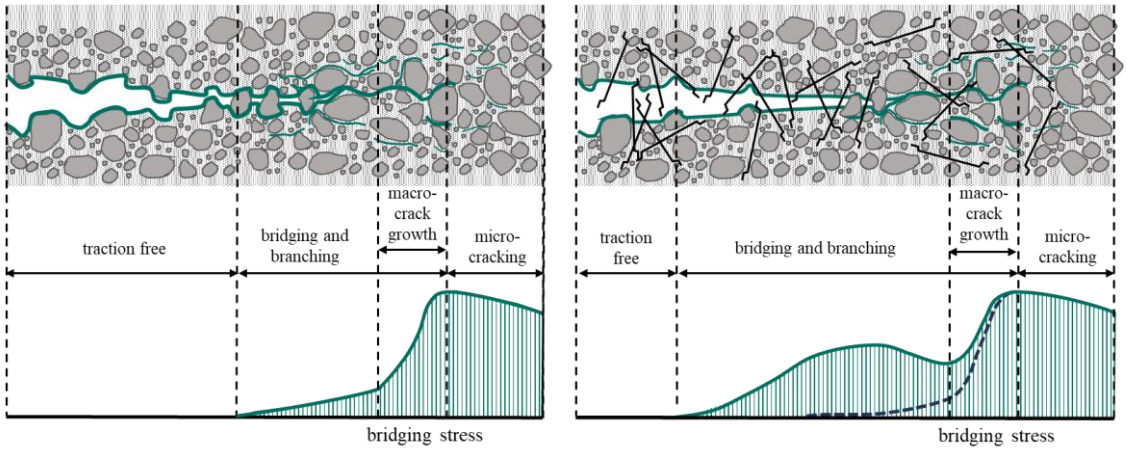

(a) (b)

Figure 1.7: Schematic representation of the fracture process under uniaxial tension for (a) plain and (b) fibre-reinforced concrete [Modified from [44]]

Microcracks are an intrinsic characteristic of concrete resulting from the internal restraints provided by the aggregates and shrinkage developing during the hardening phase. Thus, when an external load is applied, microcracks start growing at the hardened paste-aggregate interface until crack localisation occurs, resulting in macro-cracks formation and the load-bearing capacity drop. For plain concrete, crack bridging and stress redistribution among the crack surfaces are carried out by the aggregates through their bond with the concrete matrix (Figure 1.7a) [44]. When steel fibres are added to concrete, stresses are transferred over an isolated crack to the uncracked matrix through the fibre through its bond with the concrete matrix (Figure 1.7b) [44]. The fibre-matrix bond depends on several mechanisms, including the physical and/or chemical adhesion between the fibre and the matrix, their frictional resistance, and the mechanical bond provided by the fibre geometry [44].

The crack bridging and stress-transferring ability of the single fibre is directly related to the fibre-matrix interfacial bonding strength and, in particular, the fibre pull-out behaviour, *i.e.* the ability of a single fibre embedded in a concrete matrix to resist a pulling force. A weak fibre-matrix bond increases the ease of fibre pull-out and decreases its crack-bridging ability [44]. A strong fibre-matrix bond results in fibre rupture before being able to enhance the post-cracking behaviour. Although it is affected by a variety of parameters, such as fibre geometry, length, and inclination, the pull-out response can be generally described as the result of a gradual fibre-matrix debonding at the fibre interface followed by frictional slip and pull-out of the fibre [44].

Figure 1.8 shows typical load-slip diagrams obtained by performing single fibre pull-out tests on straight and hooked-end steel fibres, while Table 1.7 summarises the different mechanisms involved. For straight steel fibres, the pull-out behaviour is governed only by the chemical adhesive and frictional bonds between the fibre and the matrix. Once these mechanisms are overcome, the fibre is fully pulled out of the concrete matrix. For hooked-end steel fibres, the mechanical interlock provided by the deformed ends of the fibre increases the pull-out load after the fibre-matrix debonding occurs. The fibre hooks undergo plastic deformations, which correspond to new peaks

in the load-slip diagram. Once the fibres are completely deformed and straightened, only the frictional bond needs to be overcome to achieve complete fibre pull-out [45].

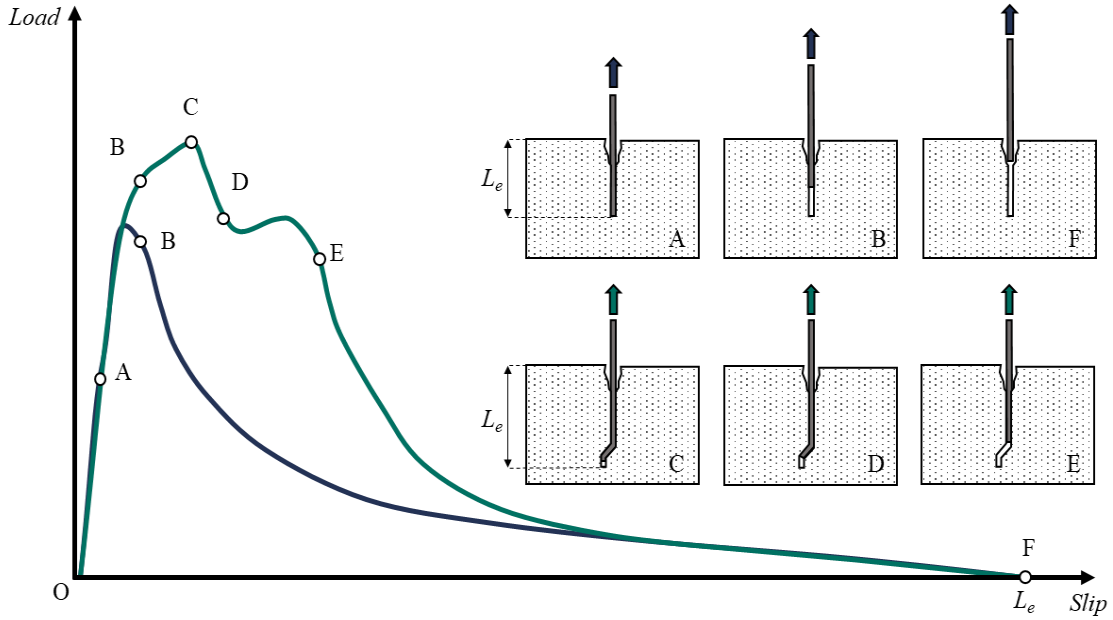

Figure 1.8: Schematic representation of the load-slip pull-out relationship for straight (blue line) and hooked-end steel fibres (green line) [Modified from [44]]

Table 1.7: Mechanisms occurring during the pull-out of straight and hooked-end steel fibres

Load-slip curve portion		Mechanism	
Straight (blue line)	Hooked-end (green line)	Straight fibres	Hooked-end fibres
OA	OA	Adhesive bond	
AB	AB	Partial debonding (B = full debonding)	
BF	BC	Frictional bond	Mechanical anchorage
	CD		Anchorage slipping
	DE		Hooks deformation
	EF		Frictional bond
F	F	Complete pull-out	

The pull-out behaviour and the fibre-matrix adhesive/chemical bond are significantly affected by the microstructure at the interface between the steel fibre and the matrix, usually referred to as the Interfacial Transition Zone (ITZ). The ITZ influences the fibre stress-transferring efficiency and, consequently, the tensile response of the composite. However, it also represents the weakest spot in the cement-based concrete matrix due to its high porosity [46]. The chemical composition of the fibre-matrix ITZ in cement-based concrete is mainly affected by the water/cement ratio

(w/c) of the concrete matrix. Increasing values of w/c increase the porosity and the volume fraction of low-density C-S-H phases while decreasing the total volume fraction of high-density C-S-H phases, which directly affects the overall mechanical properties of the ITZ [47]. For steel fibre-reinforced alkali-activated concrete (SFRAAC), the properties of the fibre-matrix ITZ depend mainly on the solution-to-binder ratio and the binder type [48]. However, alkali-activated concrete shows generally a denser ITZ between aggregates and matrix, thus, a denser fibre-matrix ITZ, than cement-based concrete [49, 50]. A better fibre-matrix bond results in higher pull-out load and toughness, leading to enhanced post-cracking behaviour and higher load-bearing capacity of the concrete member.

To improve the maximum pull-out load and energy absorption multiple hooked-end steel fibres, with double (4D) and triple (5D) bends at the end of the fibre (Figure 1.9), have been developed in recent years and their effect on the performance of normal- and high-strength cement-based concrete evaluated [51 – 54]. Abdallah and Rees [54] demonstrated that the maximum pull-out load increases with the increase of the number of bends at the end of the fibre (5D > 4D > 3D) and with the concrete compressive strength. When 4D and 5D fibres are used, an increase of the maximum pull-out load of 37.9% and 124.1%, respectively, in comparison to single hooked-end steel fibres (3D) can be observed. With the increase of the concrete matrix compressive strength from 33 MPa to 72 MPa, an increase of the maximum pull-out load between 50% (for 5D fibres) and 60% (for 3D and 4D fibres) can be observed.

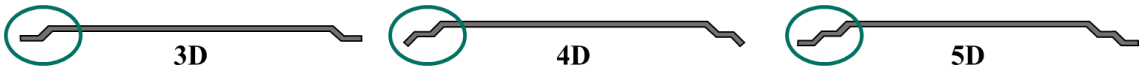

Figure 1.9: Schematic representation of single (3D), double (4D) and triple (5D) hooked-end steel fibres

Combining the geometry of multiple hooked-end steel fibres with the better fibre-matrix bond observed in alkali-activated concrete can potentially allow for obtaining a composite material outperforming steel fibre-reinforced cement-based concrete (SFRPCC). Despite its potential, only a few studies investigated the performance of alkali-activated concrete incorporating single and multiple hooked-end steel fibres. Shaikh [55] evaluated the pull-out behaviour of 3D, 4D and 5D fibres in cement-based, alkali-activated fly ash-based and alkali-activated blended mortars. The maximum pull-out load and the absorbed energy increase with the increase of the number of bends at the ends of the fibre, with 5D fibres outperforming 3D and 4D fibres. However, the pull-out behaviour in alkali-activated slag-based concrete was not investigated. El-Hassan and Elkholy [56] evaluated the effect of hybrid steel fibre reinforcement on the mechanical performance of blended alkali-activated concrete. The hybridisation of single and multiple hooked-end steel fibres at specific volume fractions led to enhanced mechanical performance than concrete without fibres or reinforced with only a single type of fibre. However, the effect of each fibre type in different dosages on different alkali-activated concrete matrices was not evaluated.

1.4 Alkali-activated concrete

Alkali-activated concrete (AAC) consists of one or more solid calcium silicates or aluminosilicate-rich precursors, reacting under mild or strongly alkaline conditions provided by a soluble alkali source, typically alkali hydroxide and alkali silicate [17, 22]. When combined with water and fine and coarse aggregates, the precursors and activators set and solidify into a hardened matrix exhibiting mechanical and durability performance comparable or superior to traditional concrete [18, 19]. Given their chemical composition (Figure 1.3), the most common supplementary cementitious materials (SCMs) used as partial cement clinker replacement in blended cement, particularly coal fly ashes and metallurgical slags, are the most widely used as binders in the production of alkali-activated concrete. Due to their latent hydraulic or pozzolanic nature, these SCMs require an alkaline solution that raises the system's pH to dissolve the solid binder and form insoluble binding phases [17].

Different chemical compositions of the precursors result in different reaction mechanisms and products. Although a proper classification of alkali-activated concrete is still missing, this class of materials is divided generally according to the CaO content of the binder into *low-calcium* (CaO ≤ 10 wt.%) and *high-calcium* systems (CaO > 10 wt.%) [14, 20, 57].

As the calcium oxide content in the binder decreases, the reaction mechanism and its products increasingly differ from those observed during the hydration process of Portland cement. Although the nature of the products of the alkaline activation mechanism depends mainly on the CaO content, the reaction process can be broadly described for both *high-* and *low-calcium* systems as *dissolution – reorientation – precipitation* [58], and it can be schematically represented as shown in Figure 1.10. When in contact with the alkaline solution, the solid aluminosilicate-rich source dissolves, releasing Na^+ and Ca^{2+} into the aqueous solution [59].

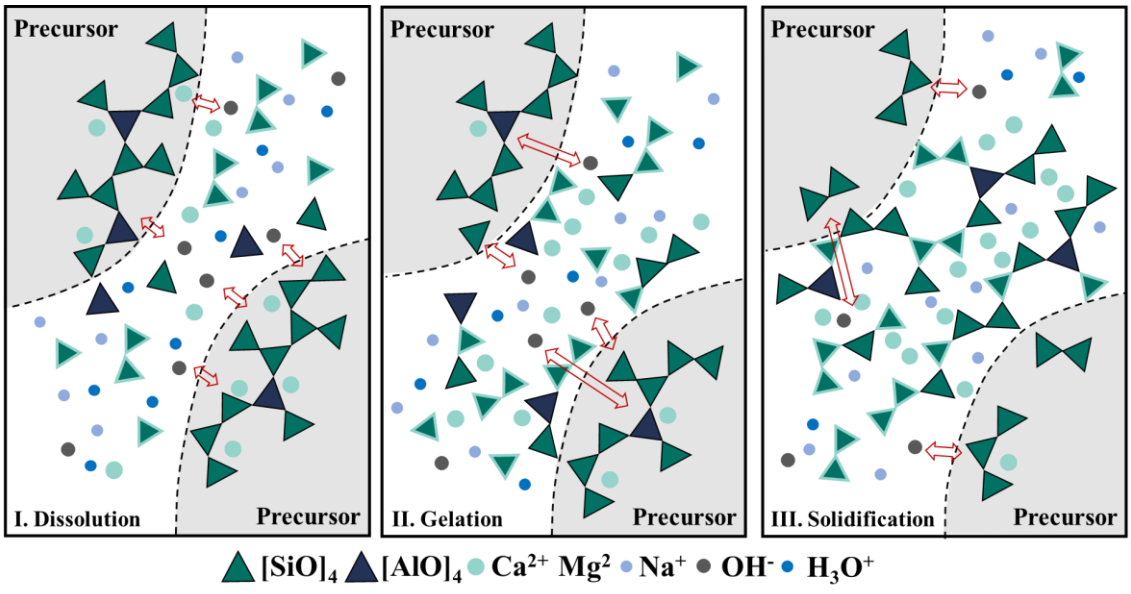

Figure 1.10: Schematic representation of the chemical reaction occurring during the alkaline activation of the aluminasilicate-rich precursor [Modified from [58]]

The increasing alkalinity of the aqueous media promotes the breakage of the Al-O-Si bond, followed by the Si-O-Si bonds and the release of Al- and Si-species, respectively [59]. With the proceeding of the dissolution process, the dissolved species achieve supersaturation and start interacting and rearranging into different strength-giving solid reaction products [20, 58].

In *high-calcium* systems, such as alkali-activated concrete obtained using Class-C fly ash (FA-C) or ground granulated blast furnace slag (GGBFS), the main reaction product is an aluminium-substituted C-A-S-H-type gel with a disordered tobermorite-like structure, which is represented schematically in Fig. 1.11a [14, 20]. Like C-S-H gel formed during cement hydration, C-A-S-H gel consists of tetrahedrally coordinated silicate chains with a dreierkette structure with aluminium replacing the silicon in bridging positions. Thus, C-A-S-H gel shows lower calcium and higher aluminium content, *i.e.* lower Ca/Si ratio (Ca/Si = 0.9 – 1.2), than C-S-H gel (Ca/Si = 1.5 – 2.0) [60]. In *low-calcium* systems, such as alkali-activated concrete obtained using Class-F fly ash (FA-F), metakaolin (MK), palm oil fuel ash (POFA) or silica fume (SF), the primary reaction products are sodium aluminosilicate hydrates (N-A-S-H) gels with highly cross-linked and zeolite-like structure (Fig. 1.11b) [14, 20].

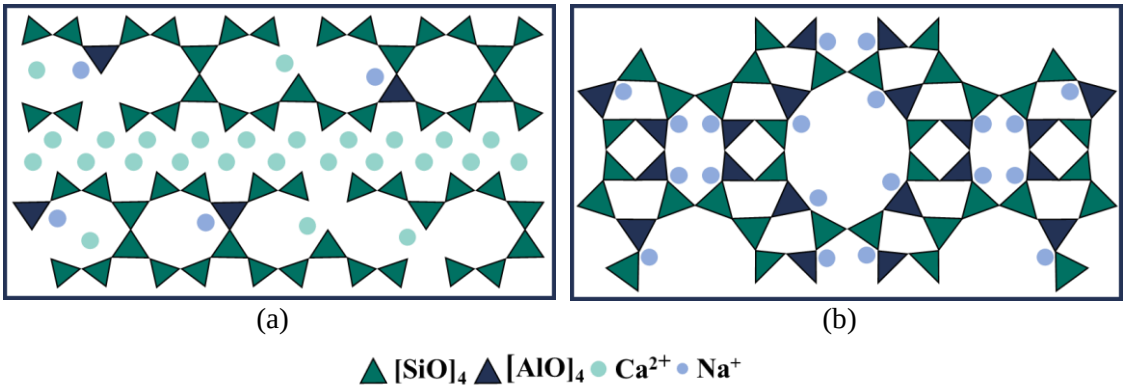

Figure 1.11: Schematic representation of (a) C-A-S-H and (b) N-A-S-H gel structures [Modified from [58]]

The short- and long-term performances of alkali-activated concrete vary according to the nature of the strength-forming reaction products (C-A-S-H and/or N-A-S-H gels), the pore network microstructure and the pore solution composition, which are unique for each binder type and mix design formulation [57]. For example, for *high-calcium* systems, the compressive strength generally increases with the increase of the alkali concentration of the activator and the silica-to-sodium oxide ratio [61 – 63], and it decreases with the solution-to-binder ratio [64]. For *low-calcium* systems, the strength increases with the increase of the activator alkalinity as well as with the curing temperature [65 – 67].

Although the classification of alkali-activated concrete into *high-calcium* and *low-calcium* systems allows for the identification of the main reaction mechanisms and products, the industrial by-product nature of the precursors, *i.e.* the variability of their chemical composition between charges and location, and the variety of suitable alkali activators result in endless mix design formulations and differences in performance for concretes of the same system. Thus, alkali-activated concrete can be designed as fit-for-purpose building materials to meet the requirements of specific applications and locations. However, alkali-activated concrete (AAC) should be preferred

to traditional concrete (PCC) only in applications where AAC can outperform PCC in terms of performance and carbon footprint, such as applications requiring high early-age performance (e.g., high-rise buildings), long-term resistance to aggressive environments (e.g., acids (sewer waters), chlorides (seawater and defrosting salts), sulfates (soils and ground waters), and elevated temperatures (e.g., pedestrian subways or roadway tunnels) [23].

1.5 Alkali-activated slag-based concrete

Due to the pozzolanic nature of the precursors, *low-calcium* systems, such as alkali-activated fly ash-based concrete, require strongly alkaline conditions, generally provided by high dosages of sodium silicate, usually combined with thermal treatments (≥ 60 °C) to accelerate the reaction process and strength development, especially at an early age [20]. Despite its widespread availability and strong demand, only one-third of the global amount of fly ash meets the requirements for usage as cement partial replacement in blended cement [24]. Furthermore, the rapid decommissioning of coal plants worldwide will limit local and regional availability of fly ash, increasing costs and emissions associated with its supply. Thus, *low-calcium* systems based on fly ashes can only be considered a viable, more sustainable alternative to traditional concrete in a few niche applications, such as the precast sector [20]. *High-calcium* systems, such as alkali-activated slag-based concrete (AASC), are often preferred to *low-calcium* systems for their similarities to traditional concrete for reaction mechanisms and products and their versatility as building materials.

1.5.1 Ground granulated blast furnace slag

Ground granulated blast furnace slag (GGBFS) is a by-product of pig iron manufacture. It forms after high-temperature smelting followed by rapid cooling of iron ore, coke and flux [68], resulting in a glassy reactive binder [20] composed primarily of CaO (35 – 40%), SiO_2 (25 – 35%), Al_2O_3 (5 – 15%), and MgO (5 – 10%) [68]. Thus, its chemical and physical properties, particularly its hydraulic behaviour, depend mainly on the steel type and production process [19]. The hydraulic activity of GGBFS can be determined from its basicity coefficient K_b, *i.e.* the ratio between the total basic and acid constituents (in wt.%), which is defined as follows [69]:

$$K_b = \frac{CaO+MgO+Fe_2O_3+K_2O+Na_2O}{SiO_2+Al_2O_3} \quad (1.1)$$

However, as Fe_2O_3, K_2O, and Na_2O are present in GGBFS in a percentage lower than 1 wt. %, their contribution to the basicity coefficient is usually neglected, and K_b is defined as the ratio between (CaO + MgO) and (SiO_2 + Al_2O_3). According to the value of K_b, GGBFS can be classified as follows: acid ($K_b < 1$), neutral ($K_b = 1$), and basic ($K_b > 1$) [69]. Additionally, the hydraulic activity of GGBFS can be defined by its hydration modulus (HM) as follows [69]:

$$HM = \frac{CaO+MgO+Al_2O_3}{SiO_2} \quad (1.2)$$

According to the data available in the literature [19, 68 – 70], to be suitable as a binder for alkali-activated concrete and ensure a good hydraulic potential, the requirements summarized in Table 1.8 should be fulfilled.

Table 1.8: Requirements to ensure a higher hydraulic potential of GGBFS as alkali-activated binder

K_b	CaO/SiO_2	Al_2O_3/SiO_2	HM
≥ 1	0.5 – 2.0	0.1 – 0.6	≥ 1.4

1.5.2 Reaction process

The dissolution process of GGBFS in contact with an alkaline solution can be determined from its rate of heat evolution over the time curve, which can be divided into the same five stages observed for Portland cement (Figure 1.4): initial period, induction period, acceleration period, deceleration period, and diffusion or stable period [71]. However, the chemical composition of the binder and the type, dosage and alkalinity of the alkali activator affect the reaction mechanism, products and microstructure of alkali-activated slag-based concrete [19, 68, 71].

The high content of Al_2O_3 and MgO (MgO/Al_2O_3 = 4 – 6 wt.% [20]) in the precursor reduces the dissolution rate of the amorphous silica, resulting in lower heat of hydration at the early stage [71]. The primary products of the slag dissolution are hydrotalcite-like phases and C-A-S-H, as at high Al_2O_3 content, the substitution of alumina in C-S-H increases, forming calcium alumino-silicate hydrates with a C/S ratio between 0.9 and 1.2 [68]. At high MgO contents, brucite is also observed as a reaction product [71]. As the MgO content increases, hydrotalcite-like phases with greater specific surface area form, filling the pores and producing a refined, denser pore structure [71]. The pH value of the alkaline solution determines the rate at which the precursor dissolves. The activation of GGBFS requires a low to mild alkalinity (pH range from 9.5 to above 12 [72 – 73]), which is usually obtained by using sodium hydroxide (NaOH) and sodium silicate (Na_2SiO_3) as activators [69], as calcium solubility decreases at higher pH [20]. The primary reaction product is C-A-S-H, while the secondary products vary depending on the activator type and dosage [71]. When NaOH is used as an activator, its high pH promotes slag dissolution, forming reaction products with rough surfaces and non-uniform spatial distribution, leading to a poor pore structure. The increased amount of silicates provided by Na_2SiO_3 as an activator causes the formation of C-A-S-H with a decreasing C/S ratio, an acceleration of the reaction rate and more compact matrix structures [71].

When aggregates are added to the alkali-activated slag-based matrix (binder and alkali activators), during the reaction process, an interfacial transition zone (ITZ) forms between the matrix and the aggregates. The matrix-aggregate ITZ is the weakest zone in the concrete matrix, and its composition directly affects the concrete mechanical and durability performance. The ITZ of AASC is rich in reaction products. At high Al_2O_3 content, needle-shaped AFt in the C-S-H network forms, filling the pores and resulting in a denser ITZ [71]. Using Na_2SiO_3 as an activator results in the formation of denser C-A-S-H and fine needle-shaped AFt, which fill the pores, decrease the matrix porosity and provide a denser microstructure and refined ITZ [71].

1.5.3 Short-term mechanical behaviour

The short-term mechanical performance of alkali-activated slag-based concrete (AASC) is directly affected by the hardened concrete reaction process and microstructure, which are strictly dependent on the properties of the concrete matrix main components, such as binder chemical and

physical properties, type and dosage of activators, aggregate type and content. Due to the variety and variability of the main components, alkali-activated slag-based concrete represents a very complex system, allowing for countless mix design formulations.

To characterise and compare the performance of the wide range of possible alkali-activated slag-based concretes, the 28-day compressive strength is commonly used as a reference value. Contrary to traditional cement-based concrete, whose compressive strength mainly depends on the water-to-binder ratio (w/b), with the compressive strength decreasing with the increase in the w/b, no clear correlation between the compressive strength of AASC and a single parameter can be observed. Figure 1.12 shows the correlation between the 28-day compressive strength and several parameters that have been demonstrated to have a direct effect on AASC performance, *i.e.* binder content, water/binder ratio, the ratio between the Na_2O content in the alkaline solution and the amount of binder (n = Na_2O/binder [g/100g]), and the modulus of the alkaline solution, defined as M_S = SiO_2/Na_2O [mol/mol]. Thus, the 28-day compressive strength of alkali-activated concrete depends on the interaction of several parameters correlating the chemical composition of its main constituents and their proportions.

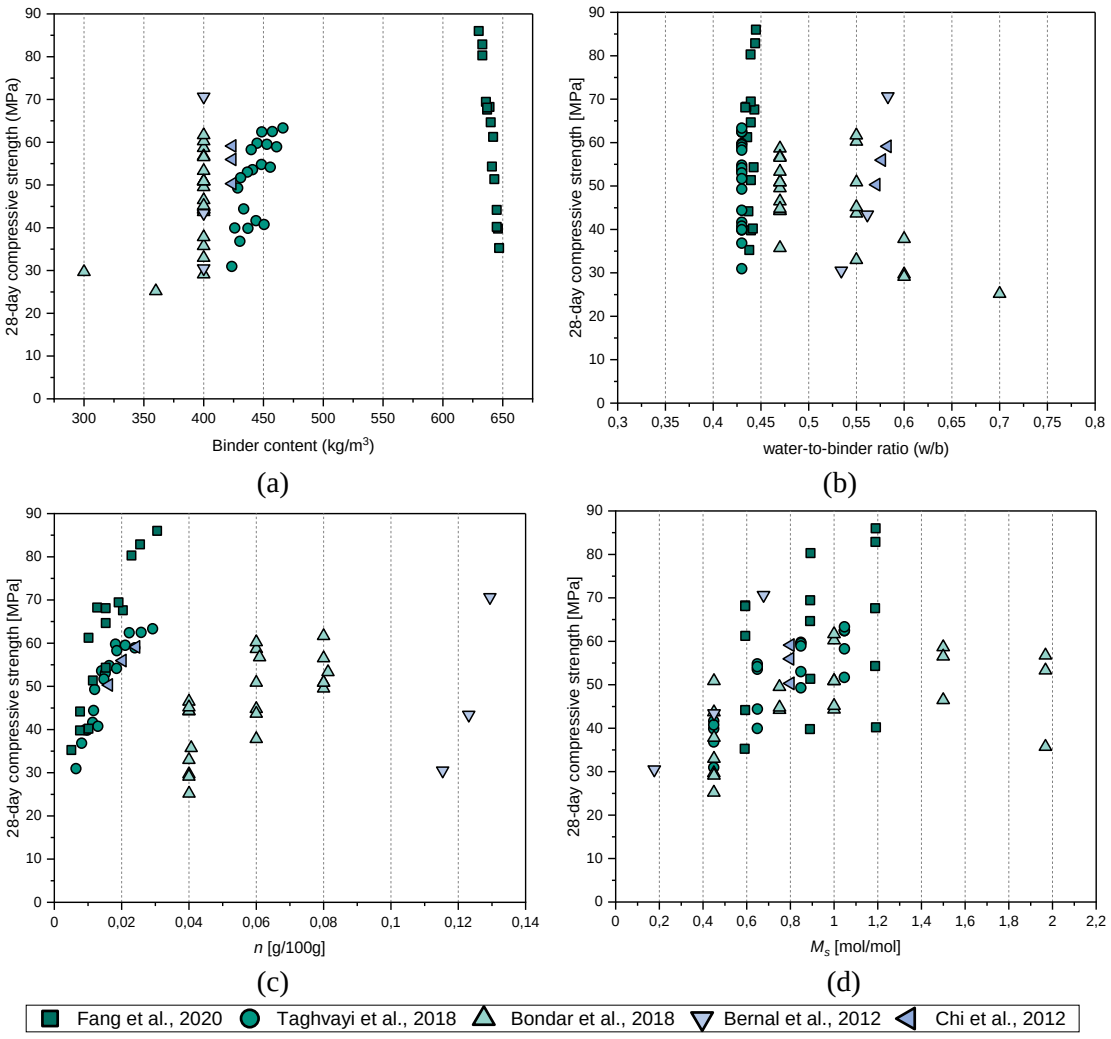

Figure 1.12: Correlation between the 28-day compressive strength and (a) the binder content, (b) the water-to-binder ratio, (c) n, and (d) M_S

The 28-day compressive strength is the key parameter in the design and dimensioning of concrete members and structures because the material performance under compressive and tensile loadings, *i.e.* modulus of elasticity, direct, splitting and flexural tensile strengths, respectively, depends directly on the concrete strength. Thus, several authors [74 – 82] evaluated experimentally the mechanical behaviour of alkali-activated slag-based concrete under compressive and tensile forces. The modulus of elasticity (E_c) represents the material stiffness, *i.e.* the ability of the material to withstand elastic deformation due to applied stresses. It mainly depends on the type and dosage of coarse aggregates and the elastic properties of the concrete paste [83], such as its compressive strength. Although demonstrated to be in the range of 10 – 40 GPa, the modulus of elasticity of alkali-activated slag-based concrete is generally lower than the one observed for PCC of the same strength grade. This could be due to the susceptibility of the concrete matrix to microcracking [75, 83] and to the lower intrinsic modulus of elasticity of the reaction products in comparison to traditional concrete [83].

Like cement-based concrete, AASC exhibits brittle behaviour under tension, *i.e.*, its tensile strength is significantly lower than its compressive strength. Thomas and Peethamparan [75] demonstrated that alkali-activated slag-based concrete generally shows higher tensile strength than PCC. For PCC, the tensile strength represents the 14.1 % of its compressive strength, while for AASC, it represents the 17.0 %. The differences in the behaviour of AASC under compressive and tensile loading compared to traditional concrete need to be considered at the design stage. Design codes and standards developed for traditional concrete cannot be applied to alternative cement-free concretes, such as alkali-activated slag-based concrete. As a result, a deeper understanding of the mechanical behaviour of such material is required.

1.5.4 Long-term behaviour

Alkali-activated slag-based concrete (AASC) has been demonstrated to be resistant to sulfate and acid attacks, as well as chloride ingress [84 – 86]. However, AASC is generally more susceptible to drying shrinkage [84, 87] than Portland cement-based concrete (PCC). Shrinkage occurs during the hardening process of concrete, causing volume variations and, at high rates, microcracking, which promotes the ingress of aggressive agents, resulting in an increased risk of corrosion and subsequent reduction in the long-term performance and service life of the concrete structure. Shrinkage is a complex phenomenon governed by different mechanisms, with drying shrinkage having the most significant effect on the material microstructure and mechanical performance. Drying shrinkage is caused by moisture loss from the surface of the gel pores to the external environment [88, 89]. As a result, the pore structure, network and degree of saturation all play a significant role in concrete drying shrinkage [88 – 90]. The large amount of not-chemically bounded interstitial water prone to evaporation [88] and the fine pore structure observed in AASC are the main causes of drying shrinkage, as they result in high capillary forces and tensile stresses [91 – 93].

Additionally, the magnitude of the shrinkage in alkali-activated slag-based concrete increases with the increase in relative humidity, whereas the shrinkage rate decreases. Unlike PCC, no strong correlation between the drying shrinkage magnitude and the moisture loss of AASC can be observed, as shrinkage can progress even with nearly constant moisture loss [92]. Although

drying shrinkage-induced microcracking represents an intrinsic feature of alkali-activated slag-based concrete and a potential risk for reinforced concrete members and structures, it can be minimised by the introduction of randomly distributed steel fibres.

1.6 Steel fibre-reinforced alkali-activated slag-based concrete

The significant drying shrinkage of the alkali-activated slag-based concrete matrix, combined with its brittle nature, increases the material's microcracking tendency and, as a result, the susceptibility of reinforced concrete members to chloride-and carbonation-induced corrosion, reducing the structure's long-term durability and service life [87, 90 – 91]. Thus, steel fibres as a partial or total replacement of the conventional reinforcement represent an advantageous solution to improve the composite short- and long-term performance, as the fibre crack bridging ability mitigates crack formation and propagation, thereby extending the concrete service life.

1.6.1 Short-term behaviour

Alkali-activated slag-based concrete (AASC) has been demonstrated extensively to exhibit comparable or even superior mechanical and durability performance than Portland cement-based concrete (PCC) of similar strength grade [18]. However, like PCC, AASC exhibits brittle behaviour under tensile and flexural loading, as well as cracking susceptibility, making it unsuitable for applications requiring high post-cracking tensile load-bear capacity and enhanced durability [18, 26]. Thus, randomly dispersed steel fibres are added to the material to improve the composite short- and long-term performance by hindering crack formation and propagation via crack-bridging and stress redistribution within the composite concrete matrix [18]. The mechanical performance of steel fibre-reinforced alkali-activated slag-based concrete (SFRAASC) depends on the characteristics of the concrete matrix, *i.e.* microstructural composition and pore structure resulting from its mix design formulation, of the steel fibres, *i.e.* shape, dimensions and dosage, and of the fibre-matrix interface [94], with fibre content playing the most crucial role.

Figure 1.13 shows the correlation between the fibre volume fraction (v_f) and the main short-term mechanical properties of single hooked-end SFRAASC available in the literature, *i.e.* cylindrical compressive strength (f'_{cylf}), modulus of elasticity (E_{cyf}), stress-strain response under uniaxial compression, splitting and flexural tensile strength (f'_{sptf} and f'_{lf}, respectively).

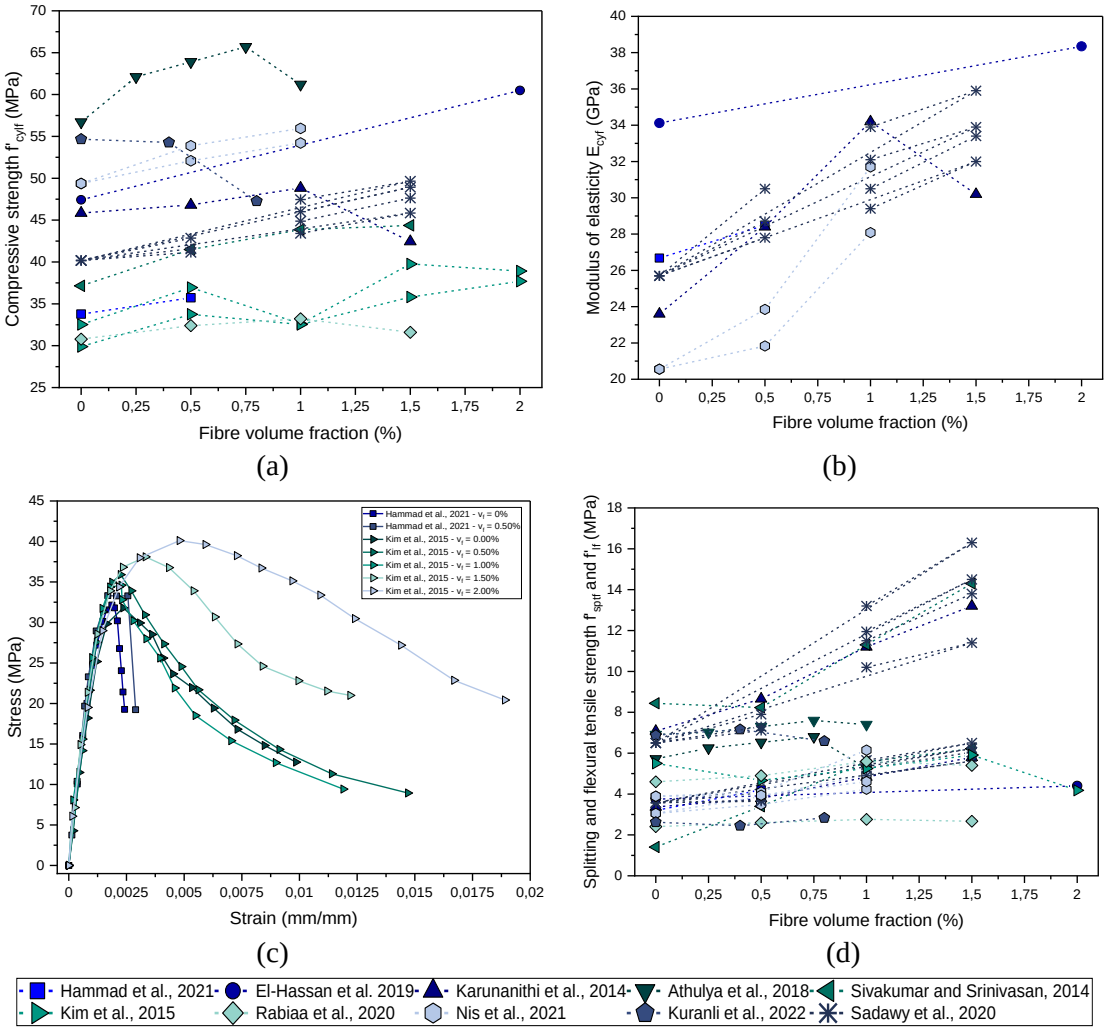

Figure 1.13: Correlation between the fibre volume fraction and (a) f'_{cylf}, (b) E_{cyf}, (c) the stress-strain response under uniaxial compression, and (d) f'_{sptf} and f'_{lf} of AASC incorporating single hooked-end steel fibres

The 28-day mean compressive strength generally increases with the increase in the fibre volume fraction up to a 2% content (Figure 1.13) [26]. The highest increase in compressive strength in comparison to the reference plain concrete is obtained by El-Hassan and Elkholy [95], and it is +27.6% for v_f = 2.00%. However, decrease in strength can be observed when the fibre dosage is further increased beyond the optimal value. Karunanithi et al. [96] observed a decrease in strength of 13.1% when the fibre volume fraction increases from 1% to 1.5%. Athulya et al. [97] demonstrated that a further increase in the fibre volume fraction from 0.75% to 1% results in a strength reduction of 6.8%.

The modulus of elasticity generally correlates linearly with the composite compressive strength [26], therefore, an increase of E_{cyf} with the increase in the fibre volume fraction can be seen (Figure 1.13b). The highest enhancement in the modulus of elasticity of +59.9% is achieved by Niș et al. [98] for a v_f = 1.00%. However, Karunanithi et al. [96] observed a decrease in the

modulus of elasticity of 11.7% when the fibre volume fraction increases from 1% to 1.5%. Although limited studies investigated the effect of steel fibre addition on the stress-strain response of SFRAASC under uniaxial compression [99 – 100], the peak stress and the corresponding peak strain increase with the increase of the fibre volume fraction (Figure 1.13c). Additionally, steel fibres enhance the post-peak residual compressive stress in comparison to the reference plain concrete and, therefore, the ductility of the composite. However, the contribution of steel fibres is more significant on the splitting and flexural tensile strengths of AASC, as shown in Figure 1.13d, with the highest increments of +341.8% and +150.8% achieved by Sivakumar and Srinivasan [101] and Sadawy et al. [102], respectively, for a v_f of 1.50% and 1.00%, respectively. Nevertheless, decreases in the tensile strength with the increase of the fibre volume fraction can be observed. Athulya et al. [97] observed a decrease in the splitting tensile strength of 22.6% when the fibre volume fraction increases from 0.75% to 1%. Kim et al. [100] observed a decrease in flexural strength of 29.3% with the fibre volume fraction increasing from 1.5% to 2%. Although several studies evaluating the mechanical performance of SFRAASC are available in the literature, studies evaluating its direct tensile response or the post-cracking residual flexural behaviour are still missing.

1.6.2 Long-term behaviour

Drying shrinkage-induced volumetric instability and microcracks raised concerns regarding the long-term behaviour of alkali-activated slag-based concrete (AASC), limiting its acceptance as a viable alternative to traditional concrete. Figure 1.14 shows the drying shrinkage behaviour of alkali-activated slag-based concrete in comparison to conventional cement-based concrete (Figure 1.14a) and the shrinkage mitigation effect of steel fibres incorporation on alkali-activated slag-based mortar and concrete (Figure 1.14b).

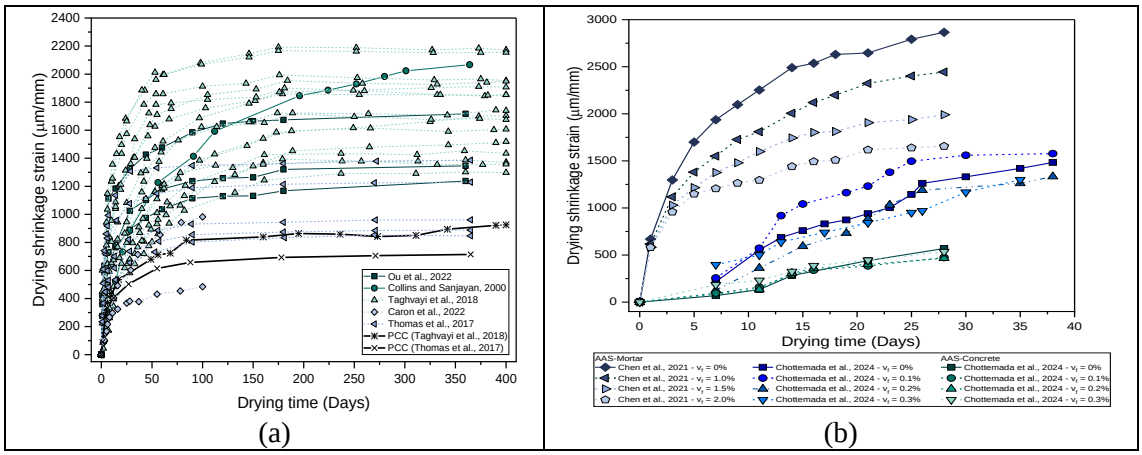

Figure 1.14: Experimental data available in the literature showing the response of (a) plain and (b) steel fibre-reinforced alkali-activated slag-based mortar and concrete to drying shrinkage

Alkali-activated slag-based concrete exhibits a drying shrinkage 1.5 to 2.5 times higher than PCC [103], as also shown in Figure 1.14a. Chottemada et al. [104] evaluated the effect of different fibre types (steel, polypropylene (PP), polyvinyl alcohol (PVA), and glass fibres) on the drying shrinkage of alkali-activated slag-based mortar and concrete. At low fibre volume fractions (up

to 0.2%), steel fibres have the least impact on the drying shrinkage of the composite in comparison to the other fibre types. Due to steel fibres' hydrophobic nature, the water on their surface tends to evaporate easily, contributing to moisture loss and shrinkage. However, at higher volume fractions, the reduction of shrinkage provided by steel fibres is comparable to other fibre types [104].

The shrinkage mitigation induced by the incorporation of steel fibres in the alkali-activated slag-based concrete matrix favours the long-term performance and durability of the composite, in particular, its corrosion resistance, when steel fibres are used as conventional reinforcement partial or total replacement. Although the same service life model can be applied to both reinforced PCC and AASC, the differences in the reaction mechanism, pore solution chemistry, and phase assemblage result in differing durations of the initiation and propagation periods in aggressive environments [105]. Although alkali-activated slag-based concrete generally exhibits improved corrosion resistance than traditional concrete due to its finer pore structure and the lower Ca/Si ratio of its reaction products (C-A-S-H) [106], the effect of chloride ions diffusion and carbonation on the service life of reinforced concrete needs to be evaluated.

1.6.2.1 Corrosion resistance of steel fibre-reinforced reinforced concrete

The partial or total replacement of conventional steel reinforcement with steel fibres enhances the concrete performance by limiting crack formation and propagation; however, the long-term durability of steel fibre-reinforced cement-based concrete (SFRPCC) and alkali-activated slag-based concrete (SFRAASC) under severe chloride and carbonation exposure remains controversial [107].

1.6.2.1.1 Chloride-induced corrosion

As for conventionally reinforced PCC (RPCC), once the critical concentration of chloride ions reaches the steel surface in SFRPCC, depassivation and pitting corrosion occur locally. However, SFRPCC exhibits significantly higher chloride threshold values than conventional RPCC, mainly due to the discontinuous nature of the fibres, the lower potential difference along their surface, and the denser fibre-matrix interfacial transition zone (ITZ), as shown in Figure 1.15 [107].

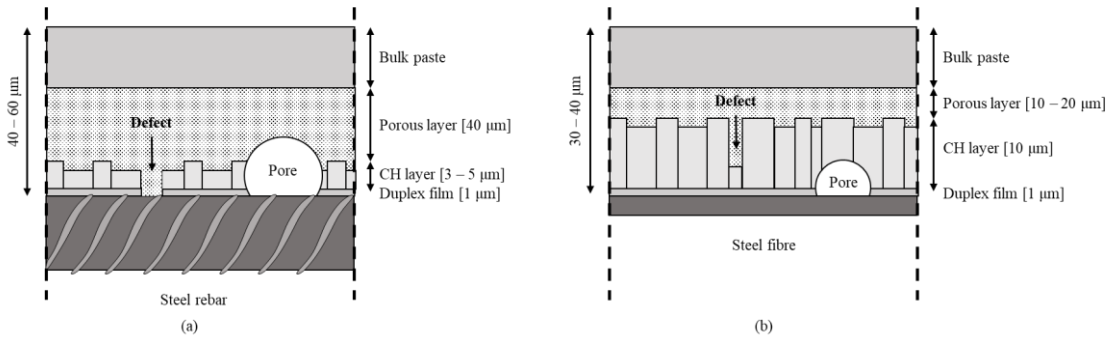

Figure 1.15: Microstructure of the steel-matrix ITZ for (a) conventionally reinforced concrete and (b) steel fibre-reinforced concrete [Modified from: [107]]

The ITZ of SFRPCC shows a larger and more homogeneous calcium hydroxide layer around the fibre, providing higher resistance to the fibres in the uncracked bulk concrete paste against chloride ingress than RPCC. Once the concrete matrix cracks, the strain generated in the fibre bridging the crack damages the fibre-matrix ITZ, creating a preferential path for chloride ions transport

and promoting corrosion. Excessive damage at the fibre-matrix interface results in a localised gradual reduction of the fibre cross-section due to chloride-induced corrosion and a drop in the residual tensile strength [107]. Field-chloride-exposed uncracked SFRPCC generally shows low corrosion damage, while cracked SFRPCC ($w \leq 0.20$ mm) exhibits surface staining due to rusting of the superficial fibres and non-harmful limited corrosion-induced cross-sectional reduction and mechanical performance deterioration [107]. The risk of fibre corrosion decreases with the narrowing of the crack's width. For wide cracks ($w \geq 0.50$ mm), chloride-induced local pit formation results in a significant reduction of the fibre cross-section and consequently of the residual tensile strength, as fibre rupture replaces fibre pull-out as the failure mechanism [107]. For narrow (0.50 mm $\geq w >$ 0.20 mm) and hairline cracks ($w \leq 0.20$ mm), the risk of fibre corrosion is not unanimously recognised, as the literature shows a large variability of the corrosion damage and reduction of the residual flexural strength after exposure [107].

Alkali-activated slag-based concrete has generally a lower diffusion coefficient than PCC, resulting in a slower diffusion of chlorides into the concrete due to its lower porosity thanks to the higher pore-filling capabilities of the C-A-S-H gel and the higher alkalinity ($13 \leq pH \leq 14.2$) of the pore solution and its highly reducing nature due to the presence of reduced sulphur species [40, 105]. High concentrations of reduced sulfur species, such as bisulfide (HS^-), in the pore solution of AASC result in a lower level of dissolved oxygen near the steel-concrete interface than PCC. Thus, more negative redox potential of the embedded reinforcement than is typically observed for oxidising binders, as well as a change in the chemistry of the passive film (Fe-S complex instead of iron oxide), which restricts the cathodic reduction of oxygen, can be observed [105]. Additionally, substituting Si by Al in the C-(A)-S-H gel reduces the positive charge on its surface, lowering the electrostatic interaction with chloride and, therefore, the chloride binding capacity of AASC compared to PCC [40].

1.6.2.1.2 Carbonation-induced corrosion

As for reinforced concrete, carbonation-induced corrosion initiates when depassivation occurs due to a decrease in the alkalinity of the concrete pore solution caused by the precipitation of calcium carbonate from the reaction of CO_2 with water in the pore solution and calcium hydroxide in the hydration products. The initiation phase is governed by the carbonation rate, with cracks acting as carbonating surfaces and locally increasing the carbonation penetration depth. Although uncracked SFRPCC typically exhibits minimal carbonation-induced corrosion damage in the form of corrosion stains at the concrete surface, considerable corrosion damage and degradation in mechanical performance have been observed in cracked SFRPCC [107]. Corrosion damage is observed in the fibres bridging the crack, as carbonation propagates throughout the entire crack surface, with fibres on the outer crack rim showing severe corrosion damage than fibres embedded more deeply in the concrete. The dense and homogeneous nature of the fibre-matrix ITZ delays carbonation in uncracked SFRPCC. Once the concrete matrix cracks, the bridging region of the fibre acts as an anode, while the embedded area serves as a cathode due to the pH gradient at the crack surface. The pH at the inner faces of the crack decreases due to leaching and carbonation, which, at larger strains, facilitates the progression of corrosion, reducing the fibre cross-section and residual flexural strength [107].

Studies assessing the corrosion mechanism, damage and impact on the long-term mechanical performance and service life of steel fibre-reinforced alkali-activated slag-based concrete are still

missing. However, the increased resistance to chloride ingress and carbonation, together with the enhanced fibre-matrix bond strength caused by the compressive hydrostatic pressure generated around the fibre by the matrix shrinkage [108], make SFRAASC a valid alternative to traditional SFRPCC as a construction material. Thus, its mechanical behaviour needs to be fully characterised experimentally to derive design constitutive models for its use in structural and non-structural applications.

1.7 Design of steel fibre-reinforced alkali-activated slag-based concrete

Design regulations define the fundamental principles and requirements for concrete members and structures dimensioning to ensure the safety of the end users throughout their entire service life. Based on countless experimental data collected over decades, empirical correlations linking the mechanical performance of Portland cement-based concrete (PCC) under various loading conditions and numerical models predicting the behaviour of each concrete-based element have been developed and collected in codes and standards. Implementing such regulations to include alternative construction materials other than traditional Portland cement-based concrete requires substantial experimental investigations to fully understand the material behaviour and its similarities and differences with conventional PCC. A perfect example is steel fibre-reinforced PCC (SFRPCC). Despite being a research topic for the last four decades, design guidelines have only recently been developed worldwide, leading to the inclusion of SFRPCC in the *fib* Model Code 2010 and its updated version, the *fib* Model Code 2020 [109].

To promote the use of alternative construction materials, such as steel fibre-reinforced alkali-activated slag-based concrete (SFRAASC), specific design guidelines and standards need to be developed. Thus, the short- and long-term mechanical behaviour and the durability performance of SFRAASC need to be evaluated experimentally, and constitutive models describing their behaviour under compression and tension need to be derived. Constitutive models comprise a mathematical framework describing the mechanical response of the material under direct compressive or tensile loadings [110]. As SFRAASC is an intrinsically heterogeneous material, it exhibits nonlinear inelastic behaviour when stresses are applied, requiring the adoption of analytical models to describe it simply yet accurately.

1.7.1 Compressive behaviour

Although the compressive behaviour of concrete can be represented by its compressive strength and modulus of elasticity, for design purposes, it is necessary to additionally evaluate the stress-strain ($\sigma_c - \varepsilon_c$) response under uniaxial compressive loading, *i.e.* the ability of the material to deform even after achieving its maximum strength. Thus, the concrete compressive constitutive model can be generally obtained analytically by fitting the experimental compressive stress-strain curves. Although several empirical models have been developed for steel fibre-reinforced cement-based concrete (SFRPCC) [111 – 116], they are not able to describe accurately the uniaxial compressive response of SFRAASC, as shown in Figure 1.16.

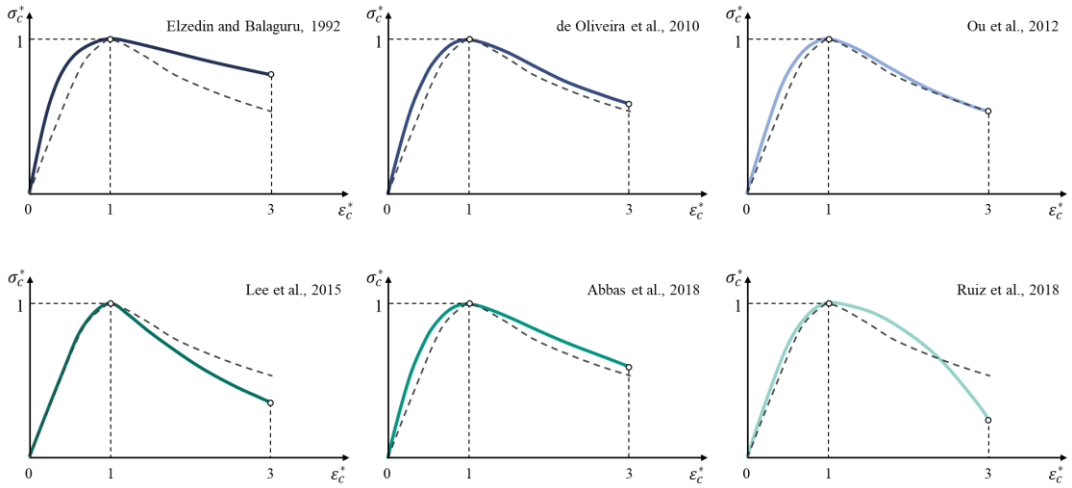

Figure 1.16: Applicability to SFRAASC of different constitutive models proposed for SFRPCC. The dashed line represents a generic normalised experimental stress-strain curve for SFRAASC

1.7.2 Tensile behaviour

As described for the compressive behaviour, the concrete tensile constitutive models are generally derived by fitting the experimental stress-strain ($\sigma_t - \varepsilon_t$) curves obtained from direct tensile strength tests. However, direct tensile strength tests are difficult to perform, especially for steel fibre-reinforced concrete, as the experimental test setup, the machine-specimen interaction, and the fibre type, content, and orientation directly affect the reliability of the experimental results [44].

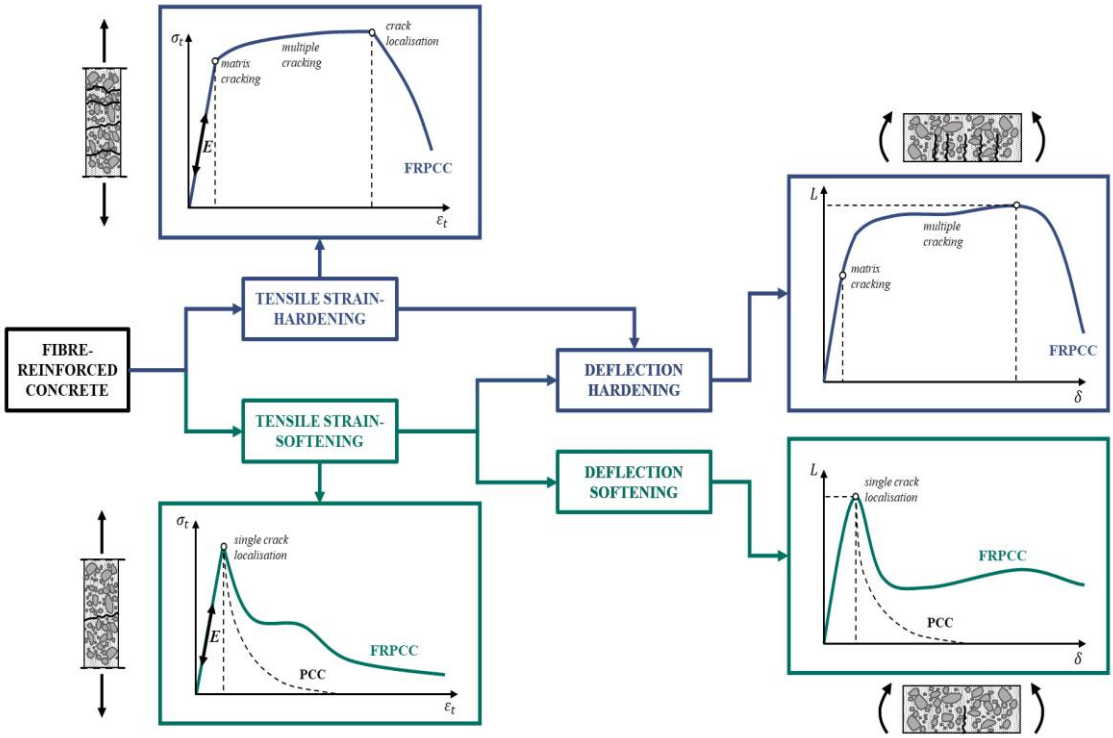

Figure 1.17: Schematic representation of the tensile and flexural response of SFRC (Modified from: [44])

Therefore, bending tests on notched beams are commonly preferred to characterise the tensile behaviour of steel fibre-reinforced concrete. However, being able to correlate the flexural tensile behaviour with the direct tensile behaviour of the material is a challenging task. As shown in Figure 1.17, a material exhibiting strain-softening under uniaxial tension, *i.e.* the stress decreases with increasing loading after the material achieved its maximum tensile stress, may show post-peak deflection softening or hardening behaviour under bending.

Despite decades of intensive investigations, no tensile constitutive law for steel fibre-reinforced Portland cement-based concrete (SFRPCC) garnering widespread consensus among researchers and engineers has yet to be proposed. Both direct and inverse approaches have been adopted by several authors to derive the tensile stress-strain ($\sigma - \varepsilon$) or stress-crack width ($\sigma - w$) relationship for SFRPCC from bending tests, as summarised in Figure 1.18 [117].

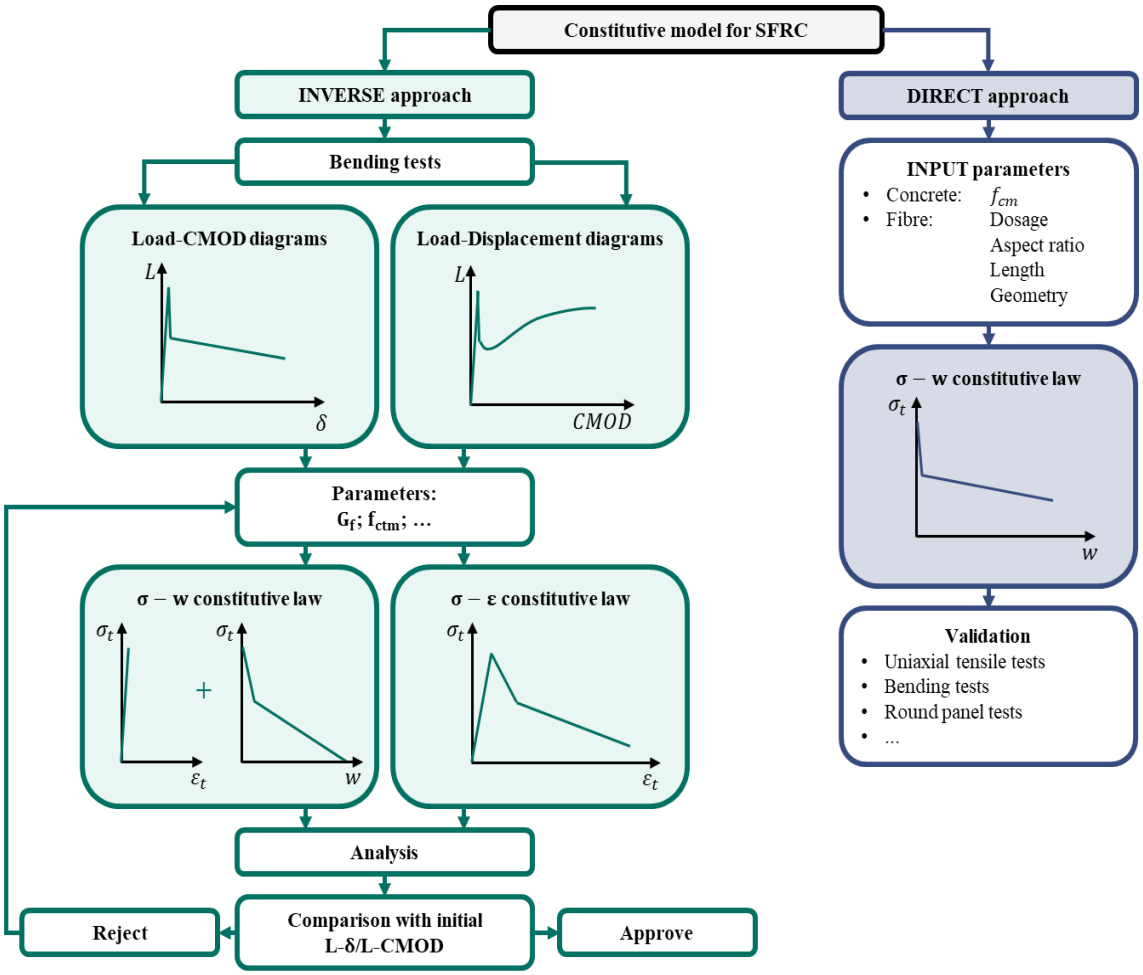

Figure 1.18: Schematic description of the inverse and direct approaches [Modified from: [117]]

To model the quasi-brittle behaviour of plain concrete the fictitious (or cohesive) crack model proposed by Hillerborg et al. [118] has been widely used. According to this model, fracture occurs under uniaxial tensile loading, and the crack propagates when the maximum tensile principal stress at the crack tip reaches the tensile strength (f_t) of the material. Once the tensile strength is reached, a microcracked zone, also known as Fracture Process Zone (FPZ) or fictitious crack, starts developing, in which stress transferring is still occurring (Figure 1.19) [118, 119].

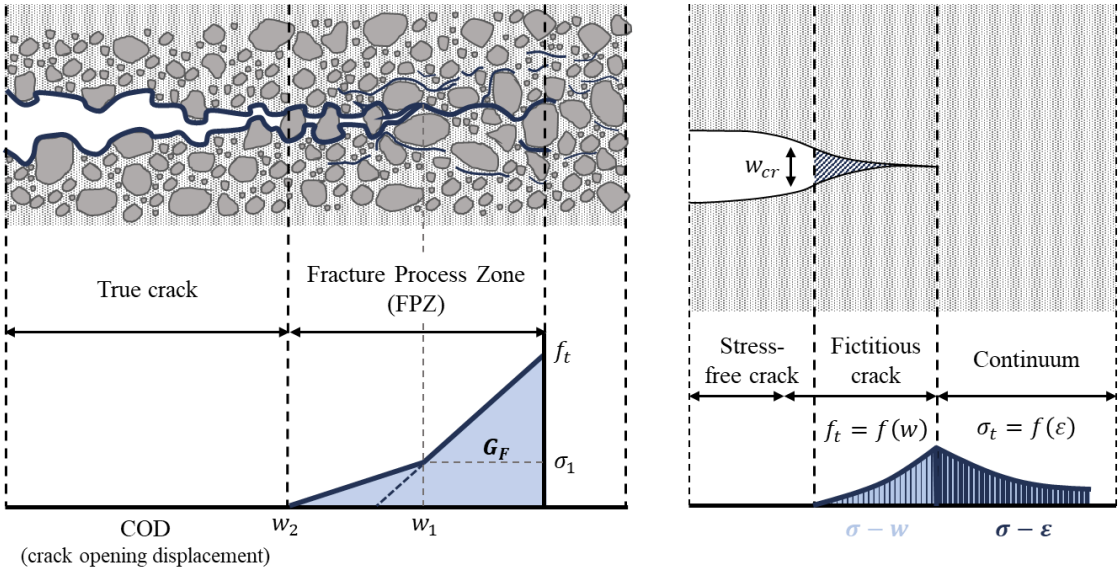

Figure 1.19: Schematic representation of the Hillerborg's fictitious crack approach [Modified from: [119, 120]]

Thus, the concrete response under uniaxial tension is represented by a pre-peak stress-strain curve, where the uncracked material is assumed to exhibit perfect linear elastic behaviour, and a post-peak stress-crack opening relationship.

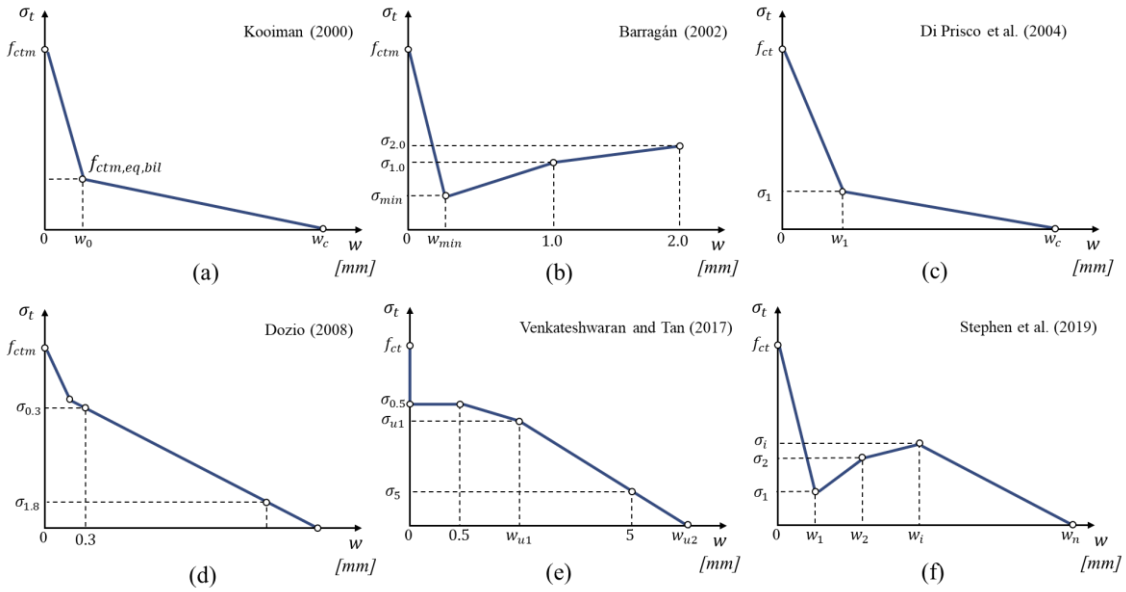

Figure 1.20: Examples of stress-crack width constitutive models proposed in the literature for steel fibre-reinforced concrete [[117, 121 – 122]]

The same model can be applied to SFRC, although the effect of the fibre crack-bridging and stress-transferring ability on the flexural behaviour of the composite needs to be considered, as they can make the difference between post-cracking tensile softening and hardening behaviour. Several authors [117, 121 – 122] used linear, bilinear or multilinear continuous non-differentiable diagrams defined through inverse analysis (Figure 1.20) to simplify the complex tensile post-cracking behaviour of SFRPCC. However, studies evaluating the flexural post-cracking behaviour of SFRAASC and deriving tensile constitutive models for design purposes are still missing.

1.7.3 Analytical and numerical modelling of steel fibre-reinforced alkali-activated slag-based concrete

1.7.3.1 Analytical methods

Analytical correlations predicting the mechanical performance of cement-based concrete from its mix design proportions and/or its compressive strength have served as the foundation for developing design codes and standards. Thus, deriving empirical strength prediction models is essential for encouraging the standardisation and application of alternative materials, such as alkali-activated slag-based concrete, in the construction sector. While several analytical correlations between mechanical performance have been proposed in the literature for plain alkali-activated slag-based concrete (AASC) [123], few studies focus on developing analytical models to predict the mechanical performance of steel fibre-reinforced alkali-activated slag-based concrete (SFRAASC) [124, 125]. Furthermore, the correlations provided for unreinforced concrete cannot always be applied to SFRAASC, as the effect of fibre incorporation on the material behaviour needs to be considered.

Although compressive constitutive models and empirical correlations predicting the mechanical performance of SFRAASC can be easily obtained analytically by fitting the experimental results, deriving the constitutive behaviour of SFRAASC under uniaxial tensile loading, is more challenging, as mentioned in Section 1.7.2. As a result, numerical simulations, such as finite element modelling (FEM), are often preferred.

1.7.3.2 Numerical simulations

For the design of structural members, displacements and stresses under different loading conditions need to be determined. For decades, classical continuum methods have been used to solve equilibrium equations and apply the material stress-strain constitutive laws [126]. Classical approaches, however, are limited to simple geometries, as more intricate structures are governed by increasingly complex equations requiring more sophisticated mathematical problem-solving techniques, such as Finite Element Methods (FEMs) [126]. In a numerical model, each concrete member or structure consists of discrete parts, *i.e.* finite elements. These finite elements are assembled to represent the deformation of the structure under the considered loading conditions and correlated to an assumed admissible displacement field determined by the finite element mesh [126].

Among the currently available finite element models developed for conventional cement-based concrete, the Concrete Damage Plasticity Model (CDPM) implemented in the ABAQUS software is increasingly being used to accurately model the non-linear deformation and irreversible damage of plain PCC in any structure type and loading condition [127].

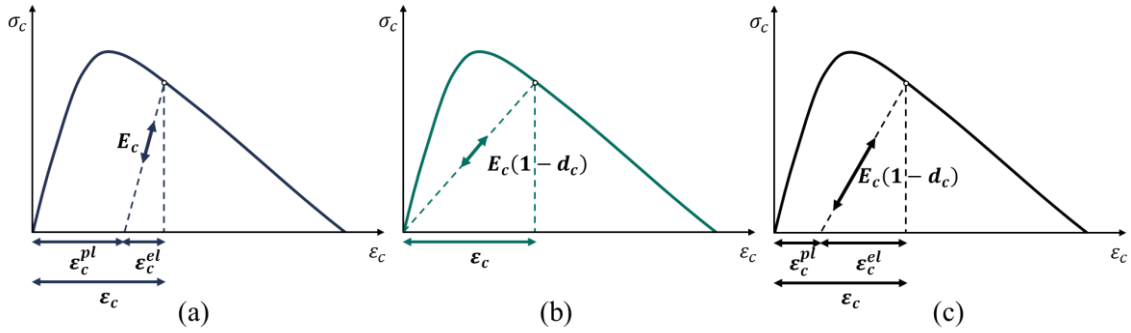

Figure 1.21: Schematic representation of (a) plasticity model, (b) damage model, and (c) damage-plasticity model describing the stress-strain response of concrete under uniaxial compression [Modified from: [128]]

The CDPM combines plasticity theory (Figure 1.21a) with continuum damage mechanics (Figure 1.21b) to account for inelastic deformation and stiffness and strength deterioration of concrete under specific loading conditions (Figure 1.21c) [128]. The linear elastic constitutive model can describe the behaviour of concrete up to the occurrence of inelastic deformations, which can be identified using a plasticity model. Damage and fracture models simulate damage progression, including stiffness degradation, and crack formation, width and propagation, respectively [110].

The CDPM defines concrete failure mechanisms under uniaxial loadings as compressive crushing and tensile cracking, represented by the compressive inelastic strain ε_c^{in} and the tensile cracking strain ε_t^{ck}, respectively, as shown in Figure 1.22. When the concrete sample is unloaded after entering the softening branch of the stress-strain curve, the degradation of elastic stiffness is described by the damage variables d_c (for compressive loading) and d_t (for tensile loading), respectively, as shown in Figure 1.22.

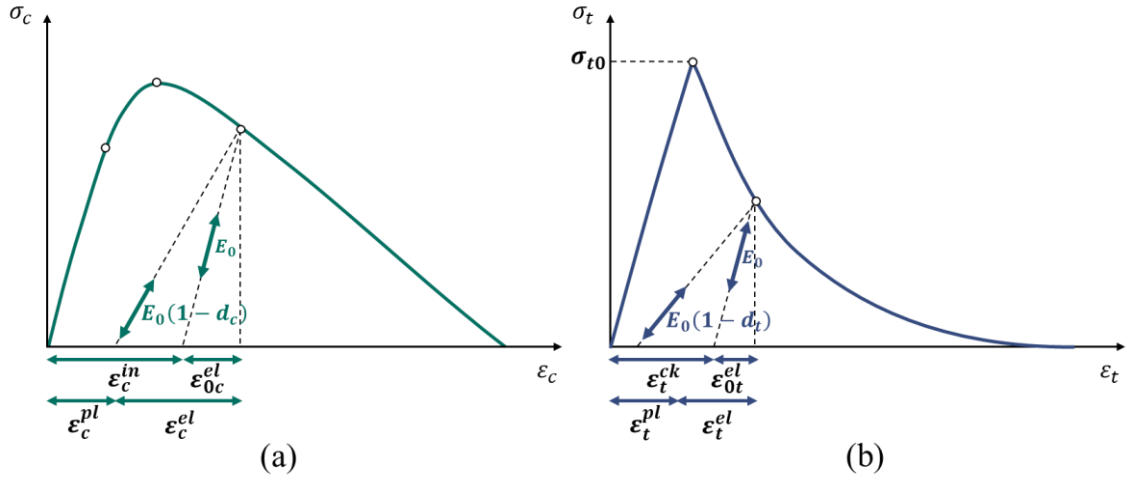

Figure 1.22: Schematic representation of (a) inelastic strain ε_c^{in} and (b) cracking strain ε_t^{ck}

Considering E_0 the concrete initial undamaged elastic stifness, the stress-strain relationship under uniaxial compressive and tensile loading can be written as follows, respectively:

$$\sigma_c = (1 - d_c) \cdot E_0 \cdot \left(\varepsilon_c - \varepsilon_c^{pl}\right), 0 \leq d_c \leq 1 \tag{1.8}$$

$$\sigma_t = (1 - d_t) \cdot E_0 \cdot \left(\varepsilon_t - \varepsilon_t^{pl}\right), 0 \leq d_t \leq 1 \quad (1.9)$$

In addition to the material response under uniaxial loading, additional plasticity parameters are required in the CDPM, *i.e.* dilation angle (Ψ), flow potential eccentricity (e), ratio of biaxial compressive yield stress to uniaxial compressive yield stress (σ_{b0}/σ_{c0}), the ratio of second stress invariant on the tensile meridian to that on the compressive meridian for the yield function, determining the shape of the yield surface (K_c), and the viscosity parameter (μ). The values of these parameters for plain cement-based concrete can be found in the literature [127, 129 – 131] and are summarised in Table 1.9.

Table 1.9: CDPM parameters available in the literature for plain cement-based concrete

Ψ	e	σ_{b0}/σ_{c0}	K_c	μ
$25° \leq \Psi \leq 40°$	0.1	1.12	$0.64 \leq K_c \leq 0.80$	0.0001

1.8 Barriers and limitations to the use of plain and steel fibre-reinforced alkali-activated slag-based concrete in the construction industry

Alkali-activated slag-based concrete (AASC) and steel fibre-reinforced alkali-activated slag-based concrete (SFRAASC) represent promising environmentally friendly alternatives to cement-based concrete (PCC) composites, but their widespread use as construction materials remains limited for the following reasons:

- *Variability of the precursors.* The chemical and physical variability of the wide range of locally available aluminosilicate-rich precursors suitable for alkali activation yields unlimited possible mix design formulations and mechanical and durability performance, which can be tailored to specific requirements for structural and non-structural applications. However, the heterogeneity of the binder limits the concrete reproducibility, limiting its reliability as construction material.

- *Lack of classification.* Although alkali-activated concrete is generally classified into *low-calcium* and *high-calcium* systems based on the calcium content of the precursors, the variability of the binder characteristics, combined with the wide range of suitable activators, results in countless clusters within the same system of concretes exhibiting similar mechanical and durability behaviour. Thus, additional experimental investigations evaluating the performance of different types of alkali-activated concrete within the same material class are needed to provide a more detailed classification based not only on the type and composition of the precursors but also on the concrete mix design formulation, such as binder content, activator type and dosage, liquid-to-binder ratio.

- *Lack of design codes and standards.* The current prescriptive design codes and standards for conventional cement-based concrete, which demand compliance with mix design composition-based criteria, do not apply to alternative cement-free concrete. Thus, a performance-based approach needs to be adopted. Mechanical and durability performance of alternative cement-free concrete must be assessed experimentally to ensure serviceability and safety by meeting the minimum performance requirements outlined in design codes and standards for traditional concrete, regardless of the concrete mix design formulation.

- *Lack of empirical design models.* Empirical strength prediction equations and material constitutive models are the basis of design codes and standards. Although the mechanical behaviour of alkali-activated slag-based concrete has been extensively investigated in the last decades, analytical models predicting its compressive and tensile behaviour are still missing.

- *Novelty of steel fibre-reinforced composites*. Although steel fibre-reinforced cement-based concrete (SFRPCC) is widely used in the construction industry as an alternative to conventionally reinforced cement-based concrete in several applications, including tunnelling and industrial flooring, dedicated design standards have only recently been developed. Furthermore, new fibre types and geometries are periodically developed and commercialised to achieve high-performance composites even at low fibre dosages.

Thus, the novelty of the alkali-activated concrete technology, combined with the ongoing advancement of steel fibre-reinforcement technology, makes steel fibre-reinforced alkali-activated slag-based concrete (SFRAASC) a completely innovative construction material whose performance needs to be evaluated experimentally to derive design tools for its use in practice.

2 Research Scope and Objective

Steel fibre-reinforced alkali-activated slag-based concrete (SFRAASC) has been demonstrated to exhibit enhanced mechanical and durability performance as a construction material, however, its mechanical behaviour has not yet been thoroughly investigated. To date, research studies evaluating experimentally the effect of single (namely 3D) and novel multiple (namely 4D and 5D) hooked-end steel fibres on the compressive and tensile behaviour of alkali-activated slag-based concrete (AASC) are still missing. The scarcity of experimental data makes it difficult to fully characterise the mechanical behaviour of these newly developed composites and to derive analytical and numerical models as the basis for design codes and building regulations. Therefore, the present research work focuses on extending the experimental database currently available in the literature and deriving empirical strength prediction models to promote the use of SFRAASC in practice.

In this research work, alkali-activated slag-based concrete (AASC) and Portland cement-based concrete (PCC) incorporating 3D, 4D and 5D steel fibres in different volume fractions up to 0.75% (60 kg/m^3) have been investigated under compressive and tensile loading. Compressive strength, modulus of elasticity, stress-strain under uniaxial compression, splitting tensile strength and flexural strength have been evaluated experimentally for each matrix and fibre type.

Table 2.1 and Table 2.2 show the chemical composition of the precursors (ground granulated blast furnace slag (GGBFS) and CEM I 42.5R) and the mix proportions used in this study. Sodium hydroxide (SH), sodium silicate (SS) and water have been mixed to achieve a silicate modulus (SiO_2/Na_2O [mol/mol]) of the solution $M_s = 0.5$ and a total concentration of Na_2O equal to 5.3% of the slag weight. The binder content, the aggregate type, grading and content have been kept constant in both AASC and PCC mixes to isolate the effect of the incorporation of steel fibres on the mechanical performance of the composites.

Table 2.1: Chemical composition of the binder used in this study [% by mass]

Binder	CaO	SiO_2	Al_2O_3	Fe_2O_3	MgO	P_2O_5	K_2O	Na_2O	K_b	HM
GGBFS	41.84	35.91	10.74	0.39	6.99	0.47	0.40	0.31	1.05	1.66
CEM	60.80	19.60	5.25	2.38	1.53	0.13	0.80	0.10	-	-

Table 2.2: Mix proportions of the reference AASC and PCC [kg/m^3]

Mix	Slag	CEM	SH	SS	Water	Sand [0-2 mm]	Fine aggregates [2-8 mm]	Coarse aggregates [8-16 mm]
AASC	425	-	50	36	154	660	495	495
PCC	-	425	-	-	229	660	495	495

Table 2.3 shows the properties of the hooked-end steel fibres used in this study. 3D, 4D and 5D fibres have the same length (l_f = 60 mm), diameter (d_f = 0.90 mm) and aspect ratio (l_f/d_f = 65), but they differ in the number of bends at the end of the fibre and in the tensile strength of the wire, with 5D fibres being the most performing of the fibres investigated.

Table 2.3: Properties of the single and multiple hooked-end steel fibres used in this study

Fibre type	Length l_f [mm]	Diameter d_f [mm]	Aspect ratio (l_f/d_f)	Tensile strength [MPa]	Strain at ultimate strength [%]
3D 65/60 BG	60	0.90	65	1160	0.80
4D 65/60 BG	60	0.90	65	1600	0.80
5D 65/60 BG	60	0.90	65	2300	6.00

Each fibre type has been added to each concrete matrix in a volume fraction of 0%, 0.25% (20 kg/m^3), 0.50% (40 kg/m^3) and 0.75% (60 kg/m^3). A total of 20 mixes have been cast and for each mix the compressive and tensile performance have been evaluated experimentally. Table 2.4 summarises the type and amount of samples used for each test performed.

Table 2.4: Properties of the single and multiple hooked-end steel fibres used in this study

Mechanical property	EN Standard	Sample geometry	Amount of samples
Compressive strength	EN 12390-3	Cubes 150 x 150 x 150 mm^3	3
		Cylinders 150 mm x 300 mm	3
Modulus of elasticity	EN 12390-13	Cylinders 150 mm x 300 mm	3
Stress-strain under uniaxial compression	-	Cylinders 150 mm x 300 mm	3
Splitting tensile strength	EN 12390-6	Cylinders 150 mm x 300 mm	6
Residual flexural strength/post-cracking behaviour	EN 14651	Notched beams 150 mm x 150 mm x 550 mm	6
Single-fibre pull-out	-	Prisms 80 mm x 80 mm x 50 mm	6

The aim of this research work is to deepen the knowledge of steel fibre-reinforced alkali-activated concrete and to propose a design tool to facilitate the transition of this material from the laboratory to real-scale applications.

3 Main Findings

This section summarises the findings of the research work carried out on alkali-activated concrete with and without single and multiple hooked-end steel fibres. Part of the experimental results have been published in scientific peer-reviewed papers, which represent the main core of this cumulative dissertation. Figure 3.1 summarises schematically the structure of this thesis and the major key findings

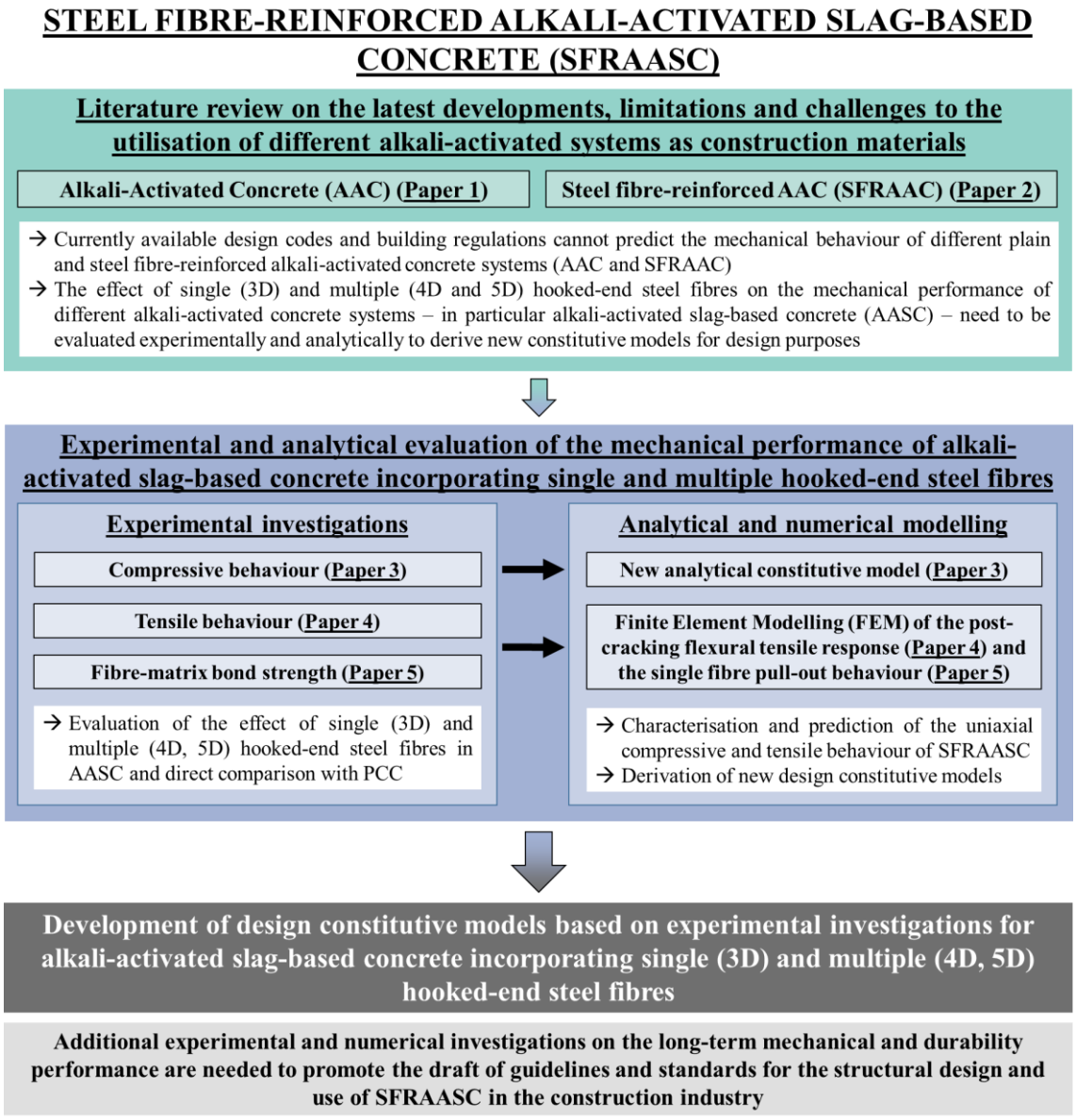

Figure 3.1: Approach and main findings of the present

Firstly, an extensive literature review on the latest developments, limitations and challenges of alkali-activated concrete, with and without the incorporation of steel fibres, as alternative construction material to traditional cement-based concrete has been carried out and summarised in **Paper 1** and **Paper 2**. Since the experimental data available in the literature evaluating the mechanical behaviour of alkali-activated slag-based concrete incorporating single and multiple hooked-end steel fibres are limited, its compressive and tensile behaviour has been investigated and reported in **Paper 3** and **Paper 4**, respectively.

Additionally, **Paper 5** evaluates the fibre-matrix bond by performing single-fibre pull-out tests and its correlation with the flexural post-cracking behaviour of the composite. In the following sections, a short overview of the main findings of each published paper is given.

3.1 Future perspectives for alkali-activated materials: from existing standards to structural applications

This section summarises the findings published in **Paper 1**:

Rossi, L.; de Lima, L.M.; Sun, Y.; Dehn, F.; Provis, J.L.; Ye, G.; De Schutter, G.;
Future perspectives for alkali-activated materials: From existing standards to structural applications. *RILEM Technical Letters* **7**: 159-177 (2022).
DOI: 10.21809/rilemtechlett.2022.160

Paper 1 provides an overview of the stage of development of the alkali-activated concrete technology, its potential as sustainable construction materials and the barriers and challenges hindering its wider commercialisation and application.

3.1.1 Alkali-activated concrete: Stage of the technology development and its potential as construction material

Alkali-activated concrete has been widely investigated in the last decades as a possible solution to reduce the cement and concrete demand, minimising the CO_2 emissions and energy consumption related to their production. The race for carbon neutrality in the construction section has intensified the interest in environmentally friendly materials, such as alkali-activated concrete, which actually date back to the first applications in the 1950s [17]. The local availability and the variability of the chemical and mineralogical composition of the aluminosilicate-rich binders and alkaline activators were the main key factors promoting the use of alkali-activated concrete in the construction field. The countless possible binder-activator combinations provide a wide range of mix design formulations which can be optimised on a case-by-case basis to fit the mechanical and durability performance requirements of the end application [22].

3.1.2 Alkali-activated concrete: Barriers and challenges

The versatility of alkali-activated concrete represents not only its main strength but also the main obstacle to its standardisation and commercialisation. The differences in chemistry and mineralogy characteristics between different binders require an optimisation of the mix design formulation when a new precursor is used. Thus, a universal mix design procedure cannot be applied to alkali-activated concrete. A classification of alkali-activated concrete according to the properties of its main components and a correlation between these characteristics and the mechanical and durability performance of the concrete mix is needed. Design standards developed for traditional Portland cement concrete correlate the concrete mix design parameters, *i.e.* cement type and content and water/binder ratio, with the mechanical performance, *i.e.* the compressive strength, of the hardened concrete. However, the high amount of parameters involved in the mix design of alkali-activated concrete makes defining a correlation between mechanical performance and mix design difficult. A shift from prescriptive to performance-based design codes and regulations is needed.

In a performance-based approach, mix design components and proportions to achieve the required mechanical and durability performance are not specified. Thus, the mechanical performance of different alkali-activated concretes obtained with different binder and activator types in different proportions needs to be evaluated experimentally to identify correlations between the concrete type and its behaviour.

In **Paper 1**, the data available in the literature on the mechanical performance of alkali-activated fly ash-based, slag-based concrete and blended systems are collected and used to compare the behaviour of alkali-activated concretes with traditional cement-based concrete. For this purpose, the analytical correlations proposed by European and international standards between the mechanical properties of concrete, *i.e.* compressive strength, modulus of elasticity and tensile strength, are considered.

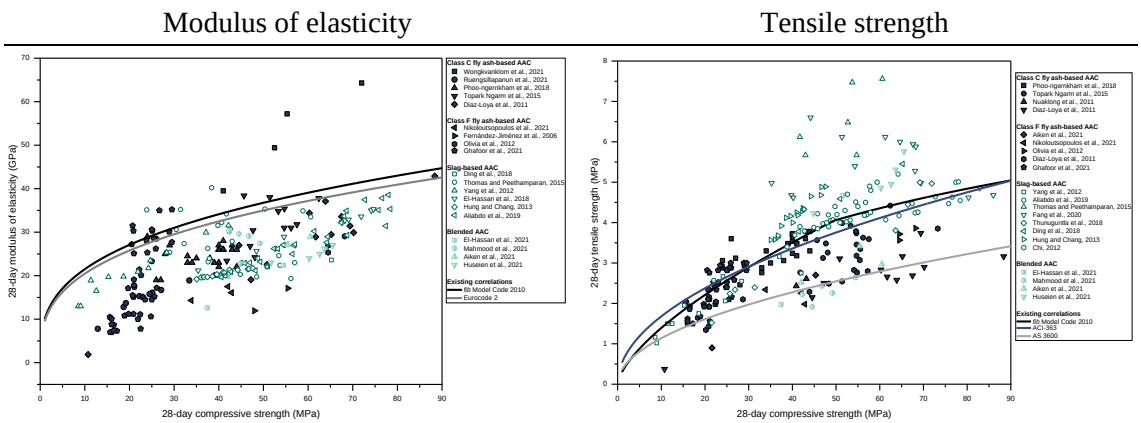

Figure 3.2: Correlation between the compressive strength and (a) the modulus of elasticity and (b) the tensile strength of different alkali-activated concretes

As shown in Fig. 3.2a, alkali-activated concretes exhibit a lower modulus of elasticity in comparison to traditional cement-based concrete of similar strength grade. Thus, the analytical correlations proposed by currently available design standards, including the *fib* Model Code 2010, overestimate the value of the modulus of elasticity for alkali-activated concretes, for each binder type. When the tensile strength is considered (Fig. 3.2b), alkali-activated slag-based concrete shows higher values of strength in comparison to fly ash-based and blended systems and no clear correlation with cement-based concrete of similar strength grade is seen. Thus, new correlations for each binder type need to be derived to describe and predict the mechanical behaviour of alkali-activated concrete.

New analytical correlations to estimate the modulus of elasticity and the tensile strength from the compressive strength have been derived in **Paper 1**. Eq. (3.1) and Eq. (3.2) represent the generalised equations used based on the ones proposed in the *fib* Model Code 2010 and Table 3.1 summarises the values of the parameters a and b fitted for each type of binder and the relative R^2 values.

$$E_c = a \cdot 21.5 \cdot \left(\frac{f_{cm}}{10}\right)^{1/3} \tag{3.1}$$

$$f_{ctm} = b \cdot (f_{cm})^{2/3} \quad (3.2)$$

where E_c and f_{ctm} are the mean experimental modulus of elasticity and the tensile strength, respectively, and f_{cm} is the mean compressive strength.

Table 3.1: Values of the parameters a and b for different alkali-activated systems

Parameter	Slag-based concrete	Fly ash-based concrete	Blended systems
a	0.738 (R^2 = 0.356)	0.583 – 0.810 (R^2 = 0.434 to 0.379)	0.673 (R^2 = 0.135)
b	0.306 (R^2 = 0.408)	0.212 – 0.297 (R^2 = 0.853 to 0.538)	0.255 (R^2 = 0.373)

Values of $a < 1$ reflect the lower modulus of elasticity of alkali-activated concretes in comparison to traditional cement-based concrete of similar strength grade. However, the low values of R^2 indicate a high scatter of the available data point, as different mix design proportions for the same binder type have been considered.

To overcome the current barriers to the standardisation of alkali-activated concretes and to broaden their application as reliable and environmentally friendly construction material a more accurate classification of alkali-activated systems based not only on the binder type and chemical composition but also on the activator type, dosage and proportions is needed. Furthermore, additional experimental data are necessary to better understand the correlation between the mix design formulation and the mechanical performance of alkali-activated concretes and predict their behaviour from the sole compressive strength as proposed in design codes and building regulations for traditional cement-based concrete.

3.2 New analytical models to predict the mechanical performance of steel fibre-reinforced alkali-activated concrete

This section summarises the findings published in **Paper 2**:

Rossi, L.; Patel, R.A.; Dehn, F.;
New analytical models to predict the mechanical performance of steel fibre-reinforced alkali-activated concrete. *Structural Concrete* (2024)
DOI: 10.1002/suco.202301104

Paper 2 evaluates the applicability of currently available empirical models to predict the mechanical performance, *i.e.* compressive strength (f'_{cuf}), modulus of elasticity (E_{cyf}), splitting (f'_{sptf}) and flexural (f'_{lf}) tensile strength, of different alkali-activated concretes incorporating steel fibres in different volume fractions. First, experimental data available in the literature for slag-based, fly ash-based, and blended alkali-activated concrete incorporating steel fibres have been collected and used to evaluate the accuracy of existing prediction models proposed for steel fibre-reinforced cement-based concrete (SFRPCC). Then, the parameters of the investigated analytical correlations have been recalibrated for each binder type.

3.2.1 Applicability of existing analytical models to steel fibre-reinforced alkali-activated concrete

Although several empirical equations have been proposed to predict the mechanical performance of steel fibre-reinforced cement-based concrete (SFRPCC), only the correlations proposed by Guler et al. [42] and Thomas and Ramaswamy [132] have been considered and summarised in Table 3.2. These analytical expressions correlate the performance of the fibre-reinforced composite to the performance of the reference concrete, *i.e.* compressive strength (f'_{cu}), and the characteristics of the steel fibres used, *i.e.* fibre volume fraction (v_f) and fibre reinforcing index (RI_v).

Table 3.2: Existing models predicting the mechanical performance of SFRPCC investigated in this paper

Mechanical property	Empirical model	Ref.
Compressive strength	$f'_{cuf} = 0.92f'_{cu} - 1.44v_f + 14.6RI_v$	[42]
Modulus of elasticity	$E_{cyf} = 4{,}58(f'_{cu})^{0.5} + 0.42f'_{cu}RI_v + 0.39RI_v$	[132]
Splitting tensile strength	$f'_{sptf} = 0.12f'_{cu} - 0.71v_f + 6.47RI_v$	[42]
Flexural strength	$f'_{lf} = 0.24f'_{cu} + 1.12v_f + 7.10RI_v$	[42]

The equation proposed by Guler et al. [42] correlating the compressive strength of the steel fibre-reinforced composite with the compressive strength of the reference concrete without fibres can

predict the strength of SFRAAC quite accurately, as steel fibres has a limited effect on the compressive strength for volume fractions lower than 1% [133 – 134]. The equations proposed by Guler et al. [42] and Thomas and Ramaswamy [132] to predict the modulus of elasticity, splitting and flexural tensile strength of SFRPCC overestimate the values of such properties for SFRAAC, regardless of the matrix type. Alkali-activated concrete shows generally lower modulus of elasticity and tensile strength than cement-based concrete of similar strength grade.

Thus, the parameters of the equations summarised in Table 3.2 are recalibrated using the experimental data available in the literature for each binder type. Table 3.3 summarises the new empirical correlations obtained for steel fibre-reinforced alkali-activated slag-based, fly ash-based and blended concrete.

Table 3.3: Proposed empirical models to derive the mechanical properties of SFRAAC

Mechanical property	Empirical models		
	Slag-based AAC	Fly ash-based AAC	Blended AAC
Compressive strength	$f'_{cuf} = 1.04f'_{cu} + 2.12RI_v$	$f'_{cuf} = 0.95f'_{cu} + 18.78RI_v$	$f'_{cuf} = 1.20f'_{cu} + 0.80RI_v$
Modulus of elasticity	$E'_{cf} = 3.68(f'_{cu})^{0.5} + 9.07RI_v$	$E'_{cf} = 4.55(f'_{cu})^{0.5} + 8.57RI_v$	$E'_{cf} = 4.28(f'_{cu})^{0.5} + 0.06f'_{cu}RI_v$
Splitting tensile strength	$f'_{sptf} = 0.07f'_{cu} + 1.85RI_v$	$f'_{sptf} = 0.10f'_{cu} + 0.87RI_v$	$f'_{sptf} = 0.08f'_{cu} + 0.19RI_v$
Flexural strength	$f'_{lf} = 0.10f'_{cu} + 4.17v_f$	$f'_{lf} = 0.10f'_{cu} + 7.05RI_v$	$f'_{lf} = 0.13f'_{cu} + 0.55RI_v$

As shown in Table 3.3, the correlations predicting the compressive strength, the modulus of elasticity and the splitting tensile strength of SFRAAC only depend on the compressive strength of the reference concrete and the fibre reinforcing index, while the fibre volume fraction has no direct effect on such performances. The same applies for the flexural strength, but only for fly ash-based and blended concrete, while for slag-based concrete the fibre volume fraction and not the fibre reinforcing index has a direct effect on the flexural strength. This could be due to the limited amount of experimental data available in the literature. Thus, additional investigations are needed to confirm the findings obtained in this paper.

Figure 3.3 shows the accuracy of the existing empirical correlations developed for SFRPCC and the newly calibrated equations proposed in this study to predict the mechanical performance of SFRAAC. Although additional experimental data are needed to validate the findings summarised in this paper, the newly calibrated analytical models can predict the mechanical performance of SFRAAC more accurately than the original models developed for SFRPCC.

Compressive strength

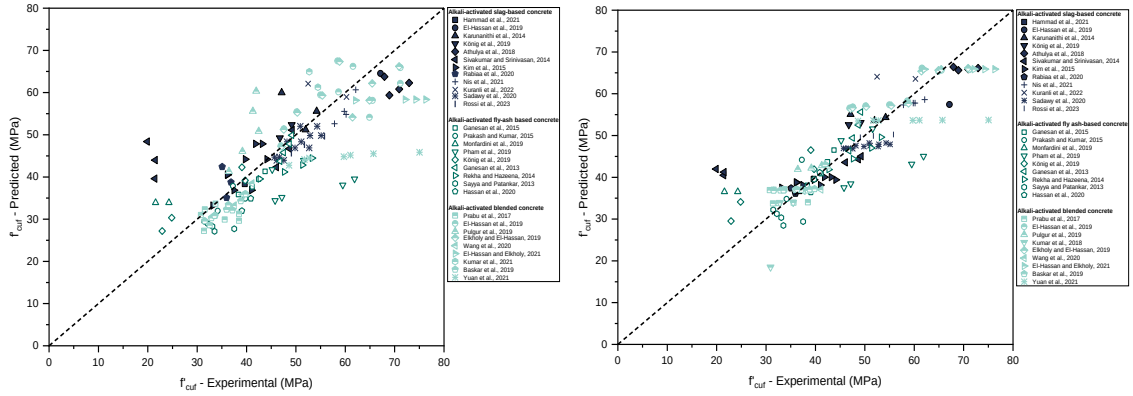

(a) (b)

Modulus of elasticity

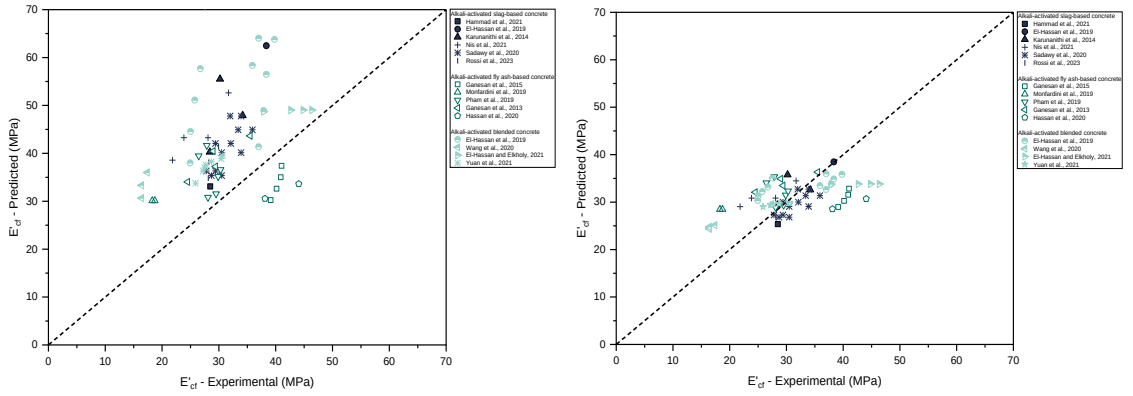

(c) (d)

Splitting tensile strength

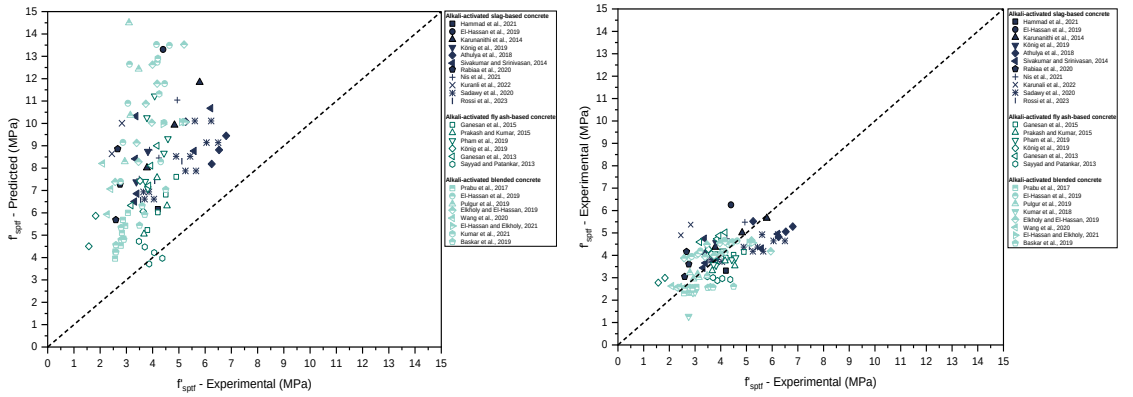

(e) (f)

Figure 3.3: Correlation between the experimental and predicted values of (a, b) compressive strength, (c, d) modulus of elasticity and (e, f) splitting tensile strength of different SFRAACs obtained by applying the original and the newly calibrated empirical equations

Flexural strength

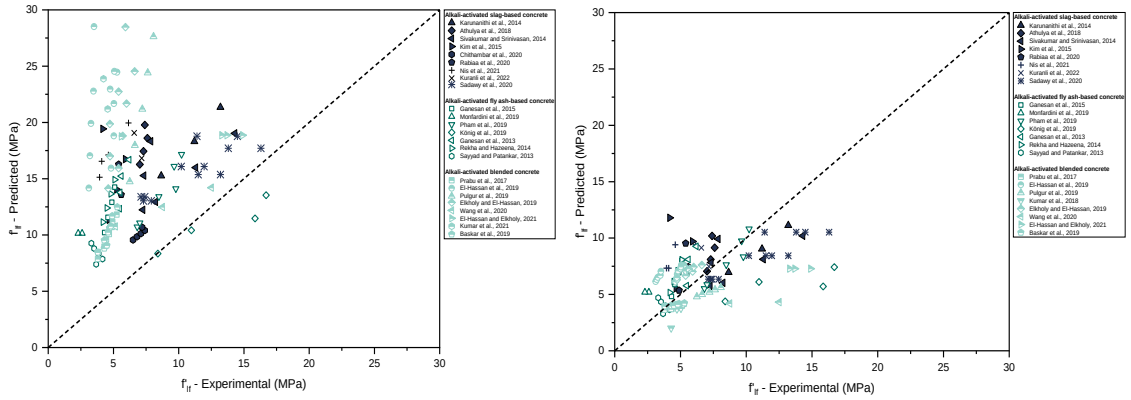

(g) (h)

Figure 3.3 (continued): Correlation between the experimental and predicted values of (g, h) flexural tensile strength of different SFRAACs obtained by applying the original and the newly calibrated empirical equations

3.3 Compressive behaviour of alkali-activated slag-based concrete incorporating single and multiple hooked-end steel fibres

This section summarises the findings published in **Paper 3**:

Rossi, L.; Patel, R.A.; Dehn, F.;
Compressive behaviour of alkali-activated slag-based concrete and Portland cement concrete incorporating novel and multiple hooked-end steel fibres.
Materials and Structures, 56-96 (2023).
DOI: 10.21809/rilemtechlett.2022.160

Paper 3 evaluates the stress-strain response under uniaxial compression of alkali-activated slag-based concrete incorporating single and multiple hooked-end steel fibres in different volume fractions. From the experimental stress-strain curves, a new analytical model to predict the compressive response of steel-fibre reinforced alkali-activated slag-based concrete has been developed. The model has been calibrated on experimental compressive stress-strain curves available in the literature and validated using the experimental data generated in this study, improving its applicability to alkali-activated slag-based concrete incorporating different steel fibre types and dosages. Additional information related to the concrete mix design, sample preparation, curing and experimental test procedures used can be found in **Paper 3**.

3.3.1 Mix design and samples preparation

Ground granulated blast furnace slag, sodium hydroxide and sodium silicate have been used as binder and alkaline activators, respectively. Single and multiple hooked-end steel fibres, namely 3D (single), 4D (double) and 5D (triple) hooked-end steel fibres, with a length of 60 mm and diameter of 0.90 mm (Figure 3.4), have been added to the alkali-activated matrix in volume fractions of 0.25%, 0.50% and 0.75%. A reference Portland cement concrete (CEM I 42.5R) with same binder content, aggregate type and grading curve, incorporating the same fibre types and dosages, has been also investigated.

Figure 3.4: Schematic representation of the geometry of 3D (left), 4D (centre) and 5D (right) hooked-end steel fibres. The arrows identify the number of bends at the ends of the fibre

Cylinders with a diameter of 150 mm and a height of 300 mm have been prepared for each matrix type, fibre type and dosage. Each experimental curve shown in the following section is the average of three samples. Each mixture is denoted by the matrix type (AASC or PCC), the fibre type (3D, 4D or 5D) and the fibre volume fraction (25 (0.25%), 50 (0.50%) or 75 (0.75%)). The reference concrete is defined as REF.

3.3.2 Stress-strain behaviour under uniaxial compression

Figure 3.5 shows the experimental compressive stress-strain curves for alkali-activated slag-based concrete (AASC) and traditional cement-based concrete (PCC) incorporating 3D, 4D and 5D fibres in different volume fractions up to 0.75%.

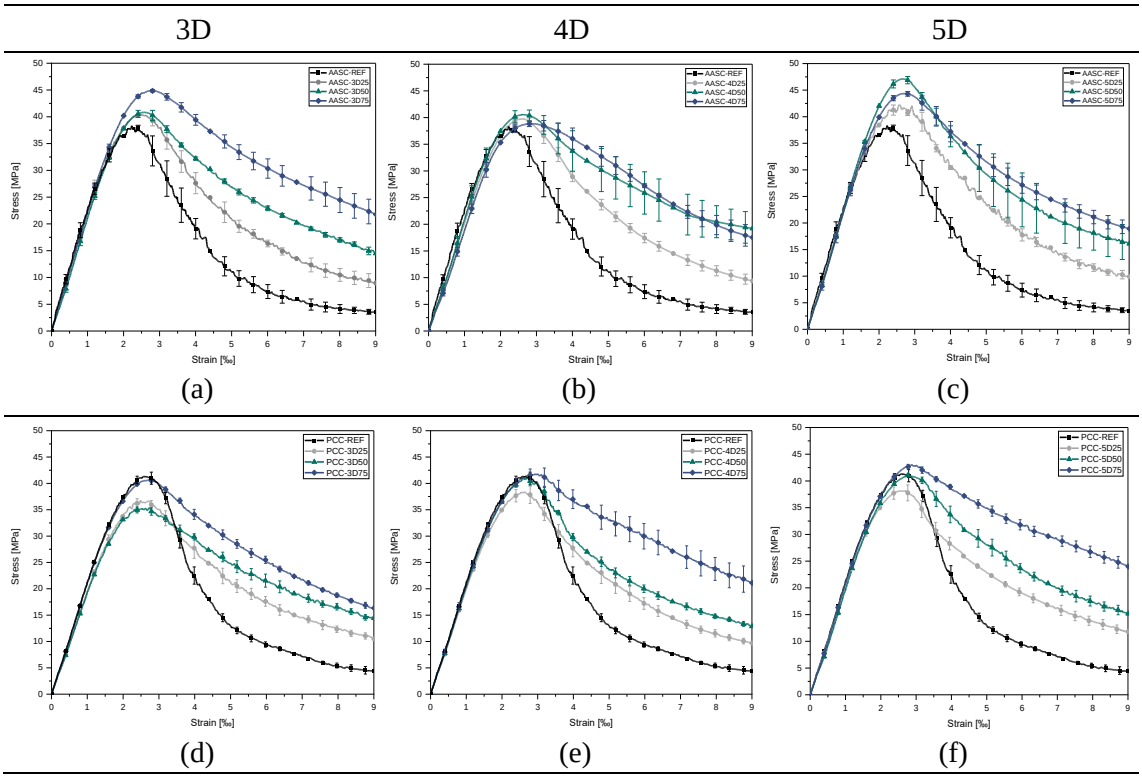

Figure 3.5: Experimental stress-strain curves for AASC and PCC mixes incorporating 3D (a, d), 4D (b, e) and 5D (c, f) hooked-end steel fibres in different volume fractions

For both AASC and PCC mixes, the incorporation of single and multiple hooked-end steel fibres enhances the post-peak load-bearing capacity of the composite, which increases with the increase of the fibre volume fraction. Although for PCC mixes hooked-end steel fibres has a limited effect on the peak stress and corresponding strain, a significant improvement can be observed for AASC mixes, *i.e.* the composite ductility increases with the increase of the fibre volume fraction for each fibre type.

3.3.3 New analytical model for the stress-strain behaviour of FRAASC under uniaxial compression

Currently available analytical models developed for plain and steel fibre-reinforced cement-based concrete are not able to predict the behaviour of alkali-activated slag-based concrete incorporating single and multiple hooked-end steel fibres under uniaxial compression. Thus, a new analytical model to describe the stress-strain response of FRAASC under uniaxial compression is proposed as follows:

$$\frac{\sigma_c}{\sigma_{c,max(FRC)}} = \begin{cases} \dfrac{\beta(\varepsilon_c/\varepsilon_{c,max(FRC)})}{\beta-1+(\varepsilon/\varepsilon_{c,max(FRC)})^{\beta}} & \varepsilon/\varepsilon_{c,max(FRC)} \leq 1 \\ e^{\gamma(1-\varepsilon_c/\varepsilon_{c,max(FRC)})} & \varepsilon/\varepsilon_{c,max(FRC)} > 1 \end{cases} \quad (3.3)$$

where σ_c is the compressive stress and ε_c is the corresponding strain, $\sigma_{c,max(FRC)}$ is the maximum compressive stress of the composite and $\varepsilon_{c,max(FRC)}$ is the corresponding peak strain, β and γ are material parameters governing the pre-peak and post-peak behaviour, respectively, as shown in Fig. 3.6.

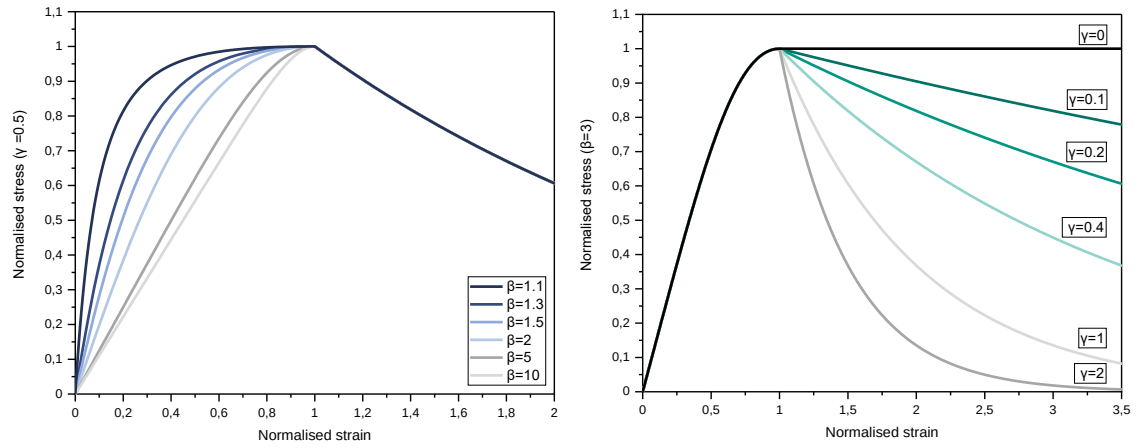

Figure 3.6: Effect of the material parameters (a) β and (b) γ on the compressive stress-strain curve of steel fibre-reinforced concrete

The pre-peak ascending branch of the stress-strain curve is mainly dependent on the matrix modulus of elasticity, while the post-peak descending branch is governed by the fibre reinforcing index and the ratio between the stress corresponding to a strain of 0.0035 mm/mm and the peak stress. The model parameters β and γ are linked to the peak stress ($\sigma_{c,max(REF)}$) and corresponding strain ($\varepsilon_{c,max(REF)}$) of the concrete plain matrix – without steel fibres – and the fibre reinforcing index, *i.e.* only knowing these three inputs it is possible to calculate the model parameters and derive the compressive stress-strain curves.

The model has been calibrated on a wide range of compressive stress-strain curves available in the literature for both steel fibre-reinforced cement-based concrete and steel fibre-reinforced alkali-activated slag-based concrete. The experimental curves obtained in this study for alkali-activated slag-based concrete mixes incorporating different hooked-end steel fibres in different volume fractions have been used to validate the proposed model. Figure 3.7 shows the experimental and analytical stress-strain curves obtained for AASC incorporating 3D, 4D and 5D hooked-end steel fibres in different volume fractions.

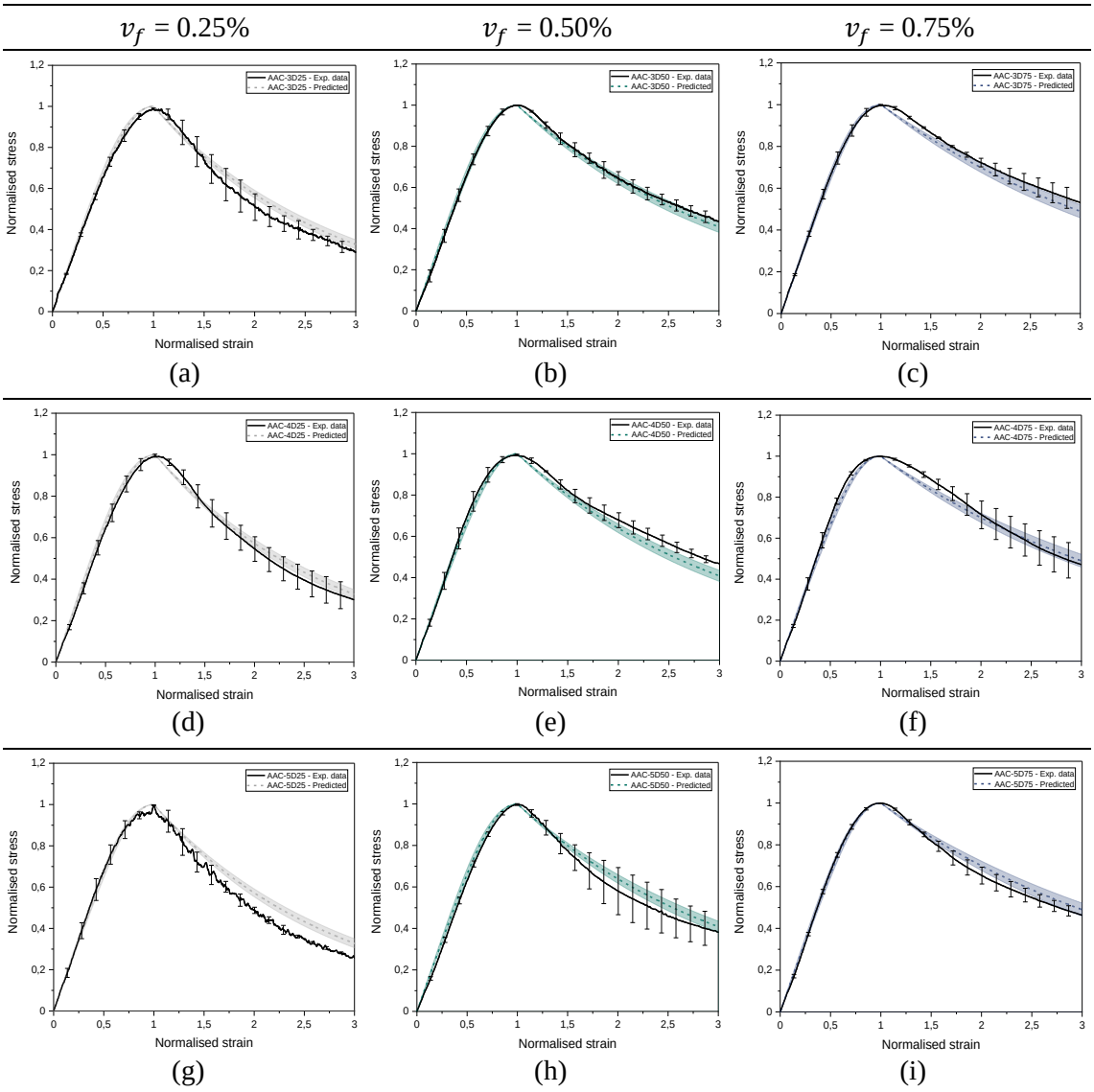

Figure 3.7: Experimental and analytical stress-strain curves of AASC incorporating (a-c) 3D, (d-f) 4D and (g-i) 5D hooked-end steel fibres in different volume fractions

Although the model can predict quite accurately the stress-strain response of steel fibre-reinforced alkali-activated slag-based concrete under uniaxial compression, additional experimental data are needed to further calibrate the model to different concrete matrices, *i.e.* fly ash-based alkali-activated concrete or blended systems, and different fibre types and volume fractions.

3.4 Flexural tensile behaviour of alkali-activated slag-based concrete and Portland cement-based concrete incorporating single and multiple hooked-end steel fibres

This section summarises the findings collected in **Paper 4**:

Rossi, L.; Patel, R.A.; Dehn, F.;
Flexural tensile behaviour of alkali-activated slag-based concrete and Portland cement-based concrete incorporating single and multiple hooked-end steel fibres
DOI: 10.1016/j.jobe.2024.111090

Paper 4 evaluates the post-cracking tensile behaviour of alkali-activated slag-based concrete and Portland cement-based concrete incorporating single and multiple hooked-end steel fibres in different volume fractions. Three-point bending tests (3PBT) on notched beams according to EN 14651 have been performed, and load-CMOD (Crack Mouth Opening Displacement) curves have been generated. The effect of concrete matrix type and the fibre geometry and volume fraction on the flexural strength corresponding to the limit of proportionality (f_{LOP}) and on the residual flexural strengths f_{R1} and f_{R3}, corresponding to a CMOD of 0.5 mm and 2.5 mm, respectively, have been evaluated. The applicability to SFRAASC of currently available empirical models developed for SFRPCC to predict the values of f_{R1} and f_{R3} has been assessed, and new correlations have been proposed. Furthermore, the tensile constitutive models proposed by the *fib* Model Code 2020 have been used as input parameters for numerical simulations to predict the flexural behaviour of SFRAASC. However, the tensile constitutive model and the assumptions of the Concrete Damage Plasticity (CDP) model used, *i.e.* homogeneous material and tensile post-cracking softening, lead to qualitatively but not quantitatively accurate results. Additional information related to the concrete mix design, sample preparation, experimental test procedures and numerical inverse analysis used can be found in **Paper 4**.

3.4.1 Post-cracking flexural behaviour

Six beams with a dimension of 150 mm x 150 mm x 550 mm have been prepared for each matrix type, fibre type and volume fraction. The post-cracking flexural behaviour has been evaluated experimentally according to EN 14651, *i.e.* the Crack Mouth Opening Displacement (CMOD) have been recorded up to a value of 4 mm. The mean experimental load-CMOD curves for SFRAASC and SFRPCC are shown in Figure 3.8.

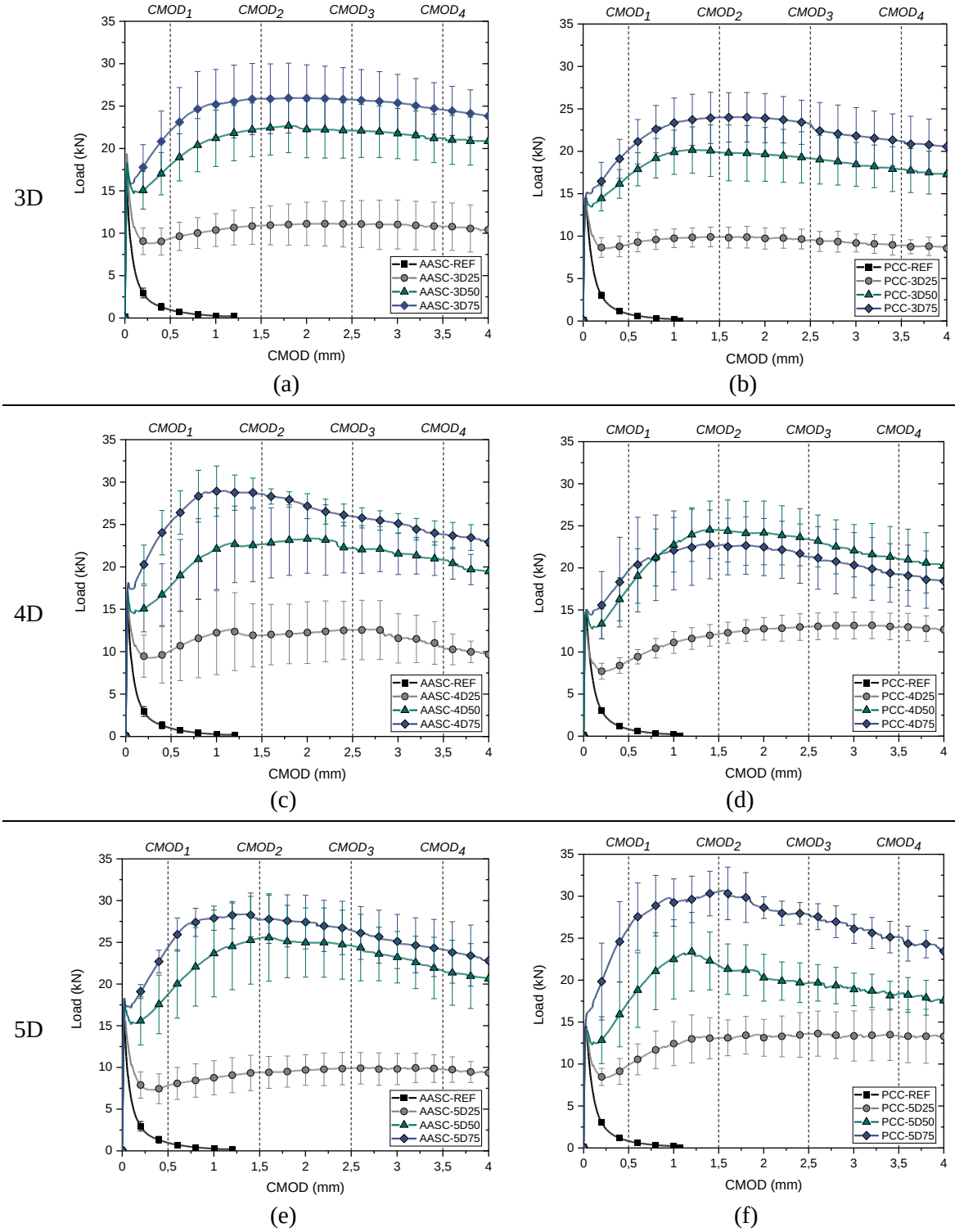

Figure 3.8: Experimental load-CMOD curves for SFRAASC and SFRPCC mixes incorporating (a, b) 3D, (c, d) 4D and (e, f) 5D hooked-end steel fibres in different volume fractions

3.4.1.1 Effect of the concrete matrix type on the flexural response

Figure 3.9 shows the effect of the concrete matrix type, *i.e.* 28-day mean compressive strength and modulus of elasticity, on the flexural strength f_{LOP} and on the residual flexural strengths f_{R1} and f_{R3} for each fibre type.

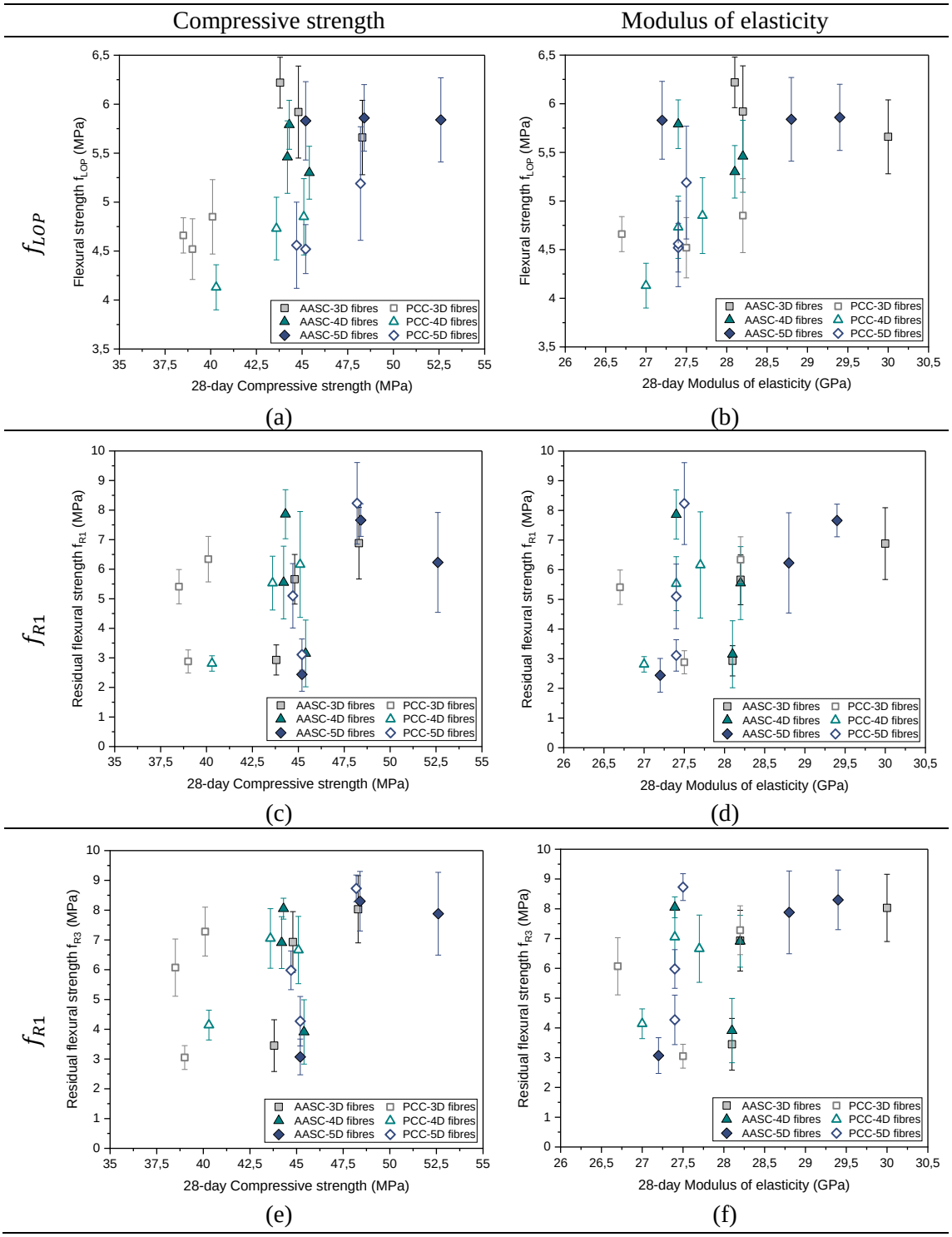

Figure 3.9: Effect of the 28-day compressive strength and modulus of elasticity on (a, b) the flexural strength f_{LOP} and (c, d) the residual flexural strengths f_{R1} and (e, f) f_{R3} for both SFRAASC and SFRPCC

Although SFRAASC mixes exhibit higher values of f_{LOP} than SFRPCC mixes for each fibre type, no clear relationship to the 28-day compressive strength and modulus of elasticity can be seen, i.e. similar values of compressive strength or elastic modulus result in significantly different values of f_{LOP}. The same behaviour can be observed for the residual flexural strengths f_{R1} and f_{R3}. No clear correlation between the mechanical performance of the concrete matrix and the residual flexural strengths can be seen. Thus, the concrete matrix performance have a limited effect on the flexural behaviour, although the matrix type can affect the fibre-matrix interaction and therefore enhance the flexural post-cracking response of the composites even for similar values of compressive strength and modulus of elasticity.

3.4.1.2 Effect of the fibre geometry and volume fraction on the flexural response

Figure 3.10 shows the effect of the fibre volume fraction and geometry on the mean values of the f_{LOP}, f_{R1} and f_{R3}, and the corresponding characteristic values $f_{R1\mathrm{k}}$ and $f_{R3\mathrm{k}}$, for each concrete matrix type. The incorporation of single and multiple hooked-end steel fibres has a limited effect on f_{LOP} of SFRPCC, whose value exceeds that of the reference concrete only for fibre volume fractions ≥ 0.50% and slightly increases with the increase of the fibre content (Figure 3.10b). Contrarily, SFRAASC mixes exhibit higher values of f_{LOP} in comparison to the reference concrete for each fibre type and volume fraction (Figure 3.10a). However, no clear correlation between the fibre dosage and f_{LOP} can be seen, also due to the high variability of the experimental results.

The effect of the fibre geometry and dosage is more significant on the post-cracking behaviour of the composite. The increase of fibre dosage corresponds to an increase in post-peak load-bearing capacity at the cracked state of the material, with the residual flexural strengths f_{R1} and f_{R3} increasing with the increase of the fibre content for both SFRAASC and SFRPCC for each fibre type, as shown in Figure 3.10c – 3.10f. SFRAASC incorporating 3D and 4D fibres outperform the corresponding SFRPCC mixes, while SFRPCC mixes incorporating 5D fibres show higher values of post-peak residual load than the corresponding SFRAASC. The characteristic values $f_{R1\mathrm{k}}$ and $f_{R3\mathrm{k}}$ follow a similar trend as the corresponding mean experimental values for each concrete matrix and fibre type, *i.e.* they generally increase with the increase of the fibre volume fraction. However, their values are significantly affected by the variability of the experimental results. Thus, the mixes showing the highest values of f_{R1} and f_{R3} do not necessarily show the highest values of $f_{R1\mathrm{k}}$ and $f_{R3\mathrm{k}}$. For example, PCC-3D75 and PCC-4D75 show similar values of f_{R1} (6.34 and 6.16 MPa, respectively) but different values of $f_{R1\mathrm{k}}$ (4.98 and 2.99 MPa, respectively). AASC-4D75 and AASC-5D75 show similar values of f_{R3} (8.05 and 8.30 MPa, respectively) but the values of $f_{R3\mathrm{k}}$ vary significantly (7.4 and 6.5 MPa, respectively).

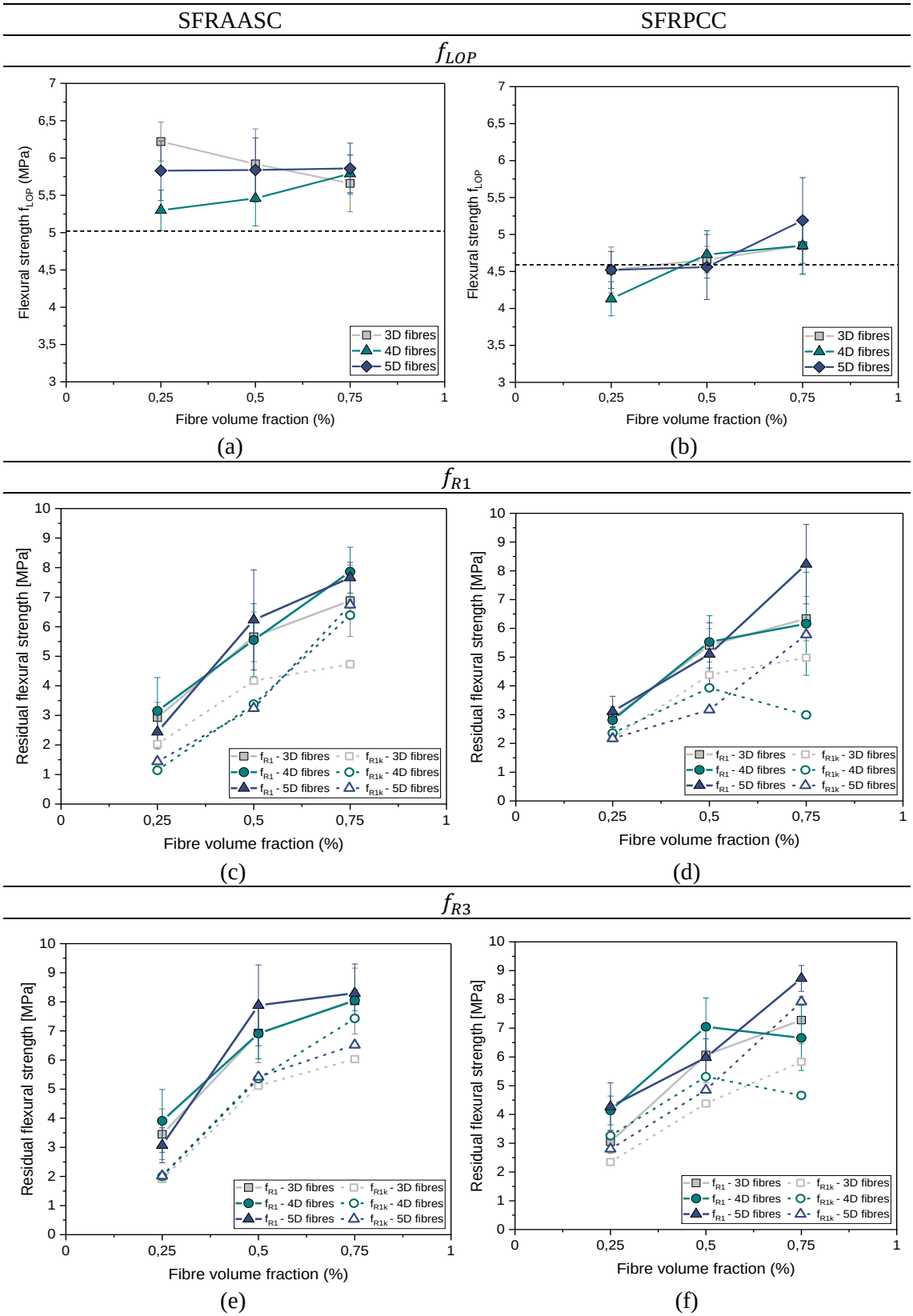

Figure 3.10: Effect of the fibre volume fraction on the flexural strength f_{LOP} and the residual flexural strengths f_{R1} and f_{R3}, and the corresponding characteristic values f_{R1k} and f_{R3k}, for both SFRAASC and SFRPCC. The dashed line represents the value of f_{LOP} for the reference mix without fibres

3.4.2 Analytical and numerical modelling

3.4.2.1 Empirical models to derive the residual flexural strengths f_{R1} and f_{R3}

According to the *fib* Model Code 2010, the experimental values of the residual flexural strengths f_{R1} and f_{R3} are used to derive tensile constitutive models for the design of steel fibre-reinforced composites. Thus, several authors proposed empirical models (Table 3.4) to derive the values of f_{R1} and f_{R3} for SFRPCC allowing a preliminary evaluation of the material performance minimising the amount of experiments needed.

Table 3.4: Existing empirical models predicting the values of f_{R1} and f_{R3} of SFRPCC

Author	Empirical model	Ref.
Moraes Neto et al., 2014	$f_{R1} = 7.5 \cdot (RI_v)^{0.8}$ $f_{R3} = 6.0 \cdot (RI_v)^{0.7}$	[135]
Venkateshwaran et al., 2018	$f_{R1} = \Psi \cdot \left(0.32(f_{cm})^{\frac{1}{2}} + 6.214RI_v + 0.034N^2\right)$ $f_{R3} = \Psi \cdot \left(0.30(f_{cm})^{\frac{1}{2}} + 7.629RI_v + 0.373N^2\right)$	[136]
Chen et al., 2021	$f_{R1} = 0.09120\left(f_{cu,0}\right)^{\frac{2}{3}} \cdot \left[1 + \left(0.0899l_f + 1.29476(N)^{\frac{1}{2}}\right) \cdot RI_v\right]$ $f_{R3} = 0.08594\left(f_{cu,0}\right)^{\frac{2}{3}} \cdot \left[1 + \left(0.0382l_f + 4.60597(N)^{\frac{1}{2}}\right) \cdot RI_v\right]$	[53]
Oettel et al., 2022	$f_{R1} = \frac{1}{0.37} \cdot k \cdot v_f \cdot \left(1 - k \cdot v_f\right) \cdot \frac{f_{LOP}}{0.39} \cdot \zeta_1 \cdot \eta_v$ $f_{R3} = \frac{1}{0.37} \cdot k \cdot v_f \cdot \left(1 - k \cdot v_f\right) \cdot \frac{f_{LOP}}{0.39} \cdot \zeta_3 \cdot \eta_v$	[137]
Faccin et al., 2022	$f_{R1} = 2.7 \cdot (f_{cm})^{\frac{1}{2}} \cdot \left(\frac{l_f}{d_f}\right)^{0.8} \cdot \left(v_f\right)^{0.9}$ $f_{R3} = 0.5 \cdot (f_{cm})^{\frac{2}{3}} \cdot \left(\frac{l_f}{d_f}\right) \cdot \left(v_f\right)^{0.85}$	[138]

$RI_v = v_f\left(l_f/d_f\right)$ = fibre reinforcing index, v_f = fibre volume fraction [%], l_f= fibre length [mm], d_f= fibre diameter [mm], $\Psi = \left(1 + l_f/100\right)^{\frac{1}{2}}$= factor accounting for the fibre length, f_{cm}= cylindrical compressive strength, N = number of bends at the fibre ends (N = 1 for 3D fibres, N = 1.5 for 4D fibres and N = 2 for 5D fibres), $f_{cu,0}$= cubic compressive strength of plain concrete, $k = \left(l_f/d_f\right)\chi$, χ = 0.3 for hooked-end steel fibres, $\zeta_1 = 1.18 - 7.5\, l_f/1000$, $\zeta_3 = 0.42 + 7.5\, l_f/1000$, $\eta_v = 1/\left(0.7 - 0.2v_f\right)$

The equations proposed by Venkateshwaran et al. [136] showed the highest accuracy of prediction, which is defined by the Integral Absolute Error (IAE) as follows:

$$IAE = \frac{\sum|Q_i - P_i|}{\sum Q_i} \cdot 100 \tag{3.4}$$

with Q_i representing the experimental data and P_i its predicted value. Thus, their general form (Eq. (3.5) and (3.6)) has been adopted to derive the values of f_{R1} and f_{R3}, and the corresponding characteristic values f_{R1k} and f_{R3k}, for SFRAASC. The coefficients of such correlations have been recalibrated using the experimental data generated in this study. The newly calibrated coefficients $A - F$ are summarised in Table 3.5.

$$f_{R1(\mathrm{k})} = \Psi \cdot \left(\mathrm{A}(f_{cm})^{1/2} + \mathrm{B}RI_v + \mathrm{C}N^2\right) \tag{3.5}$$

$$f_{R3(\mathrm{k})} = \Psi \cdot \left(\mathrm{D}(f_{cm})^{1/2} + \mathrm{E}RI_v + \mathrm{F}N^2\right) \tag{3.6}$$

Table 3.5: Values of the newly calibrated coefficients $A - F$ to derive f_{R1}, f_{R3} and the corresponding characteristic values $f_{R1\mathrm{k}}$ and $f_{R3\mathrm{k}}$ of SFRAASC

Residual flexural strength	Coefficients					
	A	B	C	D	E	F
f_{R1}	0.063	10.991	0.064	-	-	-
f_{R3}	-	-	-	0.169	11.037	0.059
$f_{R1\mathrm{k}}$	-0.103	10.466	0.053	-	-	-
$f_{R3\mathrm{k}}$	-	-	-	-0.029	11.115	0.069

For both experimental and characteristic values of the residual flexural strength, the contribution of the compressive strength and the number of bends at the end of the fibre are less relevant than the fibre reinforcing index. The negative values of the coefficients A and D, however, can be due to the limited amount of datapoints used for the calibration and to their limited variability of compressive strength values.

Figure 3.11 shows the accuracy of prediction of the currently available empirical models summarised in Table 3.4 and of the newly proposed ones for SFRAASC. Although the newly calibrated correlations provide more accurate predictions, additional experimental data are needed to validate their applicability to SFRAASC.

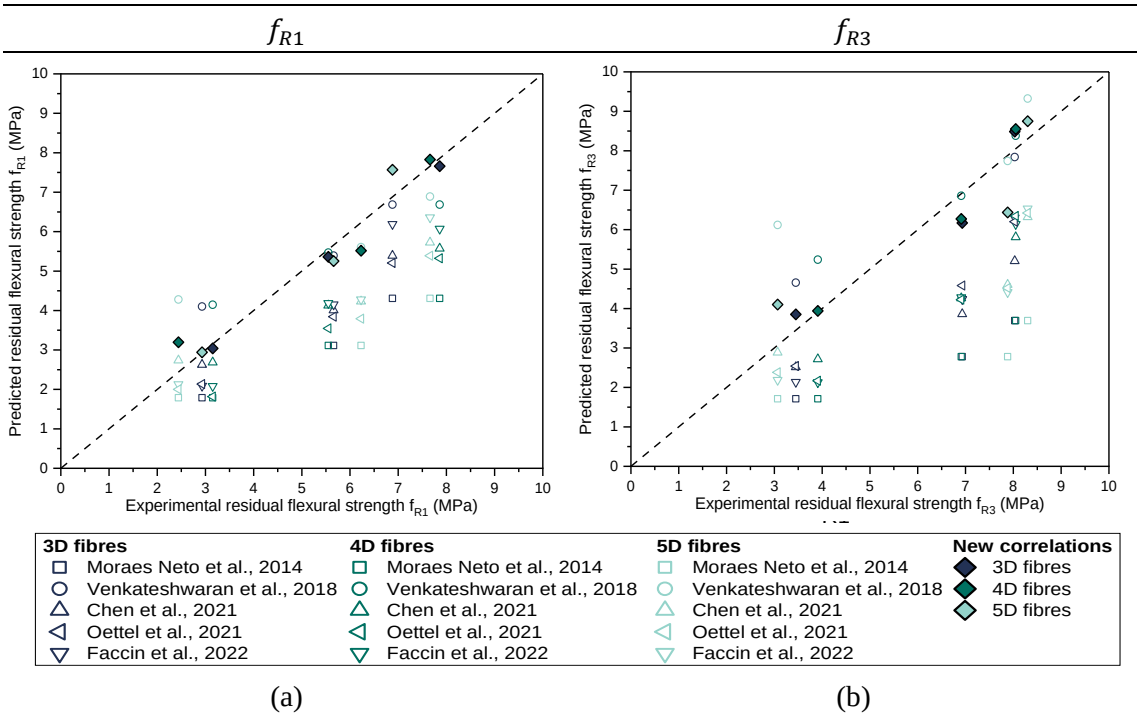

Figure 3.11: Correlation between the experimental and predicted values of (a) f_{R1} and (b) f_{R3} of SFRAASC obtained by using the currently available and newly calibrated empirical models

3.4.2.2 Verification of the *fib* Model Code 2020 tensile constitutive model

To evaluate the applicability to SFRAASC of the tensile constitutive models proposed by the *fib* Model Code 2020 for SFRPCC, Finite Element Modelling (FEM) has been used to simulate the mechanical response of SFRAASC under flexural loading. The Concrete Damage Plasticity (CDP) model available in ABAQUS Software has been used to predict the post-cracking flexural response of SFRAASC and SFRPCC. The *fib* Model Code 2020 provides for SFRPCC a bilinear stress-crack opening tensile constitutive model, with the first branch representing the response of plain PCC under uniaxial tension and the second branch the response of SFRPCC under flexural loading, as shown in Figure 1.19.

Figure 3.12 shows the experimental and numerical load-CMOD curves for both steel fibre-reinforced composites. The CDP model can capture qualitatively the post-cracking response of both SFRAASC and SFRPCC for each fibre type and volume fraction. At the lowest fibre volume fraction (0.25%), the numerical simulations can predict quite accurately the post-peak flexural behaviour of both composites. However, the peak load is overestimated, suggesting an overestimation of the tensile strength of the composite by the constitutive model. At higher fibre volume fractions, although the numerical simulations can describe the post-peak response qualitatively, they underestimate the post-cracking residual flexural strength of both SFRAASC and SFRPCC. Thus, the CDP model is not able to account for post-peak hardening flexural behaviour due to theoretical limitations, *i.e.* modelling the composite as a homogeneous material and providing monotonically decreasing tensile stress-crack opening relationships as input parameter, and shortcoming of the code-based constitutive models for both steel fibre-reinforced traditional and alternative concretes.

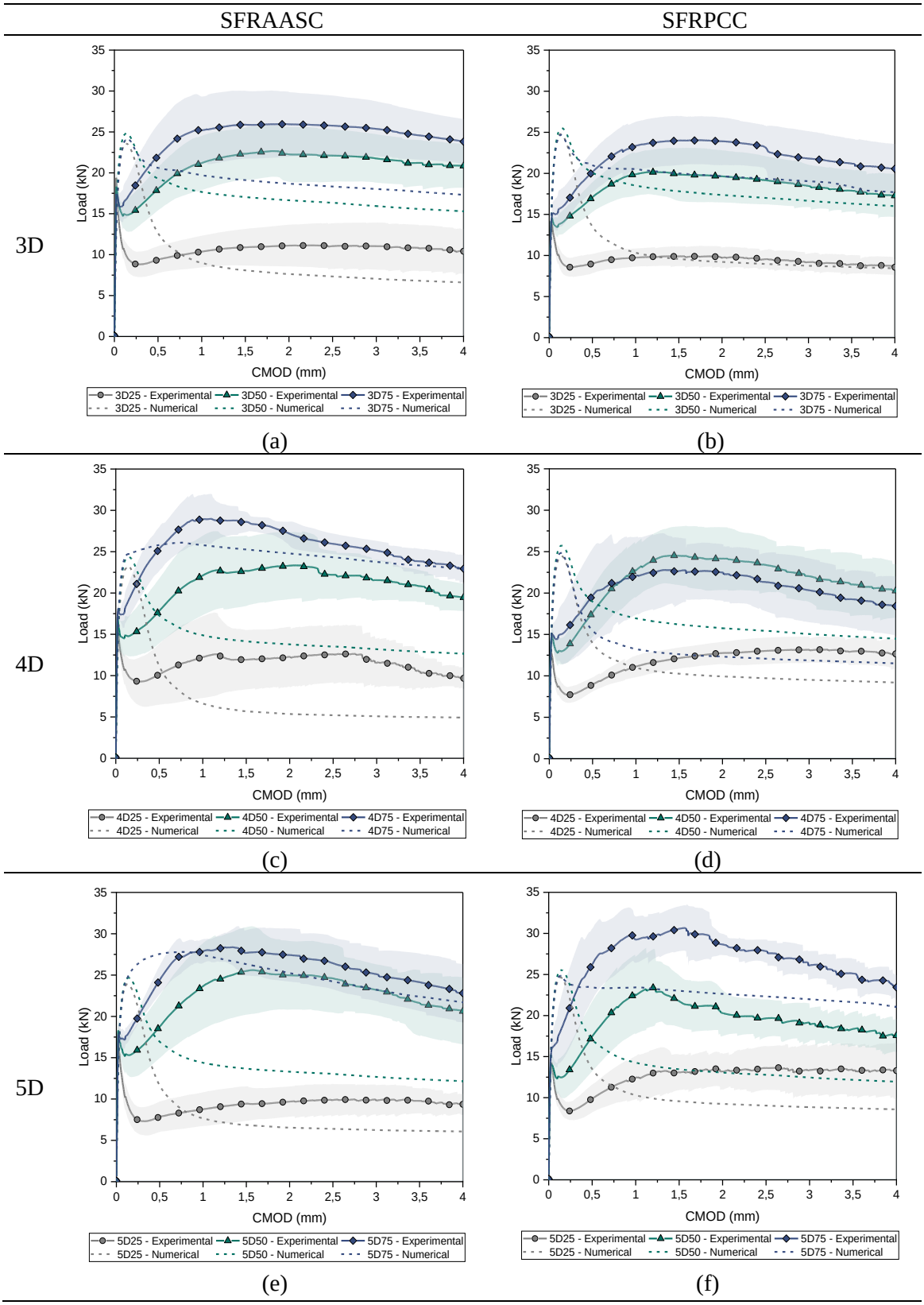

Figure 3.12: Experimental and numerical load-CMOD curves for SFRAASC and SFRPCC mixes incorporating (a, b) 3D, (c, d) 4D and (e, f) 5D hooked-end steel fibres in different volume fractions

3.5 Pull-out behaviour of single and multiple hooked-end steel fibres in alkali-activated slag-based concrete and Portland cement concrete

This section summarises the findings collected in **Paper 5**:

Rossi, L.; Patel, R.A.; Dehn, F.; Pull-out behaviour of single and multiple hooked-end steel fibres in alkali-activated slag-based concrete and Portland cement concrete.
(***to be submitted in Journal of Building Engineering***)

Paper 5 evaluates the pull-out response of single (3D) and multiple (4D and 5D) hooked-end steel fibres embedded in alkali-activated slag-based concrete (AASC) and Portland cement-based concrete (PCC). The effect of the fibre geometry, *i.e.* the number of bends at the fibre end, and the matrix characteristics, *i.e.* compressive strength and age, is investigated using the single-fibre pull-out load-displacement diagrams obtained for each fibre and concrete matrix type. Finite element modelling is used to predict the pull-out behaviour of each fibre in the different concrete matrices, with the additional implementation of inverse analysis to determine the necessary fibre-matrix interface parameters. Additional information related to the concrete mix design, sample preparation, experimental test procedures and numerical inverse analysis used can be found in **Paper 5**.

3.5.1 Single-fibre pull-out behaviour

3.5.1.1 Effect of the matrix properties

The experimental single-fibre pull-out load-displacement curves obtained for each fibre and concrete matrix type after 7 and 28 days are shown in Figure 3.13. Although the concrete matrices show similar values of compressive strength after 7 (36.6 and 41.3 MPa for AASC and PCC, respectively) and 28 days (50.2 and 49.5 MPa for AASC and PCC, respectively), all the fibres embedded in the alkali-activated slag-based concrete matrix exhibits higher values of maximum peak pull-out load in comparison to PCC. Additionally, once peak load is achieved, the several load peaks corresponding to the plastic deformation of each bend at the fibre end show higher values for AASC than PCC. Thus, the higher fibre-matrix bond strength observed for AASC can be due to the denser microstructure and fibre-matrix interfacial transition zone (ITZ) and the higher shrinkage of the concrete matrix, which results in compressive hydrostatic pressure around the fibres. Figure 3.13 also shows an increase in the variability of the experimental results with the increase in the number of bends at the fibre ends. This could be due to the introduction of additional defects and pores around the fibres with an increasing complexity in the fibre geometry.

3.5.1.2 Effect of the fibre geometry

Figure 3.14 shows the experimental pull-out load-displacement curves obtained for each fibre type and each concrete matrix after 7 and 28 days. With the increase in the number of bends at the end of the fibre, the peak pull-out load increases for both AASC and PCC (5D > 4D > 3D) at both 7 and 28 days. For both AASC and PCC, 3D and 4D fibres show a similar pull-out behaviour,

with 4D fibres achieving higher values of load corresponding to the fibre-matrix debonding (peak load) and the plastic deformation of the hooks, due to the additional bend at the fibre end.

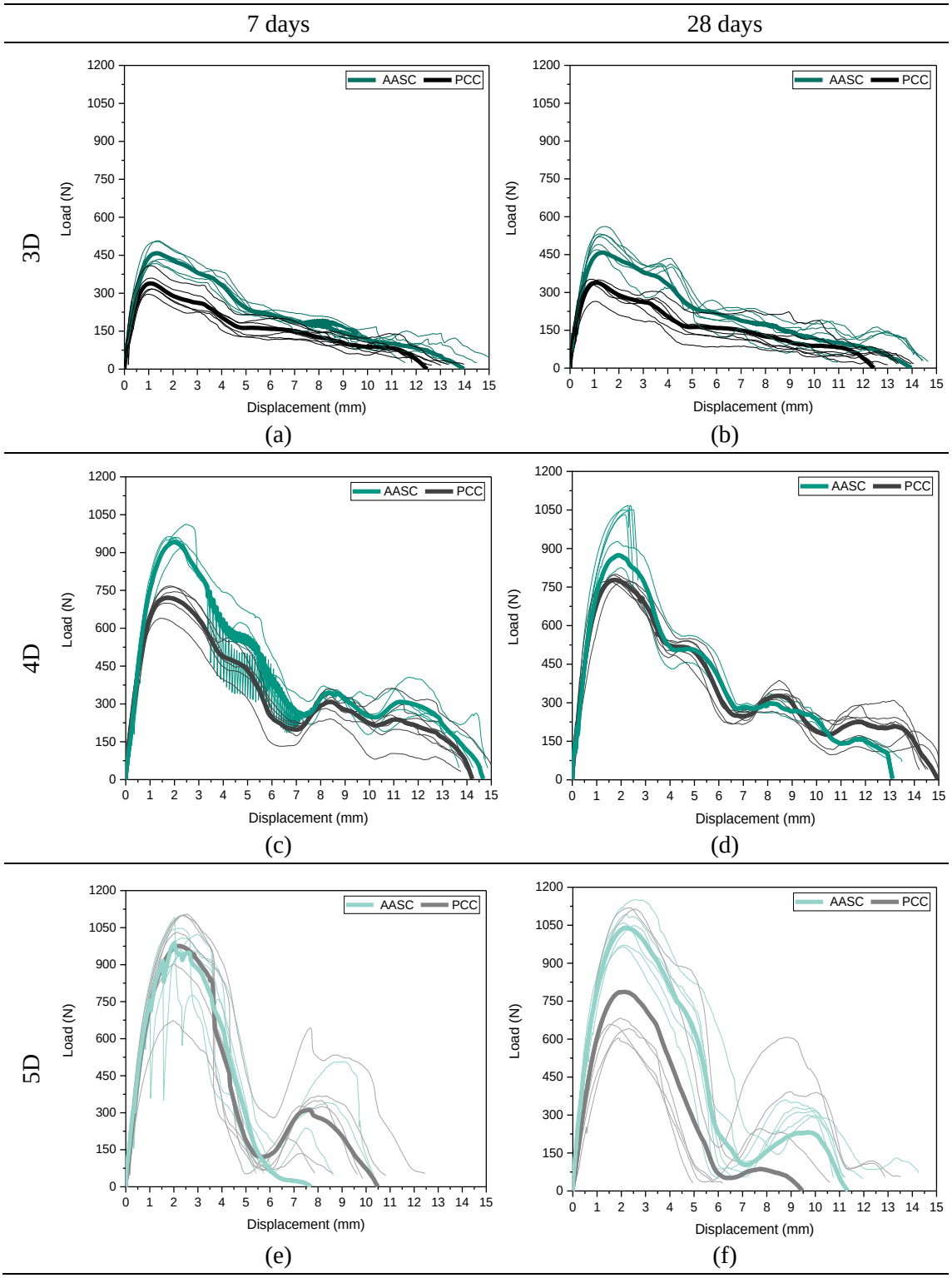

Figure 3.13: Experimental pull-out load-displacement curves for AASC and PCC at an age of 7 and 28 days

Contrarily, 5D fibres show only one additional peak after achieving the maximum pull-out load for both AASC and PCC. Thus, the bends at the end of the fibre do not undergo complete plastic deformation, being pull-out before providing additional mechanical anchorage.

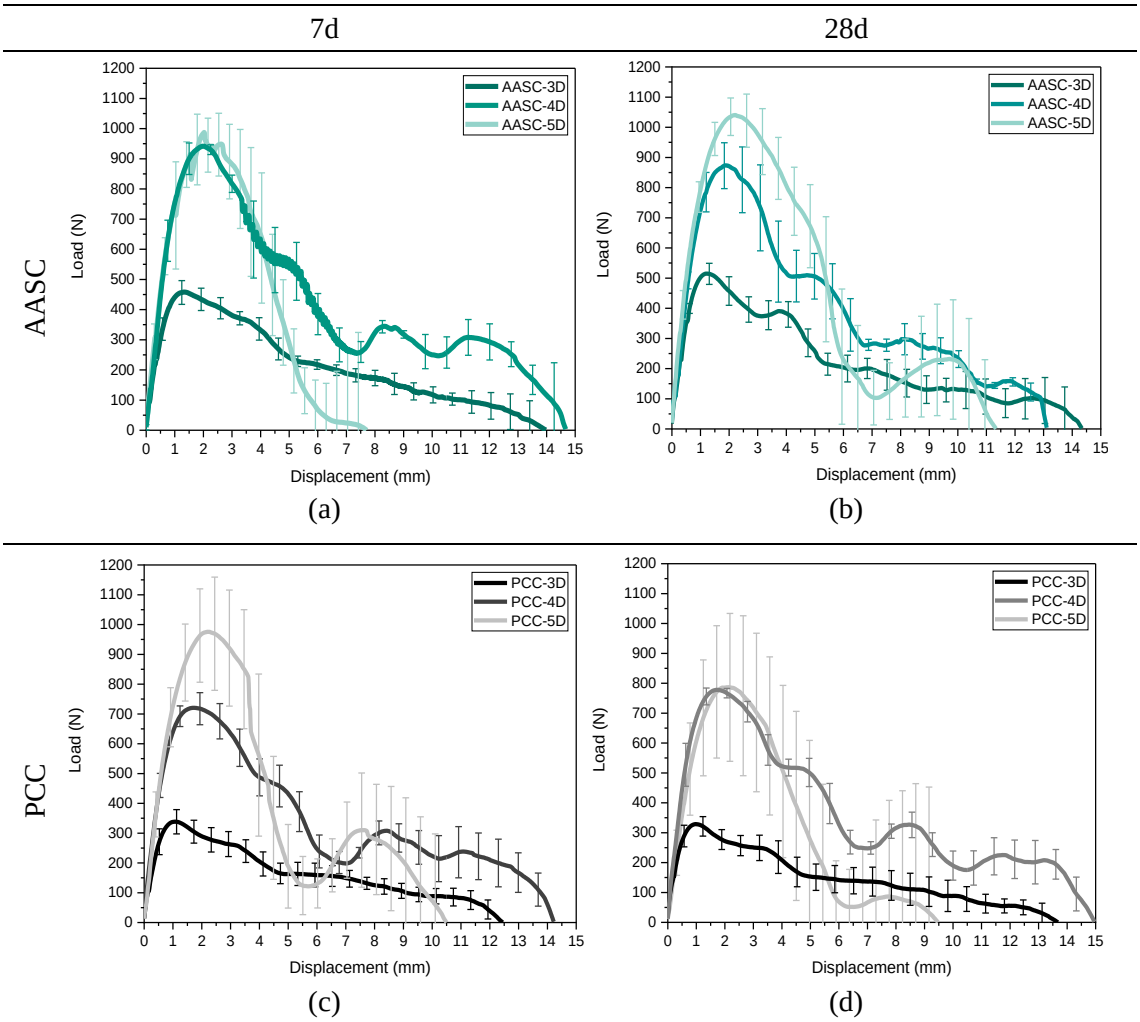

Figure 3.14: Comparison of the experimental pull-out load-displacement curves of the different fibre types for AASC and PCC at an age of 7 and 28 days

Table 3.6 and Table 3.7 summarise the values of the maximum pull-out load (P_{max}), the average and equivalent bond strength (τ_{avg} and τ_{eqv}, respectively) and the fibre material utilisation factor ($FMUF$), which are defined as follows:

$$\tau_{avg} = \frac{P_{max}}{\pi d_f L_e} \tag{3.7}$$

$$\tau_{eqv} = \frac{2W_p}{\pi d_f L_e^2} \tag{3.8}$$

$$FMUF = \frac{\sigma_{t,max}}{\sigma_{tf}} \tag{3.9}$$

where d_f is the fibre diameter, L_e is the fibre embedded length (15 mm in this study), W_p is the pull-out work, i.e. the area under the pull-out displacement curve, $\sigma_{t,max}$ is the tensile stress induced in the steel fibre at the maximum pull-out load, and σ_{tf} is the tensile strength of the fibre (Table 2.3).

Table 3.6: Values of P_{max}, τ_{avg}, τ_{eqv}, and *FMUF* for AASC and PCC at 7 days. The values in the parentheses indicate the standard deviation

Fibre type	Maximum pull-out load P_{max} [N]		τ_{avg} [MPa]		τ_{eqv} [MPa]		$FMUF$	
	AASC	PCC	AASC	PCC	AASC	PCC	AASC	PCC
3D 65/60 BG	459.0 (39.6)	339.1 (40.3)	10.8 (0.9)	8.0 (0.9)	9.45 (0.93)	6.58 (1.13)	0.62 (0.05)	0.46 (0.05)
4D 65/60 BG	958.7 (30.9)	723.1 (48.3)	22.6 (0.7)	17.1 (1.0)	19.65 (1.72)	15.54 (2.32)	0.94 (0.03)	0.71 (0.05)
5D 65/60 BG	1017.4 (48.1)	985.0 (171.4)	24.0 (1.0)	23.3 (3.7)	12.90 (2.96)	14.21 (4.22)	0.70 (0.03)	0.67 (0.12)

Table 3.7: Values of P_{max}, τ_{avg}, τ_{eqv}, and *FMUF* for AASC and PCC at 28 days. The values in the parentheses indicate the standard deviation

Fibre type	Maximum pull-out load P_{max} [N]		τ_{avg} [MPa]		τ_{eqv} [MPa]		$FMUF$	
	AASC	PCC	AASC	PCC	AASC	PCC	AASC	PCC
3D 65/60 BG	517.1 (32.7)	330.3 (33.2)	12.2 (0.7)	7.8 (0.7)	10.11 (1.82)	6.54 (1.65)	0.70 (0.04)	0.45 (0.04)
4D 65/60 BG	992.4 (96.0)	782.9 (12.4)	23.4 (2.1)	18.5 (0.27)	10.31 (5.85)	17.15 (1.33)	0.97 (0.09)	0.77 (0.01)
5D 65/60 BG	1048.1 (71.6)	803.3 (243.7)	24.7 (1.5)	18.9 (5.2)	17.35 (3.81)	12.45 (8.05)	0.72 (0.05)	0.55 (0.17)

As shown in Table 3.6 and Table 3.7, 4D fibres show the highest values of $FMUF$ compared to 3D and 4D fibres for both AASC and PCC. As the efficiency of steel fibres in enhancing the concrete matrix mechanical performance depends on the characteristic of the fibre, the concrete matrix and the fibre-matrix interface bond, 4D fibres are the one able to achieve their best performance in both concrete matrices.

3.5.1.3 Numerical modelling

The Cohesive Zone Model (CZM) available in ABAQUS Software is implemented through inverse analysis to derive from the experimental results the input parameters needed to describe the fibre-matrix bond strength, which define the traction-separation law describing the evolution of cohesive stress with displacement continuity. Figure 3.15 and Figure 3.16 show the experimental and the numerical pull-out load-displacement curves for each fibre type for both AASC and PCC at an age of 7 and 28 days, respectively.

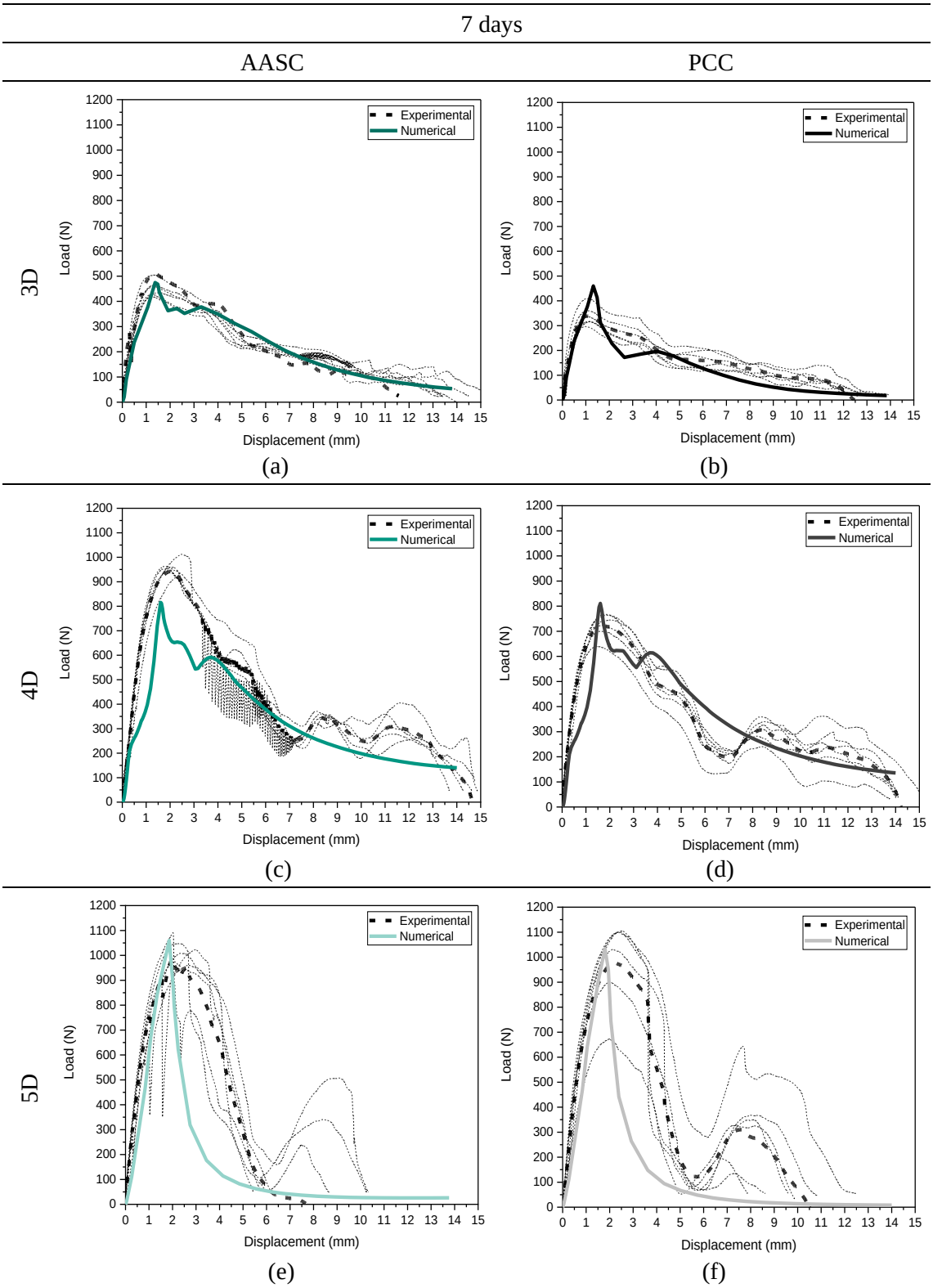

Figure 3.15: Experimental and numerical pull-out load-displacement curves of AASC and PCC incorporating (a, b) 3D, (c, d) 4D and (e, f) 5D fibres at an age of 7 days

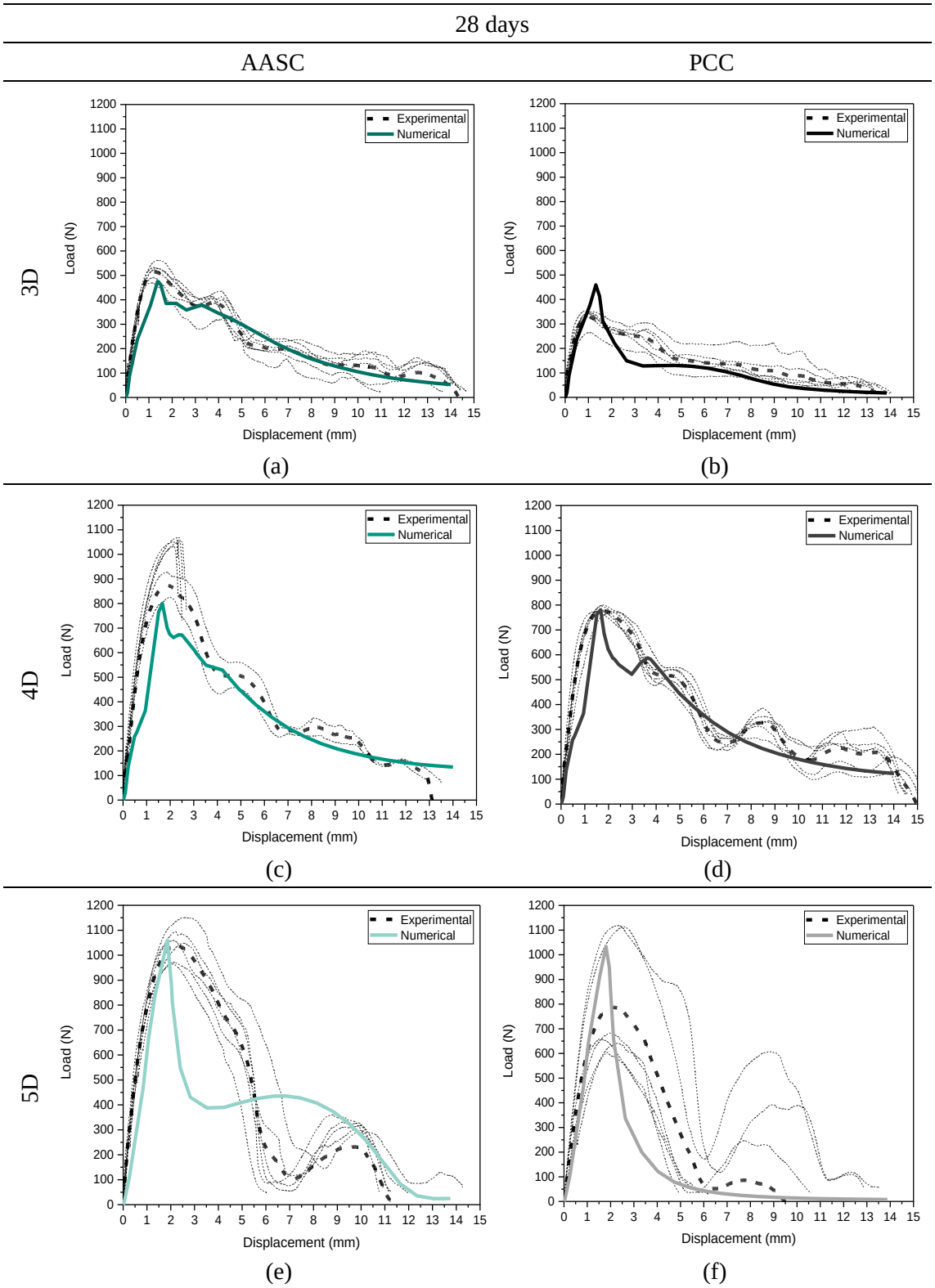

Figure 3.16: Experimental and numerical pull-out load-displacement curves of AASC and PCC incorporating (a, b) 3D, (c, d) 4D and (e, f) 5D fibres at an age of 28 days

For AASC, the numerical results can predict the maximum pull-out load and the post-peak behaviour quite accurately, with only 5D fibres deviating the most from the experimental curves, at both 7 and 28 days. For PCC, only the numerical results obtained for 4D fibres can accurately predict both maximum pull-out load and post-peak behaviour, while for 3D and 5D, an overestimation of the peak load and an underestimation of the post-peak response can be seen at both 7 and 28 days. The low level of accuracy observed for the numerical curves obtained for 5D fibres for both AASC and PCC can be due to the possible presence of microstructural defects around the more complex geometry of the fibre ends, which are not accounted for in the model assumption of homogeneous material. Thus, implementing the CZM through inverse analysis allows for accurate predictions of the single-fibre pull-out behaviour of 3D, 4D and 5D fibres embedded in AASC and PCC matrices.

3.5.1.4 Correlation between flexural behaviour and single-fibre pull-out response

The fibre-matrix average bond strength derived from the single-fibre pull-out tests has a direct effect on the post-cracking flexural response of SFRAASC. As shown in Figure 3.17, a clear correlation between the 28-day residual flexural strength f_{R1} and f_{R3} and the number of fibres at the beam cross-section (N_f) and the 28-day fibre-matrix average bond strength (τ_{avg}) can be seen.

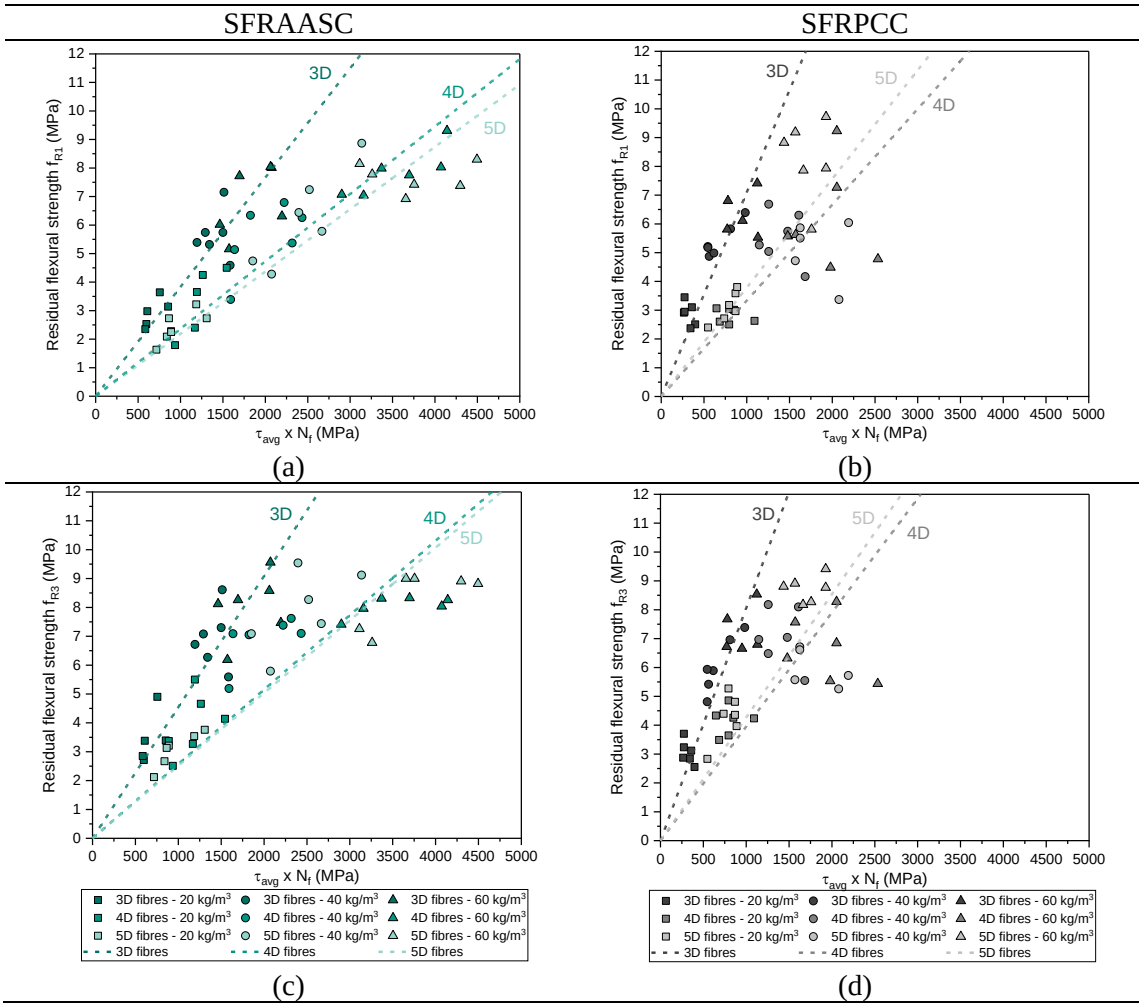

Figure 3.17: Correlation between the 28-day (a, b) f_{R1} and (c, d) f_{R3} and $N_f \cdot \tau_{avg}$ for SFRAASC and SFRPCC

3.6 Design tools for steel fibre-reinforced alkali-activated slag-based concrete

The set of analytical correlations derived from the experimental data generated in this study can serve as a starting point for developing a design tool for SFRAASC. By knowing the compressive behaviour of the alkali-activated slag-based concrete matrix, *i.e.* its cubic and cylindrical compressive strength and its stress-strain response under uniaxial compression and the fibre geometry and dosage, the compressive and tensile response of SFRAASC can be predicted using the empirical correlation summarised in Figure 3.18.

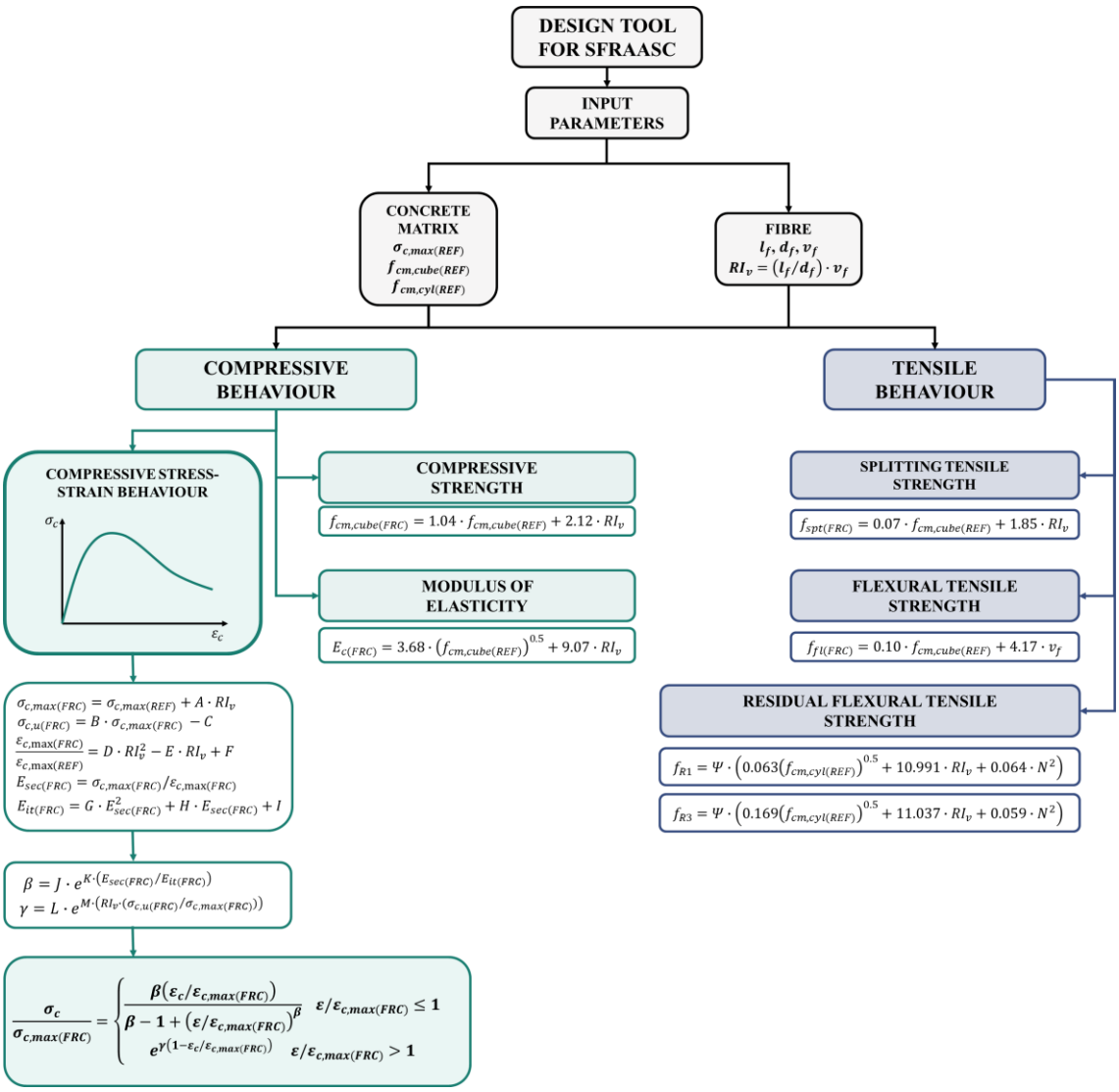

Figure 3.18: Design tool for steel fibre-reinforced alkali-activated slag-based concrete (SFRAASC)

Thus, SFRAASC can be designed to achieve specific performance requirements in compression and tension by performing a limited amount of simple experimental standard tests, such as uniaxial compressive strength on cubic and cylindrical samples.

This design tool simplifies the mix design of SFRAASC by providing the minimum fibre volume fraction and dosage required to achieve specific values of the residual flexural strength corresponding to serviceability (f_{R1}) and ultimate (f_{R3}) limit states. As shown in Table 3.8, by providing the concrete matrix cubic compressive strength ($f_{cm,cube(REF)}$) and the fibre properties, generally given by the fibre manufacturer, *i.e.* length (l_f), diameter (d_f), aspect ratio (l_f/d_f) and geometry (N – the number of bends at the fibre ends) used in this study, it is possible to derive the fibre volume fraction (v_f) and corresponding dosage (m_f) to achieve specific values of the residual flexural strengths by solving the main equations with v_f as only variable.

$$f_{cm,cyl(FRC)} = 0.9 \cdot \left(1.04 \cdot f_{cm,cube(REF)} + 2.12 \cdot \left(l_f/d_f\right) \cdot v_f\right) \quad (3.10)$$

$$f_{R1} = \Psi = \left(1 + \frac{l_f}{100}\right)^{0.5} \cdot \left(0.063 \cdot \left(f_{cm,cyl(FRC)}\right)^{0.5} + 10.991 \cdot \left(\frac{l_f}{d_f}\right) \cdot v_f + 0.064 \cdot N^2\right) \quad (3.11)$$

Table 3.8: Prediction of the fibre minimum volume fraction to achieve the required values of f_{R1} according to the design tool developed in this study

	$f_{cm,cube(REF)}$ [MPa]	l_f [mm]	l_f/d_f	N	Ψ	$f_{cm,cyl(FRC)}$ [MPa]	f_{R1} [MPa]	$v_{f,exp}$ [%]	$v_{f,pred}$ [%]	m_f [kg/m^3]
	47.4	60	65	1	1.26	44.7	2.93	0.25	0.26	20
3D	47.4	60	65	1	1.26	45.0	5.66	0.50	0.56	44
	47.4	60	65	1	1.26	45.2	6.88	0.75	0.69	54
	47.4	60	65	1.5	1.26	44.7	3.15	0.25	0.27	21
4D	47.4	60	65	1.5	1.26	45.0	5.55	0.50	0.53	42
	47.4	60	65	1.5	1.26	45.4	7.86	0.75	0.79	62
	47.4	60	65	2	1.26	44.6	2.44	0.25	0.18	14
5D	47.4	60	65	2	1.26	45.1	6.23	0.50	0.59	47
	47.4	60	65	2	1.26	45.3	7.66	0.75	0.75	59

4 Conclusions and Outlook

4.1 Conclusions

This research work assesses the effect of single (3D) and novel multiple hooked-end steel fibres (4D and 5D) on the compressive and tensile short-term mechanical performance of alkali-activated slag-based concrete (AASC), as well as a direct comparison with the performance of Portland cement-based concrete (PCC) incorporating the same fibre type and dosages. From the experimental results, analytical and numerical models have been derived to predict the behaviour of steel fibre-reinforced AASC (SFRAASC) and PCC (SFRPCC) under compressive and indirect tensile loading conditions and derive a design tool for the use of SFRAASC in practice. From the research work summarised in this thesis, the following conclusions can be drawn:

- *Compressive behaviour*. Experimental results in the literature show a limited effect of single and multiple hooked-end steel fibres on the compressive strength (CS) and modulus of elasticity (MoE) of Portland cement-based concrete (PCC) up to a fibre volume fraction of 1%. Similar results have been observed in this study for PCC mixes incorporating 3D, 4D, and 5D fibres at volume fractions of 0.25%, 0.50% and 0.75%, with the highest increment in CS (+6.7%) and MoE (+1.2%) observed for the mixes PCC-5D75 and PCC-3D75, respectively. For AASC mixes incorporating the same fibre types in the same dosages, a significant enhancement of both compressive strength (+28.7% for AASC-5D50) and modulus of elasticity (+8.6% for AASC-3D75) in comparison to the reference concrete can be seen for each fibre type, with higher fibre dosages generally achieving the highest values. This could be correlated to the denser microstructure and the higher shrinkage of the AASC matrix compared to PCC, resulting in hydrostatic pressure around the steel fibres and, hence, improved fibre-matrix bond strength. SFRAASC exhibits enhanced performance than SFRPCC when subjected to uniaxial compressive loading, showing higher values of peak compressive stress, corresponding strain and post-peak residual compressive stress increase compared to the reference plain concrete with the increase in the fibre dosage for each fibre type.

- *Tensile behaviour*. The tensile behaviour of AASC and PCC incorporating 3D, 4D, and 5D fibres has been evaluated experimentally by performing splitting tensile strength tests and three-point bending tests on notched beams for each fibre type and dosage. For both AASC and PCC mixes, the splitting tensile strength increases with the fibre volume fraction for each fibre type. Although AASC reference concrete (AASC-REF) exhibits a similar splitting tensile strength (3.16 MPa) to PCC-REF (3.27 MPa), AASC incorporating 5D fibres achieves the highest strength increment in comparison to the reference concrete (+80.4% for AASC-5D75) than PCC (+59.9% for PCC-5D75). From the experimental load-CMOD curves obtained from bending tests on notched beams, both the flexural strength (f_{LOP}) and the post-peak residual flexural strength (f_{Rj}) corresponding to a specific crack width

($CMOD_j$) can be derived for each fibre type and dosage for both AASC and PCC. The effect of steel fibres on the flexural strength f_{LOP} is generally limited, as also observed in this study, with the highest enhancement achieved by the mixes AASC-3D25 (+23.9%) and PCC-5D75 (+13.1%). No clear correlation between the fibre dosage or the fibre type and the flexural strength can be observed, *i.e.* the flexural strength does not necessarily increase with the increase in the fibre dosage. Contrarily, a clear correlation between the fibre volume fraction and the post-peak residual flexural strength can be seen, as it increases with the increase of the fibre dosage for each fibre and concrete matrix type, with AASC mixes generally outperforming PCC mixes. The better behaviour of SFRAASC compared to SFRPCC under tensile forces can be explained by the higher maximum pull-out load and average fibre-matrix bond strength than those embedded in traditional concrete. This can be due to the intrinsically higher tensile strength of the alkali-activated slag-based concrete matrix, which results from the nature of its reaction products and microstructure.

Table 5.1 summarises the effect of 3D, 4D, and 5D steel fibres on the compressive and tensile performance of AASC and PCC.

Table 4.1: Effect of single and multiple hooked-end steel fibres on the mechanical properties of AASC and PCC

Mechanical properties	Alkali-activated slag-based concrete (AASC)	Portland cement-based Concrete (PCC)
Compressive strength	↑	↓
Modulus of elasticity	↑	↓
Uniaxial compressive stress-strain response (σ/ε)	↑/↑	↓/=
Splitting tensile strength	↑	↑
Flexural strength (f_{LOP})	↑	=
Residual flexural strength (f_{Rj})	↑	↑

↑ = positive effect, ↓ = negative effect on the composite performance in comparison to the reference concrete without steel fibres

The research work presented in this study not only focused on the experimental characterisation of the short-term mechanical behaviour of SFRAASC but also provided new analytical strength prediction equations and compressive and tensile constitutive models for the design and use of SFRAASC in practice as a viable alternative to cement-based concrete. The design tool provided in this study will facilitate the design of SFRAASC to meet the performance requirements of the concrete members' end use and serve as a first step towards performance-based standards and design codes.

4.2 Outlook and Perspectives

This research work provided a deeper insight into the understanding of the short-term mechanical behaviour of alkali-activated slag-based concrete (AASC) incorporating single (3D) and multiple (4D and 5D) hooked-end steel fibres. The experimental results generated in this study add to the data currently available in the literature, which represented the starting point for deriving analytical correlations and strength prediction models for steel fibre-reinforced alkali-activated slag-based concrete (SFRAASC). However, further investigations are needed.

First, the *long-term mechanical and durability performance* of SFRAASC should be investigated experimentally in both laboratory and natural conditions to validate the material performance over its service life. The resistance of the composite to chloride-induced and carbonation-induced corrosion should be assessed experimentally to evaluate the suitability of this innovative technology as an alternative to traditional cement-based concrete in the construction industry. Thus, available test methods developed for cement-based concrete need to be validated and implemented, if necessary, to account for the different reaction mechanisms and products of the alkali-activated concrete matrix and for the addition of steel fibres of different geometries in different volume fractions. Furthermore, hybrid reinforcement, *i.e.* the simultaneous addition of different steel fibre types to the concrete matrix and galvanised steel fibres, should also be investigated as a possible solution to implement the short- and long-term mechanical and durability performance of SFRAASC.

Additionally, the *variability of the mix design's main constituents* should be investigated. Different types of precursor, such as copper slag, ferronickel slag, ladle slag, and electric arc furnace slag, with various chemical and physical characteristics as well as alkali activators than the one used in this study, should be used to evaluate the effect of single and multiple hooked-end steel fibres on the performance of the resulting composite. This would provide additional experimental data to validate or recalibrate the empirical models proposed in this study and further investigate the effect of single and multiple hooked-end steel fibres on alkali-activated slag-based concrete.

Finally, *other fibre types*, *i.e.* polypropylene (PP), polyethylene (PE), polyvinyl alcohol (PVA), or glass fibres, should be also investigated to tailor the material mechanical and durability performance to specific applications. High volume fractions ($v_f \geq 2\%$) of these microfibers allow for the development of *strain-hardening composites* exhibiting high tensile ductility and multiple microcracking behaviour or *self-healing properties*, *i.e.* the repair of autogenous or loading-initiated microcracks in the composite.

The versatility of alkali-activated concrete technology, *i.e.* the wide range of precursors and alkaline activators, combined with the variety of fibre types currently available on the market, allows the development of *tailored cement-free composites* optimised to meet the performance requirements of specific structural applications.

Universities, industries, and regulatory bodies need to cooperate closely to facilitate the transition from *laboratory materials to construction materials* and take the first *concrete* steps towards a more sustainable construction sector.

Bibliography

[1] World Metereological Organisation, ‘Rate and impact of climate change surges dramatically in 2011-2020’. [Online]. Available: https://wmo.int/news/media-centre/rate-and-impact-of-climate-change-surges-dramatically-2011-2020

[2] M. L. Nehdi, A. Marani, and L. Zhang, ‘Is net-zero feasible: Systematic review of cement and concrete decarbonization technologies’, Renew. Sustain. Energy Rev., vol. 191, p. 114169, 2024. doi: 10.1016/j.rser.2023.114169

[3] M. Abdulkareem, J. Havukainen, and M. Horttanainen, ‘How environmentally sustainable are fibre reinforced alkali-activated concretes?’, J. Clean. Prod., vol. 236, p. 117601, 2019. doi: 10.1016/j.jclepro.2019.07.076

[4] A. Favier, C. Wolf, K. L. Scrivener, and G. Habert, ‘A sustainable future for the European cement and concrete industry: Technology assessment for full decarbonisation of the industry by 2050’, ETH Zürich, 2018. doi: 10.3929/ethz-b-000301843

[5] G. Habert, S. A. Miller, V. M. John, J. L. Provis, A. Favier, A. Horvath, and K. L. Scrivener, ‘Environmental impacts and decarbonization strategies in the cement and concrete industries’, Nat. Rev. Earth Environ., vol. 1, no. 11, pp. 559–573, 2020. doi: 10.1038/s43017-020-0093-3

[6] S. Griffiths. B. K. Sovacool, D. D. Furszyfer Del Rio, A. M. Foley, M. D. Bazilian, J. Kim, J. M. Uratani, ‘Decarbonizing the cement and concrete industry: A systematic review of socio-technical systems, technological innovations, and policy options’, Renew. Sustain. Energy Rev., vol. 180, p. 113291, 2023. doi: 10.1016/j.rser.2023.113291

[7] A. Favier, K. L. Scrivener, and G. Habert, ‘Decarbonizing the cement and concrete sector: integration of the full value chain to reach net zero emissions in Europe’, in SBE19 Brussels - BAMB-CIRCPATH ‘Buildings as Material Banks - a Pathway for a Circular Future’: 5-7 February 2019, Brussels, Belgium, vol. volume 225 (2019), in IOP conference series Earth and environmental science, vol. volume 225 (2019), Bristol: IOP Publishing, 2019, p. 012009

[8] P. J. M. Monteiro, S. A. Miller, and A. Horvath, ‘Towards sustainable concrete’, Nat. Mater., vol. 16, no. 7, pp. 698–699, 2017. doi: 10.1038/nmat4930

[9] M. Pisciotta, H. Pilorgé, J. Davids, and P. Psarras, ‘Opportunities for cement decarbonization’, Clean. Eng. Technol., vol. 15, p. 100667, 2023. doi: 10.1016/j.clet.2023.100667

[10] K.-H. Yang, Y.-B. Jung, M.-S. Cho, and S.-H. Tae, ‘Effect of supplementary cementitious materials on reduction of CO2 emissions from concrete’, J. Clean. Prod., vol. 103, pp. 774–783, 2015. doi: 10.1016/j.jclepro.2014.03.018

[11] M. C. G. Juenger, R. Snellings, and S. A. Bernal, ‘Supplementary cementitious materials: New sources, characterization, and performance insights’, Cem. Concr. Res., vol. 122, pp. 257–273, 2019. doi: 10.1016/j.cemconres.2019.05.008

[12] J. Skibsted and R. Snellings, ‘Reactivity of supplementary cementitious materials (SCMs) in cement blends’, Cem. Concr. Res., vol. 124, p. 105799, 2019. doi: 10.1016/j.cemconres.2019.105799

[13] M. C. Gonçalves and F. Margarido, Eds., Materials for Construction and Civil Engineering: Science, Processing, and Design. Cham: Springer International Publishing, 2015. doi: 10.1007/978-3-319-08236-3

[14] K. Chen, D. Wu, L. Xia, Q. Cai, and Z. Zhang, ‘Geopolymer concrete durability subjected to aggressive environments – A review of influence factors and comparison with ordinary Portland cement’, Constr. Build. Mater., vol. 279, p. 122496, 2021. doi: 10.1016/j.conbuildmat.2021.122496

[15] DIN EN 197-1:2011-11, Cement - Part 1: Composition, specifications and conformity criteria for common cements, German version EN 197-1:2011. doi: 10.31030/1758792

[16] R. Snellings, ‘Assessing, Understanding and Unlocking Supplementary Cementitious Materials’, RILEM Tech. Lett., vol. 1, pp. 50–55, 2016. doi: 10.21809/rilemtechlett.2016.12

[17] J. L. Provis and J. S. J. van Deventer, Eds., Alkali Activated Materials: State-Of-the-Art Report, RILEM TC 224-AAM, 1st ed., vol. 13. in RILEM State-Of-the-Art Reports, vol. 13. Dordrecht: Springer Netherlands, 2014. doi: 10.1007/978-94-007-7672-2

[18] A. Adesina, ‘Performance of fibre reinforced alkali-activated composites – A review’, Materialia, vol. 12, p. 100782, 2020. doi: 10.1016/j.mtla.2020.100782

[19] I. Amer, M. Kohail, M. S. El-Feky, A. Rashad, and M. A. Khalaf, ‘A review on alkali-activated slag concrete’, Ain Shams Eng. J., vol. 12, no. 2, pp. 1475–1499, 2021. doi: 10.1016/j.asej.2020.12.003

[20] J. L. Provis and S. A. Bernal, ‘Geopolymers and related alkali-activated materials’, Annu. Rev. Mater. Res., vol. 44, no. 1, pp. 299–327, 2014. doi: 10.1146/annurev-matsci-070813-113515

[21] G. Habert and C. Ouellet-Plamondon, ‘Recent update on the environmental impact of geopolymers’, RILEM Tech. Lett., vol. 1, pp. 17–23, 2016. doi: 10.21809/rilemtechlett.2016.6

[22] J. L. Provis, ‘Alkali-activated materials’, Cem. Concr. Res., vol. 114, pp. 40–48, 2018. doi: 10.1016/j.cemconres.2017.02.009

[23] J. L. Provis, ‘Geopolymers and other alkali activated materials: why, how, and what?’, Mater. Struct., vol. 47, no. 1–2, pp. 11–25, 2014. doi: 10.1617/s11527-013-0211-5

[24] K. L. Scrivener, V. M. John, and E. M. Gartner, ‘Eco-efficient cements: Potential economically viable solutions for a low-CO2 cement-based materials industry’, Cem. Concr. Res., vol. 114, pp. 2–26, 2018. doi: 10.1016/j.cemconres.2018.03.015

[25] E. Chen, C. G. Berrocal, I. Löfgren, and K. Lundgren, ‘Correlation between concrete cracks and corrosion characteristics of steel reinforcement in pre-cracked plain and fibre-reinforced concrete beams’, Mater. Struct., vol. 53, no. 2, p. 33, 2020. doi: 10.1617/s11527-020-01466-z

[26] M. Amran, R. Fediuk, H. S. Abdelgader, G. Murali, T. Ozbakkaloglu, Y. Huei Lee, Y. Yong Lee, ‘Fiber-reinforced alkali-activated concrete: A review’, J. Build. Eng., vol. 45, p. 103638, 2022. doi: 10.1016/j.jobe.2021.103638

[27] S. P. Dunuweera and R. M. G. Rajapakse, ‘Cement types, composition, uses and advantages of nanocement,environmental impact on cement production, and possible solutions’, Adv. Mater. Sci. Eng., vol. 2018, no. 1, p. 4158682, 2018. doi: 10.1155/2018/4158682

[28] E. John and B. Lothenbach, ‘Cement hydration mechanisms through time – a review’, J. Mater. Sci., vol. 58, no. 24, pp. 9805–9833, 2023. doi: 10.1007/s10853-023-08651-9

[29] E. M. Gartner, J. F. Young, D. A. Damidot, and I. Jawed, ‘Hydration of Portland cement’, in J. Bensted and P. Barner (Eds), Structure and Performance of Cements, 2nd Edition, Chapter 3, pp. 57 - 113, 2001. doi: 10.1201/9781482295016

[30] A. Vazquez and T. M. Pique, ‘Biotech admixtures for enhancing portland cement hydration’, in Biopolymers and Biotech Admixtures for Eco-Efficient Construction Materials, Elsevier, 2016, pp. 81–98. doi: 10.1016/B978-0-08-100214-8.00005-1

[31] K. L. Scrivener, P. Juilland, and P. J. M. Monteiro, ‘Advances in understanding hydration of Portland cement’, Cem. Concr. Res., vol. 78, pp. 38–56, 2015. doi: 10.1016/j.cemconres.2015.05.025

[32] J. W. Bullard, H. M. Jennings, R. A. Livingston, A. Nonat, G. W. Scherer, J. S. Schweitzer, K. L. Scrivener, J. J. Thomas, ‘Mechanisms of cement hydration’, Cem. Concr. Res., vol. 41, no. 12, pp. 1208–1223, 2011. doi: 10.1016/j.cemconres.2010.09.011

[33] K. L. Scrivener, A. Ouzia, P. Juilland, and A. Kunhi Mohamed, ‘Advances in understanding cement hydration mechanisms’, Cem. Concr. Res., vol. 124, p. 105823, 2019. doi: 10.1016/j.cemconres.2019.105823

[34] E. M. Gartner and H. M. Jennings, ‘Thermodynamics of calcium silicate hydrates and their solutions’, J. Am. Ceram. Soc., vol. 70, no. 10, pp. 743–749, 1987. doi: 10.1111/j.1151-2916.1987.tb04874.x

[35] P. Barret, D. Ménétrier, and D. Bertrandie, ‘Mechanism of C3S dissolution and problem of the congruency in the very initial period and later on’, Cem. Concr. Res., vol. 13, no. 5, pp. 728–738, 1983. doi: 10.1016/0008-8846(83)90064-9

[36] B. Lothenbach and F. Winnefeld, ‘Thermodynamic modelling of the hydration of Portland cement’, Cem. Concr. Res., vol. 36, no. 2, pp. 209–226, 2006. doi: 10.1016/j.cemconres.2005.03.001

[37] N. Holmes, D. Kelliher, and M. Tyrer, ‘Thermodynamic cement hydration modelling using HYDCEM’, presented at the Civil Engineering Research in Ireland 2020, Cork Institute of Technology, Cork, Ireland, 2020, pp. 180–185

[38] B. Lothenbach, K. L. Scrivener, and R. D. Hooton, ‘Supplementary cementitious materials’, Cem. Concr. Res., vol. 41, no. 12, pp. 1244–1256, 2011. doi: 10.1016/j.cemconres.2010.12.001

[39] A. M. Neville and J. J. Brooks, Concrete technology, vol. 2nd Edition. Harlow, 2010

[40] S. Mundra, ‘Corrosion of steel in alkali-activated materials’, University of Sheffield, Sheffield, 2019. Accessed: Oct. 25, 2024. [Online]. Available: https://etheses.whiterose.ac.uk/23690/

[41] A. Ranjith, K. Balaji Rao, and K. Manjunath, ‘Evaluating the effect of corrosion on service life prediction of RC structures – A parametric study’, Int. J. Sustain. Built Environ., vol. 5, no. 2, pp. 587–603, 2016. doi: 10.1016/j.ijsbe.2016.07.001

[42] S. Guler, D. Yavuz, F. Korkut, and A. Ashour, ‘Strength prediction models for steel, synthetic, and hybrid fiber reinforced concretes’, Struct. Concr., vol. 20, no. 1, pp. 428–445, 2019. doi: 10.1002/suco.201800088

[43] Y. Wang, H. Jin, C. Demartino, W. Chen, and Y. Yu, ‘Mechanical properties of SFRC: Database construction and model prediction’, Case Stud. Constr. Mater., vol. 17, p. 01484, 2022. doi: 10.1016/j.cscm.2022.e01484

[44] I. Löfgren, Fibre-reinforced concrete for industrial construction: A fracture mechanics approach to material testing and structural analysis, vol. N.S., 2378. in Doktorsavhandlingar vid Chalmers Tekniska Högskola, vol. N.S., 2378. Göteborg: Chalmers Univ. of Technology, 2005

[45] S. Abdallah, M. Fan, and D. W. A. Rees, ‘Bonding Mechanisms and Strength of Steel Fiber–Reinforced Cementitious Composites: Overview’, J. Mater. Civ. Eng., vol. 30, 04018001 vols, no. 3, 2018. doi: 10.1061/(ASCE)MT.1943-5533.0002154

[46] M. A. Mujalli, S. Dirar, E. Mushtaha, A. Hussien, and A. Maksoud, ‘Evaluation of the Tensile Characteristics and Bond Behaviour of Steel Fibre-Reinforced Concrete: An Overview’, Fibers, vol. 10, no. 12, p. 104, 2022. doi: 10.3390/fib10120104

[47] L. Xu, F. Deng, and Y. Chi, ‘Nano-mechanical behavior of the interfacial transition zone between steel-polypropylene fiber and cement paste’, Constr. Build. Mater., vol. 145, pp. 619–638, 2017. doi: 10.1016/j.conbuildmat.2017.04.035

[48] A.-G. N. Abbas, F. N. A. A. Aziz, K. Abdan, N. A. M. Nasir, and G. F. Huseien, 'A state-of-the-art review on fibre-reinforced geopolymer composites', Constr. Build. Mater., vol. 330, p. 127187, 2022. doi: 10.1016/j.conbuildmat.2022.127187

[49] A. Bhutta, M. Farooq, C. Zanotti, and N. Banthia, 'Pull-out behavior of different fibers in geopolymer mortars: effects of alkaline solution concentration and curing', Mater. Struct., vol. 50, no. 1, 2017. doi: 10.1617/s11527-016-0889-2

[50] P. K. Sarker, R. Haque, and K. V. Ramgolam, 'Fracture behaviour of heat cured fly ash based geopolymer concrete', Mater. Des., vol. 44, pp. 580–586, 2013. doi: 10.1016/j.matdes.2012.08.005

[51] S. Abdallah, D. W. A. Rees, S. H. Ghaffar, and M. Fan, 'Understanding the effects of hooked-end steel fibre geometry on the uniaxial tensile behaviour of self-compacting concrete', Constr. Build. Mater., vol. 178, pp. 484–494, 2018. doi: 10.1016/j.conbuildmat.2018.05.191

[52] S. Abdallah, M. Fan, and D. W. A. Rees, 'Analysis and modelling of mechanical anchorage of 4D/5D hooked end steel fibres', Mater. Des., vol. 112, pp. 539–552, 2016. doi: 10.1016/j.matdes.2016.09.107

[53] G. Chen, D. Gao, H. Zhu, J. Song Yuan, X. Xiao, and W. Wang, 'Effects of novel multiple hooked-end steel fibres on flexural tensile behaviour of notched concrete beams with various strength grades', Structures, vol. 33, pp. 3644–3654, 2021. doi: 10.1016/j.istruc.2021.06.016

[54] S. Abdallah and D. W. A. Rees, 'Comparisons between pull-out behaviour of various hooked-end fibres in normal–high strength concretes', Int. J. Concr. Struct. Mater., vol. 13, no. 1, p. 27, 2019. doi: 10.1186/s40069-019-0337-0

[55] F. U. A. Shaikh, 'Pullout behavior of hook end steel fibers in geopolymers', J. Mater. Civ. Eng., vol. 31, 04019068 vols, no. 6, 2019. doi: 10.1061/(ASCE)MT.1943-5533.0002722

[56] H. El-Hassan and S. Elkholy, 'Enhancing the performance of alkali-activated slag-fly ash blended concrete through hybrid steel fiber reinforcement', Constr. Build. Mater., vol. 311, p. 125313, Jan. 2021, doi: 10.1016/j.conbuildmat.2021.125313.

[57] A. Herrmann, A. Koenig, and F. Dehn, 'Structural concrete based on alkali-activated binders: Terminology, reaction mechanisms, mix designs and performance', Struct. Concr., vol. 19, no. 3, pp. 918–929, 2018. doi: 10.1002/suco.201700016

[58] J. L. Provis, S. A. Bernal, and Z. Zhang, 'The decarbonization of construction - How can alkali-activated materials contribute?', Engineering, 2023. doi: 10.1016/j.eng.2023.09.014

[59] P. Duxson and J. L. Provis, 'Designing precursors for geopolymer cements', J. Am. Ceram. Soc., vol. 91, no. 12, pp. 3864–3869, 2008. doi: 10.1111/j.1551-2916.2008.02787.x

[60] F. Puertas, M. Palacios, H. Manzano, J. S. Dolado, A. Rico, and J. Rodríguez, ‘A model for the C-A-S-H gel formed in alkali-activated slag cements’, J. Eur. Ceram. Soc., vol. 31, no. 12, pp. 2043–2056, 2011. doi: 10.1016/j.jeurceramsoc.2011.04.036

[61] T. Bakharev, J. G. Sanjayan, and Y.-B. Cheng, ‘Alkali activation of Australian slag cements’, Cem. Concr. Res., vol. 29, no. 1, pp. 113–120, 1999. doi: 10.1016/S0008-8846(98)00170-7

[62] F. G. Collins and J. G. Sanjayan, ‘Workability and mechanical properties of alkali activated slag concrete’, Cem. Concr. Res., vol. 29, no. 3, pp. 455–458, 1999. doi: 10.1016/S0008-8846(98)00236-1

[63] A. Fernández-Jiménez, J. G. Palomo, and F. Puertas, ‘Alkali-activated slag mortars’, Cem. Concr. Res., vol. 29, no. 8, pp. 1313–1321, 1999. doi: 10.1016/S0008-8846(99)00154-4

[64] S.-D. Wang, K. L. Scrivener, and P. L. Pratt, ‘Factors affecting the strength of alkali-activated slag’, Cem. Concr. Res., vol. 24, no. 6, pp. 1033–1043, 1994. doi: 10.1016/0008-8846(94)90026-4

[65] T. Bakharev, ‘Geopolymeric materials prepared using class F fly ash and elevated temperature curing’, Cem. Concr. Res., vol. 35, no. 6, pp. 1224–1232, 2005. doi: 10.1016/j.cemconres.2004.06.031

[66] E. Deir, B. S. Gebregziabiher, and S. Peethamparan, ‘Influence of starting material on the early age hydration kinetics, microstructure and composition of binding gel in alkali activated binder systems’, Cem. Concr. Compos., vol. 48, pp. 108–117, 2014. doi: 10.1016/j.cemconcomp.2013.11.010

[67] D. Li, Y. Chen, J. Shen, J. Su, and X. Wu, ‘The influence of alkalinity on activation and microstructure of fly ash’, Cem. Concr. Res., vol. 30, no. 6, pp. 881–886, 2000. doi: 10.1016/S0008-8846(00)00252-0

[68] F. P. Torgal, J. Labrincha, C. Leonelli, A. Palomo, and P. Chindaprasirt, Eds., Handbook of alkali-activated cements, mortars and concretes, in Woodhead Publishing series in civil and structural engineering, no. 54. Amsterdam Heidelberg: Woodhead Publ., Elsevier, 2015

[69] D. W. Law, A. A. Adam, T. K. Molyneaux, and I. Patnaikuni, ‘Durability assessment of alkali activated slag (AAS) concrete’, Mater. Struct., vol. 45, no. 9, pp. 1425–1437, 2012. doi: 10.1617/s11527-012-9842-1

[70] S. Bernal, R. Gutierrez, S. Delvasto, and E. Rodriguez, ‘Performance of an alkali-activated slag concrete reinforced with steel fibers’, Constr. Build. Mater., vol. 24, no. 2, pp. 208–214, 2010. doi: 10.1016/j.conbuildmat.2007.10.027

[71] Q. Fu, M. Bu, Z. Zhang, W. Xu, Q. Yuan, and D. Niu, ‘Hydration characteristics and microstructure of alkali-activated slag concrete: A review’, Engineering, vol. 20, pp. 162–179, 2023. doi: 10.1016/j.eng.2021.07.026

[72] S. Song, D. Sohn, H. M. Jennings, and T. O. Mason, ‘Hydration of alkali-activated ground granulated blast furnace slag’, J. Mater. Sci., vol. 35, no. 1, pp. 249–257, 2000. doi: 10.1023/A:1004742027117

[73] A. Fernández-Jiménez and F. Puertas, ‘Effect of activator mix on the hydration and strength behaviour of alkali-activated slag cements’, Adv. Cem. Res., vol. 15, no. 3, pp. 129–136, 2003. doi: 10.1680/adcr.2003.15.3.129

[74] Y. Ding, J.-G. Dai, and C.-J. Shi, ‘Fracture properties of alkali-activated slag and ordinary Portland cement concrete and mortar’, Constr. Build. Mater., vol. 165, pp. 310–320, 2018. doi: 10.1016/j.conbuildmat.2017.12.202

[75] R. J. Thomas and S. Peethamparan, ‘Alkali-activated concrete: Engineering properties and stress–strain behavior’, Constr. Build. Mater., vol. 93, pp. 49–56, 2015. doi: 10.1016/j.conbuildmat.2015.04.039

[76] K.-H. Yang, A.-R. Cho, and J.-K. Song, ‘Effect of water–binder ratio on the mechanical properties of calcium hydroxide-based alkali-activated slag concrete’, Constr. Build. Mater., vol. 29, pp. 504–511, 2012. doi: 10.1016/j.conbuildmat.2011.10.062

[77] H. El-Hassan, E. Shehab, and A. Al-Sallamin, ‘Influence of different curing regimes on the performance and microstructure of alkali-activated slag concrete’, J. Mater. Civ. Eng., vol. 30, no. 9, p. 04018230, 2018. doi: 10.1061/(ASCE)MT.1943-5533.0002436

[78] Chi-Che Hung and Jiang-Jhy Chang, ‘The influence of mixture variables for the alkali-activated slag concrete on the properties of concrete’, J. Mar. Sci. Technol., vol. 21, no. 3, 2013. doi: 10.6119/JMST-012-0109-4

[79] A. A. Aliabdo, A. E. M. Abd Elmoaty, and M. A. Emam, ‘Factors affecting the mechanical properties of alkali activated ground granulated blast furnace slag concrete’, Constr. Build. Mater., vol. 197, pp. 339–355, 2019. doi: 10.1016/j.conbuildmat.2018.11.086

[80] S. Fang, E. S. S. Lam, B. Li, and B. Wu, ‘Effect of alkali contents, moduli and curing time on engineering properties of alkali activated slag’, Constr. Build. Mater., vol. 249, p. 118799, 2020. doi: 10.1016/j.conbuildmat.2020.118799

[81] C. S. Thunuguntla and T. D. Gunneswara Rao, ‘Effect of mix design parameters on mechanical and durability properties of alkali activated slag concrete’, Constr. Build. Mater., vol. 193, pp. 173–188, 2018. doi: 10.1016/j.conbuildmat.2018.10.189

[82] M. Chi, ‘Effects of dosage of alkali-activated solution and curing conditions on the properties and durability of alkali-activated slag concrete’, Constr. Build. Mater., vol. 35, pp. 240–245, 2012. doi: 10.1016/j.conbuildmat.2012.04.005

[83] Y. Ding, J.-G. Dai, and C.-J. Shi, ‘Mechanical properties of alkali-activated concrete: A state-of-the-art review’, Constr. Build. Mater., vol. 127, pp. 68–79, 2016. doi: 10.1016/j.conbuildmat.2016.09.121

[84] Z. Tian, C. Fu, and H. Ye, ‘How does carbonation of alkali-activated slag and Portland cement systems impact steel corrosion differently?’, Cem. Concr. Res., vol. 181, p. 107528, 2024. doi: 10.1016/j.cemconres.2024.107528

[85] A. Wang, Y. Zheng, Z. Zhang, K. Liu, Y. Li, L. Shi, and D. Sun, ‘The durability of alkali-activated materials in comparison with ordinary Portland cements and concretes: A review’, Engineering, vol. 6, no. 6, pp. 695–706, 2020. doi: 10.1016/j.eng.2019.08.019

[86] P. Awoyera and A. Adesina, ‘Durability properties of alkali activated slag composites: Short overview’, Silicon, vol. 12, no. 4, pp. 987–996, 2020. doi: 10.1007/s12633-019-00199-1

[87] F. Collins and J. G. Sanjayan, ‘Cracking tendency of alkali-activated slag concrete subjected to restrained shrinkage’, Cem. Concr. Res., vol. 30, no. 5, pp. 791–798, 2000. doi: 10.1016/S0008-8846(00)00243-X

[88] M. Mastali, P. Kinnunen, A. Dalvand, R. Mohammadi Firouz, and M. Illikainen, ‘Drying shrinkage in alkali-activated binders – A critical review’, Constr. Build. Mater., vol. 190, pp. 533–550, 2018. doi: 10.1016/j.conbuildmat.2018.09.125

[89] R. J. Thomas, D. Lezama, and S. Peethamparan, ‘On drying shrinkage in alkali-activated concrete: Improving dimensional stability by aging or heat-curing’, Cem. Concr. Res., vol. 91, pp. 13–23, 2017. doi: 10.1016/j.cemconres.2016.10.003

[90] Z. Ou, R. Feng, F. Li, G. Liu, and N. Li, ‘Development of drying shrinkage model for alkali-activated slag concrete’, Constr. Build. Mater., vol. 323, p. 126556, 2022. doi: 10.1016/j.conbuildmat.2022.126556

[91] H. Ye, C. Cartwright, F. Rajabipour, and A. Radlińska, ‘Understanding the drying shrinkage performance of alkali-activated slag mortars’, Cem. Concr. Compos., vol. 76, pp. 13–24, 2017. doi: 10.1016/j.cemconcomp.2016.11.010

[92] H. Ye and A. Radlińska, ‘Shrinkage mechanisms of alkali-activated slag’, Cem. Concr. Res., vol. 88, pp. 126–135, 2016. doi: 10.1016/j.cemconres.2016.07.001

[93] J. Ma and F. Dehn, ‘Shrinkage and creep behavior of an alkali-activated slag concrete’, Struct. Concr., vol. 18, no. 5, pp. 801–810, 2017. doi: 10.1002/suco.201600147

[94] S. Abdallah, M. Fan, and D. W. A. Rees, ‘Predicting pull-out behaviour of 4D/5D hooked end fibres embedded in normal-high strength concrete’, Eng. Struct., vol. 172, pp. 967–980, 2018. doi: 10.1016/j.engstruct.2018.06.066

[95] H. El-Hassan and S. Elkholy, ‘Performance evaluation and microstructure characterization of steel fiber–reinforced alkali-activated slag concrete incorporating fly ash’, J. Mater. Civ. Eng., vol. 31, 04019223 vols, no. 10, 2019. doi: 10.1061/(ASCE)MT.1943-5533.0002872

[96] S. Karunanithi and S. Anandan, ‘Flexural toughness properties of reinforced steel fibre incorporated alkali activated slag concrete’, Adv. Civ. Eng., vol. 2014, pp. 1–12, 2014. doi: 10.1155/2014/719436

[97] A. N. Ajay and E. H. George, ‘Experimental investigation on effect of inclusion of hooked steel fiber on GGBS based geopolymer concrete’, Int. J. Eng. Sci. & Res. Technol, vol. 7, no. 4, 2018. doi: 10.5281/zenodo.1228802

[98] A. Niş, N. A. Eren, and A. Çevik, ‘Effects of nanosilica and steel fibers on the impact resistance of slag based self-compacting alkali-activated concrete’, Ceram. Int., vol. 47, no. 17, pp. 23905–23918, 2021. doi: 10.1016/j.ceramint.2021.05.099

[99] N. Hammad, A. El-Nemr, and H. El-Deen Hasan, ‘The performance of fiber GGBS based alkali-activated concrete’, J. Build. Eng., vol. 42, p. 102464, 2021. doi: 10.1016/j.jobe.2021.102464

[100] S.-W. Kim, S.-J. Jang, D.-H. Kang, K.-L. Ahn, and H.-D. Yun, ‘Mechanical properties and eco-efficiency of steel fiber reinforced alkali-activated slag concrete’, Mater. Basel Switz., vol. 8, no. 11, pp. 7309–7321, 2015. doi: 10.3390/ma8115383

[101] A. Sivakumar and K. Srinivasan, ‘High performance fibre reinforced alkali activated slag concrete’, 2014. doi: 10.5281/zenodo.1097305

[102] M. A. Sadawy, A. S. Faried, and H. A. El-Ghazaly, ‘Influence of various types of steel fibre on the mechanical and physical characteristics of GGBS based geopolymer concrete’, J. Eng. Res. Rep., pp. 7–19, 2020. doi: 10.9734/JERR/2020/v12i117070

[103] H. Taghvayi, K. Behfarnia, and M. Khalili, ‘The effect of alkali concentration and sodium silicate modulus on the properties of alkali-activated slag concrete’, J. Adv. Concr. Technol., vol. 16, no. 7, pp. 293–305, 2018. doi: 10.3151/jact.16.293

[104] P. G. Chottemada, J. Rodriguez Sanchez, and A. Kar, ‘Drying shrinkage properties of fiber-reinforced alkali-activated slag and their correlations with microstructure’, Constr. Build. Mater., vol. 411, p. 134669, 2024. doi: 10.1016/j.conbuildmat.2023.134669

[105] S. Mundra, S. A. Bernal, M. Criado, P. Hlaváček, G. Ebell, S. Reinemann, G. J. G. Gluth, and J. L. Provis, ‘Steel corrosion in reinforced alkali-activated materials’, RILEM Tech. Lett., vol. 2, pp. 33–39, 2017. doi: 10.21809/rilemtechlett.2017.39

[106] C. Shi, ‘Corrosion resistance of alkali-activated slag cement’, Adv. Cem. Res., vol. 15, no. 2, pp. 77–81, 2003. doi: 10.1680/adcr.2003.15.2.77

[107] V. Marcos-Meson, A. Michel, A. Solgaard, G. Fischer, C. Edvardsen, and T. L. Skovhus, ‘Corrosion resistance of steel fibre reinforced concrete - A literature review’, Cem. Concr. Res., vol. 103, pp. 1–20, 2018. doi: 10.1016/j.cemconres.2017.05.016

[108] A. Beglarigale, S. Aydın, and C. Kızılırmak, ‘Fiber-matrix bond characteristics of alkali-activated slag cement–based composites’, J. Mater. Civ. Eng., vol. 28, no. 11, p. 04016133, 2016. doi: 10.1061/(ASCE)MT.1943-5533.0001642

[109] M. Di Prisco, G. Plizzari, and L. Vandewalle, ‘Fibre reinforced concrete: New design perspectives’, Mater. Struct., vol. 42, no. 9, pp. 1261–1281, 2009. doi: 10.1617/s11527-009-9529-4

[110] X. Ouyang, Z. Wu, B. Shan, Q. Chen, and C. Shi, ‘A critical review on compressive behavior and empirical constitutive models of concrete’, Constr. Build. Mater., vol. 323, p. 126572, 2022. doi: 10.1016/j.conbuildmat.2022.126572

[111] A. S. Ezeldin and P. N. Balaguru, ‘Normal- and High-Strength Fiber-Reinforced Concrete under Compression’, J. Mater. Civ. Eng., vol. 4, no. 4, pp. 415–429, 1992. doi: 10.1061/(ASCE)0899-1561(1992)4:4(415)

[112] L. Á. D. Oliveira Júnior, V. E. dos Santos Borges, A. Ribeiro Danin, D. V. Ramos Machado, D. de Lima Araújo, M. K. El Debs, and P. F. Rodrigues, ‘Stress-strain curves for steel fiber-reinforced concrete in compression’, Matér. Rio Jan., vol. 15, no. 2, pp. 260–266, 2010. doi: 10.1590/S1517-70762010000200025

[113] Y.-C. Ou, M.-S. Tsai, K.-Y. Liu, and K.-C. Chang, ‘Compressive behavior of steel-fiber-reinforced concrete with a high reinforcing index’, J. Mater. Civ. Eng., vol. 24, no. 2, pp. 207–215, 2012. doi: 10.1061/(ASCE)MT.1943-5533.0000372

[114] W. Abbass, M. I. Khan, and S. Mourad, ‘Evaluation of mechanical properties of steel fiber reinforced concrete with different strengths of concrete’, Constr. Build. Mater., vol. 168, pp. 556–569, 2018. doi: 10.1016/j.conbuildmat.2018.02.164

[115] S.-C. Lee, J.-H. Oh, and J.-Y. Cho, ‘Compressive behavior of fiber-reinforced concrete with end-hooked steel fibers’, Materials, vol. 8, no. 4, pp. 1442–1458, 2015. doi: 10.3390/ma8041442

[116] G. Ruiz, Á. De La Rosa, S. Wolf, and E. Poveda, ‘Model for the compressive stress–strain relationship of steel fiber-reinforced concrete for non-linear structural analysis’, Hormig. Acero, p. S043956891830069X, 2018. doi: 10.1016/j.hya.2018.10.001

[117] F. Laranjeira de Oliveira, Design-oriented constitutive model for steel fiber reinforced concrete, Doctoral thesis, Universitat Politècnica de Catalunya, Barcelona, Spain, 2010. doi: 10.5821/dissertation-2117-93486

[118] A. Hillerborg, M. Modéer, and P.-E. Petersson, ‘Analysis of crack formation and crack growth in concrete by means of fracture mechanics and finite elements’, Cem. Concr. Res., vol. 6, no. 6, pp. 773–781, 1976. doi: 10.1016/0008-8846(76)90007-7

[119] V. E. Saouma and M. A. Hariri-Ardebili, ‘Fracture mechanics of concrete’, in Aging, Shaking, and Cracking of Infrastructures, V. E. Saouma and M. A. Hariri-Ardebili, Eds., Cham: Springer International Publishing, 2021, pp. 161–189. doi: 10.1007/978-3-030-57434-5_8

[120] U. Häussler-Combe, A. Shehni, and A. Chihadeh, ‘Finite element modeling of fiber reinforced cement composites using strong discontinuity approach with explicit representation of fibers’, Int. J. Solids Struct., vol. 200–201, pp. 213–230, 2020. doi: 10.1016/j.ijsolstr.2020.04.036

[121] A. Venkateshwaran and K. H. Tan, ‘Load-carrying capacity of steel fiber reinforced concrete beams at large deflections’, Struct. Concr., vol. 19, no. 3, pp. 670–683, 2018. doi: 10.1002/suco.201700129

[122] S. J. Stephen, B. Raphael, R. Gettu, and S. Jose, ‘Determination of the tensile constitutive relations of fiber reinforced concrete using inverse analysis’, Constr. Build. Mater., vol. 195, pp. 405–414, 2019. doi: 10.1016/j.conbuildmat.2018.11.014

[123] L. Rossi et al., ‘Future perspectives for alkali-activated materials: from existing standards to structural applications’, RILEM Tech. Lett., vol. 7, pp. 159–177, 2022. doi: 10.21809/rilemtechlett.2022.160

[124] N. Ranjbar and M. Zhang, ‘Fiber-reinforced geopolymer composites: A review’, Cem. Concr. Compos., vol. 107, p. 103498, 2020. doi: 10.1016/j.cemconcomp.2019.103498

[125] L. Rossi, R. A. Patel, and F. Dehn, ‘Compressive behaviour of alkali-activated slag-based concrete and Portland cement concrete incorporating novel multiple hooked-end steel fibres’, Mater. Struct., vol. 56, no. 5, 2023. doi: 10.1617/s11527-023-02180-2

[126] F. L. Matthews, G. A. O. Davies, D. Hitchings, and C. Soutis, Finite element modelling of composite materials and structures. Boca Raton; Cambridge: CRC Press; Woodhead Publishing, 2000

[127] Y. Chi, M. Yu, Le Huang, and L. Xu, ‘Finite element modeling of steel-polypropylene hybrid fiber reinforced concrete using modified concrete damaged plasticity’, Eng. Struct., vol. 148, pp. 23–35, 2017. doi: 10.1016/j.engstruct.2017.06.039

[128] A. H. Al-Zuhairi, A. H. Al-Ahmed, A. A. Abdulhameed, and A. N. Hanoon, ‘Calibration of a new concrete damage plasticity theoretical model based on experimental parameters’, Civ. Eng. J., vol. 8, no. 2, pp. 225–237, 2022. doi: 10.28991/CEJ-2022-08-02-03

[129] T. Jankowiak and T. Łodygowski, ‘Identification of parameters of concrete damage plasticity constitutive model’, Found. Civ. Environ. Eng., vol. 6, pp. 53–69, 2005

[130] J. Lee and G. L. Fenves, ‘Plastic-damage model for cyclic loading of concrete structures’, J. Eng. Mech., vol. 124, no. 8, pp. 892–900, 1998. doi: 10.1061/(ASCE)0733-9399(1998)124:8(892)

[131] J. Lubliner, J. Oliver, S. Oller, and E. Oñate, ‘A plastic-damage model for concrete’, Int. J. Solids Struct., vol. 25, no. 3, pp. 299–326, 1989. doi: 10.1016/0020-7683(89)90050-4

[132] J. Thomas and A. Ramaswamy, ‘Mechanical properties of steel fiber-reinforced concrete’, J. Mater. Civ. Eng., vol. 19, no. 5, pp. 385–392, 2007. doi: 10.1061/(ASCE)0899-1561(2007)19:5(385)

[133] S. Abdallah, M. Fan, X. Zhou, and S. Le Geyt, ‘Anchorage effects of various steel fibre architectures for concrete reinforcement’, Int. J. Concr. Struct. Mater., vol. 10, no. 3, pp. 325–335, 2016. doi: 10.1007/s40069-016-0148-5

[134] S.-J. Lee, D.-Y. Yoo, and D.-Y. Moon, ‘Effects of hooked-end steel fiber geometry and volume fraction on the flexural behavior of concrete pedestrian decks’, Appl. Sci., vol. 9, no. 6, p. 1241, 2019. doi: 10.3390/app9061241

[135] B. N. Moraes Neto, J. A. O. Barros, and G. S. S. A. Melo, ‘Model to simulate the contribution of fiber reinforcement for the punching resistance of RC slabs’, J. Mater. Civ. Eng., vol. 26, no. 7, p. 04014020, 2014. doi: 10.1061/(ASCE)MT.1943-5533.0000913

[136] A. Venkateshwaran, K. H. Tan, and Y. Li, ‘Residual flexural strengths of steel fiber reinforced concrete with multiple hooked-end fibers’, Struct. Concr., vol. 19, no. 2, pp. 352–365, 2018. doi: 10.1002/suco.201700030

[137] V. Oettel, M. Schulz, and M. Haist, ‘Empirical approach for the residual flexural tensile strength of steel fiber-reinforced concrete based on notched three-point bending tests’, Struct. Concr., vol. 23, no. 2, pp. 993–1004, 2022. doi: 10.1002/suco.202100565

[138] E. Faccin, L. Facconi, F. Minelli, and G. Plizzari, ‘Predicting the residual flexural strength of concrete reinforced with hooked-end steel fibers: New empirical equations’, in Fibre Reinforced Concrete: Improvements and Innovations II, vol. 36, P. Serna, A. Llano-Torre, J. R. Martí-Vargas, and J. Navarro-Gregori, Eds., in RILEM Bookseries, vol. 36. , Cham: Springer International Publishing, 2022, pp. 456–468. doi: 10.1007/978-3-030-83719-8_40

Paper 1

Future perspectives for alkali-activated materials: from existing standards to structural applications

Laura Rossi, Luiz Miranda de Lima, Yubo Sun, Frank Dehn, John L. Provis, Guang Ye, Geert de Schutter

RILEM Technical Letters

Volume 7, 2022, pp. 159-177

DOI: 10.21809/rilemtechlett.2022.160

Publisher's version

RILEM Technical Letters (2022) 7: 159-177
https://doi.org/10.21809/rilemtechlett.2022.160

Future perspectives for alkali-activated materials: from existing standards to structural applications

Laura Rossi[1, 2], Luiz Miranda de Lima[3], Yubo Sun[4], Frank Dehn[1, 2], John L. Provis[5], Guang Ye[3, 4], Geert De Schutter[4]*

[1] Institute of Building Materials and Concrete Structures (IMB), Karlsruhe Institute of Technology (KIT), 76131 Karlsruhe, Germany
[2] Materials Testing and Research Institute Karlsruhe (MPA), Karlsruhe Institute of Technology (KIT), 76131 Karlsruhe, Germany
[3] Department of Materials and Environment (Microlab), Faculty of Civil Engineering and Geosciences, Delft University of Technology. Delft, the Netherlands.
[4] Magnel-Vandepitte Laboratory, Department of Structural Engineering and Building Materials, Ghent University, 9052 Ghent, Belgium.
[5] Department of Materials Science and Engineering, The University of Sheffield. Sheffield, S1 3JD, United Kingdom

Received: 29 May 2022 / Accepted: 14 December 2022 / Published online: 12 January 2023

Abstract

The production of cement and concrete contributes significantly to global greenhouse gas emissions. Alkali-activated concretes (AACs) are a family of existing alternative construction materials that could reduce the current environmental impact of Portland cement (PC) production and utilisation. Successful applications of AACs can be found in Europe and the former USSR since the 1950s and more recently in Australia, China and North America, proving their potential as construction materials. However, their utilisation is limited presently by the lack of normative and construction guidelines. Raw materials' non-uniform global availability and variable intrinsic properties, coupled with the lack of specific testing methods, raise questions regarding reproducibility and reliability. The mechanical and chemical behaviour of AACs has been investigated extensively over the past decades, strengthening its potential as a sustainable substitute for traditional PC-based concrete. Although a wide amount of studies demonstrated that AACs could meet and even exceed the performance requirements provided by European design standards, a classification of these broad spectra of materials, as well as new analytical models linking the chemistry of the system components to the mechanical behaviour of the material, still need further development. This report gives an overview of the potential of alkali-activated systems technology, focusing on the limitations and challenges still hindering their standardisation and wider application in the construction field.

Keywords: Alkali-activated concrete; Mechanical performance; Real-scale applications; Performance-based standards; Sustainable construction

1 Introduction

Portland cement (PC) production is acknowledged as one of the major causes of global anthropogenic CO_2 emissions due to the combustion of fossil fuels and the decarbonation of limestone during the high-energy-demanding production process [1]. As the demand for construction materials drives cement and concrete production, minimising emissions while supplying enough material to meet increasing demand will be challenging. To achieve the carbon neutrality proposed by the European Green Deal by 2050, the cement industry needs to act at every stage of the value chain to meet net-zero emissions by 2050 [2]. Reducing the clinker-to-binder ratio via partially replacing PC with supplementary cementitious materials (SCMs) represents a valid solution to achieve significant emission savings from cement production. However, among the available solutions to limit cement and concrete environmental impact [3], alkali-activated concretes (AACs) are a promising class of clinker-free binders able to convert a significant number of industrial by-products and wastes into construction materials, reducing emissions and energy consumption related to cement production [4,5].

The continuous progress in understanding AACs' reaction mechanisms and mechanical and durability performance, supported by a long history of successful applications, demonstrate that AACs can perform similarly or even better than traditional Portland cement-based concrete (PCC) as construction materials [6]. The wide range of solid precursors and alkali-activators suitable for alkali-activated concrete makes them extremely variable, allowing fit-for-purpose mix design formulations to achieve the mechanical and durability performance required by the end applications. However, each mix design formulation differs from the others in terms of the chemical composition of both precursors and alkaline solutions. Thus, the reaction mechanisms taking place in the different mix design formulations need to be further investigated and linked to the concrete mechanical and durability performance. The potential of AACs as a versatile building material is hindered by the lack of analytical

*Corresponding author: Geert De Schutter, geert.deschutter@ugent.be

equations and models correlating the chemistry of the reaction with the material performance, which represent the core of design regulations and standards. Current prescriptive design standards developed for Portland cement concrete need to be modified and further implemented for AACs to reflect the novelty of the material characteristics and facilitate their use in structural and non-structural applications. In addition to the lack of correlations between AACs chemistry and performance, durability data obtained from natural conditions are limited. This is mainly due to the lack of design regulations limiting the use of AACs in real-scale applications. Only a limited number of pilot-scale works have been realised in recent years, allowing monitoring of the material behaviour over its service life. Additionally, new reliable and adequate testing methods [7] to evaluate the long-term performance of AACs at a laboratory scale need to be implemented.

The purpose of this paper is to draw attention to the versatility of AAC as an alternative to traditional concrete, while also raising awareness of the barriers and limitations preventing their widespread commercialisation and use in the construction industry. A current picture of the AAC technology path, from laboratory research topic to market available product, is given to underline the general challenges related to the high chemical variability of the material components. From an analysis of available mix design components and formulations, through an overview of worldwide real-scale applications, to the need for new performance-based standards and analytical correlations between chemistry and performance, it is clear that changes in research, industry and building regulations need to be made. Therefore, the primary goal of this study is to assess the material's short-term mechanical performance, which is urgently required to develop standardised design codes for alkali-activated concrete structural applications. Understanding the material's long-term behaviour and the durability of reinforced structures, especially the performance development over time, represent another crucial challenge for the utilisation of this novel material in the construction industry, which cannot be neglected. However, as the durability of alkali-activated concrete has been investigated thoroughly in previous studies [7], it is not further discussed in this work.

In the current study, only ground granulated blast furnace slag (GGBFS), fly ashes (FA) and blended systems (GGBFS + FA), activated by sodium hydroxide (SH), sodium silicate (SS), or a combination of them, are considered. Due to the high number of data available in the literature for these types of alkali-activated binders, they have been chosen to evaluate the efficacy of current analytical models to predict the mechanical performance of high-calcium (GGBFS) and low-calcium (FA) alkali-activated systems according to the chemistry of their components. Several other existing aluminosilicate sources have been evaluated in recent years as novel precursors for alkali-activated concrete, to which the considerations made from here on can be applied. Depending on their chemical composition and amorphous content, they can undergo an activation process in which reaction mechanisms can be comparable to the ones shown by the most common GGBFS or FA. Additionally, activator types and mix design formulations can be varied and optimised to meet specific application performance demands.

2 Mix design challenges of AACs

Alkali-activated concrete, like traditional PCC, is obtained by different proportions of binder, liquid, and (fine and coarse) aggregates. However, if for PCC, binder and liquid are generally mainly cement and water, for AAC, a variety of solid precursors and chemical activators, in liquid or solid forms [8–11] are suitable for alkali-activation (Table 1).

Table 1. Main components used for the production of PCC and AAC.

Component	PCC	AAC
Binder	Cement (CEM I – CEM V) Supplementary cementitious materials (SCMs) as cement replacement	By-products of foundries and metal production plants (ferrous slags, i.e. blast furnace slags, ladle slags, electric arc furnace slags, non-ferrous slags, i.e. copper slags) By-products of combustion processes (coal fly ashes, coal bottom ashes, rice husk ashes, sugar cane bagasse ashes, palm oil fuel ashes) By-products of bauxite refining (red mud) Municipal solid wastes incineration (MSWI) ashes Mineral extraction wastes Calcined clays
Liquid	Water	Alkaline solution (alkalis and/or soluble silica sources and/or water)
Aggregates	Fine and coarse aggregates (sand and gravel)	Fine and coarse aggregates (sand and gravel)
Admixtures	Chemical/mineral admixtures	Chemical/mineral admixtures(*)

(*) Many of the chemical admixtures developed for PCC become much less effective in AAC due to the structural instability and complex interactions in the alkaline media [12].

To be suitable for the alkali-activation process, the material chosen as binder needs to contain reactive aluminosilicates, with a certain degree of amorphous content, in combination with calcium oxide (CaO), in which the amount of the latter generally defines the classification of AACs in high-calcium (CaO content > 10 wt%) and low-calcium (CaO content < 10 wt%) systems [13], [14]. Considering these requirements, a vast list of materials presents sufficient reactivity potential to be used as a binder alone or in combination with others in blended systems, as shown in Table 1. The possibility of reusing by-products from different industrial sectors is one of the main environmental advantages of AACs production [15–22]. However, the by-product nature of the binder involves a wide range of chemical and mineralogical variability, influenced by the location of the raw material source and the

primary industrial processes from which they are derived [23,24].

Among the possible binders reported in Table 1, ground granulated blast furnace slags (GGBFS) and calcareous fly ashes (name also class C fly ashes – FA-C), and siliceous fly ashes (named also class F fly ashes (FA-F)) have been chosen as representatives of high- and low-calcium alkali-activated systems, respectively, due to a larger number of studies on reaction mechanism and related products and performance. High- and low-calcium systems require different activation conditions, mainly dependent on the chemical composition and the binder amorphous phase content, besides other factors such as particle size or specific surface area, which are not considered in this study. Due to its high calcium content (CaO > 10 wt%) and its amorphous nature, GGBFS and FA-C require mild alkaline conditions for the reaction process [25], the main product of which is calcium (aluminium) silicate hydrate gels (C-(A)-S-H) [26,27]. On the other hand, FA-F shows lower latent hydraulic potential (CaO < 10 wt %) and/or higher amount of crystalline phases compared to high-Ca binders, resulting in the need for stronger alkaline solutions or heat curing [28–31] to promote the reaction mechanism and the formation of sodium aluminosilicate hydrate gels (N-A-S-H) [32,33].

The differences in the initial mineralogy and chemistry of the precursors, combined with the different alkaline activators dosages and compositions suitable to promote the reaction, introduce several new critical factors in the mix design formulation, affecting the fresh and hardened concrete properties [34,35]. Therefore, it is fundamental to understand how these chemistry-linked parameters influence the concrete behaviour, in particular compressive strength, to which all the material mechanical properties are correlated in standards and design regulations. Table 2 collects the influential factors for AAC mixtures, and how they compare to those conventionally considered for PCC mixes. The difficulties in the definition of a general mix design procedure and, consequently, in the use of formulation parameters to correlate the chemistry of the mix components with the concrete performance, represent the most challenging obstacle for the standardisation of AACs [33,35–37]. In addition, a fine analysis of a specific precursor regarding the reactive and less/non reactive components is critical and necessary for both successful choice and proper formulation of AACs [36].

Table 2. Main parameters involved in the mix design formulation of OPC and AACs

OPCC	AAC
Cement type	Precursor type Amorphous degree Reactivity index CaO/SiO_2 ratio CaO, MgO, Al_2O_3 content
Minimum cement content	Minimum precursor(s) content Na_2O/binder ratio
Water content Water/cement (w/c) ratio	Optimised choice of activator Activator type SiO_2/Na_2O ratio (Ms) Water/binder (w/b) ratio Liquid/binder (l/b) ratio
Aggregates	Aggregates
Curing parameters	Curing parameters

Unlike PCC, whose compressive strength is negatively affected by the water-to-cement ratio (w/c) [38,39], for AAC, it is difficult to establish a single parameter directly affecting the compressive strength, as multiple factors interact to influence its value and development in time. Furthermore, the water-to-cement ratio used for PCC cannot be translated into a water-to-binder ratio (w/b) for AAC, as the liquid involved in the reaction is not just water but also a combination of alkalis and/or soluble silica sources and/or extra water. Three different forms of liquid-to-binder ratios can be defined for AAC, all affecting the material performance differently. The total liquid-to-binder ratio (l/b) considers all the liquids in the mixture as a whole; the water-to-binder ratio (w/b) takes into account the amount of water included in the alkaline activators and the extra water added to the mixture; and the total alkaline activators-to-binder ratio (a/b), only includes the alkaline components of the solution. Although the total l/b and the w/b do not show a clear correlation with the compressive strength, mechanical performance can be roughly linked to the total alkaline activators-to-binder ratio (for a given total l/b and constant water content) [35].

Table 3 shows the main parameters of the alkaline solutions, i.e. the alkali concentration *n*, defined as the number of alkalis for 100g of binder [wt%], and the silicate modulus M_s, i.e. the molar ratio between SiO_2 and Na_2O, and their optimal dosage for low- and high-calcium systems. The alkali content and the silica modulus, in combination with the binder characteristics, govern the chemistry of the mix design formulation and thus the reaction mechanisms, directly affecting the mechanical properties of the material [40,41]. Due to the countless possible binders-activators combinations, it is difficult to generalise the effect of the system chemistry on the mechanical performance. For this reason, it is necessary to find and highlight recurring behaviours and correlations between chemistry and mechanical performance.

Table 3. Main characteristics of the alkaline solutions used for AAC production [13].

	Alkaline potential of the solution	Dosage of M_2O*(*n*)	M_s = $SiO2/M_2O$
Low-calcium systems (CaO content < 10 wt%)	High	7.0 – 9.0 wt%	1.0 – 2.0
High-calcium systems (CaO content > 10 wt%)	Low	3.0 – 6.0 wt%	~ 0.75

(*) M stand for the specific cation, usually K or Na [13]

3 Real-scale applications

Although the recent increasing demand for greener alternatives to traditional concrete has prompted further research and investigations into AAC, this technology and its application in construction projects are not new. The development of AAC has been undertaken in the post-World War II era, with the first applications in the 1950s [42,43] when a blast-furnace slag-based concrete activated with only calcium hydroxide or in combination with sodium sulfate, named "Purdocement", was first used in Belgium for the realisation of several buildings [43]. Since then, numerous structures have been realised, including civil waterworks, pavements, roads, conventional pre-cast products and, most recently, large-scale cast-in-situ projects (Table 4).

Despite these construction works demonstrating over 60 years of service life and their durability outside of laboratory conditions, the commercialisation of AACs did not arise until the highly considerable carbon emissions from conventional OPC manufacture became a concern. This resulted in a worldwide research campaign to better understand and characterise these new construction materials, favouring the drafting of dedicated design guidelines and specifications, which promoted their commercialisation and practical utilisation, as documented first in Australia, and recently in the United Kingdom. Table 5 lists a selection of recently commercialised alkali-activated materials whose successful utilisation in several on-site trials and projects further confirms their potential as construction materials and as traditional concrete alternatives.

Table 4. Examples of real-scale applications of AACs.

Year	Location	Construction work	Material	Ref.
1952-1959	Brussels, Belgium	Parking 58	Purdocement (GGBFS + PC activated by $Ca(OH)_2$ or Na_2SO_4)	[43]
1960-1980	Mariupol, Ukraine	2-storey and 15-storey residential buildings	Alkali-hydroxide activated GGBFS concrete	[42]
1966	Odessa, Ukraine	Drainage collector No. 5	Alkali-carbonate activated GGBFS concrete	[42]
1974	Krakow, Poland	Storehouse	Precast steel-reinforced alkali-carbonate activated GGBFS concrete	[42]
1986-1994	Lipetsk, Russia	24-storey residential building	Alkali-carbonate activated GGBFS concrete	[42]
1988	Yinshan County, Hubei Province, P.R. China	6-storey office and retail building	Sodium sulfate-activated Portland-slag cement concrete	[42]
2009	Melbourne, Australia	Salmon St Bridge	E-Crete precast footpath panel segments (180 precast footway units)	[44]
2009	Brisbane, Australia	Murrarie Plant site bridge	EFC precast bridge decks	[45]
2010	Melbourne, Australia	Thomastown Recreation and Aquatic Center	E-Crete footpaths and driveways	[44]
2012	Melbourne, Australia	Melton Library	E-Crete precast panels and in-situ works	[44]
2013	Queensland, Australia	Global Change Institute (GCI) Building, University of Queensland	EFC – 33 precast floor beam-slab elements	[45]
2013	Irvine, California, USA	Sustainable concrete solar-powered house	Precast alkali-activated fly ash concrete members	[46]
2013	Yuozhong District, Chongqing, P.R. China	Chongqing Research Institute of Construction Science office building	Cast in-situ alkali-activated GGBFS concrete	[47]
2014	Toowoomba, Australia	Toowoomba Wellcamp Airport	EFC – cast in-situ heavy-duty pavements	[45]
2017	London, UK	Thames Tideway Central, Kirtling Street	Cemfree – cast in-situ	[48]
2020	Wageningen, Netherlands	Cycle bridge	RAMAC (prefab)	[49]
2021	Chatham, UK	Chatham railway station (step-free access foundation)	Cemfree – 300 m^3 cast in-situ	[48]
2021	Le Havre, FRA	Grand Port Maritime du Havre	Exegy – concrete barrette (17 m depth)	[50]

Table 5. Examples of recently commercialised alkali-activated materials.

Product name	Company	Composition	Ref
E-Crete™	Zeobond Pty Ldt (Australia)	Fly ash and slag	[44]
EFC (Earth Friendly Concrete)	Wagners (Australia)	Blast furnace slag and fly ash chemically activated	[45]
Cemfree	DB Group (UK)	GGBFS and pulverised fuel ash (PFA)	[48]
Vertua® Ultra	CEMEX (UK)	Geopolymer clinker-free concrete	[51]
Blockwalls™	Virtus Concrete Solutions Ltd (UK)	Pre-cast geopolymer concrete blocks made from reclaimed stone, kiln ash, inert waste and sodium silicate sourced from recycled e-waste	[52]
RAMAC	SQAPE BV (NL)	Ready-mix cement-free concrete	[49]
Exegy	Soletanche Bachy (FRA)	GGBFS activated with sodium carbonate	[50]

4 Towards performance-based standards for AACs

The increasing number of successful applications of AACs in construction encouraged research institutes and construction industries to further investigate material behaviour and develop new approaches to broaden its use. However, since the positive impact of these alternative binders is coupled with several limitations, research efforts often encounter the resistance of regulatory bodies, due to the not yet overcome challenges in linking chemistry and structural performance, and the limited number of adequate durability data, hindering the standardisation process of alkali-activated concrete technology.

To promote the use of AACs as an alternative to traditional cement-based concrete, avoiding the timeframe required to draft national or international standards, performance-based design specifications represent the most feasible solution [4,53], as firstly demonstrated in Australia and most recently in the United Kingdom. This approach led in 2011 to the development of the "Concrete Institute of Australia (CIA) Recommended Practice for Geopolymer Concrete", a practical guideline defining the mechanical behaviour and the short- and long-term properties of geopolymer concrete, providing design equations and methods for its application in the construction field. In the following years, Austroads, the peak organisation of Australasian road transport and traffic agencies, developed additional specifications [54,55] for the use of geopolymer concrete in the manufacture of structural and non-structural components, promoting their utilisation in several infrastructural projects, as described in the previous section. In the same years, in the UK, the British Standards Institute Publicly Available Specification (PAS) 8820:2016 "Construction materials – alkali-activated cementitious material and concrete – Specification" represented the first attempt in Europe to develop performance-based design guidelines for the adoption of AACs in the construction industry. This guideline specifies a means of assessing the performance and durability requirements for alkali-activated concretes to facilitate and encourage their use in construction projects. The PAS 8820:2016 sets the maximum possible Portland cement content at 5% mass of binder solids and provides recommendations about concrete mixing, placement, curing and testing. In the PAS 8820:2016, the chosen alkali-activated material-based binder needs to be tested in parallel with a reference cement-based concrete and is required to achieve at least equivalent or superior mechanical and durability performance requirements defined in the BS 8500, the British standard for PCC. Existing standardised testing methods for traditional concrete are analysed and implemented, if needed, with modifications targeted at the performance of AACs. The choice to undergo the PAS process instead of the standardisation process allowed the rapid development of a specification to fulfil an immediate need in the construction industry.

For instance, the proposition of a performance-based approach for standards and design codes of a new technology requires a high degree of confidence level. Hence, it is necessary to demonstrate the safety and reliability of AACs as construction materials, and their ability to meet mechanical and durability performance requirements. The RILEM Technical Committee 247-DTA has performed round-robin testing programs to assess the reproducibility of the mechanical behaviour of different binders and their durability performance [17,56,57]. The investigations demonstrated how the variability and the complexity of the mix design formulation can lead to different results, mainly in durability parameters, even following the same mixing and testing procedures. For this reason, it is fundamental to evaluate separately the performance of AACs according to binder type and mix design proportions, which affects the hardened material behaviour. Blast furnace slags, for example, show higher intrinsic reactivity, and therefore require milder activating conditions [27,58], although it is followed by significant autogenous shrinkage levels [59–61] and potential carbonation [62]. On the other hand, fly ash requires activation-enhancing practices, such as heat curing and higher alkalinity [27,63], which, if not properly controlled, results in flash setting [56,64] and coarser microstructure, leading to issues related to the transport of undesired species [57]. Moreover, other novel precursors, the majority of which are summarised in Table 1, could deliver interesting punctual characteristics [17,65–68] and, while not sufficient to be utilised as sole precursors, could be used as part of mixtures with other components aiming to specific performance.

It is indeed necessary to classify alkali-activated concretes in classes according to the characteristic of the main constituents, analysing each class separately and developing targeted standards based on laboratory experiments data regarding both mechanical and durability performance.

5 Analytical correlations of mechanical properties of AACs

The assessment of the mechanical performance of alkali-activated concrete through laboratory testing and the evaluation of the effect of the chemistry of the mixture formulation on the material behaviour are essential for the production and classification of AACs. In addition, the design of equations and empirical correlations between mechanical properties must be defined to facilitate their use as reliable structural materials. Code-based analytical equations developed for traditional cement-based concrete (Table 6) correlate the 28-day compressive strength, a relatively easy parameter to be determined experimentally, to the mechanical properties relevant to structural design, such as (direct or indirect) tensile strength and modulus of elasticity.

As direct comparisons with PCC are always the starting point of analysis, the same correlations are expected to be observed in the case of AACs. To verify the suitability of the analytical expressions proposed in Table 6 in predicting mechanical performance, literature data regarding the mechanical properties of different types of AACs have been collected and analysed [69–91]. The 28-day compressive strength of alkali-activated mixtures obtained with different binders (GGBFS, FA-F and FA-C, and blends of GGBFS and FA-F), activated with either sodium hydroxide or sodium silicate, was used to predict their modulus of elasticity (E_c) and the tensile strength (f_{ct}) according to the correlations in Table 6. Equations using the concrete density as a parameter to estimate the modulus of elasticity have not been considered. Only literature providing fully detailed mix design formulations, including activator type and dosage (molarity of sodium hydroxide, silicate modulus, contents of components of sodium silicate), extra water content, aggregates (type and content) have been analysed [69–91]. The correlations use the characteristic cylindrical compressive strength and the tensile strength values obtained by performing splitting tensile and flexural tensile strength tests. Conversion factors were applied for the cubic-to-cylinder compressive strength and for indirect to direct tensile strength according to Eurocode 2.

Fig. 1 shows the correlations between the 28-day compressive strength and the 28-day modulus of elasticity (Fig. 1a) and tensile strength (Fig. 1b), and predictions of current code-based equations (Table 6). The two experimentally obtained properties present a direct correlation with each other, following the trends given by the design codes. It is possible to observe a largely scattered pattern of the total data points, which is decreased when each precursor is individually analysed. Although the correlation of properties of PCCs using the same code-based equations also presents dispersed data [92], Fig. 1 demonstrates that the vast majority of data points are located below the trendlines. The variable distance between reported and predicted values, according to the type of precursor, indicates that the current design codes fail to deliver a reliable and comprehensive prediction of the mechanical performance of all types of AACs. In general, a lower modulus of elasticity of alkali-activated concretes is expected compared to traditional cement-based concretes [60,74,75,93–95]. However, different precursors were observed to display different behaviours. Concrete mixes using siliceous fly ashes present values of E_c, in general, lower than calcareous fly ashes, with the latter displaying similar behaviour to slags. In the case of FA-F, curing conditions were observed to have a major influence on final properties. Heat curing, classified here as concrete mixes cured at temperatures above 50 ºC for at least 24 h (FA-F_HT), showed improved mechanical properties compared to ambient cured ones (FA-F_RT). Blending FA-F with slag approximates the E_c to the correlations proposed by the model codes, although still overestimates it.

Table 6. Current analytical equations for PCC to predict tensile strength and modulus of elasticity from the compressive strength.

Standard	Tensile (f_{ct}), splitting tensile ($f_{ct,sp}$), and flexural ($f_{ct,fl}$) strength correlated to the 28-day compressive strength (f_{ck})	Modulus of elasticity
Eurocode 2 (2021)	$f_{ctm} = 0.3 f_{ck}^{2/3}$, $f_{ck} \leq 50\ MPa$ $f_{ctm} = 1.1 f_{ck}^{1/3}$, $f_{ck} > 50\ MPa$	$E_{cm} = k_E f_{cm}^{1/3}$
fib Model Code 2010	$f_{ctm} = 0.3 f_{ck}^{2/3}$, $f_{ck} \leq 50\ MPa$ $f_{ctm} = 2.12 \ln\left(1 + 0.1\left(f_{ck} + \Delta_f\right)\right)$, $f_{ck} > 50\ MPa$ $f_{ctm} = f_{ctm,sp}$ $f_{ctm} = \alpha_{fl} f_{ctm,fl}$, $\alpha_{fl} = \frac{0.06 h_b^{0.7}}{1 + 0.06 h_b^{0.7}}$	$E_{ci} = E_{c0} \alpha_E \left(\frac{f_{ck} + \Delta_f}{10}\right)^{1/3}$
AS3600 (2009)	$f_{ctk} = 0.36\sqrt{f_{ck}}$ $f_{ctk,fl} = 0.60\sqrt{f_{ck}}$	$E_{cj} = 0.043 \rho^{1.5} \sqrt{f_{cmi}}$, $f_{cmi} \leq 40\ MPa$ $E_{cj} = 0.024 \rho^{1.5} \left(\sqrt{f_{cmi}}\right) + 12$, $f_{cmi} > 40\ MPa$
ACI-363 (2010)	$f_{ct,sp} = 0.59\sqrt{f'_c}$ $f_{ct,fl} = 0.94\sqrt{f'_c}$	$E_c = 3320\sqrt{f'_c} + 6900$
ACI-318 (2011)	$f_{ct,sp} = 0.56\sqrt{f'_c}$ $f_{ct,fl} = 0.62\sqrt{f'_c}$	$E_c = 33 \rho^{1.5} \sqrt{f'_c}$

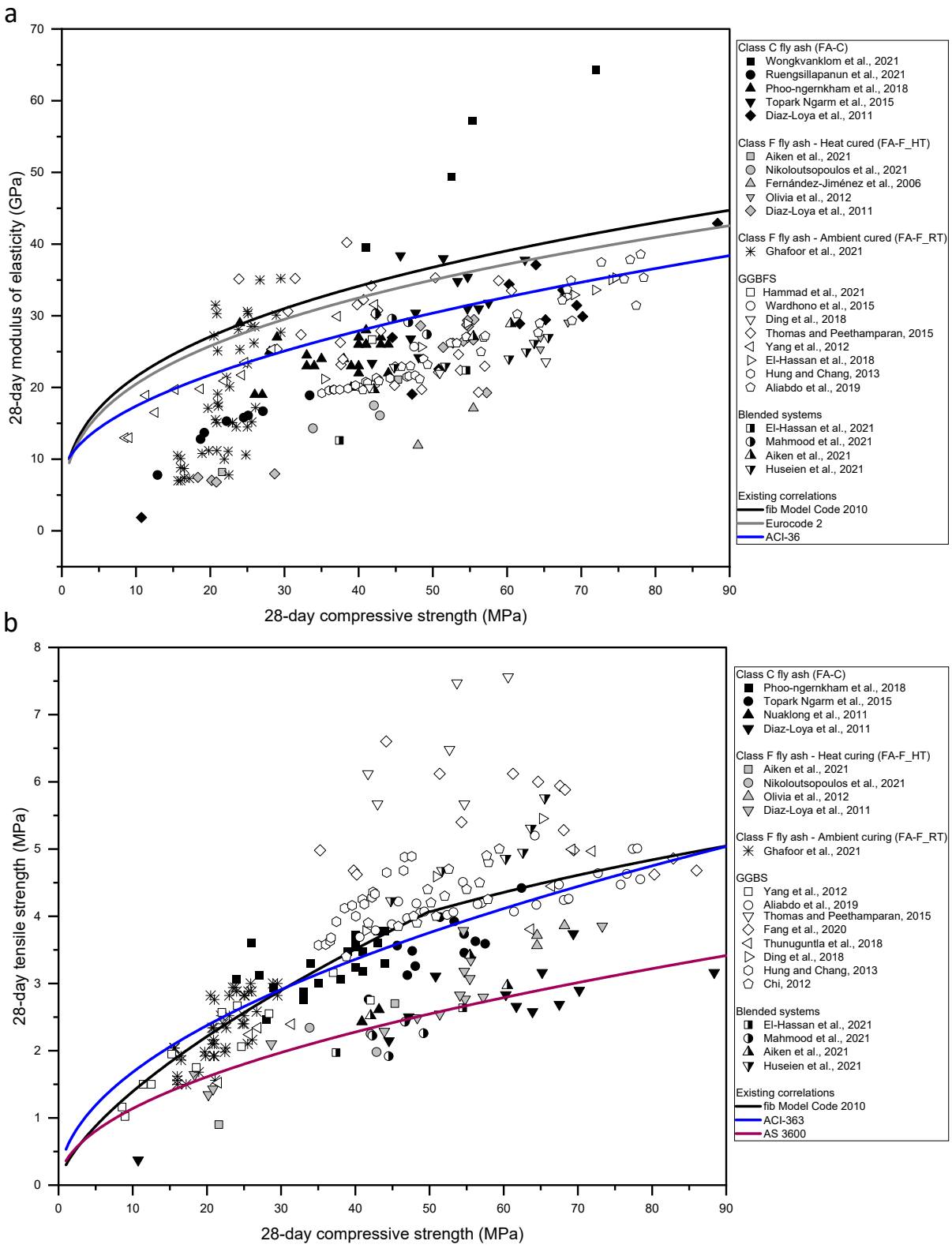

Figure 1. Correlations between compressive strength of AACs and (a) modulus of elasticity; (b) tensile strength (see Appendix for more details about the collected datapoints).

Also for the 28-day tensile strength, different behaviours according to the binder type can be noticed. High-Ca precursors tend to display higher values of tensile strength, with predictions underestimating their properties above a threshold compressive strength of 30 MPa. In the case of FA-C, the majority of the analysed data displays a strong correlation with code-based equations up to compressive strength values of 60 MPa. On the other hand, for mixtures of FA-F solely or blended with slag, code-based equations significantly overestimate their behaviour, with most data points located far below the model codes for compressive strength above 30 MPa. Below this threshold, FA-F still presents a good correlation.

Overestimation and underestimation of mechanical properties could represent significant problems for the design of concrete structures, with a direct impact on their fabrication process, nature of application, performance and service life. The elastic modulus is crucial for the understanding of concrete deformations, mainly caused by creep and load relaxation, and directly affects the long-term behaviour of the structure. Consequently, both overestimation and underestimation of E_c observed for AACs, come with concern and can affect the safety level of structural elements, and this elucidates that deformation mechanisms must be fully understood in these alternative structural materials. The overestimation of the tensile strength represents a non-negligible issue, as it can compromise the integrity of the entire structure, causing unexpected failure if higher values of maximum permissible loads are assumed. Therefore, the correlation of mechanical properties for the prediction of tensile strength should be subject to a conservative approach, which is not observed when PCC-based equations are used to estimate the performance of AAC.

Overestimation and underestimation of the 28-day mechanical properties could represent significant problems for the design of concrete structures, with a direct impact on their fabrication process, nature of application, performance and service life. The elastic modulus is crucial for the understanding of concrete deformations, mainly caused by creep and load relaxation, and directly affects the long-term behaviour of the structure. Consequently, both overestimation and underestimation of E_c observed for AACs, come with concern and can affect the safety level of structural elements, and this elucidates that deformation mechanisms must be fully understood in these alternative structural materials. The overestimation of the tensile strength represents a non-negligible issue, as it can compromise the integrity of the entire structure, causing unexpected failure if higher values of maximum permissible loads are assumed. Therefore, the correlation of mechanical properties for the prediction of tensile strength should be subject to a conservative approach, which is not observed when PCC-based equations are used to estimate the performance of AAC.

Although AACs differ from traditional concrete in terms of reaction mechanism and reaction products, the analytical expressions developed for PCC are more suitable to describe the behaviour of slag- and calcareous fly ash-based concretes, which can be explained partially by the nature of obtained reaction products. The primary phase formed for high-Ca binders is a C-A-S-H gel [96,97], chemically and structurally similar to C-S-H gels formed in PCC mixtures. Oppositely, low-Ca systems have N-A-S-H gels as the main reaction product [27,98], a phase with a strong tendency to form a cementitious matrix more cohesive than other gels, resulting in a more brittle microstructure and lower tensile strength compared to high-calcium systems [77,99] of the same strength class (> 60 MPa).

Current code-based models generally underestimate the tensile strength [35] and significantly overestimate the modulus of elasticity of AACs, as shown in Fig. 1. Following this discrepancy, recent studies investigated their mechanical properties and proposed new constitutive models to predict their performance behaviour more accurately (Table 7).

Fig. 2 shows the ability of the equations in Table 7 in predicting the mechanical performance of alkali-activated concretes. In general, the proposed correlations approximate the experimental behaviour of AACs to predicted values. However, although similar trends are observed for the estimated values, a higher variation degree between equations is noticed in Fig. 2a. This variation is even clearer for tensile strength (Fig. 2b), as the ultimate calculated values vary from 10.2 MPa (Thomas and Peethamparan [74]) to 3.84 MPa (Lee and Lee [95]) for a compressive strength value of 90 MPa.

Table 7. Current constitutive models developed for AACs.

Authors	Tensile (f_{ct}), splitting tensile ($f_{ct,sp}$), and flexural ($f_{ct,fl}$) strength correlated to the 28-day compressive strength (f'_c)	Modulus of elasticity [MPa]
Yang et al. (2012) [100]	$f_{ct} = 0.255(f'_c)^{0.65}$	$E_c = 4600\left(\frac{\rho_c}{2200}\right)^{1.5}\sqrt{f'_c}$
Lee and Lee (2013) [95]	$f_{ctm,sp} = 0.45\sqrt{f'_c}$	$E_c = 5300(f'_c)^{1/3}$
Thomas and Peethamparan (2015) [74]	$f_{ct,sp} = \frac{2}{5}(f'_c)^{\frac{7}{9}}$ $f_{ct,sp} = 1.08\sqrt{f'_c}$	$E_c = 2900\,(f'_c)^{\frac{3}{5}}$ $E_c = 4400\sqrt{f'_c}$
Xie et al. (2020) [35]	$f_{ct,fl} = 0.55(f'_c)^{0.6}$ $f_{ct,sp} = 0.35(f'_c)^{0.65}$	$E_c = 3650\sqrt{f'_c}$
Cui et al. (2020) [101]	$f_{ct} = 0.0876f'_c + 0.0585$	$E_c = 874.5(f'_c)^{0.85}$

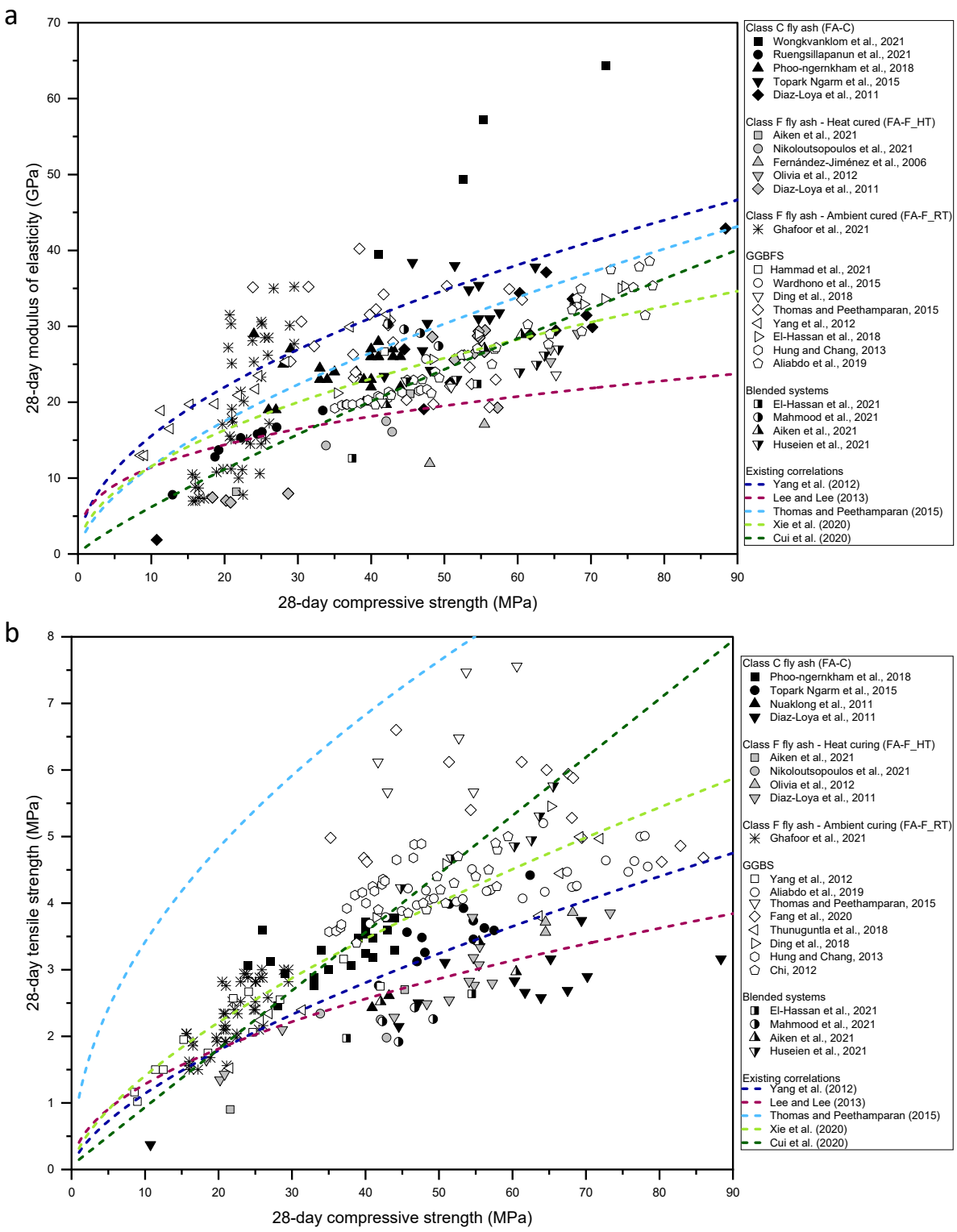

Figure 2. Correlations between compressive strength of AACs and (a) modulus of elasticity; (b) tensile strength (see Appendinx).

Despite the proposition of several equations in the last decade, each one of them focused on the analysis of a limited amount of data obtained from the available literature or experimental investigations. Thomas and Peethamparam [74] focused their work on the alkali-activation of high-Ca binders, using slag and calcareous fly ash as binders. Lee and Lee [95] dedicated their work to blends of siliceous fly ash and slags, with the former being the main component of the mixture (> 80 wt%), Yang et al. [100] worked with slag-based concrete activated with calcium hydroxide. Cui et al. [101] based the proposed equations on high temperature cured siliceous fly ash based concrete, while Xie et al. [35] derived equations based on a wide range of precursors, considering both traditional (slag and siliceous fly ash) and alternative ones (biomass waste ashes).

In general, the slope of the curves of the proposed equations in Fig. 2a is noticeably lower than in Fig. 1a. If individual precursors are considered, the prediction of the modulus of elasticity is more closely related to experimental values, indicating a lower degree of overestimation of this property. Equations proposed by Yang et al. [100] and Thomas and Peethamparam [74] reach the highest values of E_c, following the known behaviour of slag-based concretes. The work from Cui et al. [101] and Lee and Lee [95] present an overall good agreement with experimental data of mixtures containing FA-F individually and in blends with slag. An underestimation of the performance of room temperature cured siliceous fly ash by all equations represents the need for a deep understanding of the mechanisms of microstructure evolution of this class of binders.

Differences between derived equations available in the literature are inevitable, as the broad spectrum of available AACs implies many variabilities to be considered. A more significant influence of precursors and their obtainment route is observed in Fig. 2b. While the works from Yang et al. [100] and Lee and Lee [95] are in agreement with the referred precursors, equations proposed by Cui et al. [101] and Thomas and Peethamparam [74] are observed to be outliers in the chart. In both cases, part of the concrete mixtures designed by the authors was subject to high-temperature curing (80 ºC and 55 ºC, respectively). While heat-curing of slag and calcareous fly ash binders is known to significantly affect their tensile strength [29][102][103], all of the data points acquired in the present work for high-Ca based concrete mixtures represent room temperature curing processes. Consequently, an overestimation of the mechanical performance is perceived from the trendline proposed by Thomas and Peethamparam [74], although BFS-based concrete presents the highest values of tensile strength among all mixtures analysed. As for Cui et al. [101], the linear trendline presents increasing disagreement with collected data regarding the evolution of compressive strength. It can thus be assumed that high-strength AACs require a different approach for the correlation of properties, and the use of linear equations for the prediction of performance, even for the same class of concrete, should be avoided.

As visualized in both charts in Fig. 2, the equations proposed by Xie et al. [35] present a rough average of the other four. The visualization of such behaviour is expected since the author considered both high- and low-Ca precursors. However, while it can provide an initial indication of performance, the closer proximity of the other trendlines with their corresponding specific precursors indicates that it is difficult to create a unique equation englobing all types of alkali-activated binders.

The amount of data available in the literature can be used in an attempt to derive new analytical correlations between the compressive strength and other mechanical properties. However, due to the variability and complexity of the reaction process, a unique set of general equations covering all the possible mix design formulations, based exclusively on correlation of mechanical properties, cannot be derived. It is fundamental not only to consider the chemical composition of the binder, in particular its CaO and amorphous phases contents, but also the composition and dosage of the alkaline solutions, which play a fundamental role in the development of the mechanical performance of the material. This can be easily seen in Fig. 3, where new correlations to estimate the modulus of elasticity and the tensile strength have been derived using the equation type generalised in Eq. (1) and (2), respectively, for high- and low-calcium systems.

$$E_c = a \cdot 21.5 \cdot \left(\frac{f_{cm}}{10}\right)^{1/3} \quad (1)$$

$$f_{ctm} = b \cdot (f_{cm})^{2/3} \quad (2)$$

As shown in Fig. 3a-3b, for both high- and low-calcium systems, $a < 1$, to demonstrate how the modulus of elasticity is generally lower for AAC compared to PCC. Table 8 collects the derived parameters, a and b, and the related R^2 value for high- and low-calcium systems.

Table 8. Proposed parameters for Eq. (1) and (2) for alkali-activated systems.

Parameter	GGBFS	FA-C	FA-F_HT	FA-F_RT	Blended
a	15.864	17.421	12.531	14.548	14.480
R^2	0.356	0.379	0.434	0.156	0.135
b	0.306	0.277	0.212	0.297	0.255
R^2	0.408	0.296	0.853	0.538	0.373

Despite the high number of data points, the R^2 is lower than 0.43, showing how the simple classification of the material according to the CaO content is not sufficient to describe the behaviour of AAC. The same can be observed for the tensile strength, as shown in Fig. 3c-3d. The high scatter between data points collected for the same binder type indicates how also the chemistry and the amount of the activators significantly affect the mechanical properties of the material. Thus, additional investigations evaluating, not only the binder chemistry, but also the characteristics of the alkaline solution used, need to be carried out to derive analytical equations able to correlate the chemistry of the mix formulation with the mechanical properties of the hardened concrete.

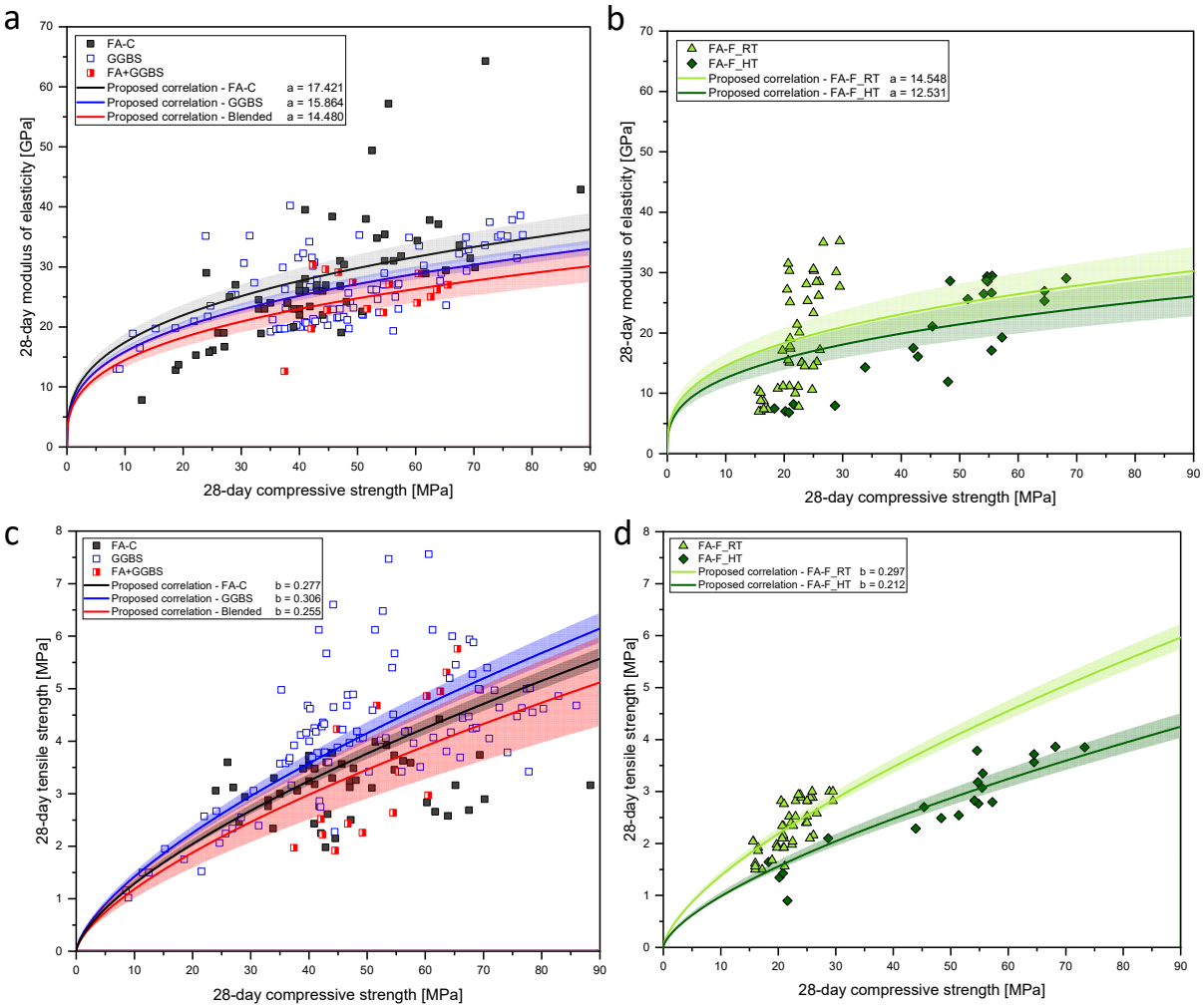

Figure 3. New correlation to predict the modulus of elasticity (a-b) and the tensile strength (c-d) from the compressive strength of high- and low-calcium systems (see Appendix).

It is important to state that, the absolute experimentally obtained values of all of the mechanical properties of AACs analyzed in this present work is, in general, sufficiently high according to minimal requirements of PCC-based design codes. In addition, despite the poor overall agreement in between compressive strength and modulus of elasticity and tensile strength for all of the collected data, it was possible to visualize similar trends in the correlation of properties when high- and low-Ca binders were evaluated individually. In addition, despite the poor overall agreement in between compressive strength and modulus of elasticity and tensile strength for all of the collected data, it was possible to visualize similar trends in the correlation of properties when high- and low-Ca binders were evaluated individually. Therefore, the adoption of performance-based standards, along with the determination of classes of binders, based on the mineralogical and chemical characteristics of precursors and activators, can represent a strong opportunity and an important step towards growth of the commercial potential of AACs.

6 Conclusions

The need to achieve carbon neutrality by 2050 has increased interest in alkali-activated binders as a more environmentally friendly alternative to traditional cement-based binders in the construction sector. Recent investigations provided not only a better understanding of the technology from a chemical, physical and mechanical point of view but also raised awareness of the additional steps necessary for the adoption of alkali-activated concretes on the European and international markets. Despite being the subject of research for decades, with positive characteristics compared to traditional construction materials, the significant number of complexities involved in the whole production chain creates a barrier to the AAC's utilisation in large-scale projects.

To overcome the existing barriers to the standardisation of AACs and to broaden their application as reliable structural engineering materials, a few challenges need to be faced:

- The classification in high- and low-calcium alkali-activated systems, based on the CaO content of the binder, with 10 wt% being the threshold value, can be used to easily distinguish the different reaction mechanisms and related products, i.e. C-A-S-H and N-A-S-H gels, respectively, but is not sufficient to predict the mechanical performance of the systems.
- Due to the varying amounts of CaO reactive fraction and amorphous phases in the precursors, differing mechanical performance can be developed by concretes obtained by alkali-activation of binders with comparable CaO content and same activators quantities and proportions. A possible way to provide a more accurate classification of the binders suitable for alkali-activated concrete and an easier prediction of its short and long-term behaviour is to couple the CaO content with the amount of its reactive fraction and the content of amorphous phases in the binder.
- Although a more accurate classification of the binder is necessary to better understand and predict its behaviour during the reaction process, it is essential to consider also the characteristics of the alkaline solutions when defining the concrete mix design. The alkali content and silica modulus of the solutions can be adjusted and tailored according to the binder type to achieve the required material mechanical and durability performance, enabling the fit-to-purpose production of alkali-activated concrete.
- New analytical correlations based on the main characteristics of both binder and alkaline solutions need to be developed to predict the mechanical performance of the material, in particular the modulus of elasticity and tensile strength, from its compressive strength to promote the formulation of design regulations suitable for alkali-activated concrete.
- Performance-based over prescriptive standards and building regulations need to be preferred to facilitate the standardisation, commercialisation and adoption of alternative construction materials such as alkali-activated concrete. Although in the last decade several alkali-activated systems-based products have become available on the market, dedicated standards at an international level are still missing, but highly necessary.

Overcoming the challenges briefly summarised in this study is certainly not an easy task to accomplish. Future investigations need to focus on a better understanding of how the chemistry of the mix design components affects the reaction mechanisms of conventional and non-conventional binders and the mechanical and durability performance of alkali-activated concretes. Only deriving new analytical correlations between mechanical properties according to the chemistry of the system can promote the drafting of design guidelines and regulations and favour the adoption of AACs. Construction industries also play a fundamental role in not only further promoting the development of fit-to-purpose marketable mix design formulations but also building pilots and real-scale projects to validate the material performance and raise awareness of its potential. This would be additionally facilitated by the adoption of performance-based standards, which require newly developed construction materials to match or exceed the mechanical and long-term behaviour of traditional concrete, without defining specific mix design components or proportions. Only continuous advances in all the above-mentioned sectors can lead to the standardisation and commercialisation of alkali-activated concrete on a global market level.

Acknowledgment

This project has received funding from the European Union's Horizon 2020 research and innovation programme under grant agreement No 813596 DuRSAAM. The opinions expressed in this document reflect only the author's view and reflect in no way the European Commission's opinions. The European Commission is not responsible for any use that may be made of the information it contains.

Authorship statement (CRediT)

Laura Rossi, Luiz Miranda de Lima and Yubo Sun: Writing – original draft, writing – review and editing, formal analysis, investigation, conceptualisation

Frank Dehn, John L. Provis, Guang Ye, Geert De Schutter: Writing – review and editing, supervision

References

[1] D. Hodgson, P. Hugues, T. Vass, Cement, IEA Report 2022 (2022), IEA, Paris. https://www.iea.org/reports/cement.
[2] Cembureau, Cementing the European Green Deal, Reaching Climate Neutrality along the Cement and Concrete Value Chain by 2050 (2020). https://cembureau.eu/media/kuxd32gi/cembureau-2050-roadmap_final-version_web.pdf
[3] A. Favier, C. De Wolf, K. Scrivener, G. Habert, A sustainable future for the European Cement and Concrete Industry: Technology assessment for full decarbonisation of the industry by 2050, ETH Zurich, 2018.
[4] J.S.J. Van Deventer, D.G. Brice, S.A. Bernal, J.L. Provis, Development, standardization, and applications of alkali-activated concretes, ASTM Spec. Tech. Publ. STP 1566 (2013) 196-212. https://doi.org/10.1520/STP156620120083
[5] P. Duxson, A. Fernández-Jiménez, J.L. Provis, G.C. Lukey, A. Palomo, J.S.J. Van Deventer, Geopolymer technology: The current state of the art, J. Mater. Sci. 42 (2007) 2917-2933. https://doi.org/10.1007/s10853-006-0637-z
[6] A. Adesina, Performance and sustainability overview of alkali-activated self-compacting concrete, Waste Dispos. Sustain. Energy. 2 (2020) 165-175. https://doi.org/10.1007/s42768-020-00045-w
[7] J.L. Provis, F. Winnefeld, Outcomes of the round robin tests of RILEM TC 247-DTA on the durability of alkali-activated concrete, in: Proceedings of the International Conference on Concrete Repair, Rehabilitation and Retrofitting (ICCRRR 2018), Cape Town, South Africa, MATEC Web of Conferences 199 (2018) 02024. https://doi.org/10.1051/matecconf/201819902024
[8] M.C.G. Juenger, F. Winnefeld, J.L. Provis, J.H. Ideker, Advances in alternative cementitious binders, Cem. Concr. Res. 41 (2011) 1232-1243. https://doi.org/10.1016/j.cemconres.2010.11.012
[9] Y. Li, X. Min, Y. Ke, D. Liu, C. Tang, Preparation of red mud-based geopolymer materials from MSWI fly ash and red mud by mechanical activation, Waste Manag. 83 (2019) 202-208. https://doi.org/10.1016/j.wasman.2018.11.019

[10] J. Rivera, F. Castro, A. Fernández-Jiménez, N. Cristelo, Alkali-Activated Cements from Urban, Mining and Agro-Industrial Waste: State-of-the-art and Opportunities, Waste and Biomass Valorization. 12 (2021) 2665-2683. https://doi.org/10.1007/s12649-020-01071-9
[11] S.A. Bernal, E.D. Rodríguez, A.P. Kirchheim, J.L. Provis, Management and valorisation of wastes through use in producing alkali - activated cement materials, J. Chem. Technol. Biotechnol. 91 (2016) 2365-2388. https://doi.org/10.1002/jctb.4927
[12] C. Lu, Z. Zhang, C. Shi, N. Li, D. Jiao, Q. Yuan, Rheology of alkali-activated materials: A review, Cem. Concr. Compos. 121 (2021) 104061. https://doi.org/10.1016/j.cemconcomp.2021.104061
[13] A. Herrmann, A. Koenig, F. Dehn, Structural concrete based on alkali-activated binders: Terminology, reaction mechanisms, mix designs and performance, Struct. Concr. 19 (2018) 918-929. https://doi.org/10.1002/suco.201700016
[14] P. Duxson, J.L. Provis, Designing precursors for geopolymer cements, J. Am. Ceram. Soc. 91 (2008) 3864-3869. https://doi.org/10.1111/j.1551-2916.2008.02787.x
[15] J.C.B. Moraes, M.M. Tashima, J.L. Akasaki, J.L.P. Melges, J. Monzó, M. V Borrachero, L. Soriano, J. Payá, Effect of sugar cane straw ash (SCSA) as solid precursor and the alkaline activator composition on alkali-activated binders based on blast furnace slag (BFS), Constr. Build. Mater. 144 (2017) 214-224. https://doi.org/10.1016/j.conbuildmat.2017.03.166
[16] I.I. Bashar, U.J. Alengaram, M.Z. Jumaat, A. Islam, H. Santhi, A. Sharmin, Engineering properties and fracture behaviour of high volume palm oil fuel ash based fibre reinforced geopolymer concrete, Constr. Build. Mater. 111 (2016) 286-297. https://doi.org/10.1016/j.conbuildmat.2016.02.022
[17] S.A. Bernal, E.D. Rodríguez, R. Mejia de Gutiérrez, J.L. Provis, S. Delvasto, Activation of metakaolin/slag blends using alkaline solutions based on chemically modified silica fume and rice husk ash, Waste Biomass Valoriz. 3 (2012) 99-108. https://doi.org/10.1007/s12649-011-9093-3
[18] Y. Liu, C. Shi, Z. Zhang, N. Li, An overview on the reuse of waste glasses in alkali-activated materials, Resour. Conserv. Recycl. 144 (2019) 297-309. https://doi.org/10.1016/j.resconrec.2019.02.007
[19] A. Maldonado-Alameda, J. Giro-Paloma, A. Svobodova-Sedlackova, J. Formosa, J.M. Chimenos, Municipal solid waste incineration bottom ash as alkali-activated cement precursor depending on particle size, J. Clean. Prod. 242 (2020) 118443. https://doi.org/10.1016/j.jclepro.2019.118443
[20] N.H. Thang, N.N. Hoa, D.T. Vu, P.T. Kien, M.A.B. Promentilla, Properties of geopolymer from coal bottom ash and water glass solution, Proceedings of the 23rd Regional Symposium on Chemical Engineering, Vung Tao City, Vietnam (2016), paper S03-26.
[21] M.C. Bignozzi, L. Barbieri, I. Lancellotti, New geopolymers based on electric arc furnace slag. Adv. Sci. Technol. 69(2010) 117-122. https://doi.org/10.4028/www.scientific.net/AST.69.117
[22] I.G. Lodeiro, N. Cristelo, A. Palomo, A. Fernández-Jiménez, Use of industrial by-products as alkaline cement activators, Constr. Build. Mater. 253 (2020) 119000. https://doi.org/10.1016/j.conbuildmat.2020.119000
[23] K. Gong, C.E. White, Impact of chemical variability of ground granulated blast-furnace slag on the phase formation in alkali-activated slag pastes, Cem. Concr. Res. 89 (2016) 310-319. https://doi.org/10.1016/j.cemconres.2016.09.003
[24] M.E. Natali, C.E. White, M.C. Bignozzi, Elucidating the atomic structures of different sources of fly ash using X-ray and neutron PDF analysis, Fuel. 177 (2016) 148-156. https://doi.org/10.1016/j.fuel.2016.03.017
[25] F. Pacheco-Torgal, J. Castro-Gomes, S. Jalali, Alkali-activated binders: A review: Part 1. Historical background, terminology, reaction mechanisms and hydration products, Constr. Build. Mater. 22 (2008) 1305-1314. https://doi.org/10.1016/j.conbuildmat.2007.10.015
[26] R.J. Myers, S.A. Bernal, R. San Nicolas, J.L. Provis, Generalized structural description of calcium-sodium aluminosilicate hydrate gels: The cross-linked substituted tobermorite model, Langmuir. 29 (2013) https://doi.org/10.1021/la4000473
[27] J.L. Provis, S.A. Bernal, Geopolymers and related alkali-activated materials, Annu. Rev. Mater. Res. 44 (2014) 299-327. https://doi.org/10.1146/annurev-matsci-070813-113515
[28] V. Živica, Effects of type and dosage of alkaline activator and temperature on the properties of alkali-activated slag mixtures, Constr. Build. Mater. 21 (2007) 1463-1469. https://doi.org/10.1016/j.conbuildmat.2006.07.002
[29] T. Bakharev, J.G. Sanjayan, Y.-B. Cheng, Effect of elevated temperature curing on properties of alkali-activated slag concrete, Cem. Concr. Res. 29 (1999) 1619-1625. https://doi.org/10.1016/S0008-8846(99)00143-X
[30] X. Jiang, R. Xiao, Y. Bai, B. Huang, Y. Ma, Influence of waste glass powder as a supplementary cementitious material (SCM) on physical and mechanical properties of cement paste under high temperatures, J. Clean. Prod. 340 (2022) 130778. https://doi.org/10.1016/j.jclepro.2022.130778
[31] X. Jiang, Y. Zhang, R. Xiao, P. Polaczyk, M. Zhang, W. Hu, Y. Bai, B. Huang, A comparative study on geopolymers synthesized by different classes of fly ash after exposure to elevated temperatures, J. Clean. Prod. 270 (2020) 122500. https://doi.org/10.1016/j.jclepro.2020.122500
[32] M.T. Junaid, O. Kayali, A. Khennane, J. Black, A mix design procedure for low calcium alkali activated fly ash-based concretes, Constr. Build. Mater. 79 (2015) 301-310. https://doi.org/10.1016/j.conbuildmat.2015.01.048
[33] N. Li, C. Shi, Z. Zhang, D. Zhu, H.-J. Hwang, Y. Zhu, T. Sun, A mixture proportioning method for the development of performance-based alkali-activated slag-based concrete, Cem. Concr. Compos. 93 (2018) 163-174. https://doi.org/10.1016/j.cemconcomp.2018.07.009
[34] S.A. Bernal, J.L. Provis, B. Walkley, R. San Nicolas, J.D. Gehman, D.G. Brice, A.R. Kilcullen, P. Duxson, J.S.J. Van Deventer, Gel nanostructure in alkali-activated binders based on slag and fly ash, and effects of accelerated carbonation, Cem. Concr. Res. 53 (2013) 127-144. https://doi.org/10.1016/j.cemconres.2013.06.007
[35] T. Xie, P. Visintin, X. Zhao, R. Gravina, Mix design and mechanical properties of geopolymer and alkali activated concrete: Review of the state-of-the-art and the development of a new unified approach, Constr. Build. Mater. 256 (2020) 119380. https://doi.org/10.1016/j.conbuildmat.2020.119380
[36] Z. Zhang, J.L. Provis, J. Zou, A. Reid, H. Wang, Toward an indexing approach to evaluate fly ashes for geopolymer manufacture, Cem. Concr. Res. 85 (2016) 163-173. https://doi.org/10.1016/j.cemconres.2016.04.007
[37] B. Sun, Y. Sun, G. Ye, G. De Schutter, A mix design methodology of slag and fly ash-based alkali-activated paste, Cem. Concr. Compos. 126 (2022) 104368. https://doi.org/10.1016/j.cemconcomp.2021.104368
[38] T.C. Powers, T.L. Brownyard, Studies of the physical properties of hardened Portland cement paste, ACI J. Proc., 43 (1946) 101-132. https://doi.org/10.14359/15302
[39] K. Van Breugel, Numerical simulation of hydration and microstructural development in hardening cement-based materials (I) theory, Cem. Concr. Res. 25 (1995) 319-331. https://doi.org/10.1016/0008-8846(95)00017-8
[40] G.S. Ryu, Y.B. Lee, K.T. Koh, Y.S. Chung, The mechanical properties of fly ash-based geopolymer concrete with alkaline activators, Constr. Build. Mater. 47 (2013) 409-418. https://doi.org/10.1016/j.conbuildmat.2013.05.069
[41] S. Aydın, B. Baradan, Effect of activator type and content on properties of alkali-activated slag mortars, Compos. Part B Eng. 57 (2014) 166-172. https://doi.org/10.1016/j.compositesb.2013.10.001
[42] J.L. Provis, J.S.J. Van Deventer, Alkali activated materials: state-of-the-art report of RILEM TC 224-AAM, Springer/RILEM, Dordrecht (2014). https://doi.org/10.1007/978-94-007-7672-2
[43] A. Buchwald, M. Vanooteghem, E. Gruyaert, H. Hilbig, N. De Belie, Purdocement: application of alkali-activated slag cement in Belgium in the 1950s, Mater. Struct. Constr. 48 (2015) 501-511. https://doi.org/10.1617/s11527-013-0200-8
[44] The Zeobond Group, https://www.Zeobond.com. (n.d.).
[45] Wagners, https://www.Wagner.com.au. (n.d.).
[46] B. Tempest, C. Snell, T. Gentry, M. Trejo, K. Isherwood, Manufacture of full-scale geopolymer cement concrete components: A case study to highlight opportunities and challenges., PCI J. 60 (2015) 39-50. https://doi.org/10.15554/pcij.11012015.39.50
[47] K. Yang, C. Yang, J. Zhang, Q. Pan, L. Yu, Y. Bai, First structural use of site-cast, alkali-activated slag concrete in China, Proc. ICE - Struct. Build. 171 (2018) 800-809. https://doi.org/10.1680/jstbu.16.00193
[48] DB Group, https://Dbgholdings.com/Cemfree/ (n.d.).
[49] RAMAC, https://www.Ramacreadymix.nl (n.d.).
[50] EXEGY, (n.d.). https://doi.org/https://www.soletanche-bachy.com/en/news/exegy-by-soletanche-bachy-first-ultra-low-carbon-concrete-foundation-barrette.
[51] Cemex, Vertua, https://www.Cemex.co.uk/Vertua-Low-Carbon-Concrete. (n.d.).

[52] Blockwalls, https://www.Blockwalls.co.uk. (n.d.).
[53] J.L. Provis, Alkali-activated cements and concretes - Durability testing to underpin standardisation, Proceedings of the Sixth International Conference on Durability of Concrete Structures, Leeds, UK (2019), 16-26.
[54] A. Shayan, Specification of geopolymer concrete: general guide, Austroads Project TS1835, Sydney (2016).
[55] Austroads, Austroads Technical Specification ATS 5330 - Supply of Geopolymer Concrete, 2020.
[56] A. Dehghani, F. Aslani, N.G. Panah, Effects of initial SiO2/Al2O3 molar ratio and slag on fly ash-based ambient cured geopolymer properties, Constr. Build. Mater. 293 (2021) 123527. https://doi.org/10.1016/j.conbuildmat.2021.123527
[57] Y. Ma, Microstructure and engineering properties of alkali activated fly ash-as an environment friendly alternative to Portland cement. Ph.D. thesis, TU Delft, Netherlands (2013).
[58] S. Ramanathan, M. Croly, P. Suraneni, Comparison of the effects that supplementary cementitious materials replacement levels have on cementitious paste properties, Cem. Concr. Compos. 112 (2020) 103678. https://doi.org/10.1016/j.cemconcomp.2020.103678
[59] Z. Li, B. Delsaute, T. Lu, A. Kostiuchenko, S. Staquet, G. Ye, A comparative study on the mechanical properties, autogenous shrinkage and cracking proneness of alkali-activated concrete and ordinary Portland cement concrete, Constr. Build. Mater. 292 (2021) 123418. https://doi.org/10.1016/j.conbuildmat.2021.123418
[60] H. Ye, A. Radlińska, Quantitative analysis of phase assemblage and chemical shrinkage of alkali-activated slag, J. Adv. Concr. Technol. 14 (2016) 245-260. https://doi.org/10.3151/jact.14.245
[61] H. Taghvayi, K. Behfarnia, M. Khalili, The effect of alkali concentration and sodium silicate modulus on the properties of alkali-activated slag concrete, J. Adv. Concr. Technol. 16 (2018) 293-305. https://doi.org/10.3151/jact.16.293
[62] S.A. Bernal, The resistance of alkali-activated cement-based binders to carbonation. In: Handbook of Alkali-Activated Cements, Mortars and Concretes, Woodhead, eds. F. Pacheco-Torgal, J.A. Labrincha, C. Leonelli, A. Palomo, P. Chindaprasirt (2015), pp. 319-332. https://doi.org/10.1533/9781782422884.3.319
[63] S. Chithiraputhiran, N. Neithalath, Isothermal reaction kinetics and temperature dependence of alkali activation of slag, fly ash and their blends, Constr. Build. Mater. 45 (2013) 233-242. https://doi.org/10.1016/j.conbuildmat.2013.03.061
[64] P. Chindaprasirt, T. Cao, Setting, segregation and bleeding of alkali-activated cement, mortar and concrete binders, In: Handbook of Alkali-Activated Cements, Mortars and Concretes, Woodhead, eds. F. Pacheco-Torgal, J.A. Labrincha, C. Leonelli, A. Palomo, P. Chindaprasirt (2015), 113-131. https://doi.org/10.1533/9781782422884.2.113
[65] A. Kusbiantoro, M.F. Nuruddin, N. Shafiq, S.A. Qazi, The effect of microwave incinerated rice husk ash on the compressive and bond strength of fly ash based geopolymer concrete, Constr. Build. Mater. 36 (2012) 695-703. https://doi.org/10.1016/j.conbuildmat.2012.06.064
[66] R. Embong, A. Kusbiantoro, N. Shafiq, M.F. Nuruddin, Strength and microstructural properties of fly ash based geopolymer concrete containing high-calcium and water-absorptive aggregate, J. Clean. Prod. 112 (2016) 816-822. https://doi.org/10.1016/j.jclepro.2015.06.058
[67] R. Si, S. Guo, Q. Dai, J. Wang, Atomic-structure, microstructure and mechanical properties of glass powder modified metakaolin-based geopolymer, Constr. Build. Mater. 254 (2020) 119303. https://doi.org/10.1016/j.conbuildmat.2020.119303
[68] X. Gao, B. Yuan, Q.L. Yu, H.J.H. Brouwers, Characterization and application of municipal solid waste incineration (MSWI) bottom ash and waste granite powder in alkali activated slag, J. Clean. Prod. 164 (2017) 410-419. https://doi.org/10.1016/j.jclepro.2017.06.218
[69] N. Hammad, A. El-Nemr, H.E.-D. Hasan, The performance of fiber GGBS based alkali-activated concrete, J. Build. Eng. 42 (2021) 102464. https://doi.org/10.1016/j.jobe.2021.102464
[70] Y. Ding, J.-G. Dai, C.-J. Shi, Fracture properties of alkali-activated slag and ordinary Portland cement concrete and mortar, Constr. Build. Mater. 165 (2018) 310-320. https://doi.org/10.1016/j.conbuildmat.2017.12.202
[71] M. Olivia, H. Nikraz, Properties of fly ash geopolymer concrete designed by Taguchi method, Mater. Des. 36 (2012) 191-198. https://doi.org/10.1016/j.matdes.2011.10.036
[72] N. Nikoloutsopoulos, A. Sotiropoulou, G. Kakali, S. Tsivilis, Physical and Mechanical Properties of Fly Ash Based Geopolymer Concrete Compared to Conventional Concrete, Buildings. 11 (2021) 178. https://doi.org/10.3390/buildings11050178
[73] M.T. Ghafoor, Q.S. Khan, A.U. Qazi, M.N. Sheikh, M.N.S. Hadi, Influence of alkaline activators on the mechanical properties of fly ash based geopolymer concrete cured at ambient temperature, Constr. Build. Mater. 273 (2021) 121752. https://doi.org/10.1016/j.conbuildmat.2020.121752
[74] R.J. Thomas, S. Peethamparan, Alkali-activated concrete: Engineering properties and stress-strain behavior, Constr. Build. Mater. 93 (2015) 49-56. https://doi.org/10.1016/j.conbuildmat.2015.04.039
[75] T.A. Aiken, J. Kwasny, W. Sha, K.T. Tong, Mechanical and durability properties of alkali-activated fly ash concrete with increasing slag content, Constr. Build. Mater. 301 (2021) 124330. https://doi.org/10.1016/j.conbuildmat.2021.124330
[76] Z. Zhang, H. Wang, Alkali-activated cements for protective coating of OPC concrete. In: Handbook of Alkali-Activated Cements, Mortars and Concretes, Woodhead, eds. F. Pacheco-Torgal, J.A. Labrincha, C. Leonelli, A. Palomo, P. Chindaprasirt (2015), pp. 605-626. https://doi.org/10.1533/9781782422884.4.605
[77] A.M. Fernandez-Jimenez, A. Palomo, C. Lopez-Hombrados, Engineering properties of alkali-activated fly ash concrete, ACI Mater. J. 103 (2006) 106-112. https://doi.org/10.14359/15261
[78] H. El-Hassan, A. Hussein, J. Medljy, T. El-Maaddawy, Performance of Steel Fiber-Reinforced Alkali-Activated Slag-Fly Ash Blended Concrete Incorporating Recycled Concrete Aggregates and Dune Sand, Buildings. 11 (2021) 327. https://doi.org/10.3390/buildings11080327
[79] A.H. Mahmood, S.J. Foster, A. Castel, Effects of mixing duration on engineering properties of geopolymer concrete, Constr. Build. Mater. 303 (2021) 124449. https://doi.org/10.1016/j.conbuildmat.2021.124449
[80] G.F. Huseien, A.R.M. Sam, R. Alyousef, Texture, morphology and strength performance of self-compacting alkali-activated concrete: Role of fly ash as GBFS replacement, Constr. Build. Mater. 270 (2021) 121368. https://doi.org/10.1016/j.conbuildmat.2020.121368
[81] Ü. Yurt, An experimental study on fracture energy of alkali activated slag composites incorporated different fibers, J. Build. Eng. 32 (2020) 101519. https://doi.org/10.1016/j.jobe.2020.101519
[82] K.-H. Yang, J.-K. Song, A.F. Ashour, E.-T. Lee, Properties of cementless mortars activated by sodium silicate, Constr. Build. Mater. 22 (2008) 1981-1989. https://doi.org/10.1016/j.conbuildmat.2007.07.003
[83] A.A. Aliabdo, M. Abd Elmoaty, M.A. Emam, Factors affecting the mechanical properties of alkali activated ground granulated blast furnace slag concrete, Constr. Build. Mater. 197 (2019) 339-355. https://doi.org/10.1016/j.conbuildmat.2018.11.086
[84] H. El-Hassan, E. Shehab, A. Al-Sallamin, Influence of different curing regimes on the performance and microstructure of alkali-activated slag concrete, J. Mater. Civ. Eng. 30 (2018) 4018230. https://doi.org/10.1061/(ASCE)MT.1943-5533.0002436
[85] A. Wardhono, D.W. Law, T.C.K. Molyneaux, Long term performance of alkali activated slag concrete, J. Adv. Concr. Technol. 13 (2015) 187-192. https://doi.org/10.3151/jact.13.187
[86] A. Wongkvanklom, P. Posi, A. Kampala, T. Kaewngao, P. Chindaprasirt, Beneficial utilization of recycled asphaltic concrete aggregate in high calcium fly ash geopolymer concrete, Case Stud. Constr. Mater. 15 (2021) e00615. https://doi.org/10.1016/j.cscm.2021.e00615
[87] K. Ruengsillapanun, T. Udtaranakron, T. Pulngern, W. Tangchirapat, C. Jaturapitakkul, Mechanical properties, shrinkage, and heat evolution of alkali activated fly ash concrete, Constr. Build. Mater. 299 (2021) 123954. https://doi.org/10.1016/j.conbuildmat.2021.123954
[88] Y.Y. Lim, T.M. Pham, J. Kumar, Sustainable alkali activated concrete with fly ash and waste marble aggregates: Strength and durability studies, Constr. Build. Mater. 283 (2021) 122795. https://doi.org/10.1016/j.conbuildmat.2021.122795
[89] T. Phoo-Ngernkham, C. Phiangphimai, N. Damrongwiriyanupap, S. Hanjitsuwan, J. Thumrongvut, P. Chindaprasirt, A mix design procedure for alkali-activated high-calcium fly ash concrete cured at ambient temperature, Adv. Mater. Sci. Eng. 2018 (2018) 2460403. https://doi.org/10.1155/2018/2460403
[90] P. Topark-Ngarm, P. Chindaprasirt, V. Sata, Setting time, strength, and bond of high-calcium fly ash geopolymer concrete, J. Mater. Civ. Eng. 27 (2015) 4014198. https://doi.org/10.1061/(ASCE)MT.1943-5533.0001157
[91] E.I. Diaz-Loya, E.N. Allouche, S. Vaidya, Mechanical properties of fly-ash-based geopolymer concrete, ACI Mater. J. 108 (2011) 300-306. https://doi.org/10.14359/51682495

[92] J. Pacheco, J. De Brito, C. Chastre, L. Evangelista, Scatter of constitutive models of the mechanical properties of concrete: Comparison of major international codes, J. Adv. Concr. Technol. 17 (2019) 102-125. https://doi.org/10.3151/jact.17.102
[93] M. Komljenović, Mechanical strength and Young's modulus of alkali-activated cement-based binders. In: Handbook of Alkali-Activated Cements, Mortars and Concretes, Woodhead, eds. F. Pacheco-Torgal, J.A. Labrincha, C. Leonelli, A. Palomo, P. Chindaprasirt (2015), pp. 171-215. https://doi.org/10.1533/9781782422884.2.171
[94] P. Nath, P.K. Sarker, Flexural strength and elastic modulus of ambient-cured blended low-calcium fly ash geopolymer concrete, Constr. Build. Mater. 130 (2017) 22-31. https://doi.org/10.1016/j.conbuildmat.2016.11.034
[95] N.K. Lee, H.-K. Lee, Setting and mechanical properties of alkali-activated fly ash/slag concrete manufactured at room temperature, Constr. Build. Mater. 47 (2013) 1201-1209. https://doi.org/10.1016/j.conbuildmat.2013.05.107
[96] J. Skibsted, M.D. Andersen, The effect of alkali ions on the incorporation of aluminum in the calcium silicate hydrate (C-S-H) phase resulting from Portland cement hydration studied by 29Si MAS NMR, J. Am. Ceram. Soc. 96 (2013) 651-656. https://doi.org/10.1111/jace.12024
[97] A. Fernández ‐ Jiménez, F. Puertas, I. Sobrados, J. Sanz, Structure of calcium silicate hydrates formed in alkaline ‐ activated slag: influence of the type of alkaline activator, J. Am. Ceram. Soc. 86 (2003) 1389-1394. https://doi.org/10.1111/j.1151-2916.2003.tb03481.x
[98] I. Garcia-Lodeiro, A. Palomo, A. Fernández-Jiménez, D.E. MacPhee, Compatibility studies between N-A-S-H and C-A-S-H gels. Study in the ternary diagram Na2O-CaO-Al2O3-SiO-2-H2O, Cem. Concr. Res. 41 (2011) 923-931. https://doi.org/10.1016/j.cemconres.2011.05.006
[99] J. Cai, X. Li, J. Tan, B. Vandevyvere, Thermal and compressive behaviors of fly ash and metakaolin-based geopolymer, J. Build. Eng. 30 (2020) 101307. https://doi.org/10.1016/j.jobe.2020.101307
[100] K.-H. Yang, A.-R. Cho, J.-K. Song, Effect of water-binder ratio on the mechanical properties of calcium hydroxide-based alkali-activated slag concrete, Constr. Build. Mater. 29 (2012) 504-511. https://doi.org/10.1016/j.conbuildmat.2011.10.062
[101] Y. Cui, K. Gao, P. Zhang, Experimental and statistical study on mechanical characteristics of geopolymer concrete, Materials (Basel). 13 (2020) 1651. https://doi.org/10.3390/ma13071651
[102] M. Chi, Effects of dosage of alkali-activated solution and curing conditions on the properties and durability of alkali-activated slag concrete, Constr. Build. Mater. 35 (2012) 240-245. https://doi.org/10.1016/j.conbuildmat.2012.04.005
[103] B.S. Gebregziabiher, R.J. Thomas, S. Peethamparan, Temperature and activator effect on early-age reaction kinetics of alkali-activated slag binders, Constr. Build. Mater. 113 (2016) 783-793. https://doi.org/10.1016/j.conbuildmat.2016.03.098
[104] P. Nuaklong, V. Sata, A. Wongsa, K. Srinavin, P. Chindaprasirt, Recycled aggregate high calcium fly ash geopolymer concrete with inclusion of OPC and nano-SiO2, Constr. Build. Mater. 174 (2018) 244-252. https://doi.org/10.1016/j.conbuildmat.2018.04.123
[105] D.H. Gray, Y.-K. Lin, Engineering properties of compacted fly ash, J. Soil Mech. Found. Div. 98 (1972) 361-380. https://doi.org/10.1061/JSFEAQ.0001744
[106] S. Fang, E.S.S. Lam, B. Li, B. Wu, Effect of alkali contents, moduli and curing time on engineering properties of alkali activated slag, Constr. Build. Mater. 249 (2020) 118799. https://doi.org/10.1016/j.conbuildmat.2020.118799
[107] C.S. Thunuguntla, T.D. Gunneswara Rao, Effect of mix design parameters on mechanical and durability properties of alkali activated slag concrete, Constr. Build. Mater. 193 (2018) 173-188. https://doi.org/10.1016/j.conbuildmat.2018.10.189
[108] C.-C. Hung, J.-J. Chang, The influence of mixture variables for the alkali-activated slag concrete on the properties of concrete, J. Mar. Sci. Technol. 21 (2013) 1.

Appendix

Table A.1. Summary of raw materials, mix design and mechanical properties (28-day compressive strength, tensile strength and modulus of elasticity) collected from studies on alkali-activated fly ash-, slag- and fly ash/slag-based concretes and used as datapoints in Fig. 1, Fig. 2 and Fig. 3.

Precursor	CaO (by mass % of precursors)	Activator (kg/m^3)		Characteristic compressive strength (MPa)	Tensile strength (MPa)	Modulus of elasticity (GPa)	Ref.
		NaOH	WG				
FA-C	22.57	96.30	96.30	72.00	-	64.30	[86]
FA-C	22.57	117.70	117.70	55.30	-	57.20	[86]
FA-C	22.57	139.10	139.10	52.50	-	49.40	[86]
FA-C	22.57	160.50	160.50	41.00	-	39.50	[86]
FA-C	27.90	280.00	-	12.90	-	7.80	[87]
FA-C	27.90	215.00	65.00	18.70	-	12.80	[87]
FA-C	27.90	200.00	80.00	19.20	-	13.70	[87]
FA-C	27.90	187.00	93.00	33.40	-	18.90	[87]
FA-C	27.90	215.00	65.00	22.20	-	15.30	[87]
FA-C	27.90	215.00	65.00	25.10	-	16.10	[87]
FA-C	27.90	215.00	65.00	24.50	-	15.80	[87]
FA-C	27.90	200.00	80.00	27.10	-	16.70	[87]
FA-C	25.79	118.00	118.00	44.00	3.30	22.00	[89]
FA-C	25.79	113.00	113.00	41.00	3.18	26.00	[89]
FA-C	25.79	108.00	108.00	33.00	2.76	23.00	[89]
FA-C	25.79	118.00	118.00	40.00	3.66	23.00	[89]
FA-C	25.79	113.00	113.00	39.00	3.48	23.00	[89]
FA-C	25.79	108.00	108.00	34.00	3.30	23.00	[89]
FA-C	25.79	118.00	118.00	40.00	3.54	22.00	[89]
FA-C	25.79	113.00	113.00	38.00	3.06	24.00	[89]
FA-C	25.79	108.00	108.00	35.00	3.00	24.00	[89]

FA-C	25.79	118.00	118.00	33.00	2.88	24.50	[89]
FA-C	25.79	113.00	113.00	29.00	2.94	27.00	[89]
FA-C	25.79	108.00	108.00	28.00	2.46	25.00	[89]
FA-C	25.79	118.00	118.00	43.00	3.78	26.00	[89]
FA-C	25.79	113.00	113.00	40.00	3.72	26.00	[89]
FA-C	25.79	108.00	108.00	39.00	3.48	20.00	[89]
FA-C	25.79	118.00	118.00	44.00	3.78	26.00	[89]
FA-C	25.79	113.00	113.00	43.00	3.60	27.00	[89]
FA-C	25.79	108.00	108.00	41.00	3.48	26.00	[89]
FA-C	25.79	118.00	118.00	40.00	3.72	27.00	[89]
FA-C	25.79	113.00	113.00	41.00	3.48	28.00	[89]
FA-C	25.79	108.00	108.00	40.00	3.24	26.00	[89]
FA-C	25.79	118.00	118.00	26.00	3.60	19.00	[89]
FA-C	25.79	113.00	113.00	27.00	3.12	19.00	[89]
FA-C	25.79	108.00	108.00	24.00	3.06	29.00	[89]
FA-C	15.51	104.00	104.00	47.67	3.48	30.40	[90]
FA-C	15.51	104.00	104.00	54.67	3.74	31.00	[90]
FA-C	15.51	104.00	104.00	53.34	3.92	34.80	[90]
FA-C	15.51	104.00	104.00	62.40	4.42	37.80	[90]
FA-C	15.51	104.00	104.00	45.64	3.56	38.40	[90]
FA-C	15.51	104.00	104.00	51.42	3.99	38.00	[90]
FA-C	15.51	69.00	138.00	41.80	2.76	23.40	[90]
FA-C	15.51	69.00	138.00	48.09	3.26	24.20	[90]
FA-C	15.51	69.00	138.00	47.02	3.12	26.80	[90]
FA-C	15.51	69.00	138.00	56.18	3.63	31.00	[90]
FA-C	15.51	69.00	138.00	54.69	3.46	35.40	[90]
FA-C	15.51	69.00	138.00	57.50	3.59	31.80	[90]
FA-C	14.20	108.00	162.00	43.20	2.61	-	[104]
FA-C	14.20	108.00	162.00	40.90	2.43	-	[104]
FA-C	22.45	111.00	111.00	67.50	2.69	33.60	[91]
FA-C	28.07	111.00	111.00	60.28	2.83	34.38	[91]
FA-C	12.93	98.00	98.00	63.89	2.58	37.11	[91]
FA-C	18.72	98.00	98.00	88.37	3.16	42.89	[91]
FA-C	23.53	111.00	111.00	69.38	3.74	31.45	[91]
FA-C	26.19	98.00	98.00	47.19	2.50	19.07	[91]
FA-C	11.66	98.00	98.00	61.70	2.66	28.91	[91]
FA-C	33.39	98.00	98.00	44.54	2.15	26.97	[91]
FA-C	28.53	98.00	98.00	65.18	3.16	29.45	[91]
FA-C	28.47	123.50	123.50	50.81	3.11	22.57	[91]
FA-C	10.60	98.00	98.00	70.19	2.90	29.90	[91]
FA-C	26.80	209.95	209.95	10.73	0.37	1.87	[91]
FA-F_HT	2.24	81.00	166.00	45.33	2.70	21.10	[75]
FA-F_HT	2.24	72.00	88.00	21.60	0.90	8.20	[75]
FA-F_HT	11.73	32.10	138.00	33.83	2.34	14.30	[72]
FA-F_HT	11.73	48.20	252.00	42.86	1.98	16.10	[72]
FA-F_HT	11.73	64.30	336.00	42.05	2.25	17.50	[72]
FA-F_HT	2.44	217.00	37.00	55.45	-	17.10	[105]
FA-F_HT	2.13	46.15	92.31	64.49	3.56	26.95	[71]
FA-F_HT	2.13	36.40	90.99	64.49	3.72	25.33	[71]
FA-F_HT	2.13	42.70	106.70	68.20	3.86	29.05	[71]
FA-F_HT	5.00	98.00	98.00	48.35	2.49	28.60	[91]
FA-F_HT	5.48	98.00	98.00	55.55	3.35	29.47	[91]
FA-F_HT	5.64	98.00	98.00	54.69	3.18	29.36	[91]
FA-F_HT	5.01	98.00	98.00	54.79	2.77	28.52	[91]
FA-F_HT	6.90	98.00	98.00	54.11	2.83	26.46	[91]
FA-F_HT	1.97	123.50	123.50	55.44	3.07	26.64	[91]
FA-F_HT	5.43	187.70	187.70	20.20	1.34	7.04	[91]
FA-F_HT	4.69	232.10	232.10	20.82	1.43	6.81	[91]
FA-F_HT	5.18	163.00	163.00	28.68	2.10	7.96	[91]
FA-F_HT	5.57	192.60	192.60	18.34	1.64	7.46	[91]
FA-F_HT	4.64	99.00	99.00	54.56	3.79	28.74	[91]
FA-F_HT	2.26	168.00	168.00	57.24	2.80	19.28	[91]
FA-F_HT	9.23	98.00	98.00	51.38	2.54	25.61	[91]
FA-F_RT	6.72	63.00	94.60	18.90	1.68	10.80	[73]
FA-F_RT	6.72	52.50	105.10	17.20	1.50	7.30	[73]
FA-F_RT	6.72	45.00	112.60	16.00	1.50	7.00	[73]
FA-F_RT	6.72	73.60	110.40	15.67	2.04	7.00	[73]
FA-F_RT	6.72	61.30	122.60	16.50	1.92	8.70	[73]
FA-F_RT	6.72	52.50	131.40	16.50	1.86	7.40	[73]
FA-F_RT	6.72	82.80	124.20	15.60	2.04	10.50	[73]

FA-F_RT	6.72	69.00	138.00	16.00	1.62	10.10	[73]
FA-F_RT	6.72	59.10	147.80	16.00	1.56	8.80	[73]
FA-F_RT	6.72	63.00	94.60	22.40	1.98	11.10	[73]
FA-F_RT	6.72	52.50	105.10	21.90	2.52	10.00	[73]
FA-F_RT	6.72	45.00	112.60	21.10	1.56	17.40	[73]
FA-F_RT	6.72	73.60	110.40	22.20	2.40	21.40	[73]
FA-F_RT	6.72	61.30	122.60	20.90	2.34	15.10	[73]
FA-F_RT	6.72	52.50	131.40	20.90	1.92	11.20	[73]
FA-F_RT	6.72	82.80	124.20	21.00	2.10	19.10	[73]
FA-F_RT	6.72	69.00	138.00	19.70	1.98	17.10	[73]
FA-F_RT	6.72	59.10	147.80	19.80	1.92	11.20	[73]
FA-F_RT	6.72	63.00	94.60	23.00	2.82	15.10	[73]
FA-F_RT	6.72	52.50	105.10	22.50	2.04	7.80	[73]
FA-F_RT	6.72	45.00	112.60	21.00	1.92	17.80	[73]
FA-F_RT	6.72	73.60	110.40	25.00	2.52	23.30	[73]
FA-F_RT	6.72	61.30	122.60	23.00	2.52	15.10	[73]
FA-F_RT	6.72	52.50	131.40	20.90	2.16	30.30	[73]
FA-F_RT	6.72	82.80	124.20	20.50	2.82	27.20	[73]
FA-F_RT	6.72	69.00	138.00	21.00	2.76	25.10	[73]
FA-F_RT	6.72	59.10	147.80	20.70	2.10	15.50	[73]
FA-F_RT	6.72	63.00	94.60	26.10	2.16	17.20	[73]
FA-F_RT	6.72	52.50	105.10	26.00	2.88	28.50	[73]
FA-F_RT	6.72	45.00	112.60	25.50	2.10	28.50	[73]
FA-F_RT	6.72	73.60	110.40	26.70	2.58	35.00	[73]
FA-F_RT	6.72	61.30	122.60	28.90	3.00	30.10	[73]
FA-F_RT	6.72	52.50	131.40	25.10	2.82	30.30	[73]
FA-F_RT	6.72	82.80	124.20	29.50	2.82	27.70	[73]
FA-F_RT	6.72	69.00	138.00	24.00	2.88	25.30	[73]
FA-F_RT	6.72	59.10	147.80	20.70	2.34	31.50	[73]
FA-F_RT	6.72	63.00	94.60	24.80	2.40	10.60	[73]
FA-F_RT	6.72	52.50	105.10	25.60	2.88	15.20	[73]
FA-F_RT	6.72	45.00	112.60	25.00	2.40	14.50	[73]
FA-F_RT	6.72	73.60	110.40	29.50	3.00	35.20	[73]
FA-F_RT	6.72	61.30	122.60	25.90	3.00	26.20	[73]
FA-F_RT	6.72	52.50	131.40	23.80	2.94	28.10	[73]
FA-F_RT	6.72	82.80	124.20	25.00	2.82	30.60	[73]
FA-F_RT	6.72	69.00	138.00	23.50	2.94	14.50	[73]
FA-F_RT	6.72	59.10	147.80	22.60	2.34	20.10	[73]
Blend	32.32	66.00	99.00	54.47	2.64	22.40	[78]
Blend	22.65	60.00	99.00	37.42	1.97	12.60	[78]
Blend	17.28	8.23	115.50	49.20	2.26	27.40	[79]
Blend	17.28	8.23	115.50	46.70	2.43	29.10	[79]
Blend	17.41	8.23	115.50	44.50	1.92	29.60	[79]
Blend	17.41	8.23	115.50	42.30	2.22	30.30	[79]
Blend	10.51	73.00	88.00	42.05	2.52	19.70	[75]
Blend	18.85	72.00	88.00	55.45	3.42	27.10	[75]
Blend	31.31	72.00	87.00	60.50	2.97	28.90	[75]
Blend	51.80	138.30	103.80	65.54	5.76	27.00	[80]
Blend	37.81	138.30	103.80	63.66	5.31	26.20	[80]
Blend	33.14	138.30	103.80	62.58	4.95	25.00	[80]
Blend	28.48	138.30	103.80	60.25	4.86	24.00	[80]
Blend	23.82	138.30	103.80	51.68	4.68	23.00	[80]
Blend	19.15	138.30	103.80	44.79	4.23	22.80	[80]
GGBFS	38.65	61.00	152.00	41.81	2.86	26.67	[69]
GGBFS	36.00	46.00	71.00	47.47	-	25.69	[85]
GGBFS	39.80	-	-	41.70	6.12	34.20	[74]
GGBFS	39.80	-	-	52.70	6.48	26.20	[74]
GGBFS	39.80	-	-	54.70	5.67	27.00	[74]
GGBFS	39.80	-	-	43.00	5.67	27.90	[74]
GGBFS	39.80	-	-	53.70	7.47	22.40	[74]
GGBFS	39.80	-	-	60.60	7.56	33.50	[74]
GGBFS	45.55	12.60	22.70	35.25	4.98	-	[106]
GGBFS	45.55	10.40	34-00	39.78	4.68	-	[106]
GGBFS	45.55	8.20	45.30	40.19	4.62	-	[106]
GGBFS	45.55	18.80	34.00	44.16	6.60	-	[106]
GGBFS	45.55	15.50	50.80	51.36	6.12	-	[106]
GGBFS	45.55	12.30	67.50	54.31	5.40	-	[106]
GGBFS	45.55	24.90	45.10	61.25	6.12	-	[106]

GGBFS	45.55	20.60	67.40	64.64	6.00	-	[106]
GGBFS	45.55	16.30	89.50	67.60	5.94	-	[106]
GGBFS	45.55	31.00	56.10	68.25	5.88	-	[106]
GGBFS	45.55	25.60	83.80	69.44	4.98	-	[106]
GGBFS	45.55	20.20	111.20	82.86	4.86	-	[106]
GGBFS	45.55	37.10	67.10	68.09	5.28	-	[106]
GGBFS	45.55	30.50	100.10	80.31	4.62	-	[106]
GGBFS	45.55	24.10	132.80	85.99	4.68	-	[106]
GGBFS	33.67	48.00	72.00	21.53	1.52	-	[107]
GGBFS	33.67	66.00	99.00	26.86	2.34	-	[107]
GGBFS	33.67	72.00	108.00	25.68	2.24	-	[107]
GGBFS	33.67	99.00	148.50	31.38	2.39	-	[107]
GGBFS	33.67	48.00	72.00	63.63	3.81	-	[107]
GGBFS	33.67	66.00	99.00	66.45	4.45	-	[107]
GGBFS	33.67	72.00	108.00	69.18	5.00	-	[107]
GGBFS	33.67	99.00	148.50	71.90	4.97	-	[107]
GGBFS	33.30	8.00	49.00	41.45	3.78	20.00	[70]
GGBFS	33.30	11.00	71.00	50.94	4.59	22.00	[70]
GGBFS	33.30	11.00	117.00	65.23	5.45	23.60	[70]
GGBFS	45.00	-	-	24.60	1.05	13.01	[100]
GGBFS	45.00	-	-	24.90	1.01	12.95	[100]
GGBFS	45.00	-	-	27.40	1.34	18.77	[100]
GGBFS	45.00	-	-	28.50	1.34	16.55	[100]
GGBFS	45.00	-	-	31.30	1.76	19.45	[100]
GGBFS	45.00	-	-	34.60	1.76	19.72	[100]
GGBFS	45.00	-	-	40.60	2.30	23.52	[100]
GGBFS	45.00	-	-	38.00	2.31	20.83	[100]
GGBFS	45.00	-	-	40.20	2.39	21.62	[100]
GGBFS	45.00	-	-	44.50	2.48	25.29	[100]
GGBFS	45.00	-	-	53.10	2.84	29.91	[100]
GGBFS	45.00	-	-	58.20	2.95	31.47	[100]
GGBFS	39.54	227-339	-	43.05	3.21	19.20	[108]
GGBFS	39.54	227-339	-	44.00	3.22	19.60	[108]
GGBFS	39.54	227-339	-	44.60	3.27	19.70	[108]
GGBFS	39.54	227-339	-	44.72	3.31	19.70	[108]
GGBFS	39.54	227-339	-	45.45	3.53	19.70	[108]
GGBFS	39.54	227-339	-	46.56	3.71	19.85	[108]
GGBFS	39.54	227-339	-	47.56	3.74	20.00	[108]
GGBFS	39.54	227-339	-	48.07	3.60	20.30	[108]
GGBFS	39.54	227-339	-	48.96	3.83	20.80	[108]
GGBFS	39.54	227-339	-	49.22	3.76	20.65	[108]
GGBFS	39.54	227-339	-	50.25	3.85	20.50	[108]
GGBFS	39.54	227-339	-	50.38	3.92	21.10	[108]
GGBFS	39.54	227-339	-	50.64	3.90	21.35	[108]
GGBFS	39.54	227-339	-	52.22	4.19	21.30	[108]
GGBFS	39.54	227-339	-	54.65	4.39	21.50	[108]
GGBFS	39.54	227-339	-	55.61	4.40	21.60	[108]
GGBFS	39.54	227-339	-	54.51	4.21	21.70	[108]
GGBFS	43.34	58.18	101.82	44.42	3.49	22.92	[83]
GGBFS	43.34	42.35	137.65	43.72	3.41	20.92	[83]
GGBFS	43.34	57.14	142.86	44.49	3.65	23.98	[83]
GGBFS	43.34	45.71	114.29	45.27	3.83	34.93	[83]
GGBFS	43.34	65.45	114.55	46.05	4.68	27.64	[83]
GGBFS	43.34	47.06	152.94	46.83	4.02	32.18	[83]
GGBFS	43.34	45.71	114.29	48.74	3.77	26.98	[83]
GGBFS	43.34	48.00	132.00	49.54	3.62	26.21	[83]
GGBFS	43.34	72.73	127.27	50.34	3.75	28.96	[83]
GGBFS	43.34	37.65	122.35	51.14	3.66	30.23	[83]
GGBFS	43.34	51.43	128.57	51.94	4.06	27.07	[83]
GGBFS	43.34	72.73	127.27	53.75	3.78	27.20	[83]
GGBFS	43.34	58.18	101.82	54.57	4.02	35.11	[83]
GGBFS	43.34	42.35	137.65	55.39	3.82	33.69	[83]
GGBFS	43.34	57.14	142.86	56.21	3.76	24.99	[83]
GGBFS	43.34	45.71	114.29	57.03	4.17	37.83	[83]

GGBFS	43.34	65.45	114.55	58.77	3.66	23.19	[83]
GGBFS	43.34	47.06	152.94	59.60	3.80	22.91	[83]
GGBFS	43.34	45.71	114.29	60.43	3.83	29.32	[83]
GGBFS	43.34	65.45	114.55	61.27	3.77	21.17	[83]
GGBFS	43.34	47.06	152.94	62.10	4.18	37.46	[83]
GGBFS	43.34	37.65	122.35	62.93	4.10	35.33	[83]
GGBFS	43.34	51.43	128.57	63.77	4.50	31.44	[83]
GGBFS	43.34	72.73	127.27	63.76	3.57	22.99	[83]
GGBFS	43.34	58.18	101.82	64.58	3.65	26.19	[83]
GGBFS	43.34	42.35	137.65	65.40	4.51	38.57	[83]
GGBFS	43.34	57.14	142.86	66.22	3.32	19.66	[83]
GGBFS	40.67	13.00	46.50	46.78	3.06	-	[102]
GGBFS	40.67	16.30	58.10	49.75	3.51	-	[102]
GGBFS	40.67	19.50	69.70	53.80	3.47	-	[102]
GGBFS	40.67	13.00	46.50	56.30	3.51	-	[102]
GGBFS	40.67	16.30	58.10	55.85	3.60	-	[102]
GGBFS	40.67	19.50	69.70	57.75	3.96	-	[102]
GGBFS	40.67	13.00	46.50	60.60	4.23	-	[102]
GGBFS	40.67	16.30	58.10	60.05	3.87	-	[102]
GGBFS	40.67	19.50	69.70	58.90	3.60	-	[102]
GGBFS	40.67	13.00	46.50	58.20	3.78	-	[102]
GGBFS	40.67	16.30	58.10	63.00	3.96	-	[102]
GGBFS	40.67	19.50	69.70	64.75	4.05	-	[102]
GGBFS	40.67	13.00	46.50	65.86	3.83	-	[102]
GGBFS	40.67	16.30	58.10	65.95	4.32	-	[102]
GGBFS	40.67	16.30	58.10	65.70	4.41	-	[102]
GGBFS	40.67	19.50	69.70	67.40	4.50	-	[102]
GGBFS	42.00	70.00	177.00	43.40	-	21.20	[84]
GGBFS	42.00	64.00	161.00	56.44	-	25.65	[84]
GGBFS	42.00	58.00	145.00	62.61	-	28.95	[84]
GGBFS	42.00	70.00	177.00	75.57	-	32.30	[84]
GGBFS	42.00	64.00	161.00	76.23	-	32.70	[84]
GGBFS	42.00	57.00	145.00	77.06	-	32.90	[84]
GGBFS	42.00	70.00	177.00	79.91	-	33.60	[84]
GGBFS	42.00	64.00	161.00	82.13	-	35.00	[84]
GGBFS	42.00	57.00	145.00	82.65	-	35.30	[84]

Paper 2

New analytical models to predict the mechanical performance of steel fiber-reinforced alkali-activated concrete

Laura Rossi, Ravi A. Patel, Frank Dehn

Structural Concrete

2024, pp. 1-12

DOI: 10.1002/suco.202301104

Publisher's version

Received: 12 December 2023 | Revised: 22 April 2024 | Accepted: 19 May 2024

DOI: 10.1002/suco.202301104

ARTICLE

fib CEB-FIP WILEY

New analytical models to predict the mechanical performance of steel fiber-reinforced alkali-activated concrete

Laura Rossi[1,2] | **Ravi A. Patel**[1,2] | **Frank Dehn**[1,2]

[1]Institute of Building Materials and Concrete Structures (IMB), Karlsruhe Institute of Technology (KIT), Karlsruhe, Germany

[2]Materials Testing and Research Institute Karlsruhe (MPA), Karlsruhe Institute of Technology (KIT), Karlsruhe, Germany

Correspondence
Laura Rossi, Institute of Building Materials and Concrete Structures (IMB), Karlsruhe Institute of Technology (KIT), 76131 Karlsruhe, Germany.
Email: laura.rossi@kit.edu

Funding information
Horizon 2020 Framework Programme, Grant/Award Number: 813596

Abstract

The use of alkali-activated concrete (AAC) as an alternative construction material to Portland cement-based concrete (PCC) has been widely encouraged by its enhanced mechanical and durability performance and environmental benefits. However, AAC exhibits low flexural and tensile strength, limiting its application in areas where high post-cracking flexural and tensile load-bearing capacity are needed. Steel fibers can be added to improve the composite ductility and toughness. Steel fiber-reinforced alkali-activated concrete (SFRAAC) is a new emerging technology with research studies evaluating the effect of fiber addition on its mechanical properties still in the early stages. To promote the application of SFRAAC, analytical models predicting their mechanical performance are needed. This study evaluates the applicability to SFRAAC of previously published analytical models developed for steel fiber-reinforced cement-based concrete (SFRPCC). Experimental data available in the literature have been collected to create an extensive database to validate and then calibrate these currently available correlations between mechanical properties for SFRAAC. The prediction models considered in this study correlate the mechanical performance of SFRAAC, that is, compressive strength, modulus of elasticity, splitting tensile strength, flexural and residual flexural strength, to the compressive strength of the reference concrete without fibers, the fiber volume fraction and the fiber reinforcing index. Thus, by knowing the performance of the AAC matrix and the fiber properties and dosage, it is possible to predict the overall mechanical behavior of the steel fiber-reinforced composite.

KEYWORDS

analytical models, fiber-reinforced alkali-activated concrete, mechanical properties, steel fibers

1 | INTRODUCTION

Steel fiber-reinforced concrete (SFRPCC) based on Portland cement has been widely used in the last decades to enhance the crack resistance of structural members and hence their durability and service life. The crack-bridging ability of the fibers improves the concrete ductility and post-cracking load-bearing capacity under tensile, shear and torsion loading.[1,2] Design-oriented strength prediction models played a fundamental role in promoting the

use of SFRPCC as a structural material in engineering practice. Being able to derive the mechanical behavior of SFRPCC, that is, compressive and tensile behavior, solely by knowing the compressive strength of the reference concrete matrix and the fiber type and dosage facilitates the formulation of concrete mix design designed to meet the performance requirements of the end application.

Although several empirical models have been proposed for SFRPCC,[1–6] their applicability is limited to the type of concrete and steel fibers used. Furthermore, only the experimental data generated in each study are used to derive strength prediction models, making them unsuitable for different types of concrete or fiber. Wang et al.[2] reviewed several empirical models to derive the main mechanical properties of SFRPCC, that is, compressive strength, splitting tensile and flexural strengths and modulus of elasticity. They observed that the compressive strength of the reference concrete and the fiber volume fraction and reinforcing index, that is, the product of the fiber volume fraction and its aspect ratio (length/diameter), are the main factors affecting the mechanical performance of SFRPCC. However, the majority of the existing models are calibrated on a limited amount of experimental data and have limited accuracy when applied to different types of steel fibers or concrete. Furthermore, several currently available empirical models correlate the mechanical performance of SFRPCC with its compressive strength, but models able to predict the compressive strength of SFRPCC from the compressive strength of the reference concrete are limited. Guler et al.[1] evaluated the applicability of several models available in the literature to predict the compressive, splitting and flexural strength of SFRPCC to their own experimental data, highlighting the necessity of new empirical models. The empirical strength prediction models proposed by Guler et al.[1] correlate the cube compressive strength, the splitting tensile strength and the flexural strength of SFRPCC solely to the cube compressive strength of the reference concrete without steel fibers, the fiber volume fraction, and reinforcing index. Only using the compressive strength of the plain concrete and the type and dosage of the steel fibers used, it is possible to derive the mechanical performance of the composite.

Among the currently available empirical models to predict the mechanical performance of SFRPCC, the linear correlations proposed by Guler et al.[1] are concise and require only three input parameters: the compressive strength of the reference concrete without fibers, the fiber

TABLE 1 Existing models for the prediction of the mechanical properties of SFRPCC.

Mechanical properties	Empirical model	Ref.
Compressive strength	$f'_{cuf} = 0.92f'_{cu} - 1.44v_f + 14.6RI_v$	1
Modulus of elasticity	$E_{cyf} = 4.58(f'_{cu})^{0.5} + 0.42f'_{cu}RI_v + 0.39RI_v$	3
Splitting tensile strength	$f'_{sptf} = 0.12f'_{cu} - 0.71v_f + 6.47RI_v$	1
Flexural strength	$f'_{lf} = 0.24f'_{cu} + 1.12v_f + 7.10RI_v$	1

Note: f'_{cuf} and f'_{cu} are the cube compressive strength of SFRPCC and PCC, respectively, f'_{spf} and f'_{lf} are the splitting tensile and flexural of SFRPCC, respectively, E_{cyf} is the modulus of elasticity of SFRPCC, v_f is the fiber volume fraction, RI_v is the fiber reinforcing index, that is, $(d_f/l_f)v_f$, with d_f and l_f being the fiber diameter and length, respectively, and f'_{cyf} the cylinder compressive strength of SFRPCC.

TABLE 2 Conversion factors accounting for the sample geometry used in the creation of the dataset used in this study.

Mechanical property	Sample geometry (experimental value)	Sample geometry (predicted value)	Equations	Ref
Compressive strength	Cylinder 100 mm × 200 mm	Cylinder 150 mm × 300 mm	$f'_{cyf(150)} = 0.94f'_{cyf(100)}$	42
	Cube 150 × 150 × 150 mm^3		$f'_{cyf(150)} = 0.90f'_{cuf(150)}$	42
	Cube 100 × 100 × 100 mm^3		$f'_{cyf(150)} = 0.81f'_{cuf(100)}$	42
Modulus of elasticity	Cylinder 100 mm × 200 mm	Cylinder 150 mm × 300 mm	$E_{cyf(150)} = E_{cyf(100)}$, $E_{cyf(150)} < 25$ GPa $E_{cyf(150)} = 0.90E_{cyf(100)} + 1.90$, $E_{cyf(150)} \geq 25$ GPa	43
Splitting tensile strength	Cylinder 100 mm × 200 mm	Cylinder 150 mm × 300 mm	$f'_{sptf(150)} = 0.89f'_{sptf(100)}$	42

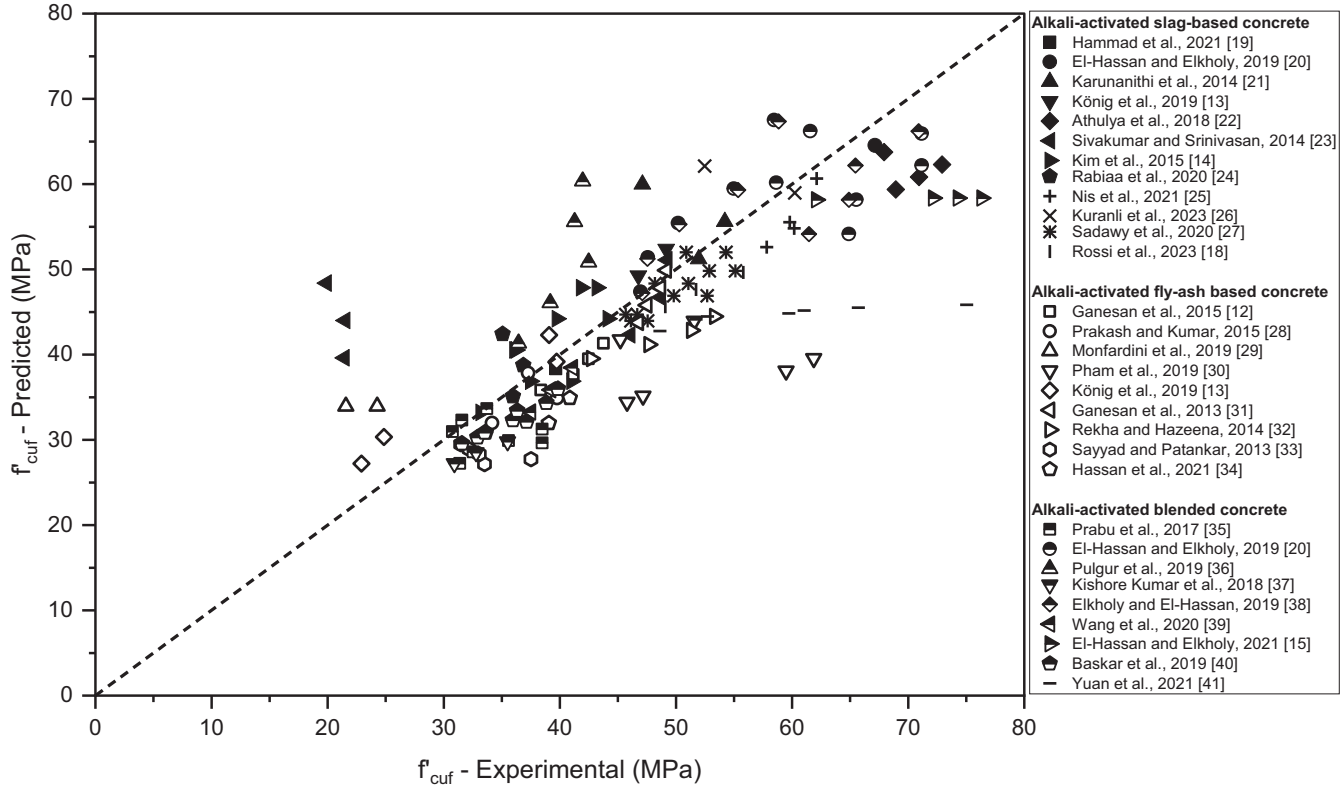

FIGURE 1 Correlation between the experimental and predicted values of the compressive strength of different alkali-activated concretes incorporating different steel fibers at different volume fractions according to the equation proposed by Guler et al.[1]

TABLE 3 IAE values of the correlation used to determine the compressive strength of SFRAAC according to Ref.[1]

	Slag-based AAC	Fly ash-based AAC	Blended AAC
IAE [%]	10.16	16.27	14.71

volume fraction, and the fiber reinforcing index. Thus, the performance of SFRPCC can be quickly predicted by performing a limited number of experiments on the reference concrete without steel fibers. However, Guler et al.[1] provided no correlation to derive the modulus of elasticity of SFRPCC from the compressive strength of the reference concrete. Thomas and Ramaswamy[3] have proposed an empirical equation correlating the modulus of elasticity of SFRPCC to the compressive strength of the reference plain concrete and the fiber reinforcing index. Thus, the correlations proposed by Guler et al.[1] and Thomas and Ramaswamy[3] have been chosen in this study as they allow predicting the performance of SFRPCC directly from the performance of the plain concrete only by knowing the characteristics of the concrete matrix and the steel fibers. Table 1 summarizes the analytical correlations between the mechanical properties of SFRPCC proposed by Guler et al.[1] and Thomas and Ramaswamy.[3]

Deriving empirical strength prediction models plays a vital role in encouraging the use of newly developed construction materials, such as alkali-activated concrete (AAC), for structural applications. AAC has been demonstrated to be a valid environmentally friendly alternative to traditional Portland cement-based concrete (PCC) as a construction material.[7,8] Nevertheless, due to intrinsic internal micro-cracks in its matrix,[9] it also exhibits brittle behavior,[9,10] resulting in poor resistance to crack propagation and low tensile strength.[9,10] As for traditional PCC, the incorporation of steel fibers in AAC enhances its tensile strength, toughness, post-cracking load-bearing capacity, and ductility.[7,10,11] However, steel fiber-reinforced alkali-activated concrete (SFRAAC) is a new emerging material and research studies addressing its mechanical performance and evaluating possible correlations between them are still scarce.[12–18] Furthermore, the intrinsic variability of the AAC matrix, caused by the variety of possible binders and alkaline activators, represents a hindrance to its classification and the characterization of its mechanical behavior. This limits the possibility of deriving a single empirical correlation

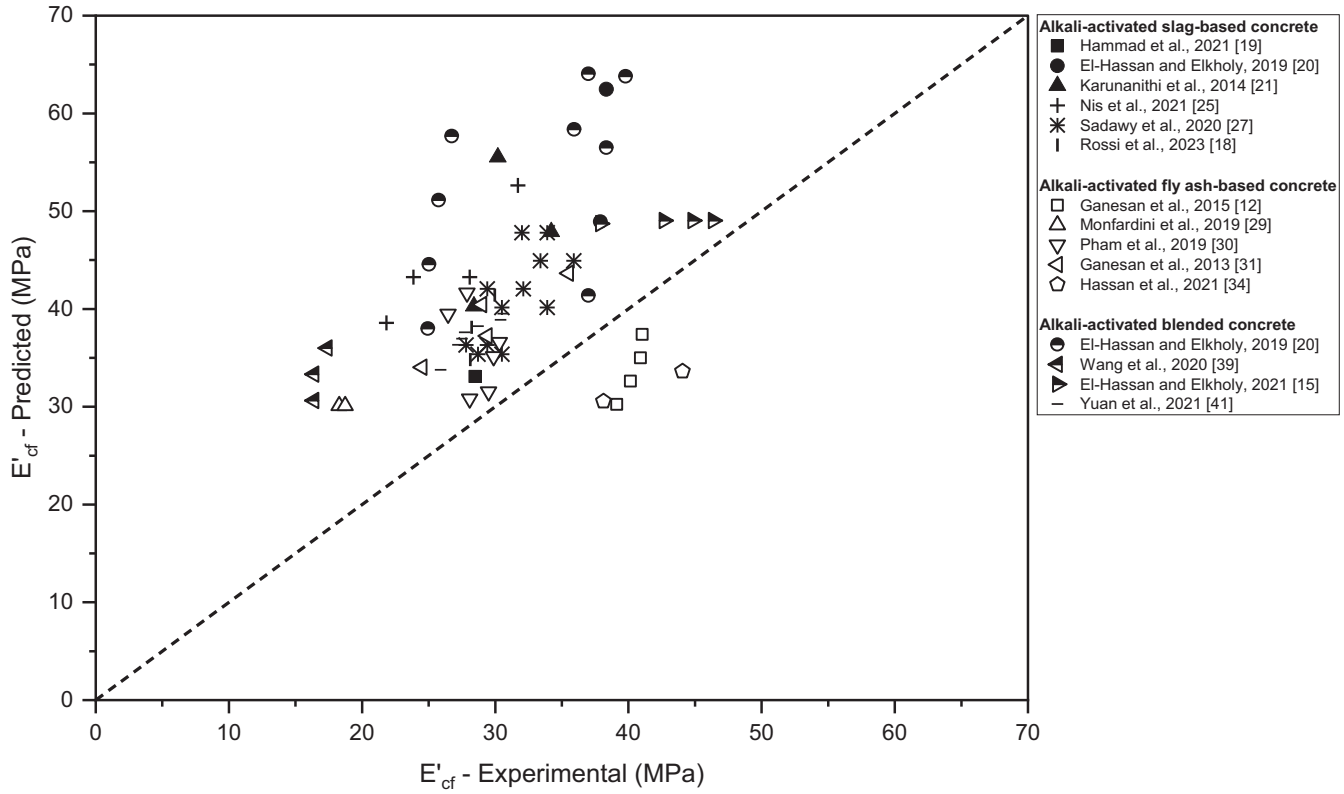

FIGURE 2 Experimental and predicted values of the modulus of elasticity of SFRAAC according to the equation proposed by Thomas and Ramaswamy.[3]

	Slag-based AAC	Fly ash-based AAC	Blended AAC
IAE [%]	28.86	23.37	32.66

TABLE 4 IAE values of the correlation used to determine the modulus of elasticity of SFRAAC according to Ref.[6]

describing the performance of the entire class of AACs. Thus, different alkali-activated systems, that is, high-calcium systems, low-calcium systems, and blended systems, are analyzed separately in this study to better understand the effect of steel fibers on different AAC matrices and to derive accurate analytical equations predicting their mechanical properties.

This study evaluates existing empirical models developed to predict the compressive strength, modulus of elasticity and splitting, and flexural tensile strength of SFRPCC for SFRAAC and recalibrates them for SFRAAC. First, a dataset is created by collecting experimental data available in the literature for different SFRAACs and data from the experimental investigations conducted by the authors in previous studies. Then, the applicability of the existing analytical correlations proposed by Guler et al.[1] and Thomas and Ramaswamy[3] for SFRPCC to SFRAAC is evaluated. Thereafter, these correlations are recalibrated to SFRAAC to improve the reliability of the proposed models.

2 | DATABASE OF MECHANICAL PROPERTIES OF SFRAAC

To evaluate the correlation between the mechanical performances of SFRAAC according to the equations summarized in Table 1, experimental data available in the literature have been collected.[12–15,18–41] Different concrete matrices and steel fiber geometries and dosages have been considered to cover most of the potential mix design formulations for SFRAAC. Data available in the literature on steel fiber-reinforced ground granulated blast furnace slag (high-calcium systems), Class-F fly ash (low-calcium systems), and blended systems (a combination of both) activated by sodium hydroxide, sodium silicate or both have been collected. Only publications reporting the 28-day mean compressive strength in addition to the modulus of elasticity and splitting tensile strength, or at least one of the latter, were considered.

The analytical models proposed by Guler et al.[1] correlate the compressive strength, the splitting tensile

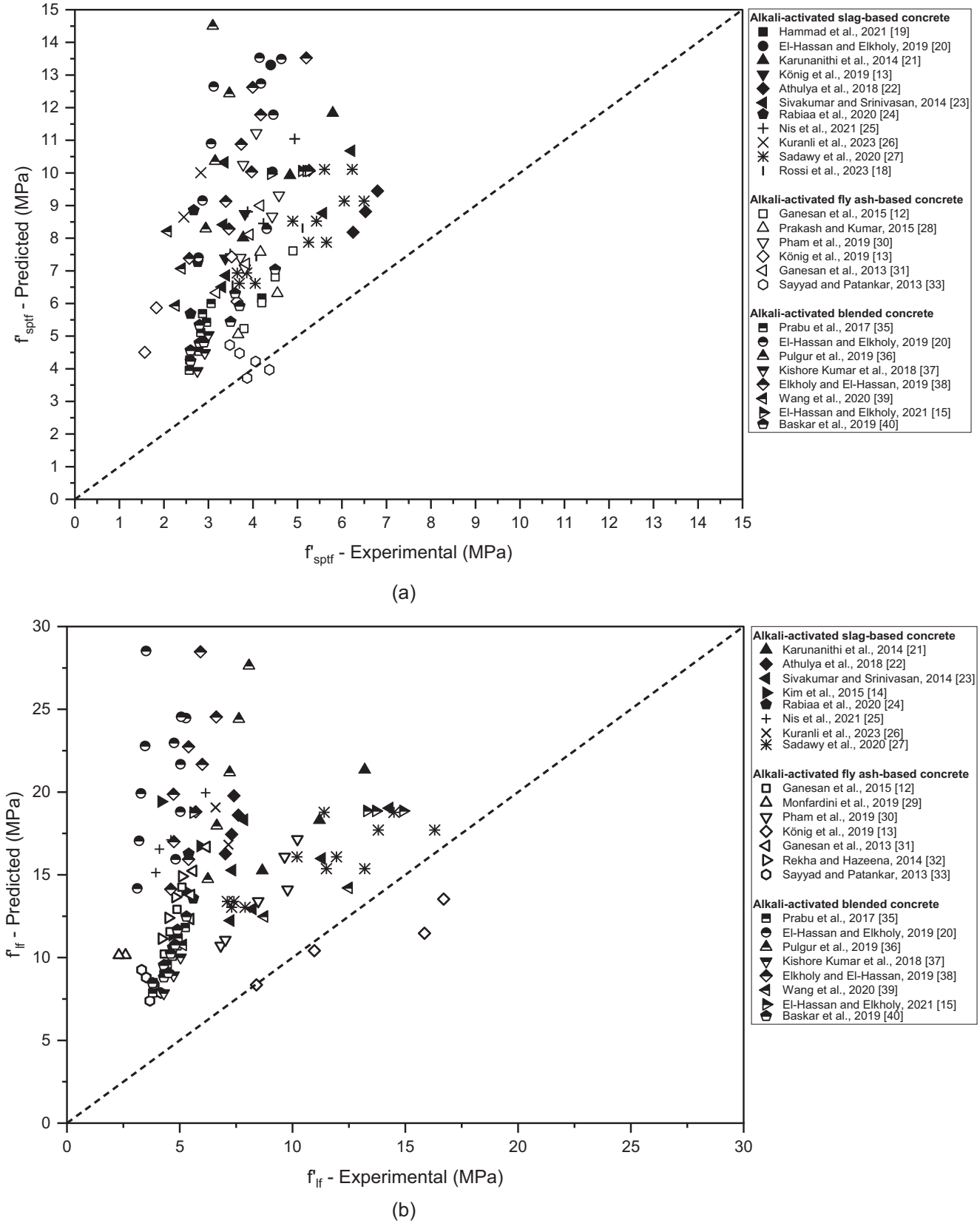

FIGURE 3 Experimental and predicted values of (a) the splitting tensile strength and (b) the flexural strength of SFRAAC according to the equations proposed by Guler et al.[1]

TABLE 5 IAE values of the correlation used to determine the splitting tensile strength and flexural strength of SFRAAC according to Guler et al.[1]

	Slag-based AAC	Fly ash-based AAC	Blended AAC
IAE [%], splitting tensile strength	45.91	43.59	60.34
IAE [%], flexural strength	47.12	50.69	65.08

TABLE 6 Proposed values of the coefficients *A*, *B*, and *C* and the corresponding IAE values for each type of alkali-activated concrete.

	New correlations		
Coefficients IAE [%]	**Slag-based AAC**	**Fly ash-based AAC**	**Blended AAC**
A	1.04	0.95	1.20
B	0.00	0.00	0.00
C	2.12	18.78	0.80
IAE	8.68	11.78	8.60

strength and the flexural tensile strength of SFRPCC to the cube compressive strength of the reference concrete. When in the literature these properties were evaluated on different sample geometries, the conversion factors summarized in Table 2 were applied.

3 | APPLICABILITY OF THE EXISTING ANALYTICAL MODELS TO SFRAAC

3.1 | Compressive strength

Figure 1 shows the correlation between the experimental and the predicted values of the compressive strength of SFRAAC using the equation proposed by Guler et al.[1] and summarized in Table 1. As shown in Figure 1, the correlation proposed by Guler et al.[1] can predict quite accurately the compressive strength of SFRAAC from the compressive strength of the reference matrix without steel fibers. Thus, the effect of the incorporation of steel fibers in AAC matrices is comparable to the one observed in cement-based concretes. Steel fibers up to a volume fraction of 1% have a limited effect on the compressive strength of the composite.[44] To evaluate the accuracy of this correlation, the integral absolute error (IAE) is used, which is defined as:

$$\mathrm{IAE} = \frac{\sum |Q_i - P_i|}{\sum Q_i} \cdot 100 \qquad (1)$$

where Q_i is the experimental data and P_i is the predicted value. Table 3 summarizes the values of IAE for each type of SFRAAC.

3.2 | Modulus of elasticity

Figure 2 shows the experimental and predicted values of the modulus of elasticity of different types of AAC incorporating steel fibers in different volume fractions obtained according to the equation proposed by Thomas and Ramaswamy.[3] AAC exhibits generally lower modulus of elasticity than cement-based concrete[45–49] and the addition of steel fibers has generally a limited effect on the modulus of elasticity.[18] The overestimation of the modulus of elasticity shown in Figure 2 reflects the lower modulus of elasticity of SFRAAC.

Table 4 shows the values of IAE for each type of AAC. Although the correlation can predict quite accurately the values of the modulus of elasticity for blended alkali-activated concrete, the accuracy of this analytical model decreases for slag-based and fly ash-based concretes.

3.3 | Splitting tensile strength and flexural strength

Figure 3 shows the correlation between the experimental and predicted values of the splitting tensile strength and the flexural strength for different SFRAACs as proposed by Guler et al.[1] The equations proposed by Guler et al.[1] highly overestimate the splitting tensile strength and the flexural strength of SFRAAC. AAC exhibits generally more brittle tensile behavior than cement-based concrete of similar strength grade.[49] Although the incorporation of steel fibers enhances the splitting and flexural tensile strengths of AAC, it is directly correlated to the tensile behavior of the reference plain concrete. Thus, SFRAAC shows lower splitting and flexural tensile

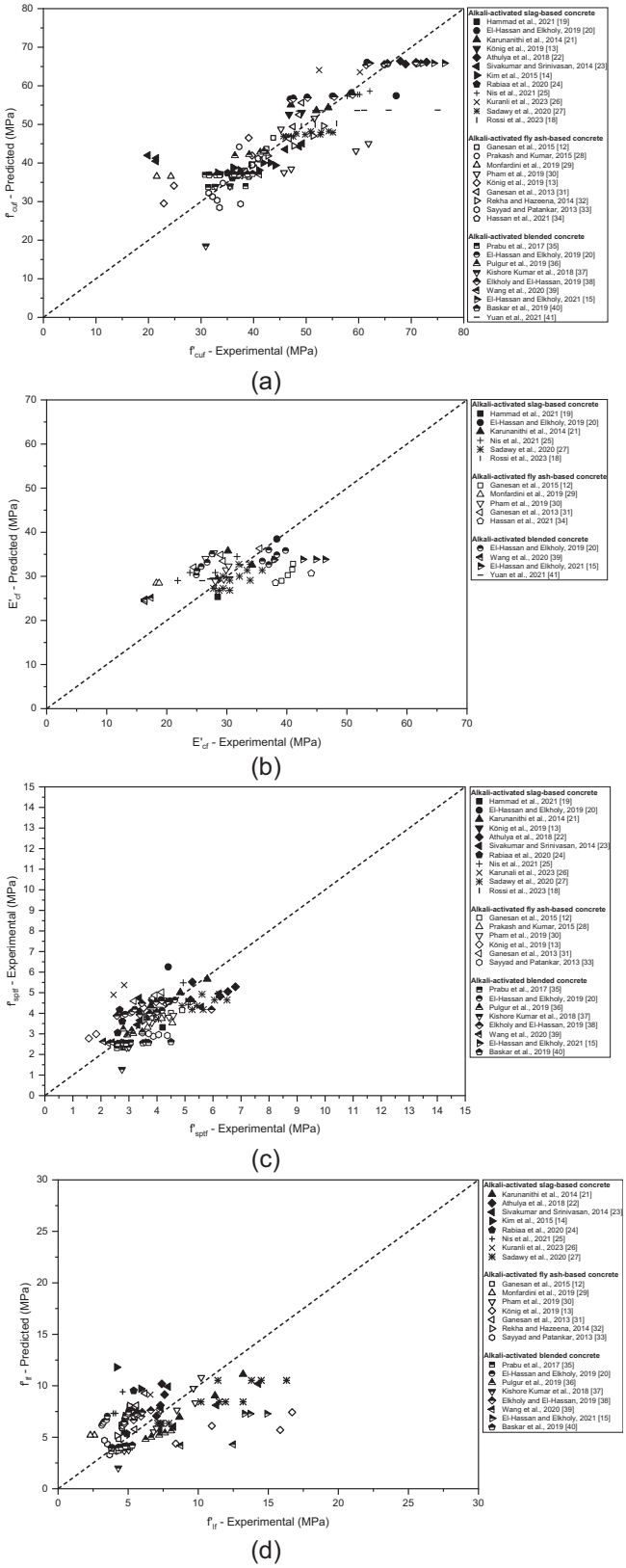

FIGURE 4 Correlation between the experimental and predicted values of (a) compressive strength, (b) modulus of elasticity, (c) splitting tensile strength, and (d) flexural strength of different alkali-activated concretes according to the new proposed equations.

strengths than SFRPCC. Table 5 shows the IAE values for each type of AAC, which confirms the inaccuracy of this correlation for these alternative types of concrete.

4 | NEW PROPOSED CORRELATIONS

The general form of the empirical equations proposed by Guler et al.[1] and Thomas and Ramaswamy[3] has been preserved and their coefficients have been recalibrated. The recalibration has been done by minimizing the objective function, which for this study is the mean of the sum of squares of the difference between the experimental data and the predicted values. The minimization is carried out using the Generalized Reduced Gradient (GRG) nonlinear optimization algorithm available in the Microsoft Excel® Solver add-in. These correlations are derived separately for slag-based, fly ash-based, and blended AAC to account for the effect of the binder type.

4.1 | Compressive strength

The correlation proposed by Guler et al.[1] to predict the compressive strength of steel-fiber reinforced concrete from the compressive strength of the reference concrete without steel fibers can be written in its general form as follows:

$$f'_{\mathrm{cuf}} = Af'_{\mathrm{cu}} - Bv_{\mathrm{f}} + C\mathrm{RI}_{\mathrm{v}} \quad (2)$$

where A, B, and C are the calibrated coefficients. The new values of these coefficients have been summarized in Table 6 along with the corresponding values of IAE for each type of SFRAAC.

As shown in Table 6, for AAC, regardless of the binder type, the fiber volume fraction does not affect the compressive strength of the composite. As most of the data points used to calibrate this correlation refer to AAC incorporating different types of steel fibers in a volume fraction $v_{\mathrm{f}} < 0.50\%$, the effect of v_{f} on the compressive strength of the composite is minimal. Thus, the value of the coefficient B is equal to 0. The new proposed coefficients give lower IAE values compared to the original model (Figure 4a), corresponding to a decrease of 14.6%, 27.6%, and 41.5% for slag-based, fly ash-based, and blended AAC, respectively.

4.2 | Modulus of elasticity

The equation proposed by Thomas and Ramaswamy[3] correlates the modulus of elasticity of SFRPCC to the compressive strength of the reference concrete and

Coefficients IAE [%]	New correlations		
	Slag-based AAC	Fly ash-based AAC	Blended AAC
D	3.68	4.55	4.28
E	0.00	0.00	0.06
F	9.07	8.57	0.00
IAE	8.04	20.87	15.74

TABLE 7 Proposed values of the coefficients *D*, *E*, and *F* and the corresponding IAE values for each type of alkali-activated concrete.

Coefficients IAE [%]	New correlations		
	Slag-based AAC	Fly ash-based AAC	Blended AAC
Splitting tensile strength			
G	0.07	0.10	0.08
H	0.00	0.00	0.00
I	1.85	0.87	0.19
IAE	19.85	18.23	16.10
Flexural strength			
J	0.10	0.10	0.13
K	4.17	0.00	0.00
L	0.00	7.05	0.55
IAE	25.31	34.98	36.27

TABLE 8 Proposed values of the coefficients *G*–*L* and the corresponding IAE values for each type of alkali-activated concrete.

TABLE 9 Proposed strength prediction models to derive the mechanical properties of slag-based, fly ash-based, and blended alkali-activated concrete incorporating steel fibers.

Mechanical properties	Proposed equations
Compressive strength	$f'_{cuf} = \begin{cases} 1.04f'_{cu} + 2.12RI_v \\ 0.95f'_{cu} + 18.78RI_v \\ 1.20f'_{cu} + 0.80RI_v \end{cases}$
Modulus of elasticity	$E'_{cf} = \begin{cases} 3.68(f\prime_{cu})^{0.5} + 9.07RI_v \\ 4.55(f\prime_{cu})^{0.5} + 8.57RI_v \\ 4.28(f\prime_{cu})^{0.5} + 0.06f'_{cu}RI_v \end{cases}$
Splitting tensile strength	$f'_{sptf} = \begin{cases} 0.07f'_{cu} + 1.85RI_v \\ 0.10f'_{cu} + 0.87RI_v \\ 0.08f'_{cu} + 0.19RI_v \end{cases}$
Flexural strength	$f'_{lf} = \begin{cases} 0.10f'_{cu} + 4.17v_f \\ 0.10f'_{cu} + 7.05RI_v \\ 0.13f'_{cu} + 0.55RI_v \end{cases}$

the fiber reinforcing index and can be written in its general form as follows:

$$E_{cyf} = D(f\prime_{cu})^{0.5} + Ef'_{cu}RI_v + FRI_v \quad (3)$$

Table 7 summarizes the new values of the coefficients *D*, *E*, and *F* and the corresponding IAE.

As shown in Table 7, for alkali-activated slag-based and fly ash-based concrete the coefficient *E* is equal to 0, that is, the modulus of elasticity of SFRAAC is directly correlated to the square root of the compressive strength of the reference concrete and the fiber reinforcing index. For blended AAC, the coefficient *F* is equal to 0, showing a limited influence of the fiber reinforcing index on the modulus of elasticity of SFRAAC. The different effects of the coefficients on the prediction of the modulus of elasticity according to the binder type can be related to the limited amount of data available in the literature for the recalibration of the empirical correlation and to their limited variety of fiber volume fractions investigated, as observed for the compressive strength. However, the proposed recalibration provides lower IAE values in comparison to the one observed for the original model, which decreases by 72.1%, 10.7%, and 51.8% for slag-based, fly ash-based, and blended AAC, respectively (Figure 4b).

4.3 | Splitting tensile strength and flexural strength

The equations for the prediction of the splitting tensile and flexural strength according to Guler et al.[1] can be written in their general form as follows:

$$f'_{sptf} = Gf'_{cu} - Hv_f + I\mathrm{RI}_v \quad (4)$$

$$f'_{lf} = Jf'_{cu} + Kv_f + L\mathrm{RI}_v \quad (5)$$

Table 8 summarizes the values of the coefficients of Equations (4) and (5) and the IAE values of each analytical correlation.

As shown in Table 8, the splitting tensile strength of AAC, regardless of the type of matrix, is not directly correlated to the fiber volume fraction but is mainly affected by the compressive strength of the matrix and the fiber reinforcing index. However, the fiber volume fraction indirectly affects the splitting tensile strength, as the fiber reinforcing index is defined as the product between the fiber aspect ratio (length/diameter) and the fiber volume fraction. As observed for the compressive strength and the modulus of elasticity, values of the coefficients corresponding to v_f equal to 0 can be due to the limited variety of the fiber volume fraction for the data points considered. Additional data related to higher fiber volume fractions would be necessary to improve the proposed correlation concerning v_f. However, the newly calibrated correlations can predict the splitting tensile strength more accurately in comparison to the original model, as shown by the values of IAE, which decrease by 56.8%, 58.02%, and 73.3% for slag-based, fly ash-based, and blended AAC, respectively (Figure 4c). Lower values of the IAE correspond to a more accurate prediction of the experimental data.

Similar behavior can be observed for the prediction of the flexural strength of AAC. For fly ash-based and blended concrete, the fiber volume fraction has a negligible effect on the flexural strength of the composite, while for slag-based AAC, the fiber volume fraction has a higher effect than the fiber reinforcing index. However, such observation can be due to the limited amount of data points collected and their narrow variability rather than to differences in the material mechanical behavior. The new proposed correlation can predict the flexural strength of SFRAAC with higher accuracy, as shown by the values of IAE decreasing by 42.3%, 31.0%, and 44.3% for slag-based, fly ash-based, and blended concrete, respectively, in comparison to the values observed for the original model (Figure 4d).

Table 9 summarizes the strength prediction equations derived in this study for slag-based, fly ash-based, and blended SFRAAC.

5 | CONCLUSIONS

This paper evaluates the applicability of the currently available analytical equations developed for steel fiber-reinforced cement-based concrete to different types of steel fiber-reinforced AAC. Available analytical correlations proposed for steel fiber-reinforced PCC have been evaluated in this paper and further calibrated using the experimental data available in the literature for steel fiber-reinforced slag-based, fly ash-based, and blended AACs.

AAC generally shows a lower modulus of elasticity and tensile behavior than cement-based concrete of similar strength grade, thus, the analytical correlations developed for SFRPCC overestimate the mechanical performance of SFRAAC and need to be recalibrated. The newly calibrated equations show higher accuracy in predicting the mechanical performance of SFRAAC, with an average improvement of the IAE of 27.9%, 44.9%, 62.8%, and 39.2% for the compressive strength, modulus of elasticity, splitting and flexural tensile strengths, respectively. The newly recalibrated analytical correlations show a negligible effect of the fiber volume fractions on the predictions of the compressive strength and the splitting tensile strength, for which the coefficients B and H, respectively, are equal to zero. This might be due to the limited range of fiber volume fractions investigated in the literature, that is, $v_f < 0.50\%$. Additional data over a wider range of fiber volume fractions, in particular at $v_f > 1\%$, are needed to validate, and further calibrate, if needed, the coefficients of these prediction models.

Evaluating the correlation between the mechanical performance of different AACs incorporating different types and dosages of steel fiber is fundamental to further understanding the behavior of these new alternative binders, facilitating their structural design and promoting their utilization for design purposes. Being able to derive the mechanical performance of SFRAAC from the performance of the reference plain concrete facilitates the formulation of the concrete mix design and the choice of its main components, that is, binder, activator, and fiber type and dosage, to meet the design requirements of the end applications.

However, this study represents only a first step in deriving analytical equations to predict the mechanical performance of SFRAAC. Additional experimental data are needed to further evaluate the effect of steel fibers on the performance of the composite and derive more accurate analytical correlations for design purposes. In particular, different types of binders, that is, different types of ashes (class-C fly ashes, palm oil fuel ashes, and rice husk ash) or slags (ladle slag, copper slag, and EAF slag), alternative binders, such as calcined clays, activated with different types of activators, and incorporating different types of steel fibers at different volume fractions should be investigated. Furthermore, newly developed steel fibers, such as double (4D) and triple (5D) hooked-end

steel fibers or hybrid steel fiber reinforcements should be evaluated, to better understand the effect of the concrete matrix and the fiber geometry and dosage on the performance of SFRAAC. This would allow a more detailed classification of the composite and the formulation of more reliable analytical prediction models for SFRAAC and promote its use in practice.

ACKNOWLEDGMENTS

The funding was provided by the DuRSAAM Project (https://cordis.europa.eu/project/id/813596/de), a MSCA-ITN - Marie Skłodowska-Curie Innovative Training Networks (ITN) part of the Horizon 2020 Framework Programme (no. 813596). The opinions expressed in this document reflect only the author's view and reflect in no way the European Commission's opinions. The European Commission is not responsible for any use that may be made of the information it contains. Open Access funding enabled and organized by Projekt DEAL.

CONFLICT OF INTEREST STATEMENT

The authors declare that they have no conflict of interest.

DATA AVAILABILITY STATEMENT

The data that supports the findings of this study are available in the supplementary material of this article.

ORCID

Laura Rossi https://orcid.org/0000-0002-9669-5796

REFERENCES

1. Guler S, Yavuz D, Korkut F, Ashour A. Strength prediction models for steel, synthetic, and hybrid fiber reinforced concretes. Struct Concr. 2019;20:428–45.
2. Wang Y, Jin H, Demartino C, Chen W, Yu Y. Mechanical properties of SFRC: database construction and model prediction. Case Stud Constr Mater. 2022;17:e01484.
3. Thomas J, Ramaswamy A. Mechanical properties of steel fiber-reinforced concrete. J Mater Civ Eng. 2007;19:385–92.
4. Abbass W, Khan MI, Mourad S. Evaluation of mechanical properties of steel fiber reinforced concrete with different strengths of concrete. Construct Build Mater. 2018;168:556–69.
5. Xu BW, Shi HS. Correlations among mechanical properties of steel fiber reinforced concrete. Construct Build Mater. 2009;23:3468–74.
6. Suksawang N, Wtaife S, Alsabbagh A. Evaluation of elastic modulus of fiber-reinforced concrete. ACI Mater J. 2018;115(2):239–249.
7. Adesina A. Performance of fibre reinforced alkali-activated composites – a review. Materialia. 2020;12:100782.
8. Wang T, Fan X, Gao C, Qu C, Liu J, Yu G. The influence of fiber on the mechanical properties of geopolymer concrete: a review. Polymers (Basel). 2023;15(4):827.
9. Abbas AGN, Aziz FNAA, Abdan K, Nasir NAM, Huseien GF. A state-of-the-art review on fibre-reinforced geopolymer composites. Construct Build Mater. 2022;330:127187.
10. Rashad AM. Effect of steel fibers on geopolymer properties – the best synopsis for civil engineer. Construct Build Mater. 2020;246:118534.
11. Chen G, Gao D, Zhu H, Song Yuan J, Xiao X, Wang W. Effects of novel multiple hooked-end steel fibres on flexural tensile behaviour of notched concrete beams with various strength grades. Structure. 2021;33:3644–54.
12. Ganesan N, Abraham R, Deepa RS. Durability characteristics of steel fibre reinforced geopolymer concrete. Construct Build Mater. 2015;93:471–6.
13. Koenig A, Wuestemann A, Gatti F, Rossi L, Fuchs F, Fessel D, et al. Flexural behaviour of steel and macro-PP fibre reinforced concretes based on alkali-activated binders. Construct Build Mater. 2019;211:583–93.
14. Kim SW, Jang SJ, Kang DH, Ahn KL, Yun HD. Mechanical properties and eco-efficiency of steel fiber reinforced alkali-activated slag concrete. Materials. 2015;8:7309–21.
15. El-Hassan H, Elkholy S. Enhancing the performance of alkali-activated slag-fly ash blended concrete through hybrid steel fiber reinforcement. Construct Build Mater. 2021;311:125313.
16. Shaikh FUA. Pullout behavior of hook end steel fibers in geopolymers. J Mater Civ Eng. 2019;31(6):04019068.
17. Faris MA, Abdullah MMAB, Muniandy R, Abu Hashim MF, Błoch K, Jeż B, et al. Comparison of hook and straight steel fibers addition on malaysian fly ash-based geopolymer concrete on the slump, density, water absorption and mechanical properties. Materials. 2021;14(5):1310.
18. Rossi L, Patel RA, Dehn F. Compressive behaviour of alkali-activated slag-based concrete and Portland cement concrete incorporating novel multiple hooked-end steel fibres. Mater Struct. 2023;56:96.
19. Hammad N, El-Nemr A, El-Deen HH. The performance of fiber GGBS based alkali-activated concrete. J Build Eng. 2021;42:102464.
20. El-Hassan H, Elkholy S. Performance evaluation and microstructure characterization of steel fiber-reinforced alkali-activated slag concrete incorporating fly ash. J Mater Civ Eng. 2019;31(10):04019223.
21. Karunanithi S, Anandan S. Flexural toughness properties of reinforced steel fibre incorporated alkali activated slag concrete. Adv Civ Eng. 2014;2014:1–12.
22. Athulya NA, Elba HG. Experimental investigation on effect of inclusion of hooked steel fiber on ggbs based geopolymer concrete. Int J Eng Sci Res Tech. 2018;7:4.
23. Sivakumar A, Srinivasan K. High performance fibre reinforced alkali activated slag concrete. Int J Civ Environ Eng. 2014;8(12):1288–1291.
24. Rabiaa E, Mohamed RAS, Sofi WH, Tawfik TA. Developing geopolymer concrete properties by using nanomaterials and steel fibers. Adv Mater Sci Eng. 2020;2020:1–12.
25. Niş A, Eren NA, Çevik A. Effects of nanosilica and steel fibers on the impact resistance of slag based self-compacting alkali-activated concrete. Ceram Int. 2021;47:23905–18.
26. Kuranlı ÖF, Uysal M, Abbas MT, Çoşgun T, Niş A, Aygörmez Y, et al. Mechanical and durability properties of steel, polypropylene and polyamide fiber reinforced slag-based alkali-activated concrete. Eur J Environ Civ Eng. 2023;27:114–39.

27. Sadawy MA, Faried AS, El-Ghazaly HA. Influence of various types of steel fibre on the mechanical and physical characteristics of GGBS based geopolymer concrete. J Eng Res Rep. 2020; 12(1):7–19.
28. Prakash AS, Kumar GS. Experimental study on geopolymer concrete using steel fibres. Int J Eng Trends Tech. 2015;21: 396–9.
29. Monfardini L, Facconi L, Minelli F. Experimental tests on fiber-reinforced alkali-activated concrete beams under flexure: some considerations on the behavior at ultimate and serviceability conditions. Materials. 2019;12(20):3356.
30. Pham KVA, Nguyen TK, Le TA, Han SW, Lee G, Lee K. Assessment of performance of fiber reinforced geopolymer composites by experiment and simulation analysis. Appl Sci. 2019;9: 3424.
31. Ganesan N, Indira PV, Santhakumar A. Engineering properties of steel fibre reinforced geopolymer concrete. Adv Concr Constr. 2013;1:305–18.
32. Rekha KP, Hazeena R. Strength and durability of fibre reinforced geopolymer concrete. Int J Scient Eng Res. 2014;5:412–6.
33. Sayyad AS, Patankar SV. Effect of steel fibres and low calcium fly ash on mechanical and elastic properties of geopolymer concrete composites. Indian J Mater Sci. 2013;2013(2):8.
34. Hassan A, Arif M, Shariq M. Structural performance of ambient-cured reinforced geopolymer concrete beams with steel fibres. Struct Concr. 2021;22:457–75.
35. Prabu B, Kumutha R, Vijai K. Effect of fibers on the mechanical properties of fly ash and GGBS based geopolymer concrete under different curing conditions. Indian J Eng Mater Sci. 2017;24:5–12.
36. Pulgur A, Divakar L, Chethan Gowda RK, Nagesh B. Influence of steel fibres on mechanical properties of geopolymer concrete. In: Drück H, Pillai RG, Tharian MG, Majeed AZ, editors. Green buildings and sustainable engineering: proceedings of GBSE 2018, Singapore. Springer Singapore; 2019. p. 423–30.
37. Kishore Kumar JS, Prabu B, Shalini A. Experimental investigation of geopolymer concrete with steel fibers under different curing exposures. Int Res J Eng Tech. 2018;5:2022–6.
38. Elkholy S, El-Hassan H. Mechanical and micro-structure characterization of steel fiber-reinforced geopolymer concrete. In: Ozevin D, Ataei H, Modares M, editors. Interdependence of structural engineering and construction management: International Structural Engineering and Construction Conference (ISEC-10), Chicago, IL, USA, 20–25 May 2019. Volume 6. Red Hook, NY: Curran Associates Inc.; 2019.
39. Wang Y, Aslani F, Valizadeh A. An investigation into the mechanical behaviour of fibre-reinforced geopolymer concrete incorporating NiTi shape memory alloy, steel and polypropylene fibres. Construct Build Mater. 2020;259:119765.
40. Baskar P, Rathinam K, Kanagarajan V. Effect of aspect ratio and volume fraction of steel fibers in strength properties of geopolymer concrete. Int J Innov Tech Expl Eng. 2019;9:3314–20.
41. Yuan X, Guan H, Shi Y. Stress–strain relationship of steel fiber reinforced alkali activated slag concrete under static compression. Adv Civ Eng. 2021;2021:1–12.
42. Muhammad Kani Al-Azzawi Z, Sarsam K. Mechanical properties of high-strength fiber reinforced concrete. Eng Tech J. 2010;28:2442–53.
43. Lee BJ, Kee SH, Oh T, Kim YY. Effect of cylinder size on the modulus of elasticity and compressive strength of concrete from static and dynamic tests. Adv Mater Sci Eng. 2015;2015:1–12.
44. Lee SJ, Yoo DY, Moon DY. Effects of hooked-end steel fiber geometry and volume fraction on the flexural behavior of concrete pedestrian decks. Appl Sci. 2019;9:1241.
45. Thomas RJ, Peethamparan S. Alkali-activated concrete: engineering properties and stress–strain behavior. Construct Build Mater. 2015;93:49–56.
46. Aiken TA, Kwasny J, Sha W, Tong KT. Mechanical and durability properties of alkali-activated fly ash concrete with increasing slag content. Construct Build Mater. 2021;301: 124330.
47. Pacheco-Torgal F, Labrincha J, Leonelli C, Palomo A, Chindaprasit P, editors. Handbook of alkali-activated cements, mortars and concretes. Burlington: Elsevier Science; 2014.
48. Nath P, Sarker PK. Flexural strength and elastic modulus of ambient-cured blended low-calcium fly ash geopolymer concrete. Construct Build Mater. 2017;130:22–31.
49. Rossi L, Miranda de Lima L, Sun Y, Dehn F, Provis JL, Ye G, et al. Future perspectives for alkali-activated materials: from existing standards to structural applications. RILEM Tech Lett. 2022;7:159–77.

AUTHOR BIOGRAPHIES

Laura Rossi received her MSc degree in Architectural Engineering—Architecture from Università degli Studi di Brescia, Italy, in 2016. She started her PhD studies at the Institute of Concrete Structures and Building Materials (IMB) and Materials Testing and Research Institute (MPA) at the Karlsruhe Institute of Technology (KIT), Germany, in 2019, under the supervision of Prof. Dr.-Ing. Frank Dehn. Her research focuses on the short-term mechanical performance of steel fiber-reinforced alternative cement-free concretes, in particular alkali-activated slag-based concrete. Email: laura.rossi@kit.edu.

Dr Ravi A. Patel obtained his PhD degree in Civil Engineering from Ghent University, Belgium, in 2016. Since 2020 he has been the leader of the working group "Numerical Modelling and Digitalisation for Building Materials and Concrete Structures" at the Institute of Concrete Structures and Building Materials (IMB) and Materials Testing and Research Institute (MPA) at the Karlsruhe Institute of Technology (KIT), Germany. His research group focuses on multiscale modeling and digital technologies for

sustainable and durable concrete structures. Email: ravi.patel@kit.edu.

Prof. Dr.-Ing. Frank Dehn obtained his MSc degree from Universität Karlsruhe (TH) and his PhD degree from Universität Leipzig in 1998 and 2002, respectively. He holds the chair for Building Materials and Concrete Construction at the Institute of Concrete Structures and Building Materials (IMB) and he is director of the Materials Testing and Research Institute (MPA) at the Karlsruhe Institute of Technology (KIT), Germany. He is also a member of national and international technical-scientific committees and expert committees for concrete technology. Email: frank.dehn@kit.edu.

SUPPORTING INFORMATION

Additional supporting information can be found online in the Supporting Information section at the end of this article.

How to cite this article: Rossi L, Patel RA, Dehn F. New analytical models to predict the mechanical performance of steel fiber-reinforced alkali-activated concrete. Structural Concrete. 2024. https://doi.org/10.1002/suco.202301104

Paper 3

Compressive behaviour of alkali-activated slag-based concrete and Portland cement concrete incorporating novel multiple hooked-end steel fibres

Laura Rossi, Ravi A. Patel, Frank Dehn

Materials and Structures

Volume 56 (96) 2023, pp. 1-23

DOI: 10.1617/s11527-023-02180-2

Publisher's version

Materials and Structures (2023)56:96
https://doi.org/10.1617/s11527-023-02180-2

ORIGINAL ARTICLE

Compressive behaviour of alkali-activated slag-based concrete and Portland cement concrete incorporating novel multiple hooked-end steel fibres

Laura Rossi · Ravi A. Patel · Frank Dehn

Received: 7 January 2023 / Accepted: 23 April 2023

Abstract This study investigates the effect of single and multiple hooked-end steel fibres on the mechanical properties of alkali-activated slag-based concrete (AASC) and compares its performance with a similar strength-grade Portland cement concrete (PCC). Three different fibre geometries, i.e. single (Dramix® 3D), double (Dramix® 4D) and triple hooked-end (Dramix® 5D) steel fibres, and three different volume fractions, i.e. 0.25%, 0.50% and 0.75% are considered. Compressive strength, modulus of elasticity and stress–strain response under uniaxial compression are evaluated. Hooked-end steel fibres have a limited effect on the compressive strength and modulus of elasticity of both AASC and PCC, regardless of fibre geometry and content. Although hooked-end steel fibres improve the compressive stress–strain behaviour of both composites, higher enhancement of peak stress, corresponding strain and post-peak response is observed for fibre-reinforced AASC (FRAASC) mixtures. To predict the stress–strain response under uniaxial compression of steel FRAASC a new analytical model is proposed and calibrated using an extensive dataset of experimental stress–strain curves available in the literature for both steel fibre-reinforced PCC and AASC. This model can predict the compressive stress–strain behaviour of FRAASC using the compressive peak stress and corresponding strain of the unreinforced matrix and the steel fibre reinforcing index (RI_v) as inputs and provides excellent results when validated against the data obtained in this study for FRAASC.

Keywords Hooked-end steel fibres · Alkali-activated fibre-reinforced concrete · Slag concrete · Mechanical properties · Stress–strain behaviour

Supplementary Information The online version contains supplementary material available at https://doi.org/10.1617/s11527-023-02180-2.

L. Rossi (✉) · R. A. Patel · F. Dehn
Institute of Building Materials and Concrete Structures (IMB), Karlsruhe Institute of Technology (KIT), 76131 Karlsruhe, Germany
e-mail: laura.rossi@kit.edu

R. A. Patel
e-mail: ravi.patel@kit.edu

F. Dehn
e-mail: frank.dehn@kit.edu

L. Rossi · R. A. Patel · F. Dehn
Material Testing and Research Institute Karlsruhe (MPA), Karlsruhe Institute of Technology (KIT), 76131 Karlsruhe, Germany

Published online: 21 May 2023

1 Introduction

Alkali-activated slag concrete (AASC) has been the subject of in-depth research in recent years as a more environmentally friendly alternative to Portland cement (PC) as a binder for concrete [1–7]. Alkali-

activated slag concrete exhibits comparable or even better mechanical and durability performance than traditional PC concrete (PCC), such as higher early-age strength and higher stability in aggressive environments [1, 4, 7–13]. Despite its promising nature, AASC exhibits more brittle behaviour than cement-based concrete [14, 15], which can be attributed to the higher autogenous shrinkage-induced micro-cracking of AASC [1, 6, 11, 12, 15–18]. This restricts the applicability of AASC in areas requiring high flexural and tensile capacity. Several studies [9, 11–13, 18–21] demonstrated that the addition of randomly distributed steel fibres is an effective way to overcome the brittleness of the alkali-activated slag-based matrix. Transferring stresses across the cracked surfaces and increasing the energy needed for crack growth, fibres mitigate crack formation and propagation. The crack bridging capacity of the fibres enhances the ductility, fracture toughness and post-cracking load-bearing capacity of the composite [11, 18]. The efficiency of fibre bridging ability largely depends on the fibre-matrix interface bond [20, 22–24]. Thus, novel multiple hooked-end fibres have been developed to improve the fibre's mechanical anchorage, tensile strength and ductility. Unlike the old generation of single hooked-end steel fibres, generally known as 3D fibres, novel multiple hooked-end steel fibres are characterised by improved geometry, i.e., additional bends at both ends of the fibre, resulting in double (4D) and triple (5D) hooked-end steel fibres. Several studies investigated the pull-out behaviour [24–26] and the influence of novel hooked-end steel fibre geometry on the post-cracking behaviour of cementitious composites [23, 27–30]. Lee et al. [27] and Abdallah et al. [29] demonstrated that the incorporation of 3D, 4D and 5D fibres up to a volume fraction of 1% has a limited effect on the compressive strength. However, fibre geometry and volume fraction significantly affect the flexural behaviour of the composite, with 4D and 5D fibres showing higher flexural strength than 3D fibres. Although several studies investigate the effect of the addition of multiple hooked-end steel fibres on the mechanical properties of cementitious composites, very few investigations focus on the incorporation of these fibres in alkali-activated slag-based concrete. Shaikh [20] investigated only the pull-out behaviour of 3D, 4D and 5D fibres in alkali-activated fly ash-based and alkali-activated fly ash-slag mortars. El-Hassan and Elkholy [6] evaluated the effect of hybrid steel fibre reinforcement in blended alkali-activated concrete, i.e. different proportions of 3D, 4D and 5D fibres were added in an alkali-activated slag-fly ash matrix. However, the effect of each fibre geometry on the performance of alkali-activated slag-based concrete has not been evaluated. The understanding of the effect of novel hooked-end steel fibres on the compressive and tensile stress–strain behaviour of alkali-activated slag concrete is still lacking. Evaluating the full-range stress–strain response of the composite under both compression and tension is fundamental to fully characterise newly developed construction materials such as fibre-reinforced AASC (FRAASC) and derive constitutive models for design and field applications.

Different analytical models have been developed to predict the behaviour of steel fibre-reinforced Portland cement concrete (FRPCC) under uniaxial compression [31–35]. The majority of these models are based on the model proposed by Carreira and Chu [36] for plain concrete and modified by Ezeldin and Balaguru [35] for steel FRPCC. Equation (1) provides the general formula of these previously mentioned models while the available analytical models for steel FRPCC are summarised in Table 1.

$$\frac{\sigma_c}{\sigma_{c,\max(\mathrm{FRC})}} = \frac{\beta\left(\varepsilon_c/\varepsilon_{c,\max(\mathrm{FRC})}\right)}{\beta - 1 + \left(\varepsilon_c/\varepsilon_{c,\max(\mathrm{FRC})}\right)^{\beta}} \tag{1}$$

where σ_c is the compressive stress, $\sigma_{c,max(FRC)}$ is the maximum compressive stress (compressive strength), ε_c is the uniaxial strain, $\varepsilon_{c,\max(\mathrm{FRC})}$ is the uniaxial strain corresponding to $\sigma_{c,\max(\mathrm{FRC})}$ and β is a material parameter. Most of the models summarised in Table 1 were fitted on a small set of experimental results, making each model strictly dependent on the test conditions [7] and the characteristics of both the matrix and the steel fibre type investigated. Furthermore, many models provide a single equation to describe the entire compressive stress–strain curve without considering the different effects of fibre geometry and volume fraction on the pre- and post-peak branch of the stress–strain curve. Only Ruiz et al. [37] and Lee et al. [38] developed a model based on two separate equations to describe the stress–strain curve under compression and take into account the different effects of steel fibre incorporation on the material behaviour. Although the equation proposed by Ruiz et al. [37] for $\varepsilon_c < \varepsilon_{c,\max(\mathrm{FRC})}$ can predict quite

Table 1 Analytical models for the compressive behaviour of steel fibre-reinforced PC concrete (PCC) and plain alkali-activated fly ash (AAFA) and fly ash-slag (AAFA/GGBS) concrete

References	Matrix type	Fibre type	Fibre geometry (l_f/d_f)	Fibre content	Analytical model and coefficients
Carreira and Chu [36]	PCC	–	–	–	$\frac{\sigma_c}{\sigma_{c,max(REF)}} = \frac{\beta\left(\varepsilon_c/\varepsilon_{c,max(REF)}\right)}{\beta-1+\left(\varepsilon_c/\varepsilon_{c,max(REF)}\right)^{\beta}}$ $\beta = \frac{1}{1-\left(\frac{\sigma_{c,max(REF)}}{\varepsilon_{c,max(REF)}E_{it(REF)}}\right)}$ $\varepsilon_{c,max(REF)} = (4.88\sigma_{c,max(REF)} + 168)10^{-5}$
Ezeldin and Balaguru [35]	PCC	HE	50/05 60/0.8 30/0.5	30 kg/m^3 45 kg/m^3 60 kg/m^3	$\frac{\sigma_c}{\sigma_{c,max(FRC)}} = \frac{\beta\left(\varepsilon_c/\varepsilon_{c,max(FRC)}\right)}{\beta-1+\left(\varepsilon_c/\varepsilon_{c,max(FRC)}\right)^{\beta}}$ $\beta = 1.093 + 0.7132(RI_w)^{-0.926}$ $\sigma_{c,max(FRC)} = \sigma_{c,max(REF)} + 3.51(RI_w)$ $\varepsilon_{c,max(FRC)} = \varepsilon_{c,max(REF)} + 446\text{x}10^{-6}(RI_w)$
Nataraja et al. [31]	PCC	C	27.5/0.5 41/0.5	39 kg/m^3 58 kg/m^3 78 kg/m^3	$\frac{\sigma_c}{\sigma_{c,max(FRC)}} = \frac{\beta\left(\varepsilon_c/\varepsilon_{c,max(FRC)}\right)}{\beta-1+\left(\varepsilon_c/\varepsilon_{c,max(FRC)}\right)^{\beta}}$ $\beta = 0.5811 + 1.93(RI_w)^{-0.7406}$ $\sigma_{c,max(FRC)} = \sigma_{c,max(REF)} + 2.1604(RI_w)$ $\varepsilon_{c,max(FRC)} = \varepsilon_{c,max(REF)} + 0.0006(RI_w)$
De Oliveira Junior et al. [32]	PCC	HE	35/0.55	1.00% 2.00%	$\frac{\sigma_c}{\sigma_{c,max(FRC)}} = \frac{\beta\left(\varepsilon_c/\varepsilon_{c,max(FRC)}\right)}{\beta-1+\left(\varepsilon_c/\varepsilon_{c,max(FRC)}\right)^{\beta}}$ $\beta = (0.0536 - 0.574v_f)\sigma_{c,max(FRC)}$ $\varepsilon_{c,max(FRC)} = (0.00048 + 0.01886v_f)\ln\sigma_{c,max(FRC)}$
Ou et al. [33]	PCC	HE	30/0.5 30/0.6 35/0.5 50/0.5 50/1.0 60/1.0	0%–3.40%	$\frac{\sigma_c}{\sigma_{c,max(FRC)}} = \frac{\beta\left(\varepsilon_c/\varepsilon_{c,max(FRC)}\right)}{\beta-1+\left(\varepsilon_c/\varepsilon_{c,max(FRC)}\right)^{\beta}}$ $\beta = 0.71(RI_v)^2 - 2.00RI_v + 3.05$ $\sigma_{c,max(FRC)} = \sigma_{c,max(REF)} + 2.35(RI_v)$ $\varepsilon_{c,max(FRC)} = \varepsilon_{c,max(REF)} + 0.0007(RI_v)$
Abbas et al. [34]	PCC	HE	40/0.62 50/0.62 60/0.75	0.50% 1.00% 1.50%	$\frac{\sigma_c}{\sigma_{c,max(FRC)}} = \frac{\beta\left(\varepsilon_c/\varepsilon_{c,max(FRC)}\right)}{\beta-1+\left(\varepsilon_c/\varepsilon_{c,max(FRC)}\right)^{\beta}}$ $\beta = 1.401(RI_v)^2 - 1.56RI_v + 2.42$ $\sigma_{c,max(FRC)} = \sigma_{c,max(REF)} + 5.59(RI_v)$ $\varepsilon_{c,max(FRC)} = \varepsilon_{c,max(REF)} + 0.000261(RI_v)$
Lee et al. [38]	PCC	HE	50/1.05 35/0.55 30/0.38	0.50% 1.00% 1.50% 2.00%	$\sigma_c = \sigma_{c,max(FRC)}\frac{A\left(\varepsilon_c/\varepsilon_{c,max(FRC)}\right)}{A-1+\left(\varepsilon_c/\varepsilon_{c,max(FRC)}\right)^{B}}$ $A = B = \frac{1}{1-\left(\frac{\sigma_{c,max(FRC)}}{\varepsilon_{c,max(FRC)}E_{c(FRC)}}\right)}$, $\varepsilon/\varepsilon_{c,max(FRC)} \le 1$ $\begin{cases} A = 1 + 0.723(\text{RI}_v)^{-0.957} \\ B = \left(\frac{\sigma_{c,max(FRC)}}{50}\right)^{0.064}\left[1 + 0.882(\text{RI}_v)^{-0.882}\right] \end{cases}$, $\varepsilon/\varepsilon_{c,max(FRC)} > 1$ $\varepsilon_{c,max(FRC)} = (0.0003(RI_v) + 0.0018)\sigma_{c,max(FRC)}^{0.12}$

Table 1 continued

References	Matrix type	Fibre type	Fibre geometry (l_f/d_f)	Fibre content	Analytical model and coefficients
Ruiz et al. [37,44]	PCC				$\frac{\sigma_c}{\sigma_{c,max(FRC)}} = \begin{cases} \frac{\alpha\left(\varepsilon_c/\varepsilon_{c,max(FRC)}\right) - \left(\varepsilon_c/\varepsilon_{c,max(FRC)}\right)^2}{1+(\alpha-2)\left(\varepsilon_c/\varepsilon_{c,max(FRC)}\right)}, & \varepsilon_c/\varepsilon_{c,max(FRC)} \le 1 \\ 1-\frac{1}{4}\left(1-\sigma_R^*\right)\left(\varepsilon_c/\varepsilon_{c,max(FRC)}-1\right)^2, & \varepsilon_c/\varepsilon_{c,max(FRC)} > 1 \end{cases}$ $\alpha = 1{,}05\ \varepsilon_{c,max(FRC)} \frac{E_{c(FRC)}}{\sigma_{c,max(FRC)}}$ $\sigma_R^* = 0.8279 + 0.3888\ l_f^*(35.03\ v_f - 1),\ l_f^* = l_f/30$ $\sigma_{c,max(FRC)} = \sigma_{c,max(REF)}(1 + 4.17 l_f^* v_f)$ $\varepsilon_{c,max(FRC)} = \varepsilon_{c,max(REF)}\left[1 + 0.4823\lambda(v_f - 0.002606 l_f^*)\right]$ λ = fibre aspect ratio
Hardjito et al. [39]	AAFA	–	–	–	$\sigma_c = \sigma_{c,max(REF)} \frac{n\left(\varepsilon_c/\varepsilon_{c,max(REF)}\right)}{n-1+\left(\varepsilon_c/\varepsilon_{c,max(REF)}\right)^{nk}}$ $n = 0.8 + \left(\frac{\sigma_{c,max(REF)}}{17}\right)$ $k = \begin{cases} 1, & \varepsilon_c/\varepsilon_{c,max(REF)} \le 1 \\ 0.67 + \left(\frac{\sigma_{c,max(REF)}}{62}\right), & \varepsilon_c/\varepsilon_{c,max(REF)} > 1 \end{cases}$
Noushini et al. [41]	AAFA	–	–	–	$\frac{\sigma_c}{\sigma_{c,max(REF)}} = \frac{n\left(\varepsilon_c/\varepsilon_{c,max(REF)}\right)}{n-1+\left(\varepsilon_c/\varepsilon_{c,max(REF)}\right)^n}$ $n = \begin{cases} n_1 = \left[1.02 - 1.17\left(E_{sec(REF)}/E_{c(REF)}\right)\right]^{-0.45}, & \varepsilon_c/\varepsilon_{c,max(REF)} \le 1 \\ n_2 = n_1 + (\omega + 28\zeta), & \varepsilon_c/\varepsilon_{c,max(REF)} > 1 \end{cases}$ $\omega = C\left(12.4 - 0.015\sigma_{c,max(REF)}\right)^{-0.5}$ $\zeta = 0.83e^{\left(-911/\sigma_{c,max(REF)}\right)}$
Cong et al. [42]	AAFA/ GGBS	–	–	–	$\frac{\sigma_c}{\sigma_{c,max(REF)}} = \frac{m\left(\varepsilon_c/\varepsilon_{c,max(REF)}\right)}{m-1+\left(\varepsilon_c/\varepsilon_{c,max(REF)}\right)^\beta}$ $m = 2.0 + \left(\frac{E_{c(REF)}}{19.5}\right)$ $\beta = 5 + 10\left(\frac{-8.4}{\sigma_{c,max(REF)}}\right)$

HE = hooked-end steel fibres, C = crimped steel fibres, $E_{it(FRC)}$ and $E_{it(REF)}$ = initial secant modulus at 40% of the peak stress for fibre-reinforced and plain concrete, respectively; $E_{c(FRC)}$ and $E_{c(REF)}$= modulus of elasticity for fibre-reinforced and plain concrete, respectively; l_f = fibre length; v_f = fibre volume fraction; RI_w and RI_v = reinforcing index ($l_f/d_f \bullet v_f$) calculated using the fibre weight and volume fraction, respectively; $\sigma_{c,max(FRC)}$ and $\sigma_{c,max(REF)}$ = compressive strength of fibre-reinforced and plain concrete, respectively; $\varepsilon_{c,max(FRC)}$ and $\varepsilon_{c,max(REF)}$ = strain corresponding to peak stress of fibre-reinforced and plain concrete, respectively

accurately the pre-peak ascending branch of the stress–strain curve of steel FRPCC, the parabolic equation describing the post-peak descending branch is not able to represent the real compressive response of the composite, characterised by exponential softening behaviour. Lee et al. [38] proposed a two-equation model governed by two material parameters. In the pre-peak phase of the stress–strain response under uniaxial compression, the two parameters have the same value and the model corresponds to the one proposed by Ezeldin and Balaguru [35]. In the post-peak phase, the model parameters have different values linked to the fibre reinforcing index RI_v (defined as the product of the fibre aspect ratio (l_f/d_f) and the fibre volume fraction (v_f)) to take into account the fibre-bridging effect once cracks start growing and propagating.

Analytical equations to predict the stress–strain behaviour under uniaxial compression of alkali-activated concretes have been developed in recent years and are also summarised in Table 1. Hardjito et al. [39] evaluated the stress–strain response of heat-cured fly

ash-based alkali-activated concrete and demonstrated that the model proposed by Collins et al. [40] for PCC predicts quite accurately both the ascending and descending branch of the experimental curves. Noushini et al. [41] investigated the compressive response of heat-cured alkali-activated fly ash-based concrete and proposed new material parameters to better predict the ascending and descending branches of the stress–strain curve. Cong et al. [42] analysed the compressive stress–strain response of blended alkali-activated fly ash-slag concrete and proposed new analytical equations fitting the experimental stress–strain curves. Despite the current availability of analytical equations describing the stress–strain response of alkali-activated fly ash-based concretes, models to predict the compressive stress–strain behaviour of AASC with the incorporation of steel fibres are still missing. Although several studies investigated the performance of alkali-activated slag-based concrete reinforced with steel fibres, only a few focused on the full-range stress–strain response under uniaxial compression without providing any analytical model [21, 43].

The present study fills the research gap highlighted above and provides an in-depth understanding of the mechanical behaviour under uniaxial compression of alkali-activated slag-based concrete incorporating single and multiple hooked-end steel fibres in different volume fractions up to 0.75%. The compressive behaviour of the plain and fibre-reinforced AASC was characterised by the compressive strength, modulus of elasticity and stress–strain response under uniaxial compression. The same tests are also performed on traditional PCC reinforced with the same fibre types and contents to better evaluate the behaviour of different fibre geometries in different concrete matrices. The experimental results obtained for FRPCC, in combination with available literature data for steel FRPCC and FRAASC, have been used to propose and calibrate a new analytical model. This model can predict the stress–strain response of both AASC and PCC incorporating steel fibres, considering the matrix compressive peak stress and corresponding strain and the fibre reinforcing index RI_v as the only input parameters. The experimental data collected for FRAASC in this study are then used to validate the model. This allows for the verification of the suitability of the proposed model to any fibre and concrete type and, in particular, to AASC reinforced with single and multiple hooked-end steel fibres.

2 Experimental programme

2.1 Materials

2.1.1 GGBS

The ground granulated blast furnace slag (GGBS) used in this study was supplied by the Dutch company Ecocem Benelux B.V. Its chemical composition was obtained by X-ray fluorescence (XRF) as shown in Table 2. The basicity coefficient $K_b = (CaO + MgO)/(SiO_2 + Al_2O_3)$ and the hydration modulus $HM = (CaO + MgO + Al_2O_3)/SiO_2)$, in % by mass, were 1.05 and 1.66, respectively.

2.1.2 Alkaline activators

The alkaline activator used was a combination of sodium silicate (*waterglass*), sodium hydroxide and water. Sodium silicate (SS) solution was a commercially available product supplied by the company Woellner with a specific gravity of 1.37 g/cm^3 and a silicate modulus $M_{s(SS)}$(the molar ratio of SiO_2 to Na_2O) of 3.4. The silicate modulus of the alkaline solution was adjusted by adding sodium hydroxide solution (NaOH with 50% solid content) to achieve $M_{s(sol)}$= 0.5 [mol/mol] and a total concentration of 5.3% of Na_2O (expressed as a percentage of the slag weight). Additional water was added to the alkaline solution to achieve a liquid/binder ratio of 0.48, [kg/kg], where both the extra water and the water included in the activators is considered as liquid component. The different components of the alkaline activator were pre-mixed 24 h prior casting to reduce the heat released by the exothermic reaction between sodium hydroxide and sodium silicate solutions [5, 8] and avoid flash setting.

2.1.3 Portland cement

Portland cement (PC) CEM I 42.5 R produced by HeidelbergCement with a specific surface of 319.8 m^2/kg and loss on ignition of 4.57% was used. The chemical composition is also shown in Table 2.

Table 2 Chemical and physical properties of GGBS and PC (% by mass)

Binder	CaO (%)	SiO_2 (%)	Al_2O_3 (%)	Fe_2O_3 (%)	MgO (%)	P_2O_5 (%)	K_2O (%)	Na_2O (%)	Specific gravity [kg/m^3]	Blaine fineness (m^2/kg)
GGBS	41.84	35.91	10.74	0.39	6.99	0.47	0.40	0.31	2856.7	488.1
PC	60.80	19.60	5.25	2.38	1.53	0.13	0.80	0.10	3033.3	319.8

2.1.4 Fine and coarse aggregates

Quartzite gravel from the river Rhine with different maximum sizes, i.e. 8 mm and 16 mm, were used as fine and coarse aggregates, respectively. Natural river sand with a maximum size of 2 mm was also used.

2.1.5 Hooked-end steel fibres

Glued single and multiple hooked-end steel fibres, commercially available with the name of Dramix® 3D 65/60 BG, Dramix® 4D 65/60 BG and Dramix® 5D 65/60 BG, were supplied by NV Bekaert SA. The fibre geometry and properties are shown in Fig. 1 and Table 3, respectively. The three different fibre types used in this study have the same length (60 mm) and aspect ratio ($l_f/d_f = 65$) and differ from each other in terms of fibre tensile strength ($\sigma_{f,u}$) and the number of bends at the fibre hooked ends.

2.2 Mix proportions

AAS and PC concrete were designed to achieve the same strength and workability class, i.e. similar 28-day cubic mean compressive strength of 50 MPa (C35/45) and consistency class (F3-F4). The mix proportions for both AASC and PCC are shown in Table 4. To better assess the effect of hooked-end steel fibres in the different concrete matrices, the same binder content and aggregates type and proportions have been used for both AASC and PCC. Each fibre type has been added to the reference mixture of Table 4 in different volume fractions, i.e. 0.25% (20 kg/m^3), 0.50% (40 kg/m^3) and 0.75% (60 kg/m^3).

A total of 20 mixes, 10 for each binder type, have been investigated. The matrix type (AASC or PCC), the fibre geometry (3D, 4D or 5D) and the fibre volume fraction (0.25%, 0.50% and 0.75%) define each mix. For example, the mix AASC-4D50 refers to the alkali-activated slag-based concrete reinforced with 4D fibres in a volume fraction of 0.50%. The plain concrete without fibres is referred as reference (REF).

2.3 Specimen preparation

To allow a better comparison between AASC and PCC mixes, the same casting procedure has been used. First, sand, fine and coarse aggregates and binder were dry-mixed in a 250-L concrete mixer for 90 s. The liquid component (the alkaline solution or water, for AASC and PCC, respectively) was then added and mixed for additional 2 min. Finally, steel fibres were added, and the mixing further prolonged up to a total of 7 min, to achieve homogeneous fibre distribution in the fresh concrete. The final mixture was then poured into the moulds. For each mixture, 9 cylinders with diameter of 150 mm and height of 300 mm and 3 cubes of 150 mm dimensions were prepared. To avoid segregation of both aggregates and fibres in the samples, the moulds were filled in a single layer and compacted on a vibrating table for 20 s at 40 Hz. The specimen were demoulded 24 h after casting and cured according to the binder type. PCC samples were cured underwater (20 ± 2 °C) for 27 days, while AASC specimens were wrapped in foil and placed in a

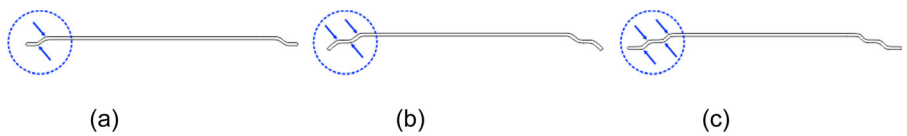

Fig. 1 Configurations of the different hooked-end steel fibres: **a** double bend (3D), **b** triple bend (4D), and **c** quadruple bend (5D). Arrows show the number of fibre bends

Table 3 Hooked-end steel fibres properties

Fibre type	Length (l_f) (mm)	Diameter (d_f) (mm)	Aspect ratio (l_f/d_f)	Fibre tensile strength ($\sigma_{f,u}$)[a] (MPa)	Strain at ultimate strength[a] (%)
3D 65/60 BG	60	0.90	65	1160	0.8
4D 65/60 BG	60	0.90	65	1600	0.8
5D 65/60 BG	60	0.90	65	2300	6.0

[a]Provided by NV Bekaert SA [45]

Table 4 Mix proportions of AASC and PCC

	GGBS (kg/m^3)	CEM I (kg/m^3)	Sodium hydroxide (kg/m^3)	Sodium silicate (kg/m^3)	Water (kg/m^3)	Sand (0–2 mm) (kg/m^3)	Fine aggregates (2–8 mm) (kg/m^3)	Coarse aggregates (8–16 mm) (kg/m^3)
AASC	425	–	50	36	154	660	495	495
PCC	–	425	–	–	229	660	495	495

climate room at (20 ± 2) °C and 65% relative humidity until testing date. Underwater curing should be prevented for alkali-activated concrete mixtures to avoid the leaching effect of alkalis in water [19].

2.4 Testing procedure

The effect of hooked-end steel fibres on the compressive behaviour of AASC and PCC is evaluated by the 28-day compressive strength, modulus of elasticity and stress–strain response under uniaxial compression. To guarantee uniform distribution of the compressive load between the sample surfaces and the testing machine plates, both top and bottom surfaces were ground the day before the testing date.

Three cubes and three cylinders were then tested to evaluate the 28-day mean compressive strength according to EN 12390–3. The modulus of elasticity was determined on three cylindrical samples according to EN 12390–13:2014 (part B), and three additional cylinders have been used to investigate the stress–strain response under compression.

The stress–strain behaviour under compression was evaluated using an MTS compression-tension testing machine with 2500 kN capacity with a constant loading head displacement rate of 0.30 mm/min. The presence of a spherical calotte above the upper plate of the machine guarantees that the load is always applied in the centre of the sample surface, avoiding load eccentricity. Four external linear variable differential transformers (LVDTs) were installed between both ends of the specimens, as shown in Fig. 2, to assess the axial plate-to-plate deformation and evaluate the post-peak stress–strain response up to a strain value of 0.01 (10‰).

The plate-to-plate strain measurement can lead to higher strain values in the pre-peak region compared to mid-span deformation measurement, although it is not disturbed by the cracking of the sample surfaces. This results in a better reading of the post-peak descending branch [46, 47], where the effect of hooked-end steel fibres on the compressive response is more pronounced. Therefore, axial plate-to-plate deformation measurements were chosen in this study.

Figure 3a shows a generic stress–strain curve obtained experimentally as the average of three cylindrical samples. The non-linearity at the origin (in the red circle) is usually due to the specimen versus testing machine stiffness and micro-cracking at the aggregate-matrix interfaces [36].

Due to the test setup, it is not possible to derive from the stress–strain curve the modulus of elasticity E_0. The modulus of elasticity is typically calculated by measuring the deformation in the central zone of a

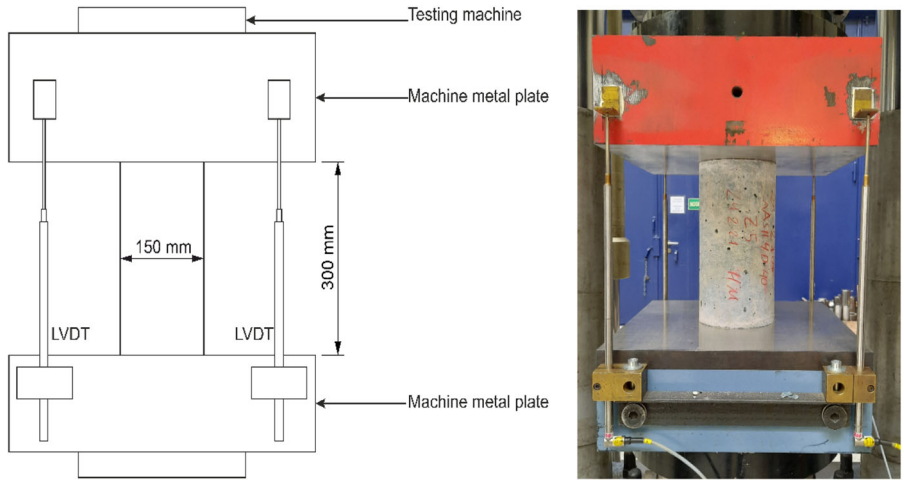

Fig. 2 Test set-up to evaluate the stress–strain response under uniaxial compression

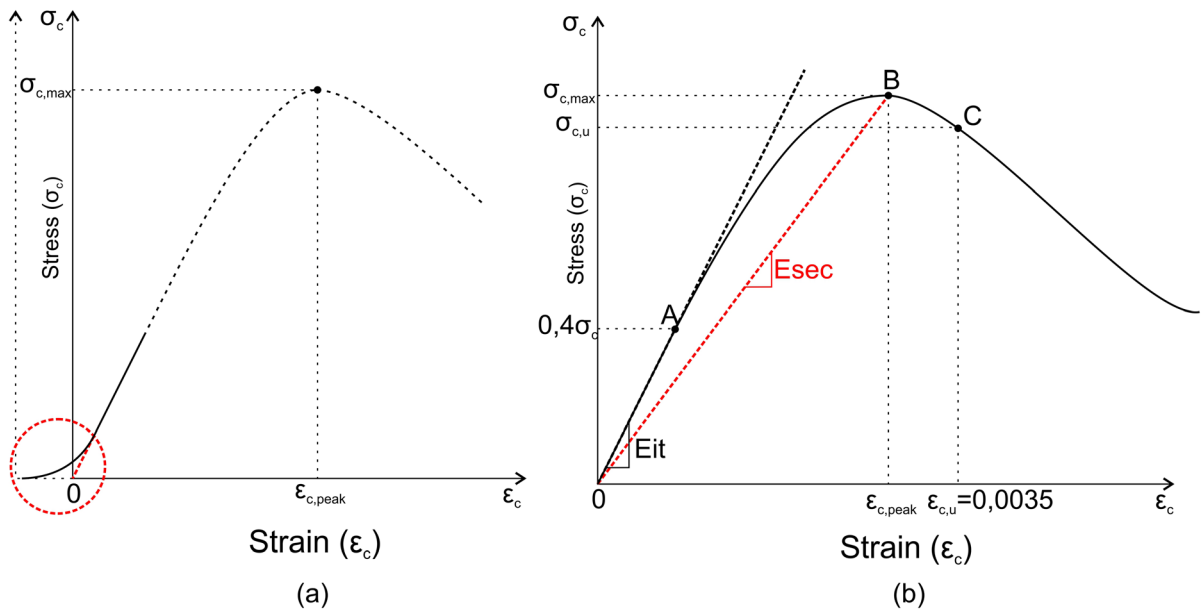

Fig. 3 General experimental stress–strain curve obtained as an average of three samples **a** and **b** definition of the compressive parameters E_{it} (initial secant modulus at 40% of the peak stress) and E_{sec} (secant modulus)

loaded cylinder, which is widely assumed to be subjected to a near-uniform uniaxial compressive stress due to the negligible frictional restraint at the specimen-plate interfaces [48]. When measuring the deformation of the central zone of the sample under uniaxial compression, the modulus of elasticity E_0 can be derived from the experimental stress–strain curve as the slope of the linear section 0A (Fig. 3b). However, measuring the plate-to-plate deformation results in an underestimation of the modulus of elasticity, due to the frictional restraints and resulting complex state of compressive stresses at the end of the sample [48]. Thus, for comparison purpose, the parameters E_{it} and E_{sec}, i.e. the initial secant modulus and the secant modulus, respectively, are defined for each experimental average stress–strain curve. The initial secant modulus represents the slope the linear region OA up to a stress corresponding to 40% of the peak stress. The secant modulus is defined as the slope of the line connecting the origin with the maximum

stress (OB). From the definition of E_0, E_{it} and E_{sec}, it is clear that $E_0 > E_{it} > E_{sec}$.

3 Results

3.1 Compressive strength and modulus of elasticity

Figure 4 shows the mean compressive strength of both cubic and cylindrical samples and the modulus of elasticity for AASC reinforced with 3D, 4D and 5D fibres at 0%, 0.25%, 0.50% and 0.75% fibre volume fractions. AASC mixes incorporating hooked-end steel fibres show enhanced cubic and cylindrical compressive strength compared to the reference unreinforced mix, regardless of fibre geometry and volume fraction.

However, the increase in compressive strength provided by fibre incorporation is not directly correlated to the fibre volume fraction, as the highest values of strength are not always achieved at the highest fibre dosage for each fibre type. Only for 3D fibres, the mix incorporating the highest fibre volume fraction achieves the highest compressive strength values of 55.8 MPa and 48.3 MPa for cubes and cylinders, respectively. For 4D and 5D fibres, the highest values of compressive strength are obtained for the mixes AASC-4D25 and AASC-5D50, respectively. The effects of fibre content on the compressive strength of composites reinforced with different fibre types can be correlated to the distribution and orientation of the fibres in the samples [49]. Fibres aligned perpendicular to the crack opening in the stress direction can lead to higher values of compressive strength [13] due to the fibre crack bridging and stress transferring effect. As shown in Fig. 4a, both cubic and cylindrical samples show similar strength variations with the increase of the fibre volume fraction for each fibre type. The highest values of cubic and cylindrical compressive strength, 57.8 MPa and 52.6 MPa, respectively, are achieved by the mix AASC-5D50, corresponding to an increase in strength in comparison to the strengths of the reference mix of 21.8% and 28.6%, respectively. Despite the similar trend observed for the cubic and cylindrical compressive strength of FRAASC, the conversion factor correlating the cubic to the cylindrical compressive strengths differs with the fibre geometry. The correlation between cubic and cylindrical compressive strength for each fibre type and volume fraction is evaluated and discussed in the supplementary information.

Figure 4b shows the 28-day mean modulus of elasticity of AASC mixes reinforced with 3D, 4D and 5D fibres in different fibre volume fractions. The incorporation of hooked-end steel fibres enhances the

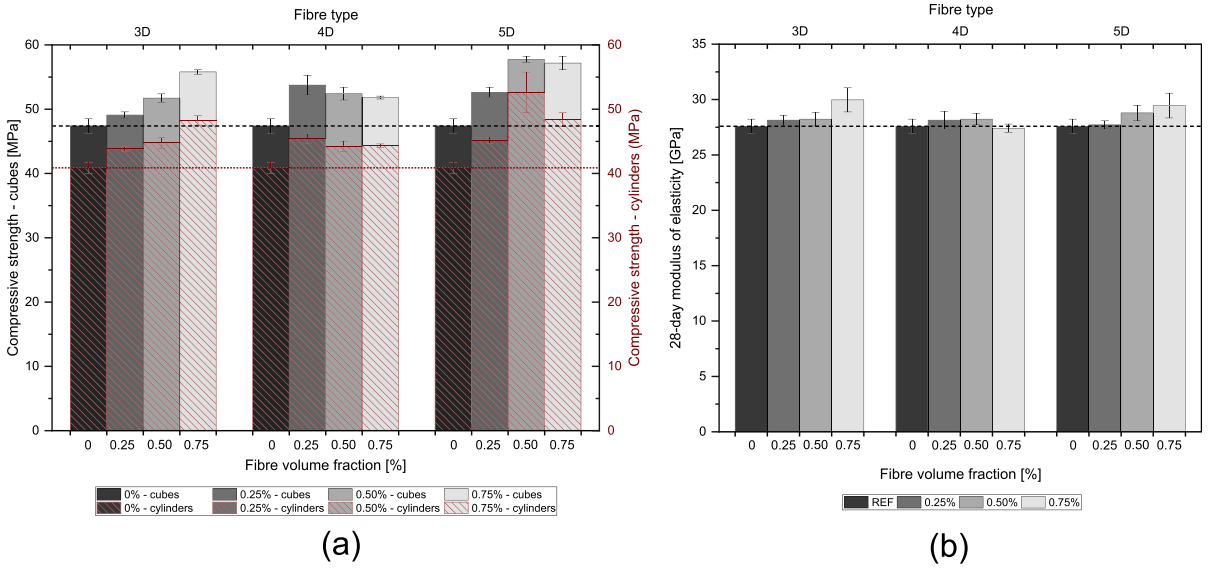

Fig. 4 28-day mean cubic and cylindrical compressive strength **a** and modulus of elasticity **b** of AASC reinforced with 3D, 4D and 5D steel fibres in different volume fractions

modulus of elasticity of the plain matrix, regardless of the fibre geometry and volume fraction. The modulus of elasticity increases with the increase of the fibre volume fraction, regardless of the fibre type. The slight increment of the modulus of elasticity with the incorporation of steel fibres up to 1% volume fraction can be attributed to the high stiffness of the fibres and the strong fibre-matrix interaction [14, 50]. The mix AASC-4D75 is the only exception in the present study. The decrease of the modulus of elasticity with the increase of the fibre volume fraction from 0.50 to 0.75% can be due to fibre distribution and orientation, which affect the porosity of the composite [14, 50], resulting in a negative effect on the modulus of elasticity.

3.2 Stress–strain behaviour under uniaxial compression

The compressive stress–strain response of fibre-reinforced alkali-activated concrete is linear and similar to that of plain concrete up to a stress corresponding to around 40% of the peak stress, as shown in Fig. 5. Micro-cracks start forming and propagating as the stresses increase, marginally activating the crack-bridging capacity of the hooked-end steel fibres. However, steel fibres have a minimal effect on the pre-peak ascending branch of the stress–strain curve, regardless of the fibre geometry and volume fraction. As stresses approach the maximum stress $\sigma_{c,max}$, the isolated micro-cracks formed start propagating in an unpredictable way, due to the material inhomogeneity and the presence of fibres, leading to the formation of several macro-cracks. For the unreinforced mixture, once the maximum compressive stress is reached, the load-bearing capacity of the material decreases rapidly, resulting in a quasi-brittle behaviour corresponding to a steep post-peak descending branch of the diagram. Fibre-reinforced mixtures exhibit a softer post-peak descending branch as a result of the transverse confinement effect of the hooked-end steel fibres [38].

Figure 5 shows the experimental stress–strain curves obtained for AASC reinforced with 3D, 4D and 5D fibres in different volume fraction. The incorporation of hooked-end steel fibres, regardless of the fibre geometry and volume fraction, enhances both the peak stress ($\sigma_{c,max}$) and corresponding strain ($\varepsilon_{c,max}$) of the composites in comparison to the reference concrete, as also shown in Fig. 6a, b.

The compressive peak stress increment has no clear correlation to the fibre content variation, but it follows the same trend observed for the compressive strength as shown in Fig. 4a. The corresponding peak strain increases with the increase of the fibre volume fraction, achieving the highest values at the highest fibre volume fraction, regardless of the fibre geometry. The incorporation of hooked-end steel fibres at a volume fraction of 0.75% enhances the compressive peak strain of the plain matrix by 22.5%, 28.8% and 21.6%, for 3D, 4D and 5D fibres, respectively. The increase in value of $\varepsilon_{c,max}$ leads to a reduction of the initial secant modulus E_{it} and the secand modulus E_{sec} in comparison to the reference mix, as shown in Fig. 6c. However, the increased strain corresponding to the peak stress coupled with the softer post-peak descending branch of the stress–strain response

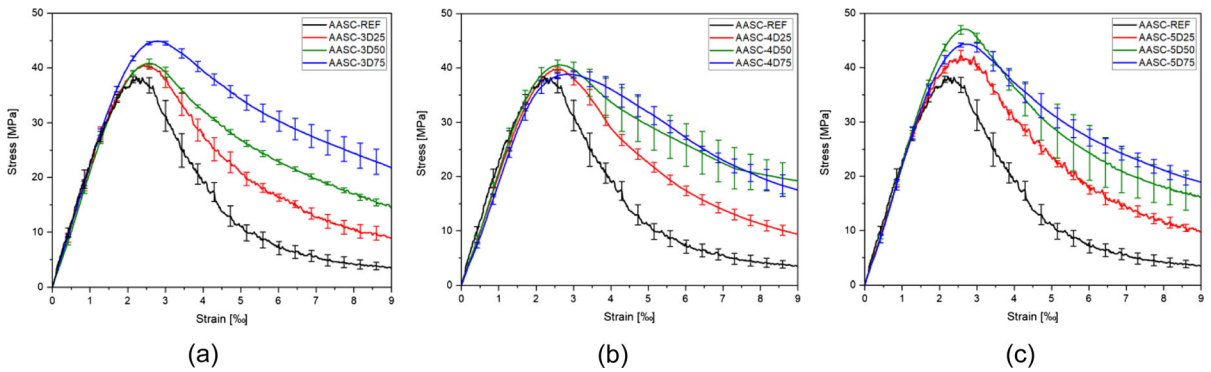

Fig. 5 Experimental stress–strain curves obtained for AASC reinforced with **a** 3D fibres, **b** 4D fibres and **c** 5D fibres in different fibre volume fractions

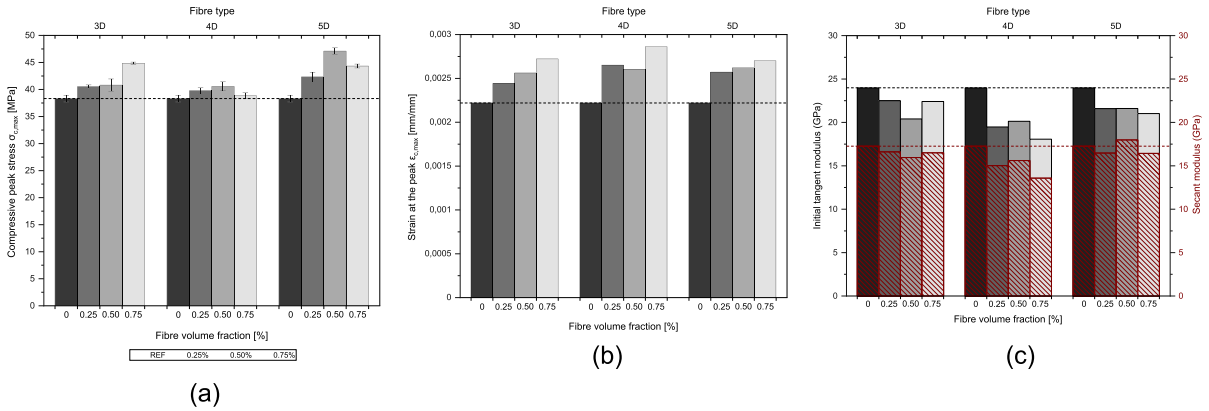

Fig. 6 Effect of fibre geometry and content on **a** the compressive peak stress, **b** the strain at the peak and **c** the secant and initial secant moduli

demonstrates the improved ductility of the material when reinforced with hooked-end steel fibres.

3.3 Comparison with fibre-reinforced Portland cement concrete (FRPCC)

3.3.1 Compressive strength and modulus of elasticity

Figure 7a shows the cubic and cylindrical compressive strength of PCC mixes reinforced with different hooked-end steel fibres at different fibre volume fractions. Although the PCC reference mix shows similar mean cubic compressive strength as AASC, 49.46 MPa and 47.40 MPa, respectively, the incorporation of hooked-end steel fibres shows a different behaviour in the two matrix types. In contrast to FRAASC (see Fig. 4a), hooked-end steel fibres have a limited effect on the compressive strength of PCC. AASC mixes show an increment of strength in comparison to the reference mix up to 21.8% (AASC-5D50), while PCC mixes achieve a maximum increment of only 1.54% (PCC-5D75). A similar

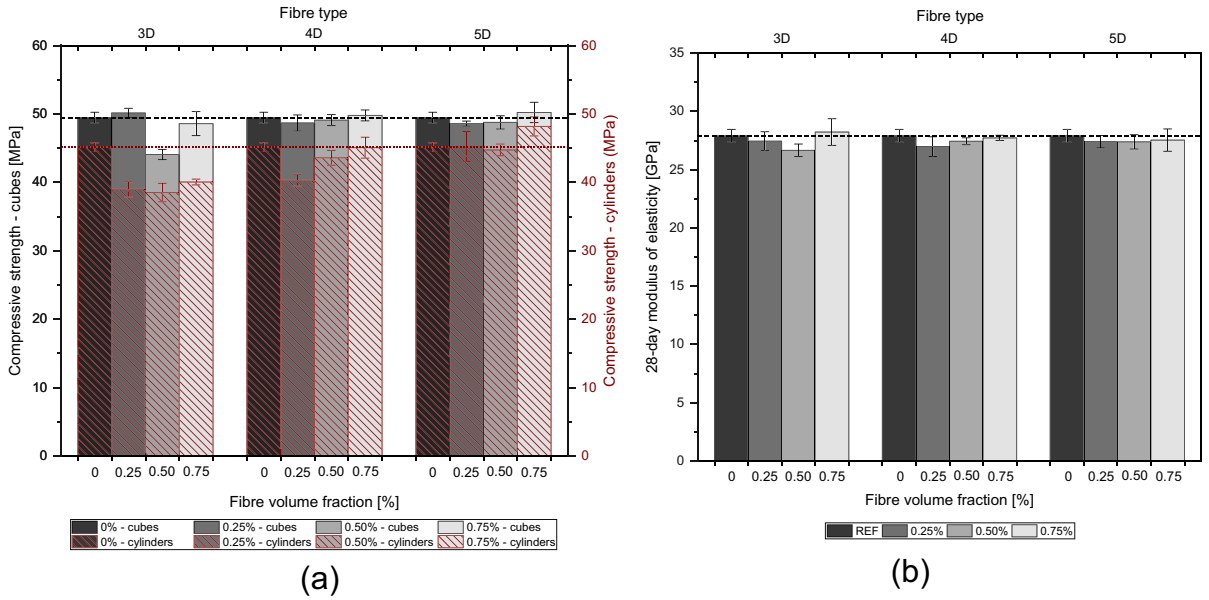

Fig. 7 28-day mean cubic and cylindrical compressive strength **a** and modulus of elasticity **b** of PCC reinforced with 3D, 4D and 5D steel fibres in different volume fractions

behaviour for PCC was reported also by Lee et al. [27], in which the incorporation of 3D, 4D and 5D fibres does not significantly affect the compressive strength values up to a volume fraction of 1%.

Beglarigale et al. [51] demonstrated that alkali-activated slag composites reinforced with hooked-end steel fibres exhibit superior bond strength compared to traditional PCC. The improved fibre-matrix interaction can be attributed to the higher shrinkage behaviour of AASC in comparison to PCC. The higher shrinkage in AASC matrix generates a hydrostatic pressure around the fibre, improving the fibre-matrix bond [51]. In addition, the stresses generated by the shrinkage-induced micro-cracking provide an early activation of the steel fibres, resulting in improved mechanical performance of AASC when compared to PCC. As for FRAASC (Sect. 3.1), the correlation between cubic and cylindrical compressive strength of PCC reinforced with single and multiple hooked-end steel fibres is evaluated and discussed in the supplementary information.

Figure 7b shows the 28-day mean modulus of elasticity of PCC mixes reinforced with single and multiple hooked-end steel fibres in different volume fractions. Although the PCC-REF mix shows similar modulus of elasticity as AASC-REF, 27.91 GPa and 27.58 GPa, respectively, hooked-end steel fibres have a different effect on the two matrices. For AASC, the modulus of elasticity increases with the increase of the fibre volume fraction (Fig. 4b), with AASC-3D75 achieving the highest value of 29.96 GPa (+ 8.6% than AASC-REF). For PCC mixes, the incorporation of steel fibres leads to a reduction of the modulus of elasticity in comparison to the reference mix, with only the PCC-3D75 mix showing an increase of 1.15%. The modulus of elasticity is mainly dependent on the coarse aggregate type and content and the compressive strength of the matrix, with fibres playing a minor role [52]. However, hooked-end steel fibres have a more positive effect on the modulus of elasticity of AASC than PCC. As the coarse aggregates type and amount is kept constant in AASC and PCC mixtures, the increase of modulus of elasticity provided by the hooked-end steel fibres in AASC composites can be related to the enhanced compressive strength of the composite caused by the stronger fibre-matrix bond and to the higher shrinkage of the AASC matrix in comparison to traditional concrete [51], as previously explained.

3.3.2 *Stress–strain under uniaxial compression*

Figure 8 shows the experimental stress–strain curves obtained for PCC mixtures reinforced with 3D, 4D and 5D fibres in different volume fractions and the direct comparison with AASC. Hooked-end steel fibres have a limited effect on the compressive peak stress and corresponding peak strain of PCC composites, with only the mixtures reinforced with 0.75% fibre volume fraction showing minimal improvements. For lower fibre contents the fibre incorporation has a negligible or even negative effect on these parameters in comparison to the reference plain concrete. However, a significant enhancement of the residual stress at higher strain values can be seen for PCC matrix for all the fibres types, with the higher fibre volume fraction and fibre bends providing the highest residual compressive stress at ultimate strain, corresponding to a softer post-peak descending branch in the stress–strain diagram.

Figure 9a, c show the correlations between the peak stress and the corresponding strain of both PCC and AASC mixes with the fibre reinforcing index RI_v, respectively. Although the peak compressive stress increases with the increase of the fibre reinforcing index from 0.167 to 0.50 (Fig. 9a) for both AASC and PCC, AASC mixes show higher values than PCC, regardless of the fibre geometry. When the strain corresponding to the peak stress is considered (Fig. 9c), PCC mixes show higher values than AASC at $RI_v = 0.50$. However, to evaluate the contribution of hooked-end steel fibres on the compressive stress–strain response of both AASC and PCC mixes, the $\sigma_{c,max(FRC)}/\sigma_{c,max(REF)}$ and the $\varepsilon_{c,max(FRC)}/\varepsilon_{c,max(REF)}$ ratios need to be considered. $\sigma_{c,max(FRC)}/\sigma_{c,max(REF)}$ represents the ratio between the peak stress of the mix incorporating steel fibres ($\sigma_{c,max(FRC)}$) and the peak stress of the reference concrete ($\sigma_{c,max(REF)}$), while $\varepsilon_{c,max(FRC)}/\varepsilon_{c,max(REF)}$ represents the ratio of the value of the strain corresponding to the peak stress of fibre-reinforced and reference mixes, respectively. As shown in Fig. 9b, hooked-end steel fibres have a positive effect on the compressive peak stress of AASC, as the $\sigma_{c,max(FRC)}/\sigma_{c,max(REF)}$ ratio is higher than 1, regardless of the fibre geometry and reinforcing index. For PCC mixes, only the mixes containing 4D and 5D fibres in volume fractions higher than 0.25% show values of $\sigma_{c,max(FRC)}/\sigma_{c,max(REF)}$ higher than 1.

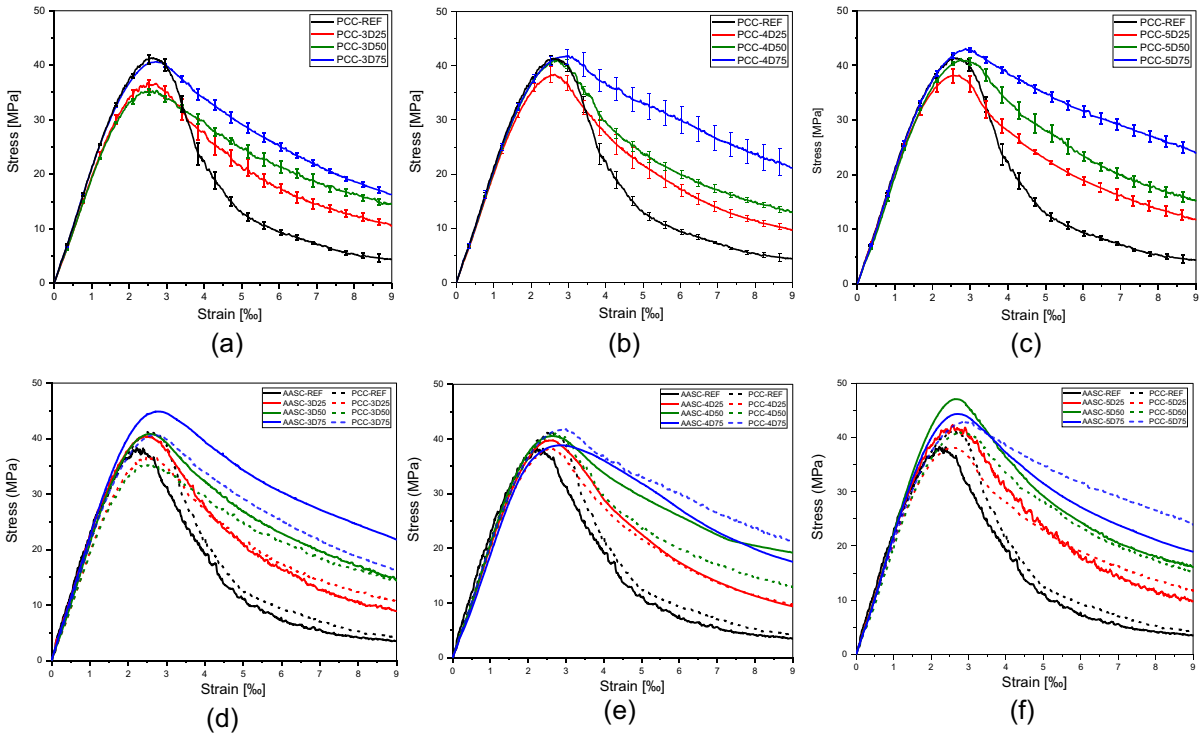

Fig. 8 Experimental stress–strain curves of PCC mixes reinforced with **a** 3D, **b** 4D and **c** 5D hooked-end steel fibres in different volume fractions and direct comparison with AASC reinforced with **d** 3D, **e** 4D and **f** 5D fibres

The incorporation of 3D fibres in volume fractions up to 0.75% has no beneficial effect on the compressive peak stress of the PCC matrix.

As shown in Fig. 9d, the incorporation of hooked-end steel fibres has a beneficial effect on the compressive strain corresponding to the peak stress, as the value of the ratio between the strain corresponding to the peak of the mixes incorporating steel fibres and the reference mix ($\varepsilon_{c,max(FRC)}/\varepsilon_{c,max(REF)}$) is higher than 1 for both PCC and AASC, regardless of the fibre geometry and volume fraction. However, in comparison to PCC, AASC mixes show a higher increment of strain corresponding to peak stress in comparison to the reference matrix when steel fibres are added, indicating a higher ductility. The higher ductility of the steel fibre-reinforced AASC mixes in comparison to PCC can be better seen in Fig. 9e, f. The value of the stress corresponding to the ultimate strain of 0.0035 ($\sigma_{c,u(FRC)}$) (Fig. 9e) gives an indication of the slope of the post-peak descending branch of the stress–strain curve, where higher values of $\sigma_{c,u(FRC)}$ correspond to softer descending curves and higher ductility. To isolate the effect of fibre geometry and reinforcing index on the ductility of the composite, the values of $\sigma_{c,u(FRC)}$ are normalised to the values of the reference mix ($\sigma_{c,u(REF)}$) and are shown in Fig. 9f. Although the values of the $\sigma_{c,u(FRC)}/\sigma_{c,u(REF)}$ ratio are higher than 1 for both AASC and PCC, AASC mixes show a higher increment of ductility in comparison to the reference mix for each fibre type and volume fraction than PCC.

4 Analytical modelling of the stress–strain behaviour

4.1 Model description and calibration

Currently available models to predict the stress–strain under uniaxial compression of fibre-reinforced concrete (Table 1) cannot be applied to PCC and AASC reinforced with single and multiple hooked-end steel fibres. This is because these models are derived and calibrated using a limited number of experimental data and they are strictly dependent on the fibre type, dosage and matrix strength investigated. Furthermore,

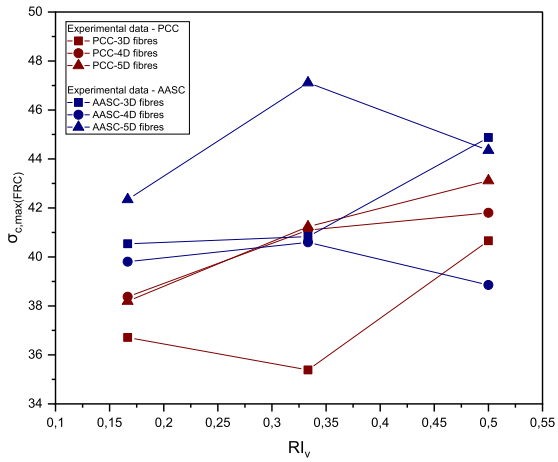
Experimental data - PCC
PCC-3D fibres
PCC-4D fibres
PCC-5D fibres
Experimental data - AASC
AASC-3D fibres
AASC-4D fibres
AASC-5D fibres
σc,max(FRC)
RIv

(a)

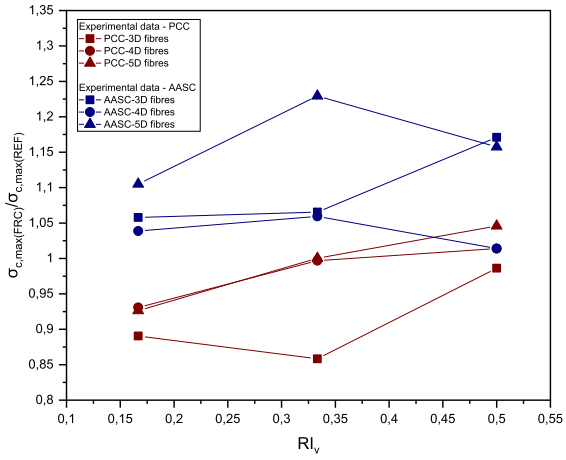
Experimental data - PCC
PCC-3D fibres
PCC-4D fibres
PCC-5D fibres
Experimental data - AASC
AASC-3D fibres
AASC-4D fibres
AASC-5D fibres
σc,max(FRC)/σc,max(REF)
RIv

(b)

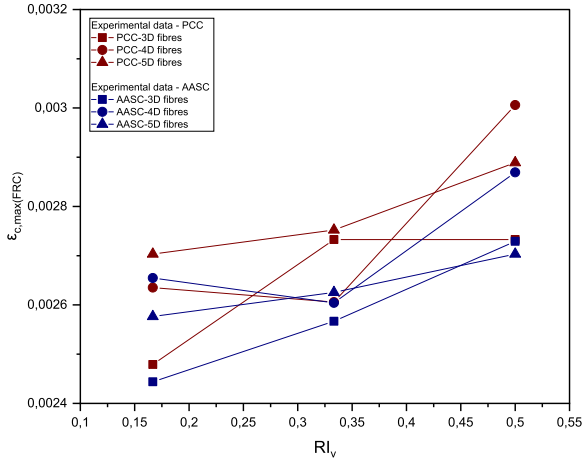
Experimental data - PCC
PCC-3D fibres
PCC-4D fibres
PCC-5D fibres
Experimental data - AASC
AASC-3D fibres
AASC-4D fibres
AASC-5D fibres
εc,max(FRC)
RIv

(c)

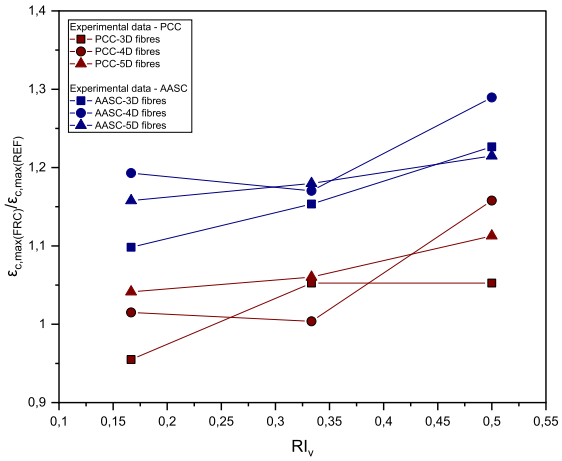
Experimental data - PCC
PCC-3D fibres
PCC-4D fibres
PCC-5D fibres
Experimental data - AASC
AASC-3D fibres
AASC-4D fibres
AASC-5D fibres
εc,max(FRC)/εc,max(REF)
RIv

(d)

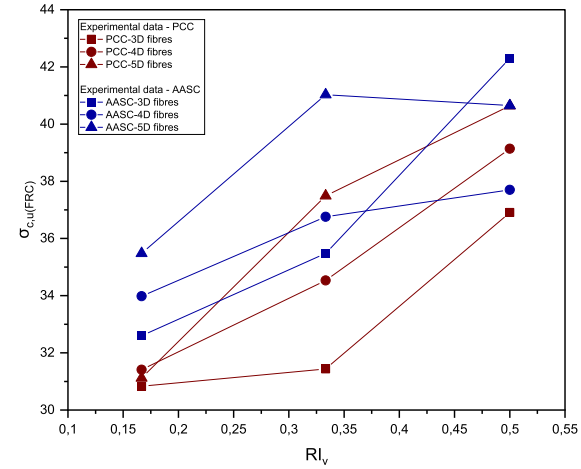
Experimental data - PCC
PCC-3D fibres
PCC-4D fibres
PCC-5D fibres
Experimental data - AASC
AASC-3D fibres
AASC-4D fibres
AASC-5D fibres
σc,u(FRC)
RIv

(e)

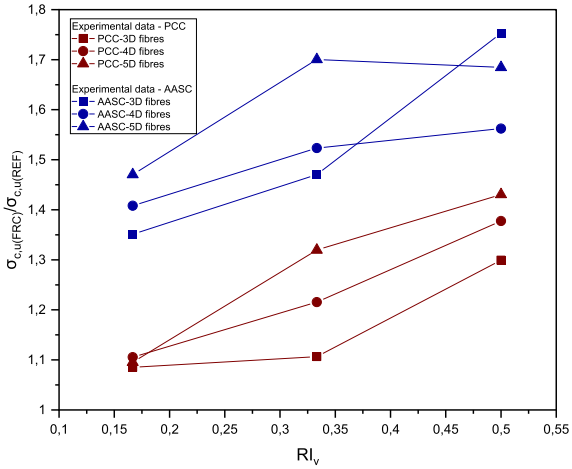
Experimental data - PCC
PCC-3D fibres
PCC-4D fibres
PCC-5D fibres
Experimental data - AASC
AASC-3D fibres
AASC-4D fibres
AASC-5D fibres
σc,u(FRC)/σc,u(REF)
RIv

(f)

◀**Fig. 9** Comparison of the correlation between reinforcing index RI_v and: **a** the peak stress $\sigma_{c,max(FRC)}$, **b** the $\sigma_{c,max(FRC)}/\sigma_{c,max(REF)}$ ratio, **c** the strain corresponding to the peak stress $\varepsilon_{c,max(FRC)}$, **d** the $\varepsilon_{c,max(FRC)}/\varepsilon_{c,max(REF)}$ ratio, **e** the stress $\sigma_{c,u(FR)}$ corresponding to a strain of 0.0035 and **f** the $\sigma_{c,u(FRC)}/\sigma_{c,u(REF)}$ ratio for both PCC and AASC

most of the available models are based on a single equation, neglecting the difference in the effect of steel fibres incorporation on the pre-and post-peak response of the compressive stress–strain curves. This provides an overestimation of the compressive behaviour in both the pre- and post-peak phases.

Figure 10 shows the experimental stress–strain curves obtained for the plain AASC and the mixes reinforced with 3D, 4D and 5D fibres at 0.75% fibre volume fraction and the predicted curves obtained applying the models developed to alkali-activated concrete (Table 1). The model developed by Hardjito et al. [39] can predict the response of plain alkali-activated slag-based concrete quite accurately (Fig. 10a), while the models proposed by Noushini et al. [41] and Cong et al. [42], highly under- or overestimate, respectively, the post-peak descending branch of the curve. However, all the models are unable to predict the post-peak behaviour of AASC incorporating single and multiple hooked-end steel fibres, as shown in Fig. 10b–d, as the

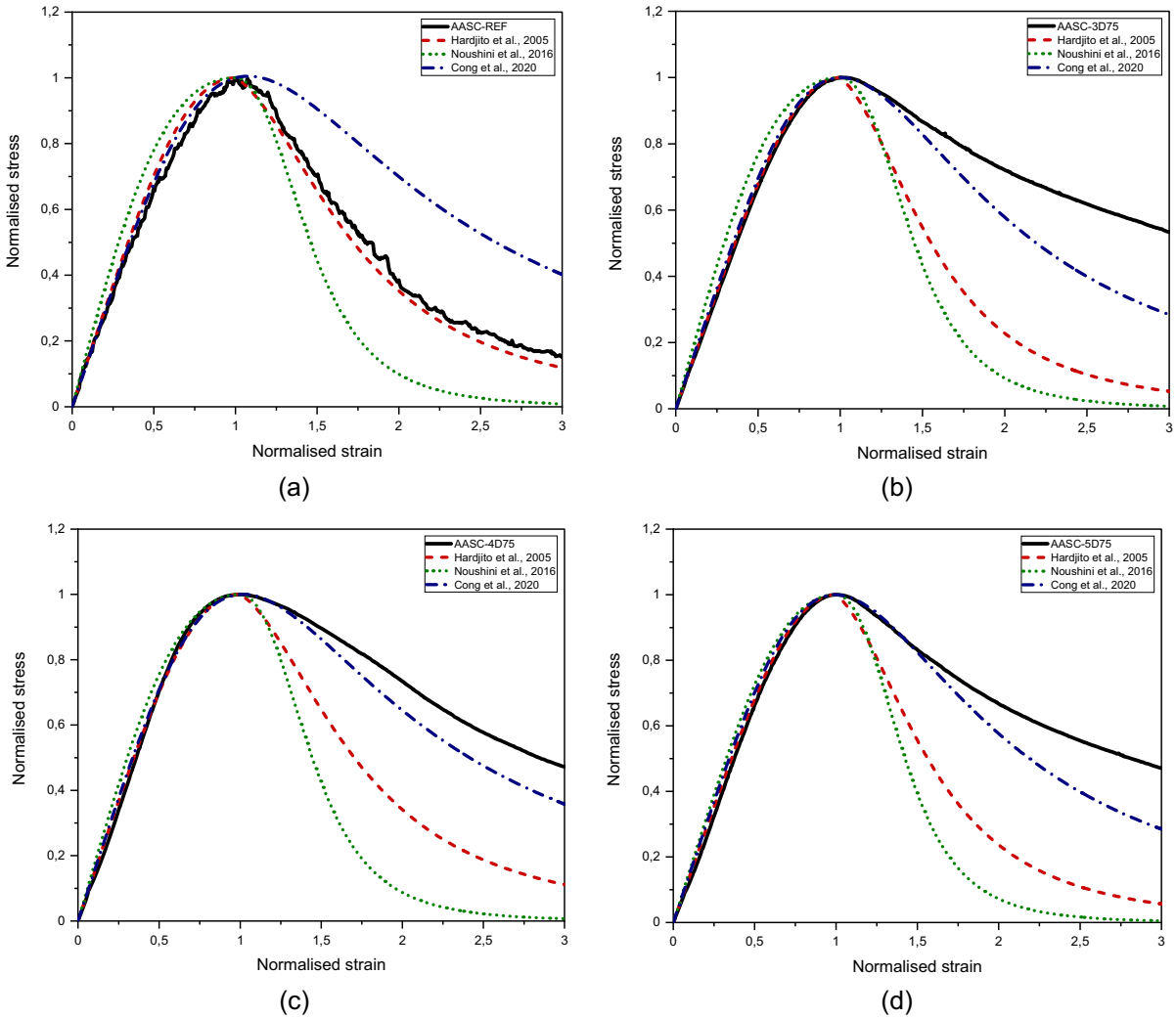

Fig. 10 Experimental and predicted stress–strain curves according to current models developed for alkali-activated concrete for **a** AASC-REF, **b** AASC-3D75, **c** AASC-4D75 and **d** AASC-5D75

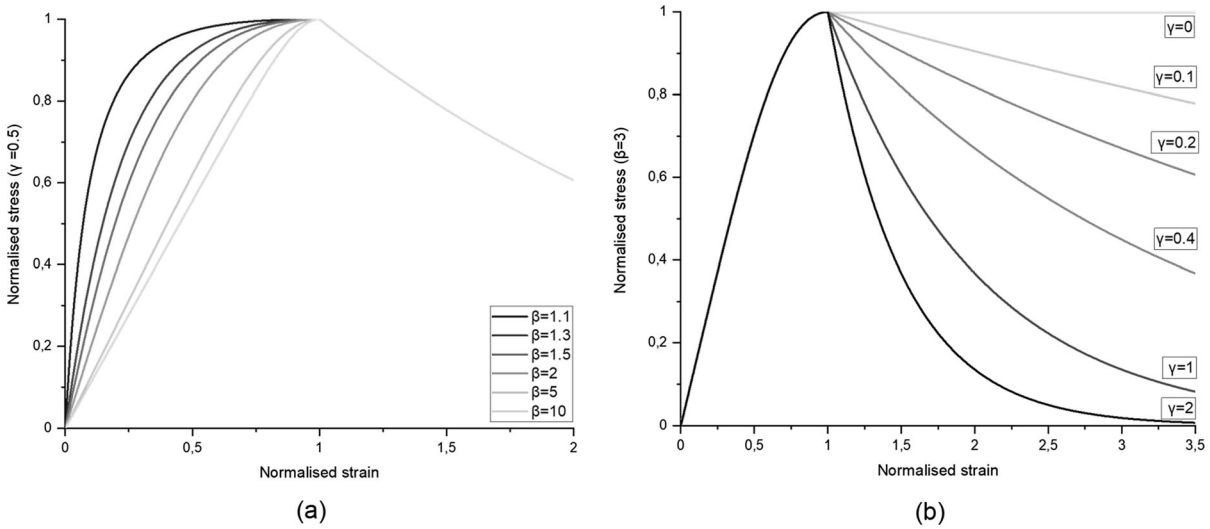

Fig. 11 Effect of the material parameters **a** β and **b** γ on the compressive stress–strain curve of fibre-reinforced concrete

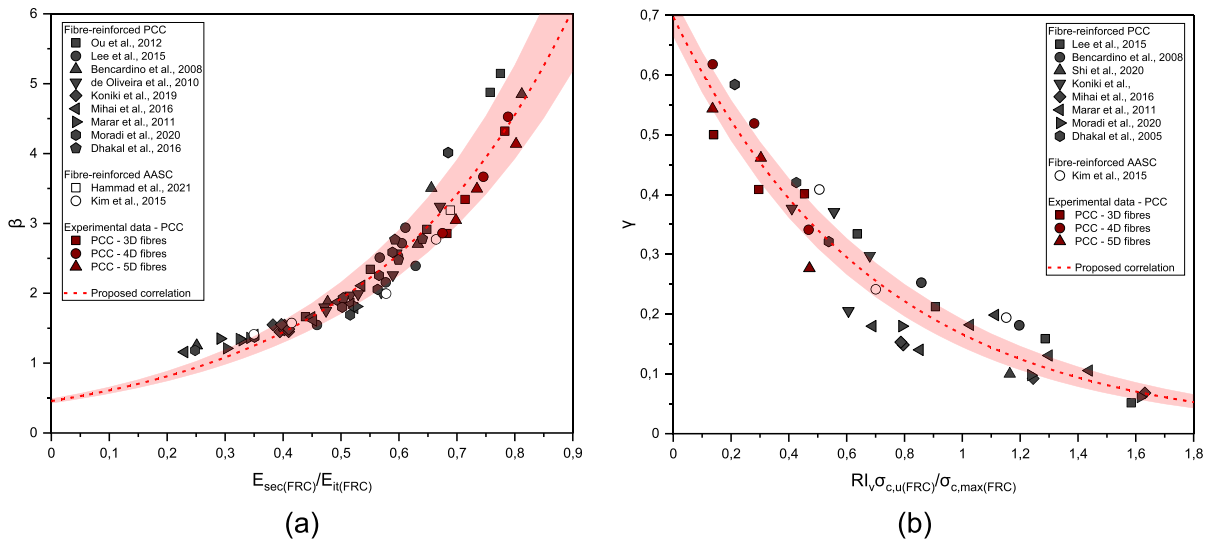

Fig. 12 Proposed correlations to derive the values of **a** β and **b** γ. The shaded areas represent the 95% confidence interval of the parameters of Eq. (3) and (4), respectively

effect of fibre incorporation is not considered in these models.

For this reason, a new analytical model is proposed, which describes the normalised ascending and descending branches of the stress–strain curve through two analytical expressions. In the proposed model, the pre-peak response is based on the function proposed by Ezeldin and Balaguru [35]. The post-peak descending branch is modelled using an exponential decay equation, which has been commonly used in the past to describe the post-cracking softening behaviour of unreinforced concrete [53]. The final analytical expression of the proposed model is given in Eq. 2.

$$\frac{\sigma_c}{\sigma_{c,\max(\mathrm{FRC})}} = \begin{cases} \dfrac{\beta\left(\varepsilon_c/\varepsilon_{c,\max(\mathrm{FRC})}\right)}{\beta - 1 + \left(\varepsilon/\varepsilon_{c,\max(\mathrm{FRC})}\right)^{\beta}} & \varepsilon/\varepsilon_{c,\max(\mathrm{FRC})} \le 1 \\ e^{\gamma\left(1-\varepsilon_c/\varepsilon_{c,\max(\mathrm{FRC})}\right)} & \varepsilon/\varepsilon_{c,\max(\mathrm{FRC})} > 1 \end{cases} \quad (2)$$

where σ_c is the compressive stress and ε_c is the corresponding strain, $\sigma_{c,\max(\mathrm{FRC})}$ is the maximum

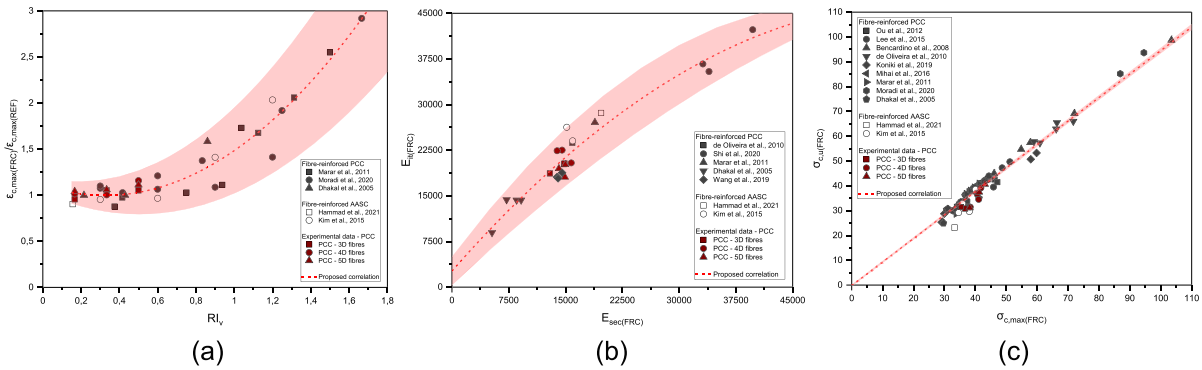

Fig. 13 Proposed correlations to derive the values of **a** $\varepsilon_{c,max(FRC)}$, **b** $E_{it(FRC)}$ and **c** $\sigma_{c,u(FRC)}$. The shaded areas represent the 95% confidence interval of the parameters of Eqs. (7), (8) and (9), respectively

compressive stress of the composite and $\varepsilon_{c,max(FRC)}$ is the corresponding peak strain, β and γ are material parameters governing the pre-peak and post-peak behaviour, respectively, as shown in Fig. 11. The parameter β controls the ascending pre-peak branch of the stress–strain curve, where fibres play a minimal role. Hence the parameter β is only dependent on the ratio between the secant modulus E_{sec} and the initial secant modulus E_{it} of the composite. Increasing values of β corresponds to decreasing steepness of the ascending branch. The parameter γ governs the steepness of the post-peak descending branch. Values of γ increasing from the 0 to ∞ represent the variation of material behaviour from perfectly plastic to brittle, respectively.

The proposed model was calibrated on a wide range of stress–strain curves available in the literature for steel fibre-reinforced PCC [32, 33, 38, 47, 54–60], AASC composites [21, 43] and the experimental results obtained in this study for PCC mixes reinforced with single and multiple hooked-end steel fibres. The objective function used for the model calibration is defined as the absolute value of the difference between the experimental data and the predicted values obtained applying the proposed model equations. Minimising this objective function provides the values of the parameter β and γ for each stress–strain curve

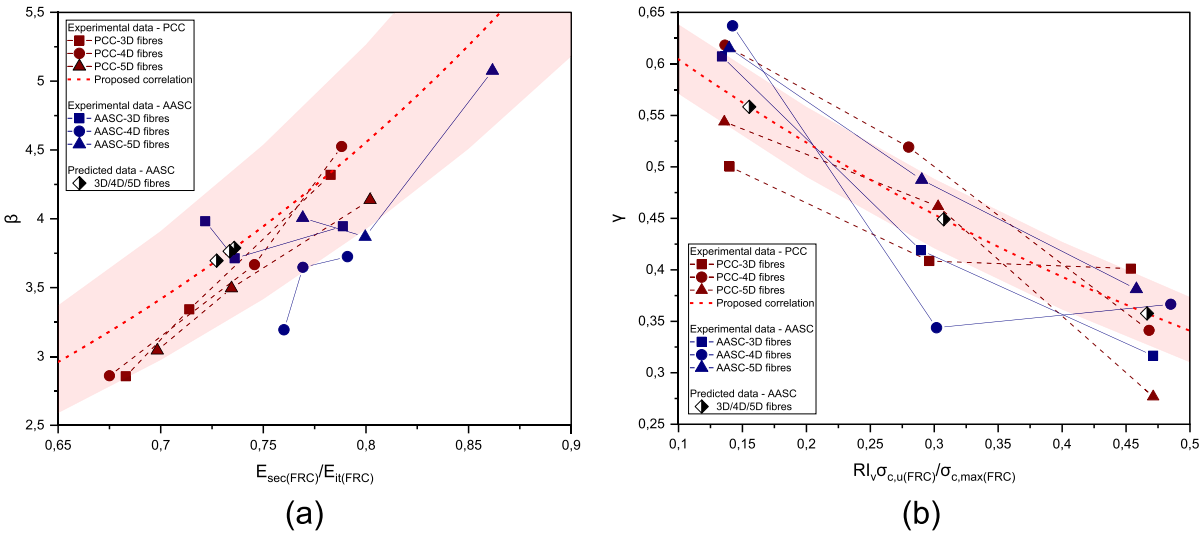

Fig. 14 Values of the parameters **a** β and **b** γ obtained by fitting the experimental data for both fibre-reinforced PCC and AASC and the predicted values of AASC used for the model validation. The shaded areas represent the 95% confidence interval of the parameters of Eqs. (3) and (4), respectively

considered. The minimisation is carried out using the Generalised Reduced Gradient (GRG) non-linear optimisation algorithm available in the Microsoft Excel® Solver add-in. The collected values of β and γ were then correlated to the parameters governing the pre- and post-peak responses. These parameters are E_{it} and E_{sec} for the ascending branch, while for the descending branch the fibre reinforcing index (RI_v) and the ultimate stress corresponding to a strain of 0.0035, defined in the Eurocode 2 as the ultimate compressive strain in plain PCC ($\sigma_{c,u}$). The proposed correlations of the material parameters β and γ with E_{it}, E_{sec} and RI_v are defined by Eq. (3) and (4) and shown in Fig. 12.

$$\beta = (0.457 \pm 0.030)e^{(2.874\pm0.100)\left(E_{\mathrm{sec(FRC)}}/E_{\mathrm{it(FRC)}}\right)} \quad \left(\mathrm{R}^2 = 0.926\right) \tag{3}$$

$$\gamma = (0.697 \pm 0.032)e^{(-1.432\pm0.092)\left(\mathrm{RI_v}\sigma_{c,u(\mathrm{FRC})}/\sigma_{c,\max(\mathrm{FRC})}\right)} \quad \left(R^2 = 0.901\right) \tag{4}$$

As shown in Fig. 12a, the values of the material parameter β obtained by fitting the proposed model to the stress–strain curves available in the literature for both steel fibre-reinforced PCC and AASC and the experimental curves obtained in this study for PCC fall in the range of the confidence interval of the proposed Eq. (3). Greater variability in the values of parameter γ can be seen in Fig. 12b. Finally, correlations can be established between $\sigma_{\mathrm{c,max(FRC)}}$, $\varepsilon_{\mathrm{c,max(FRC)}}$ and $E_{it(FRC)}$ of the steel fibre-reinforced composite and $\sigma_{c,max(REF)}$, $\varepsilon_{c,max(REF)}$ and $E_{it(REF)}$ of the reference concrete. These correlations between unreinforced concrete and the fibre-reinforced composite are summarised below and shown in Fig. 13:

$$E_{sec(FRC)} = \sigma_{\mathrm{c,max(FRC)}}/\varepsilon_{c,amx(FRC)} \tag{5}$$

$$\sigma_{c,\max(\mathrm{FRC})} = \sigma_{c,\max(\mathrm{REF})} + 4.8853\mathrm{RI_v} \quad \left(R^2 = 0.935\right) \tag{6}$$

$$\varepsilon_{c,\max(\mathrm{FRC})}/\varepsilon_{c,\max(\mathrm{REF})} = 1.064\mathrm{RI_v^2} - 0.689\mathrm{RI_v} + 1.109 \quad \left(R^2 = 0.915\right) \tag{7}$$

$$E_{it(\mathrm{FRC})} = -0.0000114E^2_{\mathrm{sec(FRC)}} + 1.418E_{\mathrm{sec(FRC)}} + 2625.13 \quad \left(R^2 = 0.929\right) \tag{8}$$

Furthermore, the value of $\sigma_{c,u(FRC)}$ is defined as follows:

$$\sigma_{c,u(\mathrm{FRC})} = 0.9927\sigma_{c,\max(\mathrm{FRC})} - 2.317 \quad \left(R^2 = 0.977\right) \tag{9}$$

Figure 13 shows the fitted correlations for $\varepsilon_{\mathrm{c,max(FRC)}}$, $E_{it(FRC)}$ and $\sigma_{c,u(FRC)}$. Despite the limited amount of data for alkali-activated slag-based concrete available in the literature, the proposed correlations (Eqs. (6)–(9)) are able to capture the values obtained for both PCC and AASC reinforced with steel fibres, especially the values obtained experimentally for PCC reinforced with novel hooked-end steel fibres.

Table 5 Fitted and predicted values of the parameters β and γ for AASC mixes reinforced with 3D, 4D and 5D fibres

Mix	β-fitted	β-predicted	γ-fitted	γ-predicted
AASC-3D25	3.982	3.696	0.607	0.558
AASC-3D50	3.713	3.789	0.419	0.449
AASC-3D75	3.946	3.764	0.317	0.358
AASC-4D25	3.194	3.696	0.637	0.558
AASC-4D50	3.648	3.789	0.344	0.449
AASC-4D75	3.725	3.764	0.366	0.358
AASC-5D25	4.007	3.696	0.615	0.558
AASC-5D50	3.870	3.789	0.487	0.449
AASC-5D75	5.077	3.764	0.381	0.358

4.2 Model validation

Figure 14 shows the values of the parameters β and γ obtained by fitting the experimental stress–strain curves of both fibre-reinforced PCC and AASC and the predicted values of β and γ for fibre-reinforced AASC obtained by using the proposed model. Although the predicted values of $E_{\mathrm{sec}(FRC)}/E_{it(FRC)}$ for fibre-reinforced AASC is slightly underestimated by the proposed correlation (Fig. 14a), the predicted values of β fall in the range of the fitted values, i.e. between 3.2 and 5.1.

Due to the lack of available experimental stress–strain curves for steel FRAASC, the fitted values of the parameter γ do not fall in the confidence interval proposed (Fig. 14b). Table 5 shows the fitted and

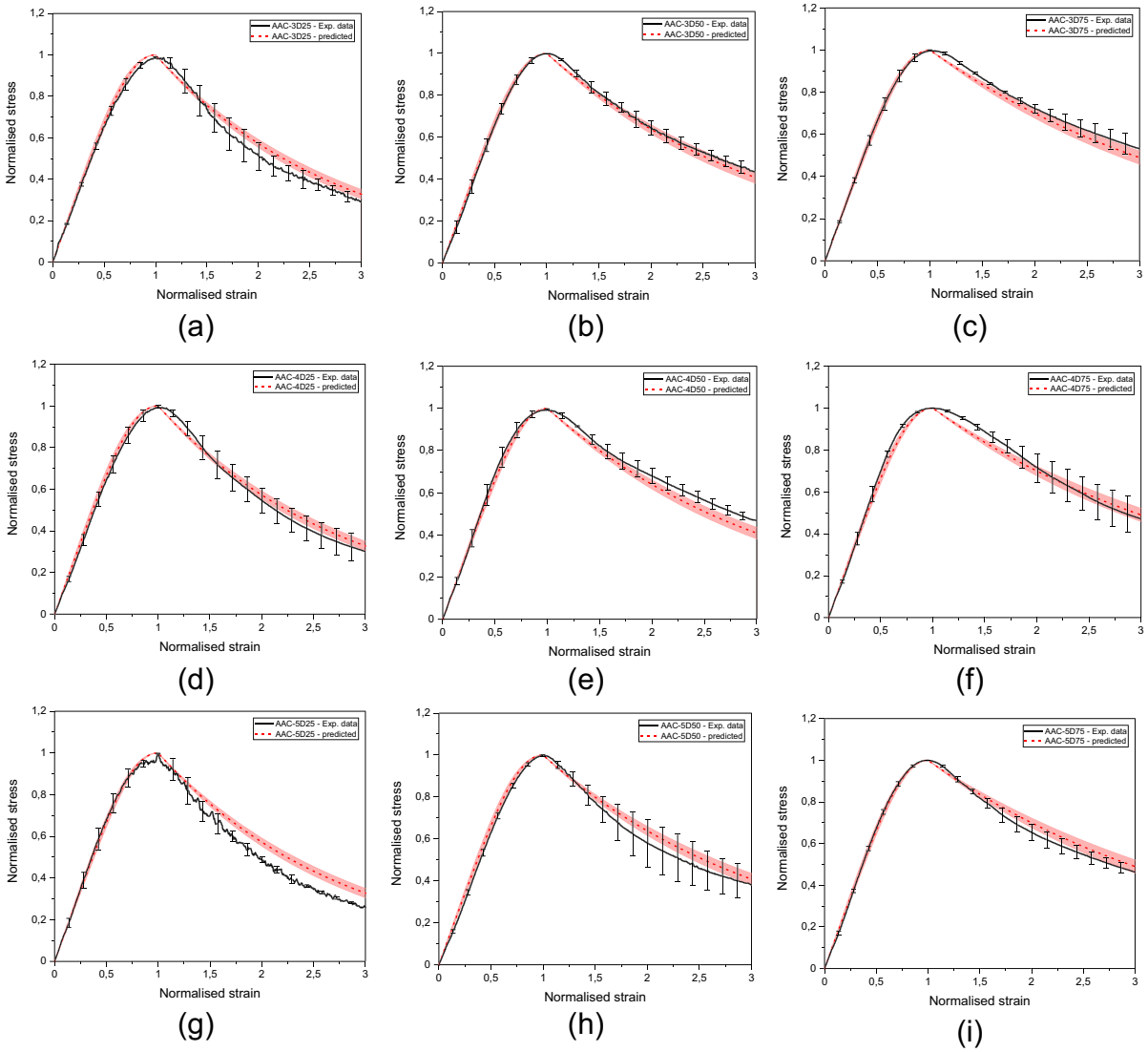

Fig. 15 Experimental and predicted stress–strain curves for AASC reinforced with **a–c** 3D, **d–f** 4D and **g–i** 5D fibres in different volume fractions. The shaded areas represent the 95% confidence interval of the parameters of fitting curves

predicted values of the parameters β and γ for AASC reinforced with single and multiple hooked-end steel fibres in different fibre volume fractions.

As shown in Fig. 14 and Table 5, only three different values of the parameters β and γ are used to predict the compressive stress–strain response of the AASC mixes reinforced with three different fibre types investigated in this study. Although 3D, 4D and 5D fibres differ for the number of bends at both ends of the fibre, they have the same aspect ratio (l_f/d_f), resulting in the same values of fibre reinforcing index ($(l_f/d_f) \bullet v_f$) for each fibre type. Although the fibre geometry is not taken into account, the proposed model is able to predict the compressive stress–strain response of steel fibre-reinforced AASC mixes quite accurately.

Knowing only the behaviour of the plain reference concrete under uniaxial compression and the fibre volumetric reinforcing index, the proposed model can predict the compressive response of steel fibre-reinforced composites, regardless of the matrix type and the fibre geometry and content. To verify this, the experimental stress–strain curve obtained in this study

for AASC are predicted using the proposed model and the results shown in Fig. 15.

Although the proposed model can predict quite accurately the compressive response of fibre-reinforced AASC, additional experimental data might be needed to better differentiate the model parameters for alkali-activated slag-based concrete reinforced with different steel fibres geometries.

5 Conclusions

This study investigated experimentally the compressive behaviour of alkali-activated slag-based concrete reinforced with single and multiple hooked-end steel fibres, i.e. 3D, 4D and 5D, at different volume fractions up to 0.75%. The behaviour of steel fibre-reinforced AASC was compared with the same strength grade Portland cement concrete reinforced with the same fibre types and dosages. Finally, an analytical model is proposed and calibrated using the compressive stress–strain curves obtained for PCC, steel fibre-reinforced PCC and AASC available in the literature to predict the compressive response of steel FRAASC under uniaxial compression. The proposed model does not differentiate between matrix type (i.e. PCC and AASC) and fibre geometries. The following conclusions can be drawn from this study:

- The incorporation of single and multiple hooked-end steel fibres, regardless of the fibre geometry, provides a higher compressive strength increment for AASC (with a maximum of 21.8% for AASC-5D50) than PCC (with a maximum of 1.5% for PCC-5D75).
- Single and multiple hooked-end steel fibres have a limited effect on the modulus of elasticity of both AASC and PCC, with a maximum increment of up to 3 MPa. However, the incorporation of fibres in AASC shows a higher increase in the modulus of elasticity (with a maximum of 8.7% for AASC-3D75) than PCC mixes (with a maximum of 1.2% for PCC-3D75).
- The incorporation of single and multiple hooked-end steel fibres in AASC and PCC enhances the material ductility, which can be described by the $\varepsilon_{c,max(FRC)}/\varepsilon_{c,max(REF)}$ and $\sigma_{c,u(FRC)}/\sigma_{c,u(REF)}$ ratios. In comparison to the reference mix, both AASC and PCC show an increase of strain corresponding to the peak stress and stress at ultimate strain, resulting in softer post-peak descending branches of the compressive stress–strain curve. However, the improvement provided by the steel fibre incorporation is much more for AASC than PCC for all fibre geometries and volume fractions that were studied.

A model is proposed and calibrated on the stress-strain curves available in the literature for steel fibre-reinforced PCC and AASC in combination with the experimental data obtained in this study for PCC reinforced with 3D, 4D and 5D fibres in different volume fractions. The experimental compressive stress-strain curves obtained for AASC have been only used to validate the model, demonstrating the ability of the model to predict the stress-strain response under compression of steel fibre-reinforced AASC for different fibre content and fibre geometry. Only by knowing the compressive peak stress and corresponding strain of the concrete matrix and the fibre reinforcing index, all the model parameters can be calculated and the stress-strain curve predicted. It should be emphasised that due to the lack of available data in the literature for steel fibre-reinforced AASC, the calibration of the model proposed in this study mainly relies on the data for steel fibre-reinforced PCC. In addition, due to the lack of a significant amount of datasets on both AASC and PCC incorporating 4D and 5D steel fibres, the effect of the fibre geometry is not considered in the proposed model. With a wider amount of available datasets, this assumption may be revisited.

Acknowledgements This project has received funding from the European Union's Horizon 2020 research and innovation programme under Grant Agreement No 813596 DuRSAAM. The opinions expressed in this document reflect only the author's view and reflect in no way the European Commission's opinions. The European Commission is not responsible for any use that may be made of the information it contains.

Author contributions LR: Conceptualisation, Methodology, Validation, Formal analysis, Investigation, Writing—Original Draft. RAP: Conceptualisation, Methodology, Formal analysis, Writing—Review & Editing. FD: Resources, Supervision, Funding acquisition, Writing—Review & Editing.

Funding Open Access funding enabled and organized by Projekt DEAL.

Declarations

Conflict of interest The authors declare that they have no known financial interests or personal relationship that could have appeared to influence the subject matter or materials discussed in this manuscript.

References

1. Ding Y, Dai J-G, Shi C-J (2016) Mechanical properties of alkali-activated concrete: a state-of-the-art review. Constr Build Mater 127:68–79. https://doi.org/10.1016/j.conbuildmat.2016.09.121
2. Provis JL, Bernal SA (2014) Geopolymers and related alkali-activated materials. Annu Rev Mater Res 44(1):299–327. https://doi.org/10.1146/annurev-matsci-070813-113515
3. Provis JL, van Deventer JSJ (eds) (2014) Alkali activated materials: state-of-the-art report, RILEM TC 224-AAM, 1st edn. Springer, Dordrecht
4. Farhan NA, Sheikh MN, Hadi MN (2019) Investigation of engineering properties of normal and high strength fly ash based geopolymer and alkali-activated slag concrete compared to ordinary Portland cement concrete. Constr Build Mater 196:26–42. https://doi.org/10.1016/j.conbuildmat.2018.11.083
5. Amer I, Kohail M, El-Feky MS, Rashad A, Khalaf MA (2021) A review on alkali-activated slag concrete. Ain Shams Eng J 12(2):1475–1499. https://doi.org/10.1016/j.asej.2020.12.003
6. El-Hassan H, Elkholy S (2021) Enhancing the performance of Alkali-Activated Slag-Fly ash blended concrete through hybrid steel fiber reinforcement. Constr Build Mater 311:125313. https://doi.org/10.1016/j.conbuildmat.2021.125313
7. Thomas RJ, Peethamparan S (2015) Alkali-activated concrete: engineering properties and stress–strain behavior. Constr Build Mater 93:49–56. https://doi.org/10.1016/j.conbuildmat.2015.04.039
8. Ding Y, Dai J-G, Shi C-J (2018) Fracture properties of alkali-activated slag and ordinary Portland cement concrete and mortar. Constr Build Mater 165:310–320. https://doi.org/10.1016/j.conbuildmat.2017.12.202
9. Bernal SA, Mejía de Gutiérrez R, Pedraza AL, Provis JL, Rodriguez ED, Delvasto S (2011) Effect of binder content on the performance of alkali-activated slag concretes. Cem Concr Res 41(1):1–8. https://doi.org/10.1016/j.cemconres.2010.08.017
10. Chi M (2012) Effects of dosage of alkali-activated solution and curing conditions on the properties and durability of alkali-activated slag concrete. Constr Build Mater 35:240–245. https://doi.org/10.1016/j.conbuildmat.2012.04.005
11. Adesina A (2020) Performance of fibre reinforced alkali-activated composites—a review. Materialia 12:100782. https://doi.org/10.1016/j.mtla.2020.100782
12. Niş A, Eren NA, Çevik A (2021) Effects of nanosilica and steel fibers on the impact resistance of slag based self-compacting alkali-activated concrete. Ceram Int 47(17):23905–23918. https://doi.org/10.1016/j.ceramint.2021.05.099
13. Farhan NA, Sheikh MN, Hadi MNS (2018) Engineering properties of ambient cured alkali-activated fly ash-slag concrete reinforced with different types of steel fiber. J Mater Civ Eng. https://doi.org/10.1061/(ASCE)MT.1943-5533.0002333
14. Amran M, Fediuk R, Abdelgader HS, Murali G, Ozbakkaloglu T, Lee YH, Lee YY (2022) Fiber-reinforced alkali-activated concrete: a review. J Build Eng 45:103638. https://doi.org/10.1016/j.jobe.2021.103638
15. Ranjbar N, Zhang M (2020) Fiber-reinforced geopolymer composites: a review. Cem Concr Compos 107:103498. https://doi.org/10.1016/j.cemconcomp.2019.103498
16. Yuan X, Chen W, Lu Z, Chen H (2014) Shrinkage compensation of alkali-activated slag concrete and microstructural analysis. Constr Build Mater 66:422–428. https://doi.org/10.1016/j.conbuildmat.2014.05.085
17. Collins F, Sanjayan J (2001) Microcracking and strength development of alkali activated slag concrete. Cem Concr Compos 23(4–5):345–352. https://doi.org/10.1016/S0958-9465(01)00003-8
18. Bernal S, de Gutierrez R, Delvasto S, Rodriguez E (2010) Performance of an alkali-activated slag concrete reinforced with steel fibers. Constr Build Mater 24(2):208–214. https://doi.org/10.1016/j.conbuildmat.2007.10.027
19. Koenig A, Wuestemann A, Gatti F, Rossi L, Fuchs F, Fessel D, Dathe F, Dehn F, Minelli F (2019) Flexural behaviour of steel and macro-PP fibre reinforced concretes based on alkali-activated binders. Constr Build Mater 211:583–593. https://doi.org/10.1016/j.conbuildmat.2019.03.227
20. Shaikh FUA (2019) Pullout Behavior of Hook End Steel Fibers in Geopolymers. J Mater Civ Eng. https://doi.org/10.1061/(ASCE)MT.1943-5533.0002722
21. Hammad N, El-Nemr A, El-Deen Hasan H (2021) The performance of fiber GGBS based alkali-activated concrete. J Build Eng 42:102464. https://doi.org/10.1016/j.jobe.2021.102464
22. Abdallah S, Fan M, Rees DWA (2018) Bonding mechanisms and strength of steel fiber-reinforced cementitious composites: overview. J Mater Civ Eng. https://doi.org/10.1061/(ASCE)MT.1943-5533.0002154

23. Abdallah S, Rees DW, Ghaffar SH, Fan M (2018) Understanding the effects of hooked-end steel fibre geometry on the uniaxial tensile behaviour of self-compacting concrete. Constr Build Mater 178:484–494. https://doi.org/10.1016/j.conbuildmat.2018.05.191
24. Abdallah S, Fan M, Rees DW (2016) Analysis and modelling of mechanical anchorage of 4D/5D hooked end steel fibres. Mater Des 112:539–552. https://doi.org/10.1016/j.matdes.2016.09.107
25. Dehghani A, Aslani F (2021) Effect of 3D, 4D, and 5D hooked-end type and loading rate on the pull-out performance of shape memory alloy fibres embedded in cementitious composites. Constr Build Mater 273:121742. https://doi.org/10.1016/j.conbuildmat.2020.121742
26. Abdallah S, Fan M, Zhou X (2016) Effect of hooked-end steel fibres geometry on pull-out behaviour of ultra-high performance concrete. World Acad Sci Eng Technol Int J Civil Environ Eng. https://doi.org/10.5281/zenodo.1128020
27. Lee S-J, Yoo D-Y, Moon D-Y (2019) Effects of hooked-end steel fiber geometry and volume fraction on the flexural behavior of concrete pedestrian decks. Appl Sci 9(6):1241. https://doi.org/10.3390/app9061241
28. Venkateshwaran A, Tan KH, Li Y (2018) Residual flexural strengths of steel fiber reinforced concrete with multiple hooked-end fibers. Struct Concrete 19(2):352–365. https://doi.org/10.1002/suco.201700030
29. Abdallah S, Fan M, Zhou X, Le Geyt S (2016) Anchorage effects of various steel fibre architectures for concrete reinforcement. Int J Concr Struct Mater 10(3):325–335. https://doi.org/10.1007/s40069-016-0148-5
30. Chen G, Gao D, Zhu H, Song Yuan J, Xiao X, Wang W (2021) Effects of novel multiple hooked-end steel fibres on flexural tensile behaviour of notched concrete beams with various strength grades. Structures 33:3644–3654. https://doi.org/10.1016/j.istruc.2021.06.016
31. Nataraja MC, Dhang N, Gupta AP (1999) Stress–strain curves for steel-fiber reinforced concrete under compression. Cem Concr Compos 21(5–6):383–390. https://doi.org/10.1016/S0958-9465(99)00021-9
32. Oliveira Júnior LÁ de, Borges VEdS, Danin AR, Machado DVR, Araújo DdL, El Debs MK, Rodrigues PF (2010) Stress-strain curves for steel fiber-reinforced concrete in compression. Matéria (Rio J) 15(2):260–266. https://doi.org/10.1590/S1517-70762010000200025
33. Ou Y-C, Tsai M-S, Liu K-Y, Chang K-C (2012) Compressive behavior of steel-fiber-reinforced concrete with a high reinforcing index. J Mater Civ Eng 24(2):207–215. https://doi.org/10.1061/(ASCE)MT.1943-5533.0000372
34. Abbass W, Khan MI, Mourad S (2018) Evaluation of mechanical properties of steel fiber reinforced concrete with different strengths of concrete. Constr Build Mater 168:556–569. https://doi.org/10.1016/j.conbuildmat.2018.02.164
35. Ezeldin AS, Balaguru PN (1992) Normal- and high-strength fiber-reinforced concrete under compression. J Mater Civ Eng 4(4):415–429. https://doi.org/10.1061/(ASCE)0899-1561(1992)4:4(415)
36. Carreira DJ, Chu K-H (1985) Stress-strain relationship for plain concrete in compression. ACI JP 82(6):797–804. https://doi.org/10.14359/10390
37. Ruiz G, La Rosa Á de, Wolf S, Poveda E (2018) Model for the compressive stress–strain relationship of steel fiber-reinforced concrete for non-linear structural analysis. Hormigón y Acero. https://doi.org/10.1016/j.hya.2018.10.001
38. Lee S-C, Oh J-H, Cho J-Y (2015) Compressive behavior of fiber-reinforced concrete with end-hooked steel fibers. Materials 8(4):1442–1458. https://doi.org/10.3390/ma8041442
39. Hardjito D, Wallah SE, Sumajouw D, Rangan B (2005) Introducing fly ash-based geopolymer concrete: manufacture and engineering properties. In: Tam CT (ed) Proceedings of the 30th conference on our world in concrete & structures: 23–24 August 2005, Singapore, pp. 271–278. CI-Premier Pte. Ltd, Singapore
40. Collins MP, Mitchell D, MacGregor JG (1993) Structural design considerations for high-strength concrete. Concr Int 15(5):27–34
41. Noushini A, Aslani F, Castel A, Gilbert RI, Uy B, Foster S (2016) Compressive stress-strain model for low-calcium fly ash-based geopolymer and heat-cured Portland cement concrete. Cem Concr Compos 73:136–146. https://doi.org/10.1016/j.cemconcomp.2016.07.004
42. Cong X, Zhou W, Elchalakani M (2020) Experimental study on the engineering properties of alkali-activated GGBFS/FA concrete and constitutive models for performance prediction. Constr Build Mater 240:117977. https://doi.org/10.1016/j.conbuildmat.2019.117977
43. Kim S-W, Jang S-J, Kang D-H, Ahn K-L, Yun H-D (2015) Mechanical properties and eco-efficiency of steel fiber reinforced alkali-activated slag concrete. Materials 8(11):7309–7321. https://doi.org/10.3390/ma8115383
44. Ruiz G, La Rosa Á de, Poveda E, Zanon R, Schäfer M, Wolf S (2022) Compressive behavior of steel-fiber reinforced concrete in Annex L of new Eurocode 2. Hormigón y Acero. https://doi.org/10.33586/hya.2022.3092
45. Bekaert Product datasheets. https://construction.bekaert.com/en-us/construction/steel-fiber-concrete-reinforcement/dramix-solutions/toolbox/product-datasheets
46. Choi S, Thienel K-C, Shah SP (1996) Strain softening of concrete in compression under different end constraints. Mag Concr Res 48(175):103–115. https://doi.org/10.1680/macr.1996.48.175.103
47. Marar K, Erenb Ö, Yitmena İ (2011) Compression specific toughness of normal strength steel fiber reinforced concrete (NSSFRC) and high strength steel fiber reinforced concrete (HSSFRC). Mat Res 14(2):239–247. https://doi.org/10.1590/S1516-14392011005000042
48. Kotsovos MD (1983) Effect of testing techniques on the post-ultimate behaviour of concrete in compression. Mat Constr 16(1):3–12. https://doi.org/10.1007/BF02474861
49. Afroughsabet V, Biolzi L, Ozbakkaloglu T (2016) High-performance fiber-reinforced concrete: a review. J Mater Sci 51(14):6517–6551. https://doi.org/10.1007/s10853-016-9917-4
50. Farhan KZ, Johari MAM, Demirboğa R (2021) Impact of fiber reinforcements on properties of geopolymer composites: a review. J Build Eng 44:102628. https://doi.org/10.1016/j.jobe.2021.102628
51. Beglarigale A, Aydın S, Kızılırmak C (2016) Fiber-matrix bond characteristics of alkali-activated slag cement-based

composites. J Mater Civ Eng. https://doi.org/10.1061/(ASCE)MT.1943-5533.0001642
52. Suksawang N, Wtaife S, Alsabbagh A (2018) Evaluation of elastic modulus of fiber-reinforced concrete. ACI Mater J 115(2). https://doi.org/10.14359/51701920
53. Yip W-K (1996) New damage variable in failure analysis of concrete. J Mater Civ Eng 8(4):184–188. https://doi.org/10.1061/(ASCE)0899-1561(1996)8:4(184)
54. Bencardino F, Rizzuti L, Spadea G, Swamy RN (2008) Stress-strain behavior of steel fiber-reinforced concrete in compression. J Mater Civ Eng 20(3):255–263. https://doi.org/10.1061/(ASCE)0899-1561(2008)20:3(255)
55. Koniki S, Ravi Prasad D (2019) Mechanical properties and constitutive stress–strain behaviour of steel fiber reinforced concrete under uni-axial stresses. J Build Rehabil 4(1):6. https://doi.org/10.1007/s41024-019-0044-x
56. Mihai IC, Jefferson AD, Lyons P (2016) A plastic-damage constitutive model for the finite element analysis of fibre reinforced concrete. Eng Fract Mech 159:35–62. https://doi.org/10.1016/j.engfracmech.2015.12.035
57. Moradi M, Bagherieh AR, Esfahani MR (2020) Constitutive modeling of steel fiber-reinforced concrete. Int J Damage Mech 29(3):388–412. https://doi.org/10.1177/1056789519851159
58. Dhakal RP, Wang C, Mander JB (2005) Behaviour of steel fibre reinforced concrete in compression. In: Lü Z (ed) Innovation & sustainability of structures: proceedings of the international symposium on innovation & sustainability of structures in civil engineering, Southeast University Nanjing, China, November 20–22, 2005. Southeast University Press, Nanjing.
59. Shi X, Park P, Rew Y, Huang K, Sim C (2020) Constitutive behaviors of steel fiber reinforced concrete under uniaxial compression and tension. Constr Build Mater 233:117316. https://doi.org/10.1016/j.conbuildmat.2019.117316
60. Wang X, Zhang S, Wang C, Cao K, Wei P, Wang J (2019) Effect of steel fibers on the compressive and splitting-tensile behaviors of cellular concrete with millimeter-size pores. Constr Build Mater 221:60–73. https://doi.org/10.1016/j.conbuildmat.2019.06.069

Paper 4

Flexural tensile behaviour of alkali-activated slag-based concrete and Portland cement-based concrete incorporating single and multiple hooked-end steel fibres

Laura Rossi, Maria Paula Zappitelli, Ravi A. Patel, Frank Dehn

Journal of Building Engineering

Volume 98, 2024, p. 111090

DOI: 10.1016/j.jobe.2024.111090

Publisher's version

Journal of Building Engineering 98 (2024) 111090

Contents lists available at ScienceDirect

Journal of Building Engineering

journal homepage: www.elsevier.com/locate/jobe

Flexural tensile behaviour of alkali-activated slag-based concrete and Portland cement-based concrete incorporating single and multiple hooked-end steel fibres

Laura Rossi [a,b,*], Maria Paula Zappitelli [c], Ravi A. Patel [a,b], Frank Dehn [a,b]

[a] Institute of Building Materials and Concrete Structures (IMB), Karlsruhe Institute of Technology (KIT), 76131, Karlsruhe, Germany
[b] Material Testing and Research Institute Karlsruhe (MPA), Karlsruhe Institute of Technology (KIT), 76131, Karlsruhe, Germany
[c] Department of Civil Engineering, Engineering College, National University of La Plata (UNLP), Street 1 and 47, La Plata, Argentina

ARTICLE INFO

Keywords:
Multiple hooked-end steel fibres
Alkali-activated concrete
Residual flexural tensile strength
fib model code 2020
FEM

ABSTRACT

In this study, three-point bending tests on notched beams according to EN 14651 have been performed to evaluate the flexural post-cracking behaviour of alkali-activated slag-based concrete (AASC) and Portland cement-based concrete (PCC) incorporating single (3D) and multiple (4D, 5D) hooked-end steel fibres in different volume fractions up to 0.75 %. According to the experimental results, the post-cracking residual flexural strength increases with the increase in the fibre volume fraction for each fibre and concrete matrix type. AASC mixes incorporating 3D and 4D fibres show higher values of residual flexural strength for the same crack opening than PCC mixes with the same fibre type and dosage. Only for the mixes incorporating 5D fibres, steel fibre-reinforced PCC (SFRPCC) mixes outperform steel fibre-reinforced AASC (SFRAASC) mixes in terms of post-cracking behaviour. According to EN 14651, the values of the residual strengths f_{R1} and f_{R3}, corresponding to a crack mouth opening displacement (CMOD) of 0.5 mm and 2.5 mm, respectively, and their corresponding characteristic values f_{R1k} and f_{R3k}, respectively, can be derived from the experimental load-CMOD curves. Following the *fib* Model Code 2020, each mix can then be classified according to the values of f_{R1k} and the f_{R3k}/f_{R1k} ratio. As a result, empirical models have been developed for SFRPCC to predict the values of f_{R1} and f_{R3} and the applicability of such models to SFRAASC is evaluated in this study. Once the values of f_{R1k} and f_{R3k} are known, tensile constitutive models can be derived according to the *fib* Model Code 2020 and used as input parameters for finite element modelling. In this study, the accuracy of the code-based constitutive model to predict the flexural behaviour of SFRAASC and SFRPCC is evaluated using the concrete damage plasticity (CDP) model available in ABAQUS. The numerical model based on the tensile stress-strain curve in the *fib* Model Code 2020 can qualitatively capture the post-cracking behaviour of SFRAASC and SFRPCC incorporating 3D, 4D and 5D at 0.25 % fibre volume fraction, despite overestimating their tensile strength. For higher fibre volume fractions, the CDP model, in conjunction with the mode I parameters derived from the *fib* Model Code 2020, is unable to adequately describe the post-hardening behaviour exhibited by the composites.

* Corresponding author. Institute of Building Materials and Concrete Structures (IMB), Karlsruhe Institute of Technology (KIT), 76131 Karlsruhe, Germany.

E-mail addresses: laura.rossi@kit.edu (L. Rossi), paula.zappitelli@ing.unlp.edu.ar (M.P. Zappitelli), ravi.patel@kit.edu (R.A. Patel), frank.dehn@kit.edu (F. Dehn).

https://doi.org/10.1016/j.jobe.2024.111090
Received 22 July 2024; Received in revised form 4 October 2024; Accepted 16 October 2024
Available online 18 October 2024

1. Introduction

One of the most effective ways to reduce the brittleness of Portland cement-based concrete (PCC) and to enhance its ductility and energy absorption capacity is the use of randomly distributed steel fibres. Steel fibres hinder crack propagation and provide stress transfer by bridging the cracked sections of the concrete member [1–3]. The performance of steel fibre-reinforced cement-based concrete (SFRPCC) depends mainly on the characteristics of the concrete matrix, fibres and their bond properties [2,4,5]. Single hooked-end steel fibres (generally named 3D) have been used widely in applications requiring high tensile strength and modulus of elasticity, such as tunnel linings, joint-less industrial concrete floors, and irrigation and wastewater systems [2,3,5,6]. To improve the crack-bridging efficiency of steel fibres in concrete, multiple hooked-end steel fibres, *i.e.* double hooked-end (4D) and triple hooked-end (5D) fibres, have been recently developed and commercialised. The additional bends at both ends of the fibres enhance the fibre-matrix interface bond, resulting in higher resistance to fibre pull-out and therefore higher tensile and flexural performance of the composite [3,7,8]. Despite being relatively new, 4D and 5D steel fibres and the effect of their novel geometries on the performance of normal- and high-strength traditional cement-based concrete have been the subject of several studies [2,3,9–11]. According to Chen et al. [2], the better fibre-matrix anchorage provided by the multiple hooks at the end of 4D and 5D fibres provides a significant increase in the post-cracking behaviour of steel fibre-reinforced PCC in comparison to PCC incorporating 3D fibres. Venkateshwaran et al. [11] reported a limited effect of the number of hooked ends of the steel fibre on the flexural strength of the composite, but an enhancement of post-cracking residual flexural strength of 9–12 % was observed when 3D fibres were replaced by 5D fibres.

Although steel fibre-reinforced cement-based concrete (SFRPCC) has been widely used for structural and non-structural applications in the last decades, the high embodied CO_2 emissions and energy consumptions related to Portland cement production require the development of more environmentally friendly alternative binders, such as alkali-activated slag-based concrete (AASC) [12–16]. AASC can outperform PCC in terms of mechanical and durability performance [1,13,14,17,18]. However, alkali-activated slag-based concrete can exhibit a more brittle behaviour and higher autogenous shrinkage than PCC, limiting its resistance to crack formation and propagation [1,13,15,19]. Different fibre types have been added to alkali-activated concrete matrices to investigate their effect on the material response under various loading conditions [1,12,15,20–41]. However, studies evaluating the effect of single and multiple hooked-end steel fibres on the composite performance are limited with no research investigating the influence of 4D and 5D steel fibres on the post-cracking behaviour of steel fibre-reinforced alkali-activated slag-based concrete (SFRAASC). El-Hassan and Elkholy [19] focused on alkali-activated slag-fly ash blended concrete reinforced with hybrid steel fibre reinforcement, *i.e.* a combination of single and novel multiple hooked-end steel fibres in different volume fractions. Even though the main mechanical performances, *i.e.* compressive strength, modulus of elasticity, splitting and flexural tensile strength, were evaluated experimentally, the post-cracking flexural behaviour of the composites was not investigated. Koenig et al. [34] evaluated the flexural performance of alkali-activated slag-based concrete (AASC) and cement-based concrete (PCC) incorporating a steel fibre mix of 1/3 short straight fibres and 2/3 single hooked-end steel fibres in different volume fractions by performing three-point bending tests according to EN 14651. Both composites exhibit a post-cracking softening behaviour when reinforced with a fibre volume fraction of 0.60 %. Although SFRAASC shows a higher drop in load than SFRPCC after the peak is achieved, the residual flexural load increases with the increase in CMOD values, while it decreases for SFRPCC. Despite providing new insights on the post-cracking flexural behaviour of steel fibre-reinforced alkali-activated slag-based concrete, the study of Koenig et al. [34] does not evaluate the effect of single hooked-end steel fibres or novel steel fibres on the performances of the composite. Shaikh [42] evaluated the pull-out behaviour of 3D, 4D and 5D fibres in alkali-activated slag-fly ash-based and cement-based mortars. Although alkali-activated slag-fly ash blended mortar exhibits a higher maximum pull-out load, toughness and bond strength than cement-based mortar, the flexural performance of such composites is not investigated.

Evaluating the flexural post-cracking behaviour of SFRAASC experimentally is essential to understand and predict its behaviour as well as to derive tensile constitutive models, *i.e.* stress-strain ($\sigma - \varepsilon$) or stress-crack opening ($\sigma - w$) relationships, which are fundamental for the preliminary design and dimensioning of concrete structural members. The ideal approach to derive the tensile stress-strain ($\sigma - \varepsilon$) relationship for steel fibre-reinforced concrete is to perform direct uniaxial tensile tests. However, direct tensile tests are difficult to perform accurately [43] and the reliability of the results is highly influenced by the fibre type, dosage and orientation. Due to their ease of execution, three-point bending tests on notched beams according to EN 14651 are generally preferred to evaluate the post-cracking behaviour of steel fibre-reinforced composites. From the flexural post-cracking behaviour, several authors [43–46] and design codes, such as the *fib* Model Code 2020 [47], proposed simplified or more accurate tensile constitutive models can be derived for preliminary design or numerical simulations, respectively.

This paper evaluates experimentally the flexural post-cracking behaviour of alkali-activated slag-based concrete and Portland cement-based concrete incorporating single (3D) and multiple (4D and 5D) hooked-end steel fibres in different fibre volume fractions up to 0.75 %. From the experimental Load-CMOD curves the values of the residual flexural strengths f_{R1} and f_{R3} and their corresponding characteristic values f_{R1k} and f_{R3k} are derived to classify the composites according to the *fib* Model Code 2020

recommendations. The applicability to SFRAASC of currently available empirical models for SFRPCC to derive the values of the residual flexural strength f_{R1} and f_{R3} is investigated and a new recalibrated model is proposed for SFRAASC. Finally, the applicability of the linear tensile constitutive laws available in the *fib* Model Code 2020 for SFRAASC and SFRPCC is evaluated. Such tensile constitutive models are used as input parameters for numerical simulations by finite element modelling using the Concrete Damage Plasticity (CDP) model available in ABAQUS.

2. Experimental programme

2.1. Materials

The alkali-activated slag-based concrete matrix was made from ground granulated blast furnace slag (GGBS), water, sodium hydroxide (SH), sodium silicate (SS), and fine and coarse aggregates. To obtain an alkaline solution with a total concentration of 5.3 % Na_2O (expressed as a percentage of slag weight), SH (50 % solid content), SS with a molar ratio $M_s = 3.4$ [mol/mol] and water were pre-mixed 24 h prior casting to reduce heat release [19,34] and prevent fresh concrete rapid setting. CEM I 42.5R was used to produce a reference Portland cement-based concrete. Table 1 shows the chemical composition of the binders.

Glued steel fibres were supplied by NV Bekaert SA. The selected fibres are classified as single hooked-end (Dramix® 3D 65/60 BG), double hooked-end (Dramix® 4D 65/60 BG) and triple hooked-end (Dramix® 5D 65/60 BG) depending on the number of bends at the fibre ends (Fig. 1).

The properties of the steel fibres are given in Table 2. Four different fibre volume fractions – 0 %, 0.25 % (20 kg/m^3), 0.50 % (40 kg/m^3) and 0.75 % (60 kg/m^3) – were added to the reference concrete matrices.

The mix proportions of the plain reference AASC and PCC concrete matrices are given in Table 3. The same binder content, aggregate type, and proportions were used to achieve a similar slump flow class (F4) and 28-day mean compressive strength (Table 3). The twenty mixes, ten for each concrete matrix, are designated as X-YDZ, where X denotes the matrix type (AASC or PCC), YD represents the fibre geometry (3D, 4D or 5D) and Z the fibre volume fraction (0.25 %, 0.50 % and 0.75 %). The reference mixes without fibres are designated as AASC-REF and PCC-REF for alkali-activated slag-based concrete and Portland cement-based concrete, respectively.

2.2. Mixing and sample preparation

The same mixing procedure was followed for all the mixtures. First, the binder was mixed for 90 s with fine and coarse aggregates. Then, the liquid component – the pre-mixed alkaline solution for AASC and water for PCC – was added to the dry components and mixed for two additional minutes to achieve a homogeneous mixture. Finally, before the freshly made concrete was poured into the moulds, steel fibres were added and thoroughly mixed to achieve a total mixing time of 7 min. The equipment used to cast the samples is shown in Fig. 2.

Three cylinders of diameter of 150 mm and height of 300 mm and six 150 mm × 150 mm × 550 mm beams (Fig. 3) were cast for each mixture to assess its 28-day mean compressive strength and flexural response under three-point bending, respectively. The samples were cast from different batches of the same concrete mix. To allow setting and reduce drying shrinkage, plastic covers, damp jute, and plastic foil were placed on the fresh concrete-filled moulds for the first 24 h. After demoulding, the SFRPCC samples were cured underwater (20 ± 2) °C, while the SFRAASC specimens were wrapped in foil [48] and stored in a climate room at (20 ± 2) °C and 65 % relative humidity until the testing date. After a 21-day curing period, a notch measuring 5 ± 1 mm in width and 25 ± 1 mm in depth was sawed at the mid-span of the side face of each beam in accordance with EN 14651.

2.3. Experimental procedure

The 28-mean compressive strength of SFRAASC and SFRPCC was assessed on three cylinders with a diameter of 150 mm and a height of 300 mm, according to EN 12390–3. The post-cracking flexural behaviour was evaluated on six notched beams according to EN 14651. Two rigid steel frames equipped with linear variable differential transducers (LVDTs) were installed at the mid-width of the beam specimens to measure the crack mouth opening displacement (CMOD) at the bottom of the notch on both sides of the beam. The experimental setup is shown in Fig. 4.

Table 1
Chemical composition of GGBS and CEM I.

Binder	CaO [%]	SiO_2 [%]	Al_2O_3 [%]	Fe_2O_3 [%]	MgO [%]	P_2O_5 [%]	K_2O [%]	Na_2O [%]
GGBS	41.84	35.91	10.74	0.39	6.99	0.47	0.40	0.31
CEM I	60.80	19.60	5.25	2.38	1.53	0.13	0.80	0.10

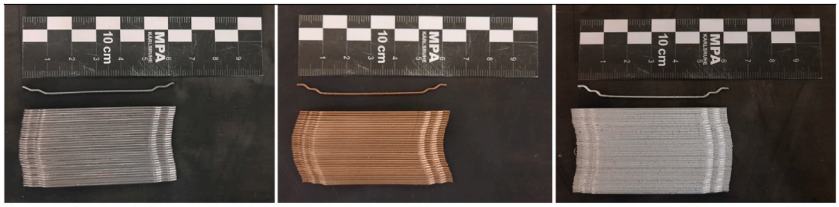

Fig. 1. Single and multiple Dramix® hooked-end steel fibres: (a) 3D, (b) 4D and (c) 5D.

Table 2
Properties of 3D, 4D and 5D hooked-end steel fibres.

Fibre type	Length (l_f) [mm]	Diameter (d_f) [mm]	Aspect ratio (l_f/d_f)	Fibre tensile strength ($\sigma_{f,u}$)[a] [MPa]	Strain at ultimate strength [%]
3D 65/60 BG	60	0.90	65	1160	0.8
4D 65/60 BG	60	0.90	65	1600	0.8
5D 65/60 BG	60	0.90	65	2300	6.0[a]

[a] Provided by the fibre manufacturer (NV Bekaert SA).

Table 3
Mix proportions (in kg/m^3), slump flow class and 28-day compressive strength of the different concrete matrices reference mixes.

Mix	GGBS	CEM	SH	SS	Water	Fine and coarse aggregates			Slump flow class	28-day Compressive strength [MPa]
						0–2 mm	2–8 mm	8–16 mm		
AASC	425	–	50	36	154	660	495	495	F4	50.2
PCC	–	425	–	–	229	660	495	495	F4	49.5

Fig. 2. Mixing and casting equipment: (a) 250-L concrete mixer, (b) weighted mix components, (c) vibration table and beam moulds (top), and freshly mixed alkali-activated slag-based concrete (bottom).

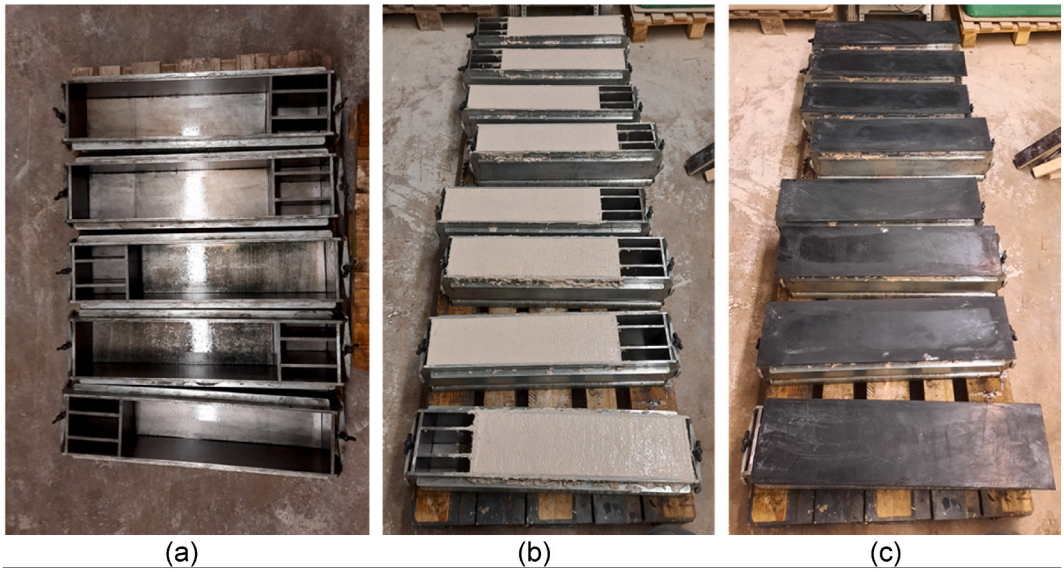

Fig. 3. Beam moulds (a) before casting, (b) after filling with fresh concrete and (c) with plastic covers to minimise drying shrinkage.

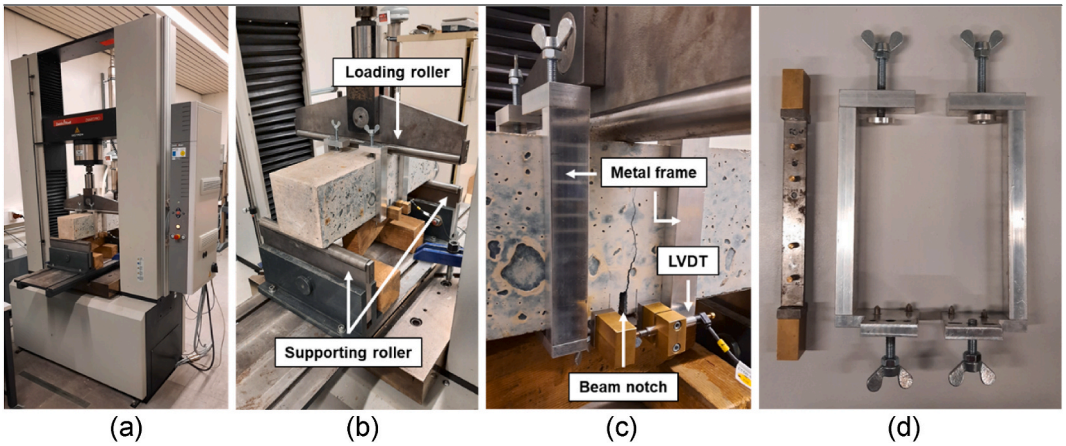

Fig. 4. Three-point bending test experimental setup: (a) testing machine, (b) arrangement of loading, (c) metal frame equipped with LVDTs, and (d) detail of the metal frame.

3. Results and discussion

3.1. Flexural tensile strength

From the experimental load-CMOD curves, the flexural strength corresponding to the Limit of Proportionality (f_{LOP}) and the residual flexural strengths f_{Rj} corresponding to $CMOD_j$ (j = 1, 2, 3, 4) can be derived for each concrete matrix and steel fibre type according to EN 14651 as follows:

$$f_{LOP} = \frac{3 \cdot F_{LOP} \cdot l}{2 \cdot b \cdot h_{sp}^2} \tag{1}$$

$$f_{Rj} = \frac{3 \cdot F_j \cdot l}{2 \cdot b \cdot h_{sp}^2} \quad (2)$$

where F_{LOP} is the load corresponding to the Limit of Proportionality (LOP), *i.e.* the highest load value in the CMOD range from 0 to 0.05 mm, F_j is the load corresponding to $CMOD_j$ (j = 1, 2, 3, 4), *i.e.* 0.5 mm ($CMOD_1$), 1.5 mm ($CMOD_2$), 2.5 mm ($CMOD_3$) and 3.5 mm ($CMOD_4$), respectively, and l, b, and h_{sp} are the span of the concrete beam specimen (500 mm in this study), the width of the sample (150 mm in this study), the distance between the tip of the notch and the top of the beam (125 mm in this study). Additionally, according to the *fib* Model Code 2020 [47], the values of the characteristic residual flexural tensile strengths f_{R1k} and f_{R3k}, corresponding to $CMOD_1 = 0.5$ mm and $CMOD_3 = 2.5$ mm respectively, can be derived as follows:

$$f_{Rjk} = f_{Rj} - k \cdot \sigma \quad (3)$$

where f_{Rj} is the residual flexural strength defined in Eq. (2), k is a constant linked to the number n of samples tested ($k = 1.770$ when $n = 6$, as in this study) and σ is the standard deviation of the mean residual flexural strength f_{Rj}.

3.2. Post-cracking flexural tensile behaviour

3.2.1. Classification according to the fib Model Code 2020

The characteristic flexural tensile strengths f_{R1k} and f_{R3k} and their ratio, *i.e.* f_{R3k}/f_{R1k}, are used to classify the post-cracking flexural tensile behaviour of steel fibre-reinforced concrete composites through a number and a letter, respectively. The number (1.0, 1.,5, 2.0, 2.5, 3.0, 4.0, 5,0, 6.0, 7.0, 8.0 [MPa]) denotes the f_{R1k} class, corresponding to the characteristic strength at serviceability limit state (SLS), while the letter (a, b, c, d and e) corresponds to specific values of the f_{R3k}/f_{R1k} ratio, defined as follows:

Table 4
Experimental values of f_c, E_c, f_{LOP}, f_{Rj} (j = 1, 2, 3, 4), f_{R1k}, f_{R3k}/f_{R1k} and the classification of each mix according to the *fib* Model Code 2020.

Mix	f_c [MPa]	E_c [GPa]	f_{LOP} [MPa]	f_{R1} [MPa]	f_{R2} [MPa]	f_{R3} [MPa]	f_{R4} [MPa]	f_{R1k} [MPa]	f_{R3k}/f_{R1k} [MPa]	Class
AASC-REF	40.9 (0.86)	27.6 (0.64)	5.02 (0.11)	0.30 (0.10)	–	–	–	–	–	–
PCC-REF	45.2 (0.64)	27.9 (0.55)	4.59 (0.23)	0.29 (0.08)	–	–	–	–	–	–
AASC-3D25	43.8 (0.35)	28.1 (0.42)	6.22 (0.26)	2.93 (0.51)	3.40 (0.70)	3.45 (0.87)	3.36 (0.88)	2.03	0.94	2c
AASC-3D50	44.8 (0.84)	28.2 (0.61)	5.92 (0.47)	5.66 (0.84)	7.00 (1.03)	6.93 (1.02)	6.65 (0.89)	4.17	1.23	4d
AASC-3D75	48.3 (0.73)	30.0 (1.09)	5.66 (0.38)	6.88 (1.21)	8.07 (1.28)	8.03 (1.13)	7.66 (0.90)	4.73	1.27	4d
PCC-3D25	39.0 (1.11)	27.5 (0.81)	4.52 (0.31)	2.88 (0.39)	3.16 (0.41)	3.05 (0.40)	2.86 (0.39)	2.18	1.08	2d
PCC-3D50	38.5 (1.36)	26.7 (0.54)	4.66 (0.18)	5.41 (0.58)	6.29 (1.04)	6.07 (0.96)	5.66 (0.83)	4.38	1.00	4c
PCC-3D75	40.1 (0.43)	28.2 (1.15)	4.85 (0.38)	6.34 (0.77)	7.53 (0.92)	7.28 (0.82)	6.66 (0.93)	4.98	1.17	4d
AASC-4D25	45.4 (0.76)	28.1 (0.80)	5.30 (0.27)	3.15 (1.13)	3.70 (1.12)	3.91 (1.08)	3.26 (0.62)	1.14	1.75	1e
AASC-4D50	44.2 (0.80)	28.2 (0.50)	5.46 (0.37)	5.55 (1.23)	7.06 (1.32)	6.91 (0.87)	6.48 (0.57)	3.38	1.59	3e
AASC-4D75	44.3 (2.45)	27.4 (0.39)	5.79 (0.25)	7.86 (0.83)	8.87 (0.38)	8.05 (0.35)	7.40 (0.47)	6.39	1.16	6d
PCC-4D25	40.3 (0.86)	27.0 (0.85)	4.13 (0.23)	2.81 (0.26)	3.90 (0.40)	4.14 (0.50)	3.98 (0.38)	2.36	1.38	2e
PCC-4D50	43.6 (1.09)	27.4 (0.30)	4.73 (0.32)	5.53 (0.91)	7.68 (1.10)	7.05 (1.00)	6.85 (1.12)	3.93	1.35	3e
PCC-4D75	45.1 (1.53)	27.7 (0.22)	4.85 (0.39)	6.16 (1.79)	7.08 (1.28)	6.66 (1.13)	5.78 (1.06)	2.99	1.56	2,5e
AASC-5D25	45.2 (0.47)	27.7 (0.36)	5.83 (0.40)	2.44 (0.57)	2.94 (0.64)	3.07 (0.60)	3.04 (0.47)	1.44	1.40	1e
AASC-5D50	52.6 (3.16)	28.8 (0.68)	5.84 (0.43)	6.23 (1.69)	8.44 (2.02)	7.88 (1.39)	7.02 (1.37)	3.24	1.68	3e
AASC-5D75	48.4 (1.11)	29.4 (1.12)	5.86 (0.34)	7.66 (0.55)	8.69 (0.90)	8.30 (1.00)	7.57 (1.09)	6.74	0.97	6c
PCC-5D25	45.2 (2.20)	27.4 (0.52)	4.52 (0.25)	3.11 (0.53)	4.11 (0.68)	4.27 (0.83)	4.49 (0.71)	2.17	1.29	2d
PCC-5D50	44.7 (0.86)	27.4 (0.61)	4.56 (0.44)	5.10 (1.09)	6.63 (1.00)	5.98 (0.65)	5.58 (0.55)	3.17	1.53	3e
PCC-5D75	48.2 (1.39)	27.5 (0.96)	5.19 (0.58)	8.23 (1.38)	9.58 (0.88)	8.73 (0.45)	7.87 (0.59)	5.78	1.37	5e

v_f = fibre volume fraction. The values in the brackets represent the standard deviation.

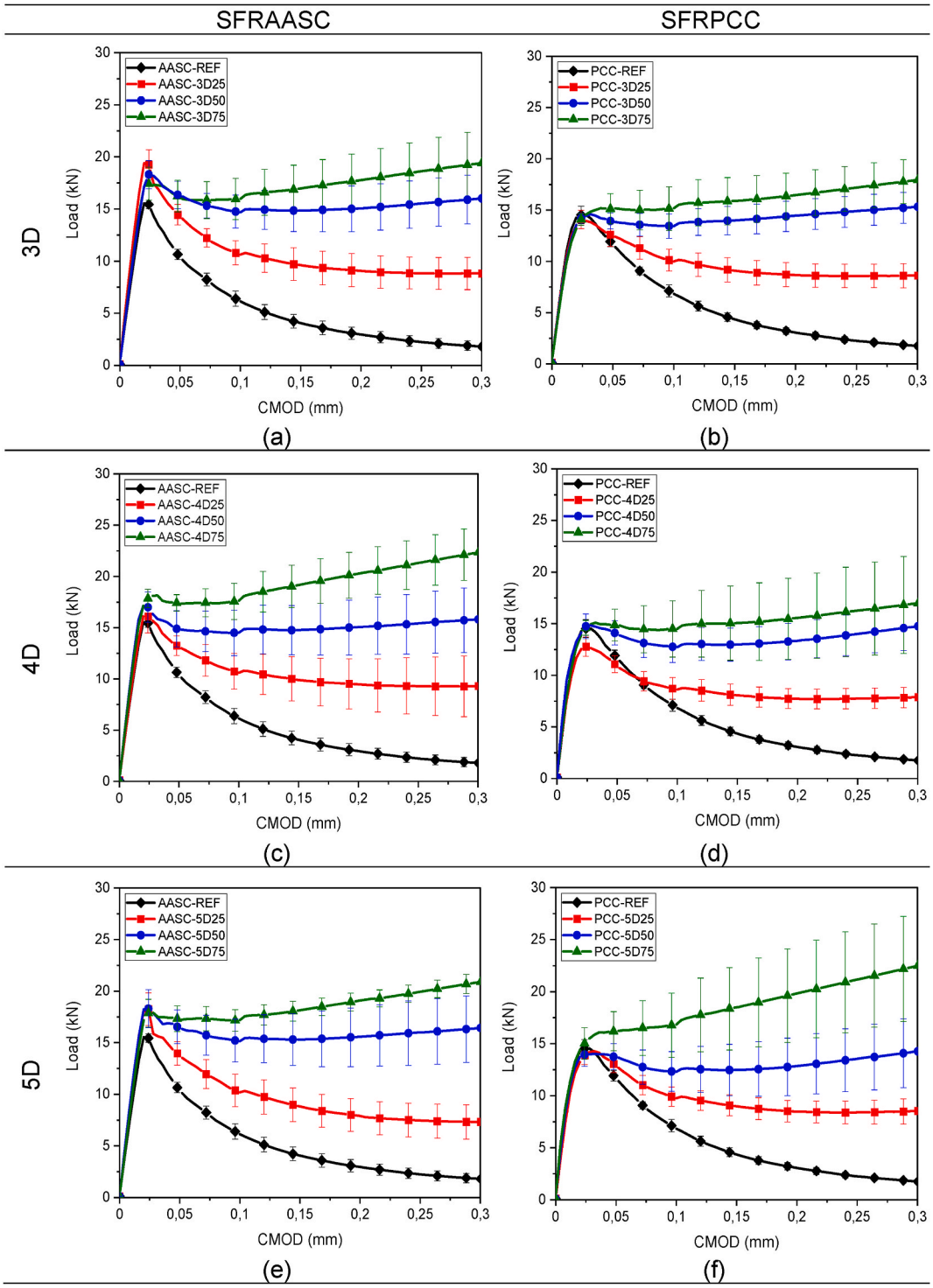

Fig. 5. Load-CMOD curves and relative standard deviation of SFRAASC and SFRPCC mixes reinforced with (a, b) 3D fibres, (c, d) 4D fibres, and (e, f) 5D fibres, respectively, at different volume fractions up to a CMOD = 0.30 mm.

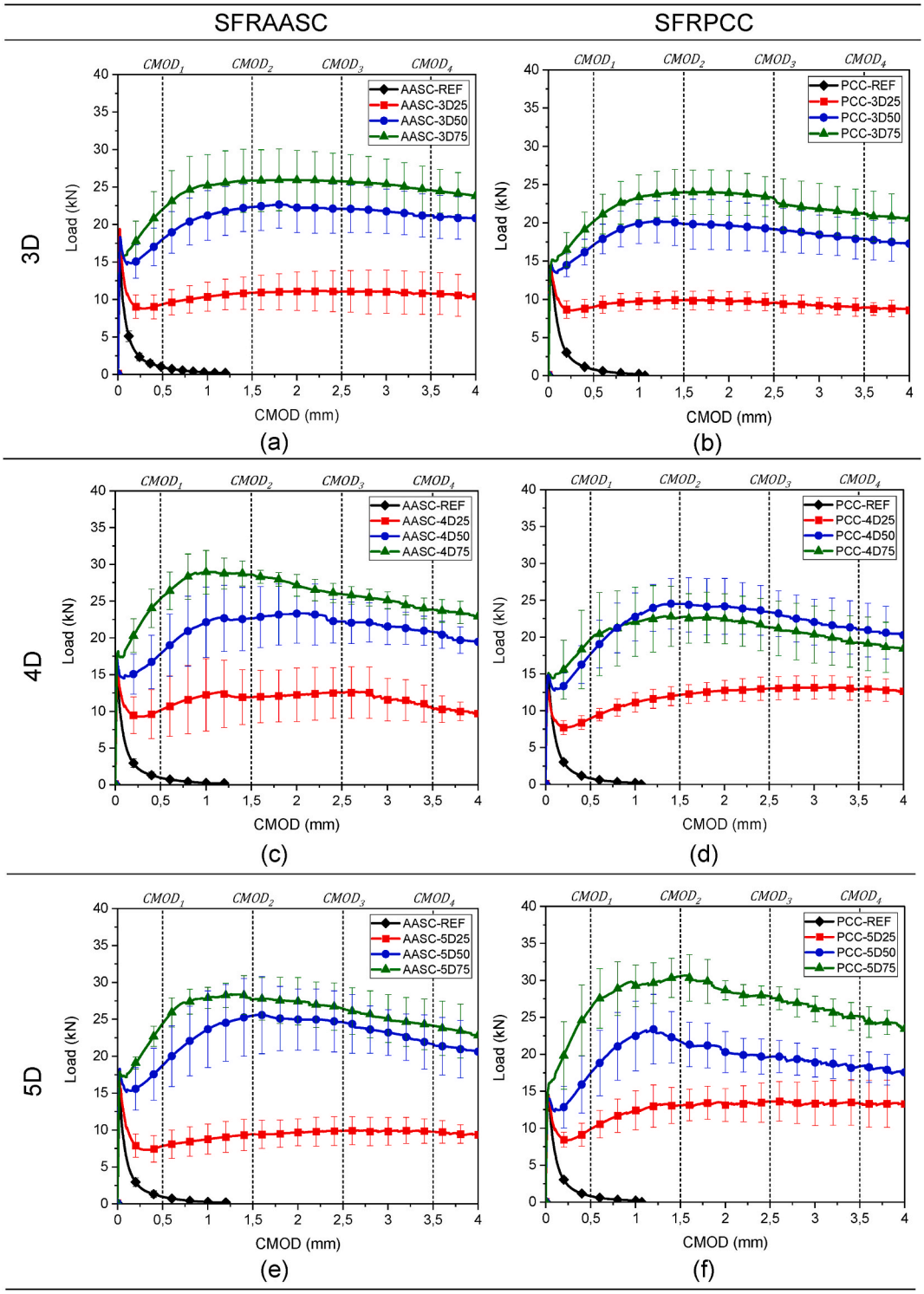

Fig. 6. Average load-CMOD curves and relative standard deviation of SFRAASC and SFRPCC mixes reinforced with (a, b) 3D fibres, (c, d) 4D fibres, and (e, f) 5D fibres, respectively, at different volume fractions.

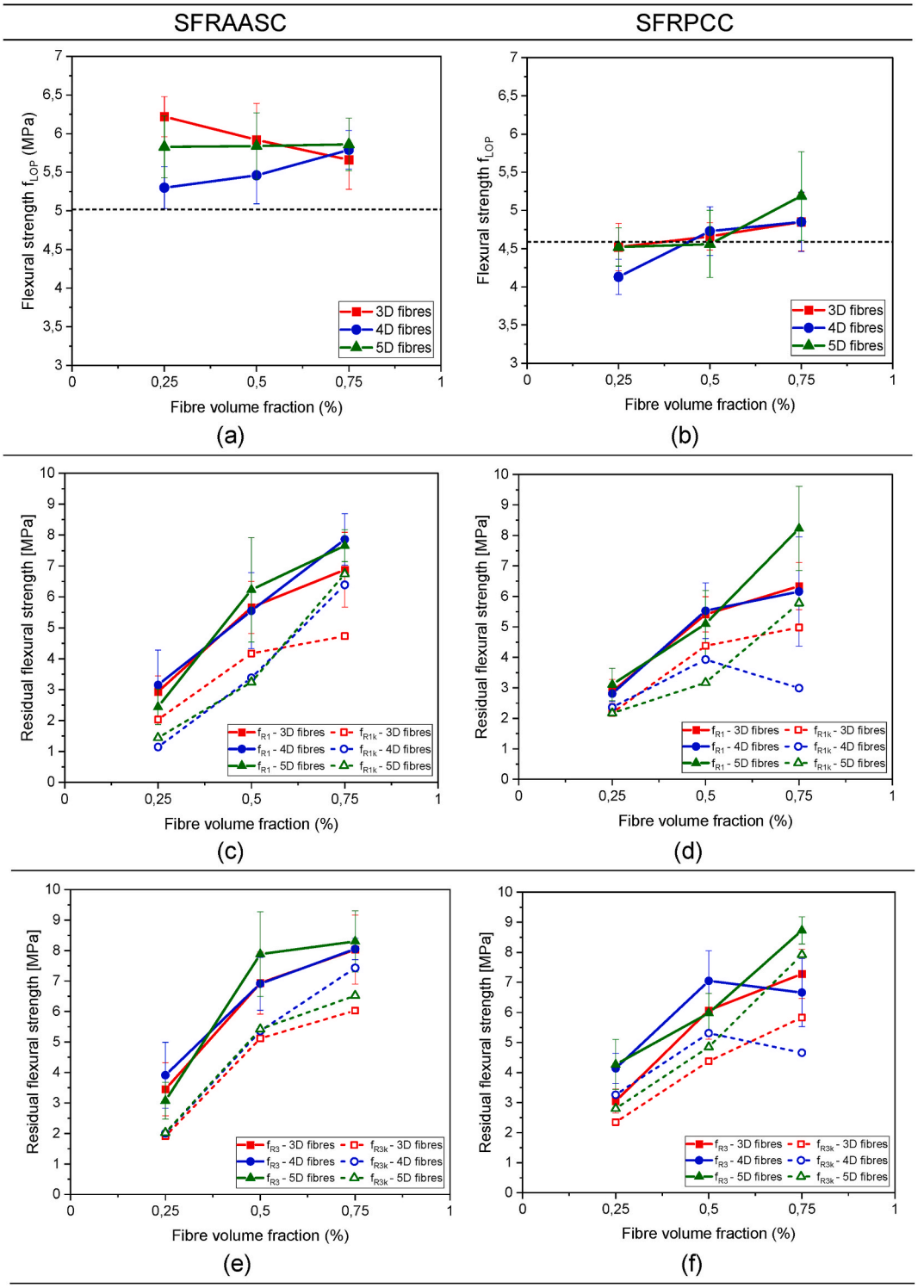

Fig. 7. Correlation between the fibre volume fraction and (a, b) the flexural strength f_{LOP}, (c, d) the residual flexural strength f_{R1} and f_{R1k}, and (e, f) the residual flexural strength f_{R3} and f_{R3k}, for each fibre geometry for SFRAASC and SFRPCC mixes, respectively. The dashed line in (a, b) indicates the value of f_{LOP} for the reference mix.

a if $0.5 < f_{R3k}/f_{R1k} < 0.7$

b if $0.7 \leq f_{R3k}/f_{R1k} < 0.9$

c if $0.9 \leq f_{R3k}/f_{R1k} < 1.1$

d if $1.1 \leq f_{R3k}/f_{R1k} < 1.3$

e if $1.3 \leq f_{R3k}/f_{R1k}$

Table 4 summarises the values of the 28-day mean cylindrical compressive strength (f_c), the flexural strength f_{LOP}, the residual flexural strength f_{Rj} (j = 1, 2, 3, 4) corresponding to CMOD values of 0.5 mm, 1.5 mm, 2.5 mm and 3.5 mm, respectively, the characteristic residual flexural strengths f_{R1k} and f_{R3k}, and the material class according to the *fib* Model Code 2020. In addition, the values of 28-day modulus of elasticity (E_c), evaluated by the authors in a previous study on samples obtained from different batches of the same concrete mixes [48], are given in Table 4.

3.2.2. Effect of the concrete matrix properties on f_{LOP}

According to the results summarised in Table 4, the 28-day compressive strength has a different effect on f_{LOP} for SFRAASC and SFRPCC. For SFRPCC, a direct correlation between the compressive strength and f_{LOP} can be observed, *i.e.* f_{LOP} generally increases with the increase of the compressive strength. For all fibre types, the increase in compressive strength with the fibre content increases f_{LOP}. For SFRAASC, the opposite can be observed, *i.e.* the compressive strength and f_{LOP} are indirectly correlated. For 3D fibres, the increase in compressive strength with the increase in the fibre volume fraction corresponds to a decrease in f_{LOP}, while for 4D fibres a decrease in compressive strength corresponds to an increase in f_{LOP}. For 5D fibres, variations in the compressive strength do not affect the values of f_{LOP}. Although for SFRPCC the highest value of f_{LOP} corresponds to the highest value of compressive strength (PCC-5D75), the same does not apply for SFRAASC, as the highest value of f_{LOP} is achieved by the mix AASC-3D25, while the highest value of compressive strength is observed for the mix AASC-5D50.

Although alkali-activated concrete generally exhibits a lower modulus of elasticity than traditional cement-based concrete [49], as also shown in Table 4 for the reference mixes, the incorporation of hooked-end steel fibres at different volume fractions enhances the modulus of elasticity of SFRAASC, which is higher than the one of SFRPCC for each fibre type (Table 4). However, no clear correlation between the modulus of elasticity and f_{LOP} can be seen. As for the compressive strength, the highest value of f_{LOP} does not necessarily correspond to the highest value of the modulus of elasticity. For SFRPCC the highest value of f_{LOP} is achieved by the mix PCC-5D75, while the highest value of the modulus of elasticity is achieved by the mix PCC-3D75. For SFRAASC the highest value of f_{LOP} is achieved by the mix AASC-3D25, while the highest value of E_c is observed for the mix AASC-3D75. Although the modulus of elasticity is generally directly correlated to the compressive strength of the material, discrepancies in the correlation between the compressive strength and f_{LOP} and between the modulus of elasticity and f_{LOP} could be related to the sample preparation, *i.e.* different concrete batches of the same mix.

3.2.3. Effect of fibre type and volume fraction on f_{LOP}

Fig. 5 shows the experimental load-CMOD curves up to a CMOD value of 0.3 mm to evaluate the effect of the fibre type and volume fraction on the flexural strength f_{LOP} of both SFRAASC and SFRPCC. Single and multiple hooked-end steel fibres generally have a limited effect on f_{LOP}, which is mainly dependent on the compressive strength and load-bearing capacity of the plain concrete matrix [1]. This can be seen for SFRPCC mixes, as the f_{LOP} decreases in comparison to the reference plain concrete for each fibre type at a volume fraction of 0.25 %, achieving the lowest value for the mix PCC-4D25 (−10 % in comparison to PCC-REF), while it increases with the increase in the fibre volume fraction up to 0.75 % for each fibre type, with PCC-5D75 showing the highest value (+13.1 % in comparison to PCC-REF). For SFRAASC, the value of f_{LOP} is higher for each concrete mix incorporating steel fibres in contrast to the reference mix, although different correlations between the values of f_{LOP} and the fibre type and dosage can~~not~~ be seen. For 3D fibres, f_{LOP} reaches its higher value at the lower fibre content (AASC-3D25) and decreases with the increase in the fibre volume fraction. For 4D fibres, f_{LOP} increases with the increase in the fibre volume fraction, while for 5D fibres, all volume fractions exhibits similar values of f_{LOP}.

Although for SFRPCC mixes the fibre type and dosage seem to have no clear and significant effect on the flexural strength f_{LOP}, with the concrete matrix playing a more relevant role, for SFRAASC mixes, the incorporation of steel fibres enhances f_{LOP}, with 3D fibres providing the highest increment (+23.9 % than AASC-REF) at the lowest fibre content.

3.2.4. Effect of the concrete matrix properties on the post-peak response

As shown in Table 4, the values of the residual flexural strengths f_{R1} and f_{R3} increase with the fibre volume fraction for each fibre and concrete matrix type. Although the fibre geometry and dosage have a more significant effect on the post-cracking flexural

behaviour of the composite, a clear correlation between f_{R1} and f_{R3} and the concrete matrix properties can be seen, *i.e.* f_{R1} and f_{R3} generally increase with the increase in compressive strength and modulus of elasticity for SFRAASC and SFRPCC. Only for SFRAASC incorporating 4D fibres, a decrease in compressive strength and modulus of elasticity with the fibre volume fraction results in an increase of f_{R1} and f_{R3}. However, as observed for f_{LOP}, the highest values of compressive strength and modulus of elasticity do not necessarily correspond to the highest values of f_{R1} and f_{R3}. Once the concrete matrix achieves the peak flexural strength, the post-cracking behaviour is mainly governed by the steel fibres, as the crack starts propagating and the stresses cannot be sustained by the cracked concrete matrix.

3.2.5. Effect of fibre type and volume fraction on the post-peak response

Fig. 6 shows the experimental load-CMOD curves obtained for each fibre and concrete matrix type. Both plain concrete reference mixes exhibit a brittle failure, *i.e.* the load abruptly drops after achieving its maximum value, due to the initial cracking of the matrix and the absence of fibres transferring stresses through the surfaces of the crack [50].

When steel fibres are introduced into the concrete matrices, a more ductile post-cracking behaviour can be observed for both SFRAASC and SFRPCC mixes (Fig. 6). With the increment of the fibre volume fraction from 0.25 % to 0.50 %, the increased number of fibres at the crack surface mitigates the post-peak drop of load and enhances the post-cracking response, resulting in higher residual flexural load and corresponding strength, for each matrix and fibre type. The additional increase of fibre volume fraction from 0.50 % to 0.75 % leads to a post-cracking deflection hardening behaviour, in which the post-cracking load drop is completely neutralised and the fibres at the crack surface can bear and transfer the bending tensile stresses through the crack surfaces to the matrix. Steel fibre incorporation significantly affects the post-peak descending branch of the load-CMOD curve and the values of the residual flexural strengths. Although the increase of the fibre volume fraction from 0.25 % to 0.50 % corresponds to an almost doubled increase in the residual flexural strength, a further increase of fibre content from 0.50 % to 0.75 % volume fraction provides a limited enhancement of the residual flexural strengths. SFRAASC mixes outperforming SFRPCC mixes when reinforced with 3D and 4D fibres, whereas with 5D fibres, SFRPCC mixes exhibit higher values of residual flexural strength as shown in Fig. 6 and Table 4.

Fig. 7 shows the correlation between the fibre volume fraction and the values of f_{LOP}, f_{R1} and f_{R3}, and the corresponding characteristic values f_{R1k} and f_{R3k}, for each concrete matrix and fibre type. As shown in Fig. 9a and 9b, SFRAASC exhibits higher flexural strength (f_{LOP}) than SFRPCC for each fibre type and volume fraction. Single and multiple hooked-end steel fibres improve the initial cracking load of SFRAASC due to the early activation of their crack bridging effect possibly due to micro-cracking induced by the higher autogenous shrinkage compared to SFRPCC mixes [34]. For both SFRAASC and SFRPCC, however, the increase of fibre volume fraction has a limited effect on the flexural strength f_{LOP}, which slightly increases for SFRPCC and slightly decreases for SFRAASC, for each fibre type, with the increase of the fibre dosage.

However, for SFRAASC, an improvement of f_{LOP} in comparison to the plain reference mix can be seen already at the lowest fibre volume fraction (0.25 %) for each fibre type. For SFRPCC improvements can be seen at a higher volume fraction, i.e. 0.50 %, whereas at 0.25 % fibre content, lower values of f_{LOP} than the reference mix are observed regardless of the fibre geometry.

Table 5
Empirical equations to predict the residual flexural strengths of SFRPCC.

Author	Empirical equations
Moraes Neto et al. [52]	$f_{R1} = 7.5 \cdot (RI_v)^{0.8}$ $f_{R3} = 6.0 \cdot (RI_v)^{0.7}$
Venkateshwaran et al. [11]	$f_{R1} = \Psi \cdot \left(0.32 \cdot (f_{cm})^{1/2} + 6.214 \cdot RI_v + 0.034 \cdot N^2\right)$ $f_{R3} = \Psi \cdot \left(0.30 \cdot (f_{cm})^{1/2} + 7.629 \cdot RI_v + 0.373 \cdot N^2\right)$
Chen et al. [2]	$f_{R1} = 0.09120 \cdot \left(f_{cu,0}\right)^{2/3} \cdot \left[1 + \left(0.0899 \cdot l_f + 1.29476 \cdot (N)^{1/2}\right) \cdot RI_v\right]$ $f_{R3} = 0.08594 \cdot \left(f_{cu,0}\right)^{2/3} \cdot \left[1 + \left(0.0382 \cdot l_f + 4.60597 \cdot (N)^{1/2}\right) \cdot RI_v\right]$
Oettel et al. [53]	$f_{R1} = \frac{1}{0.37} \cdot k \cdot v_f \cdot (1 - k \cdot v_f) \cdot \frac{f_{LOP}}{0.39} \cdot \zeta_1 \cdot \eta_v$ $f_{R3} = \frac{1}{0.37} \cdot k \cdot v_f \cdot (1 - k \cdot v_f) \cdot \frac{f_{LOP}}{0.39} \cdot \zeta_3 \cdot \eta_v$
Faccin et al. [51]	$f_{R1} = 2.7 \cdot (f_{cm})^{1/2} \cdot \left(\frac{l_f}{d_f}\right)^{0.8} \cdot (v_f)^{0.9}$ $f_{R3} = 0.5 \cdot (f_{cm})^{2/3} \cdot \left(\frac{l_f}{d_f}\right) \cdot (v_f)^{0.85}$

$RI_v = v_f \cdot (l_f/d_f)$ = fibre reinforcing index, v_f = fibre volume fraction [%], l_f = fibre length [mm], d_f = fibre diameter [mm], $\Psi = (1 + l_f/100)^{1/2}$ = factor accounting for the fibre length, f_{cm} = cylindrical compressive strength, N = number of bends at the fibre ends ($N = 1$ for 3D fibres, $N = 1.5$ for 4D fibres and $N = 2$ for 5D fibres), $f_{cu,0}$ = cubic compressive strength of plain concrete, $k = (l_f/d_f) \cdot \chi$, $\chi = 0.3$ for hooked-end steel fibres, $\zeta_1 = 1.18 - 7.5 l_f/1000$, $\zeta_3 = 0.42 + 7.5 l_f/1000$, $\eta_v = 1/(0.7 - 0.2 v_f)$.

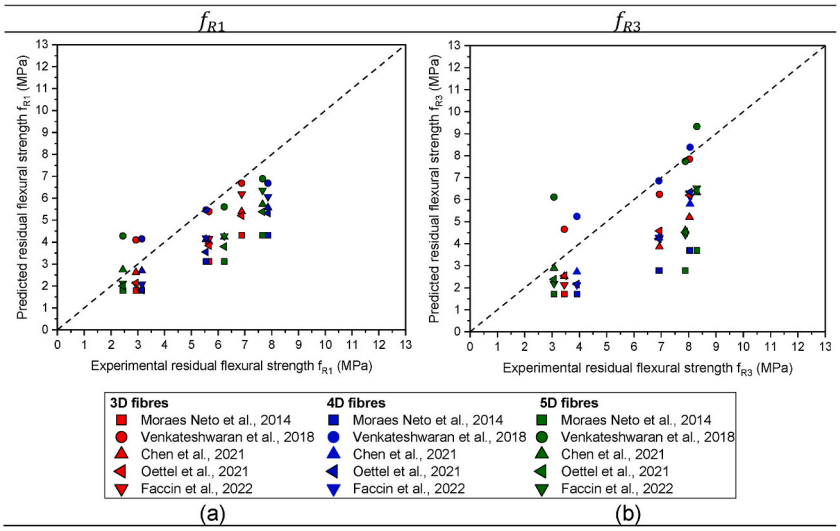

Fig. 8. Correlation between the experimental and the predicted values of (a) f_{R1} and (b) f_{R3} for SFRAASC incorporating 3D, 4D and 5D steel fibres.

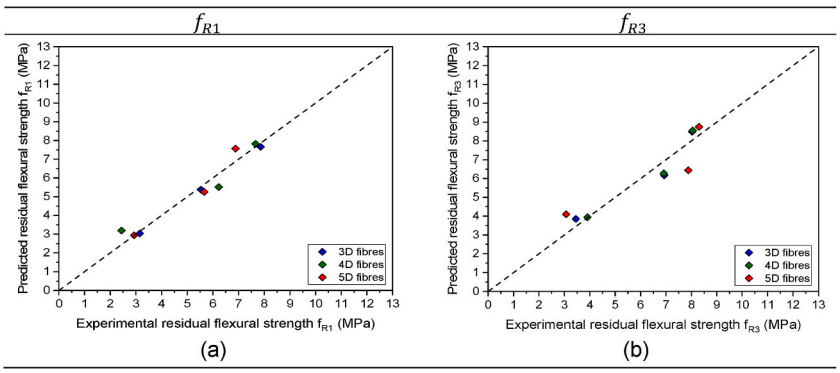

Fig. 9. Correlation between the experimental and the predicted values of (a) f_{R1} and (b) f_{R3} for SFRAASC incorporating 3D, 4D and 5D steel fibres obtained by using the newly calibrated correlations.

Table 6
IAE values of the currently available empirical models used to predict the residual flexural strengths f_{R1} and f_{R3} of SFRAASC.

Empirical model	IAE [%]					
	3D		4D		5D	
	f_{R1}	f_{R3}	f_{R1}	f_{R3}	f_{R1}	f_{R3}
Moraes Neto et al. [52]	40.5	55.5	44.4	56.6	43.6	57.5
Venkateshwaran et al. [11]	10.6	11.3	13.6	9.1	19.8	21.9
Chen et al. [2]	22.3	37.1	25.2	32.2	25.9	28.3
Oettel et al. [53]	27.7	27.6	35.5	32.5	31.5	30.8
Faccin et al. [51]	19.6	31.2	25.5	33.5	21.8	31.8

For both SFRAASC and SFRPCC, the values of the residual strengths f_{R1} and f_{R3} increases with the increase of the fibre volume fraction for each type of fibre, with only PCC mixes incorporating 4D fibres showing a decrease of f_{R3} when the fibre volume fraction increases from 0.50 % to 0.75 %. Alkali-activated slag-based concrete mixes reinforced with 3D fibres outperform PCC mixes incorporating the same fibre type, with f_{R1} and f_{R3} showing higher values than SFRPCC, as also shown in Table 4. When 4D fibres are added, SFRAASC mixes show higher values of f_{R1} than SFRPCC mixes for each volume fraction. For all mixes, except for the mix AASC-4D75, SFRAASC shows lower value of f_{R3} compared to SFRPCC. When 5D fibres are considered, the PCC mixes outperform the AASC mixes, with only the mix AASC-5D50 showing higher values of f_{R1} and f_{R3} than PCC. The characteristic values f_{R1k} and f_{R3k} follow a similar trend as the corresponding mean experimental values f_{R1} and f_{R3} for each concrete matrix and fibre types, *i.e.* they generally increase with the fibre content. However, the values of f_{R1k} and f_{R3k} are significantly affected by the variability of the experimentally

determined values of f_{R1} and f_{R3}. Thus, the mixes showing the highest values of f_{R1} and f_{R3} do not necessarily show the highest values of f_{R1k} and f_{R3k}. For example, PCC-3D75 and PCC-4D75 show similar values of f_{R1}, 6.34 and 6.16 MPa, respectively, while the value of f_{R1k} varies significantly (4.98 and 2.99 MPa, respectively). AASC-4D75 and AASC-5D75 show similar values of f_{R3} (8.05 and 8.30 MPa, respectively) but different values of f_{R3k} (7.4 and 6.5 MPa, respectively). Additional investigations are needed to evaluate the effect of the variability of the results on the performance of the composite, as significant variability can nullify the effect of increased fibre volume fractions.

3.3. Empirical models to derive the residual flexural strengths f_{R1} and f_{R3}

The ability to predict the values of the characteristic residual flexural strengths f_{R1k} and f_{R3k} based on the concrete matrix compressive strength and the fibre geometry and volume fraction reduces the number of experiments required to evaluate the material performance, enabling preliminary structural design and verification in reduced time and cost. Several authors [11,43,51–53] proposed empirical models to predict the residual flexural strengths f_{R1} and f_{R3} rather than their corresponding characteristic values f_{R1k} and f_{R3k} by knowing the compressive strength of the reference plain concrete and the fibre geometry and volume fraction. This is mostly because the previous version of the *fib* Model Code (*fib* Model Code 2010) required the determination of the characteristic values f_{R1k} and f_{R3k} solely for material classification rather than for design purposes. Additionally, experimental data in the literature rarely include the standard deviation from the mean values of f_{R1} and f_{R3}, making calculating the corresponding characteristic values more challenging. Table 5 summarises the currently available empirical equations to predict f_{R1} and f_{R3} developed for steel fibre-reinforced Portland cement-based concrete (SFRPCC).

Fig. 8 shows the correlation between the experimental and the predicted values of the residual flexural strengths f_{R1} and f_{R3} for SFRAASC calculated using the empirical equations collected in Table 5. To evaluate the accuracy of prediction of each empirical equation, the Integral Absolute Error (IAE) is introduced as follows:

$$\mathrm{IAE} = \frac{\sum |Q_i - P_i|}{\sum Q_i} \cdot 100 \tag{4}$$

where Q_i is the experimental data and P_i is the predicted value. Table 6 summarises the values of IAE for each empirical model collected in Table 5 and for each fibre type investigated in this study. The lower the values of IAE, the more accurate the prediction. As shown in Table 6, the correlations proposed by Moraes Neto et al. [52] and Venkateshwaran et al. [11] are the ones showing the highest and the lowest values of IAE, respectively.

The correlations proposed by Moraes Neto et al. [52] correlate the residual flexural strengths f_{R1} and f_{R3} only with the fibre reinforcing index RI_v without considering the fibre geometry, in particular, the number of hooks at the fibre ends, resulting in an underestimation of both the residual flexural strengths for SFRAASC incorporating single (3D) and multiple hooked-end steel fibres (4D and 5D). The equations proposed by Venkateshwaran et al. [11] can predict the values of the residual strengths f_{R1} and f_{R3} for SFRAASC quite accurately for each fibre type.

Although calibrated for SFRPCC, the empirical equations proposed by Venkateshwaran et al. [11] show the best accuracy of prediction also for SFRAASC. The general form of such correlations is given in Eqs. (5) and (6), where A, B, C, D, E and F are the coefficients to be recalibrated using the experimental data generated in this study for SFRAASC.

$$f_{R1} = \Psi \cdot \left(A \cdot (f_{cm})^{1/2} + B \cdot RI_v + C \cdot N^2 \right) \tag{5}$$

$$f_{R3} = \Psi \cdot \left(D \cdot (f_{cm})^{1/2} + E \cdot RI_v + F \cdot N^2 \right) \tag{6}$$

with $\Psi = \left(1 + l_f/100\right)^{1/2}$, f_{cm} is the mean cylindrical compressive strength, $RI_v = v_f \cdot \left(l_f/d_f\right)$ is the fibre reinforcing index (v_f = fibre volume fraction, l_f = fibre length, d_f = fibre diameter) and N is the number of hooked ends of the steel fibres ($N = 1$ for 3Dfibres, $N = 1.5$ for 4D fibres and $N = 2$ for 5D fibres).

The coefficients A – F have been recalibrated by minimising the objective function defined as the mean of the sum of the squares of the difference between the experimental and predicted values. The Generalised Reduced Gradient (GRG) non-linear optimisation algorithm available in Microsoft Excel® Solver add-in has been used to carry out the recalibration. The newly calibrated equations are:

$$f_{R1} = \Psi \cdot \left(0.063 \cdot (f_{cm})^{1/2} + 10.991 \cdot RI_v + 0.064 \cdot N^2 \right) \tag{7}$$

Table 7
IAE values of the original and newly calibrated empirical correlations.

Empirical model	IAE [%]					
	3D		4D		5D	
	f_{R1}	f_{R3}	f_{R1}	f_{R3}	f_{R1}	f_{R3}
Venkateshwaran et al. [11]	10.6	11.3	13.6	9.1	19.8	21.9
New correlations	7.1	8.8	3.5	6.2	3.4	15.2

Table 8
Values of the coefficients $A - F$ proposed by Venkateshwaran et al. and the newly calibrated ones.

Empirical model	Coefficient					
	f_{R1k}			f_{R3k}		
	A	B	C	D	E	F
Venkateshwaran et al. [11]	0.226	5.447	−0.149	0.201	6.830	0.182
New correlations	−0.103	10.466	0.053	−0.029	11.115	0.069

Table 9
IAE values of the original and newly calibrated empirical correlations.

Empirical model	IAE [%]					
	3D		4D		5D	
	f_{R1k}	f_{R3k}	f_{R1k}	f_{R3k}	f_{R1k}	f_{R3k}
Venkateshwaran et al. [11]	13.2	15.3	31.6	19.2	29.0	19.5
New correlations	20.9	13.0	10.2	10.0	12.5	11.9

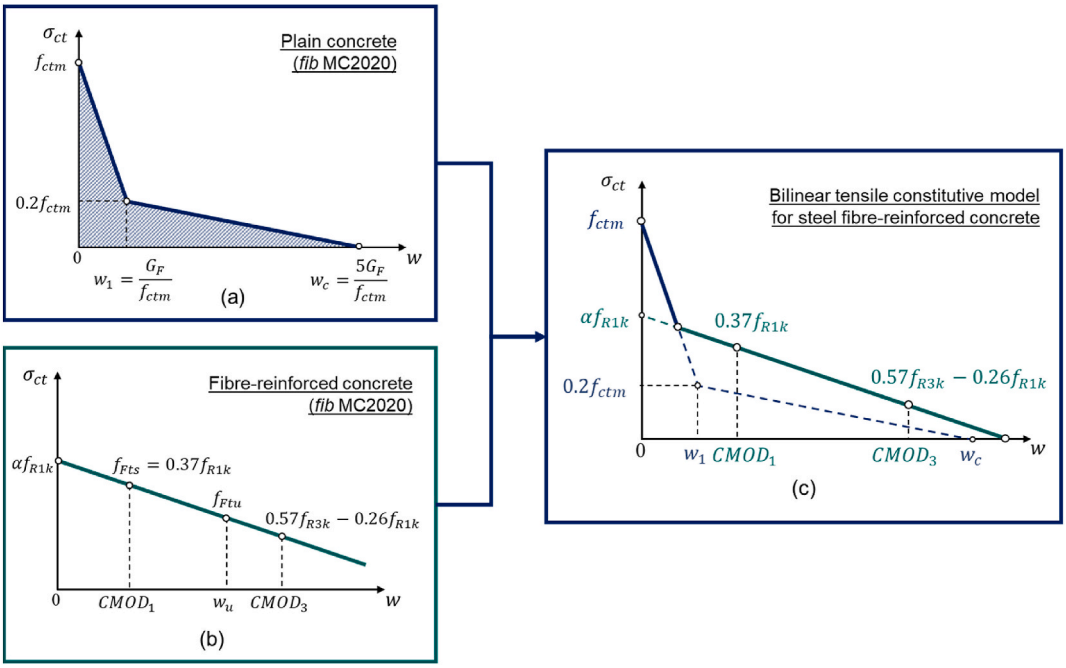

Fig. 10. Tensile constitutive models for (a) plain concrete and (b) steel fibre-reinforced concrete according to the *fib* Model Code 2020. The post-cracking bilinear tensile stress-crack opening for steel fibre-reinforced concrete is described by (c).

$$f_{R3} = \Psi \cdot \left(0.169 \cdot (f_{cm})^{1/2} + 11.037 \cdot RI_v + 0.059 \cdot N^2\right) \tag{8}$$

Table 7 shows the IAE values for the newly calibrated coefficients, while Fig. 9 shows the correlation between the experimental and predicted values of f_{R1} and f_{R3} obtained by using the newly proposed empirical models. Significant improvements in the accuracy of the prediction of f_{R1} can be observed for all fibre types, whereas minor improvements can be seen for f_{R3}.

Venkateshwaran et al. [11] proposed empirical equations to derive the characteristic residual flexural strengths f_{R1k} and f_{R3k} based on the same general correlations proposed in Eq. (5) and Eq. (6). Following the same approach used in this section for f_{R1} and f_{R3}, the coefficients of such equations can be recalibrated using the characteristic values f_{R1k} and f_{R3k} calculated from the experimental values obtained in this study. The newly recalibrated equations can be written as follows:

$$f_{R1k} = \Psi \cdot \left(-0.103 \cdot (f_{cm})^{1/2} + 10.466 \cdot RI_v + 0.053 \cdot N^2\right) \tag{9}$$

$$f_{R3k} = \Psi \cdot \left(-0.029 \cdot (f_{cm})^{1/2} + 11.115 \cdot RI_v + 0.069 \cdot N^2 \right) \quad (10)$$

Tables 8 and 9 summarise the coefficients $A - F$ proposed by Venkateshwaran et al. [11] and the newly calibrated ones, and their corresponding IAE values, respectively. As observed for the residual flexural strength f_{R1} and f_{R3}, the contribution of the compressive strength and the number of bends at the end of the fibre is less relevant for SFRAASC than SFRPCC, while the fibre reinforcing index RI_v seems to play a more significant effect. Negative values of the coefficients A and D could be the result of the limited amount of data used for the calibration and their limited variability. The experimental data used by Venkateshwaran et al. [11] exhibit a 28-day compressive strength ranging from 28.1 to 56.1 MPa, while in this study the 28-day compressive strength of SFRAASC ranges from 43.8 to 52.6 MPa. Thus, additional experimental data are needed to validate such conclusion.

As shown in Table 9, the values of the IAE decreases for each fibre type, proving the need of further calibration of currently existing empirical equations for alternative binders such as alkali-activated slag-based concrete incorporating steel fibres.

3.4. Verification of the fib Model Code 2020 tensile constitutive model

3.4.1. fib Model Code 2020 tensile costitutive model

A bilinear tensile stress-crack opening constitutive model describing the tensile post-cracking behaviour of steel fibre-reinforced concrete can be derived from three-point bending tests (Fig. 10c). According to the *fib* Model Code 2020 [47], the first branch of the curve can be derived from the post-cracking response of plain concrete under uniaxial tension (Fig. 10a).

The stress-crack opening relationship is described as follows:

$$\sigma_{ct} = \begin{cases} f_{ctm} \cdot (1 - 0.8 \cdot (w/w_1)), w < w_1 \\ f_{ctm} \cdot (0.25 - 0.05 \cdot (w/w_1)), w_1 < w \leq w_c \end{cases} \quad (11)$$

where $w_1 = G_F/f_{ctm}$ and $w_c = 5 \cdot G_F/f_{ctm}$ are the crack openings at $\sigma_{ct} = 0.20 \cdot f_{ctm}$ and $\sigma_{ct} = 0$, respectively, and f_{ctm} and G_F are the tensile strength and the fracture energy, respectively. For plain concrete, f_{ctm} and G_F can be derived as follows:

$$f_{ctm} = 1.8 \cdot \ln(f_{ck}) - 3.1 \quad (12)$$

$$G_F = 85 \cdot (f_{ck})^{0.15} = 85 \cdot (f_{cm} - 8)^{0.15} \quad (13)$$

where f_{ck} and f_{cm} represent the characteristic and mean cylindrical compressive strength of the plain concrete, respectively. The second branch of the tensile constitutive model is defined by the *fib* Model Code 2020 for steel fibre-reinforced cement-based concrete (SFRPCC). The linear post-cracking stress-crack opening correlation represents the behaviour of SFRPCC at the serviceability limit state (SLS), which is assumed to be elastoplastic in uniaxial tension and elastic in uniaxial compression. At the ultimate limit state (ULS), the compressive stress is concentrated at the upper part of the cross-section and a crack opening of 2.5 mm at the lower part is considered [54].

As shown in Fig. 10b, the post-cracking stress-crack opening relationship depends on the characteristic values of the residual flexural tensile strengths f_{R1k} and f_{R3k}, corresponding to a crack mouth opening displacement (CMOD) of 0.5 mm ($CMOD_1$) and 2.5 mm ($CMOD_3$), respectively.

Once the values of the characteristic values f_{R1k} and f_{R3k} have been calculated, the tensile stress-crack opening relationships according to the *fib* Model Code 2020 can be derived, introducing the residual flexural strengths f_{Fts} and f_{Ftu}. The first represents the residual flexural strength corresponding to the serviceability limit state (SLS), *i.e.* the post-cracking strength for serviceability crack opening of 0.5 mm, while the latter represents the residual flexural strength corresponding to the ultimate limit state (ULS), *i.e.* the post-cracking strength for ultimate crack opening of 2.5 mm. The values f_{Fts} and f_{Ftu} can be calculated as follows:

$$f_{Fts} = 0.37 \cdot f_{R1k} \quad (14)$$

$$f_{Ftu} = f_{Fts} - \frac{w_u}{CMOD_3}\left(f_{Fts} - 0.57 \cdot f_{R3k} + 0.26 \cdot f_{R1k}\right) \geq 0 \quad (15)$$

where w_u = maximum crack opening accepted in structural design. In this study, a value of w_u equal to 2.5 mm is used, thus, Eq. (15) can be rewritten as follows:

Table 10
CDP model parameters available in the literature for plain PCC and the values used for SFRPCC and SFRAASC.

Parameter	Plain PCC (from the literature)	SFRPCC and SFRAASC (this study)
σ_{b0}/σ_{c0}	1.12	1.16
K_c	$0.64 \leq K_c \leq 0.80$	0.6667
Φ	$25° \leq \Phi \leq 40°$	50°
e	0.1	0.1

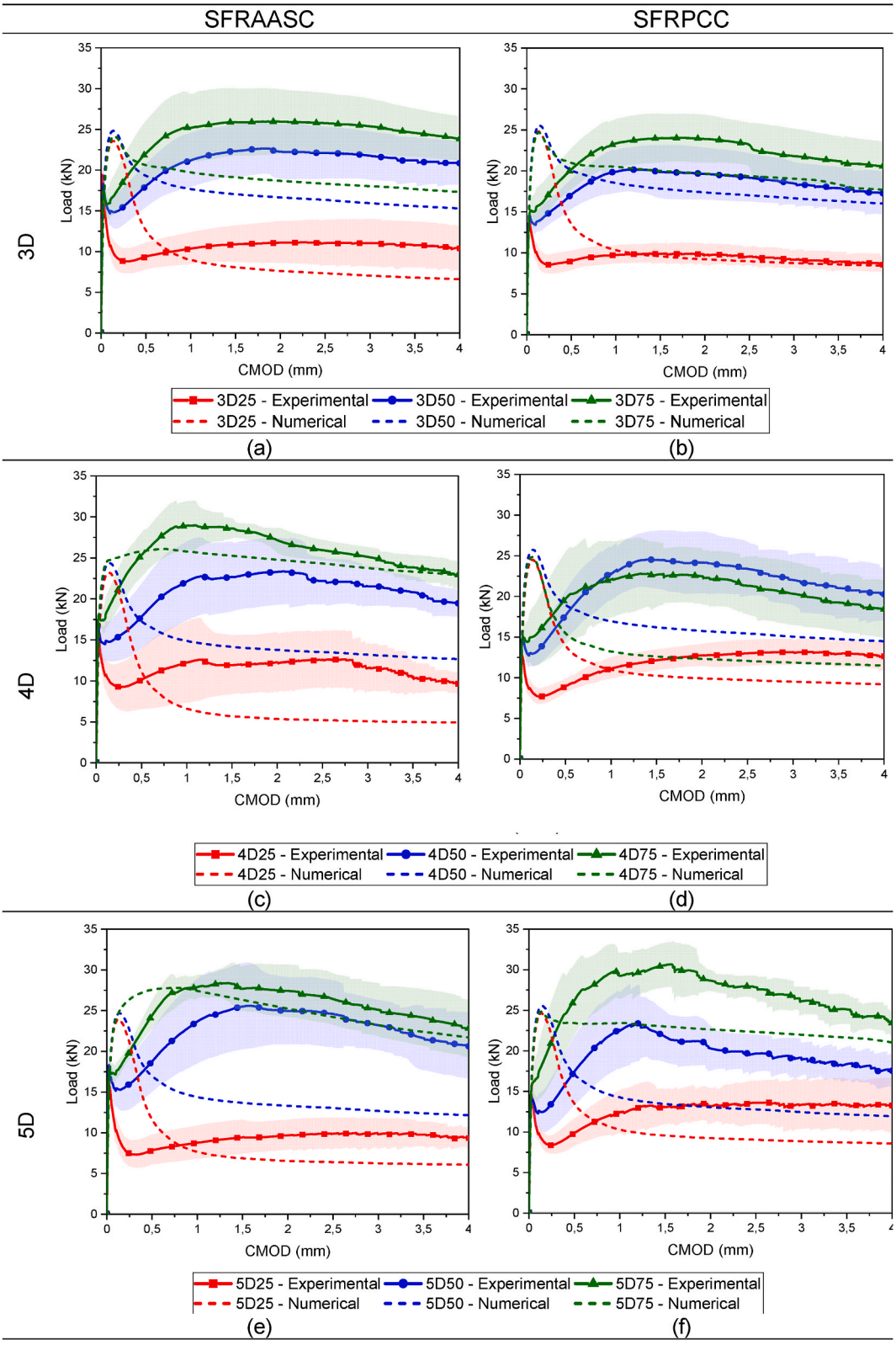

Fig. 11. Experimental and numerical Load-CMOD curve for each concrete matrix and steel fibre type.

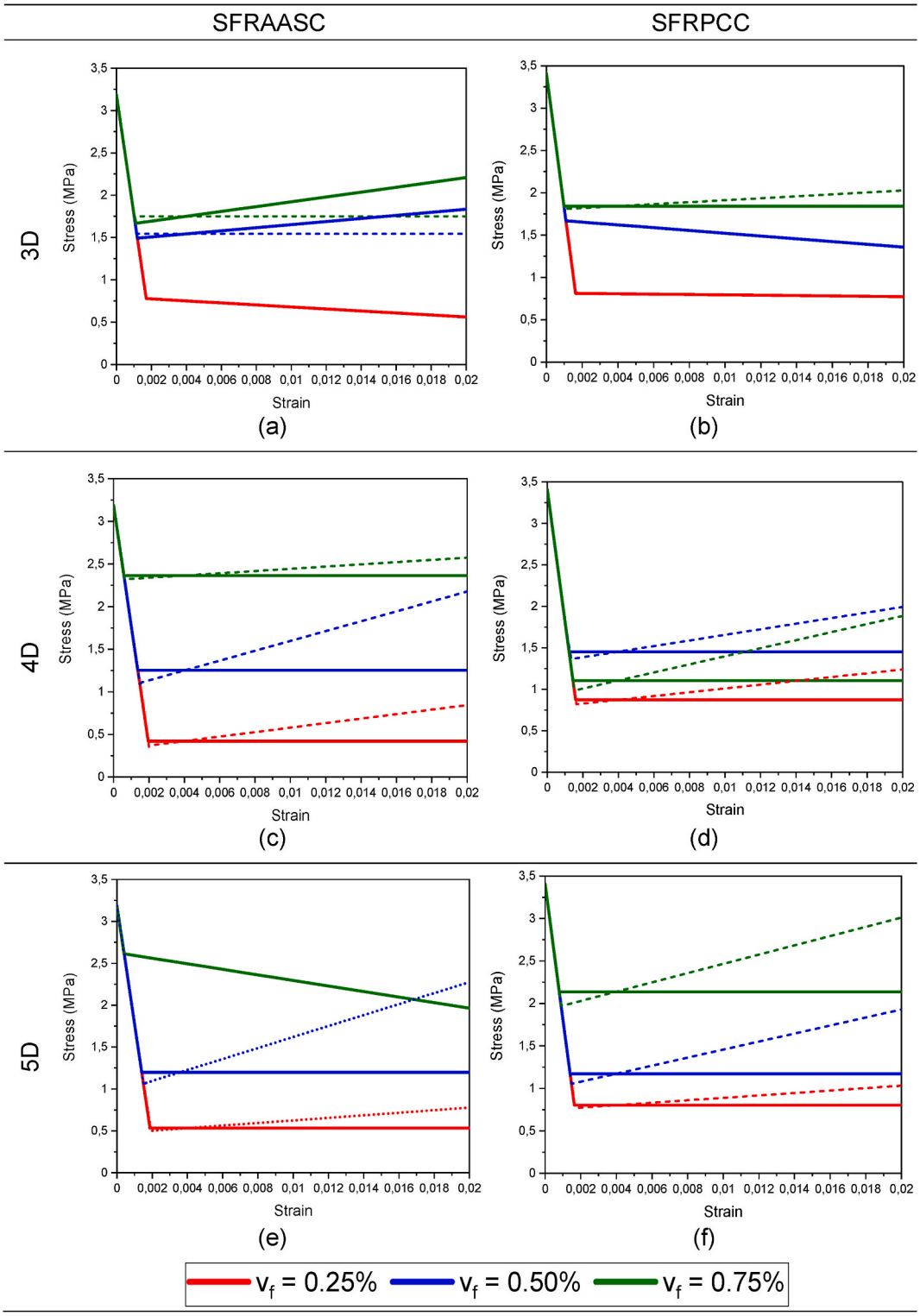

Fig. 12. Bilinear stress-strain tensile relationships for SFRAASC and SFRPCC. The dashed lines indicate the correlations obtained from the *fib* Model Code 2020 while the bold lines represent the correlations used for the numerical simulations.

$$f_{Ftu} = 0.57 \cdot f_{R3k} - 0.26 \cdot f_{R1k} \quad (16)$$

Once the values of the residual flexural strengths f_{R1} and f_{R3} and the corresponding characteristic values f_{R1k} and f_{R3k} are known, the tensile constitutive laws proposed by the *fib* Model Code 2020 can be derived for each fibre and concrete matrix type and used as input parameters for numerical simulations. From the stress-crack opening relationships, stress-strain curves can be derived according to the following equations:

$$\varepsilon_{SLS} = 0.5\ mm/l_{cs} \quad (17)$$

$$\varepsilon_{ULS} = w_u/l_{cs} \quad (18)$$

where l_{cs} is the characteristic length, which is assumed to be 125 mm in this study for each concrete matrix and fibre type.

3.4.2. Numerical simulations

The Concrete Damage Plasticity (CDP) model available in ABAQUS Software has been chosen for numerical simulations. The CDP model combines isotropic damage elasticity and isotropic compressive and tensile plasticity, allowing the prediction of the behaviour of unreinforced concrete. Although originally developed for plain cement-based concrete, several authors [55–58] applied the CDP model to fibre-reinforced concrete too, considering the composite as a homogeneous continuous material and refining the model plasticity parameters to consider the effect of fibre incorporation. These parameters, such as the ratio of the initial biaxial compressive yield stress to the initial uniaxial yield stress (σ_{b0}/σ_{c0}), the ratio of the second stress invariant on the tensile meridian to the compressive meridian at the initial yield (K_c), dilation angle (Φ) and eccentricity (e) can be obtained experimentally or they can be found in the literature for traditional cement-based concrete (PCC) with and without steel fibres [56,59–61]. The same parameters used for SFRPCC are used also for SFRAASC and they are summarised in Table 10.

Fig. 11 shows the experimental and numerical load-CMOD curves obtained for each concrete matrix and steel fibre type. For both SFRAASC and SFRPCC, the numerical model is able to capture qualitatively the post-cracking response for each fibre type and dosage. For the lowest fibre volume fraction (0.25 %), the numerical model can predict quite accurately the post-peak response of both composites. However, the peak load is overestimated, suggesting an over-prediction of the tensile strength by the constitutive model. At higher fibre volume fractions the numerical results underestimate the post-peak behaviour for both composites and all fibre types. Improving the tensile constitutive law does not necessarily lead to better numerical predictions, as demonstrated through inverse analysis in Appendix A. This suggests the inability of the CDP model to account for post-peak hardening behaviour in tension regime as shown in Fig. 11 due to theoretical limitations. As a result, the effective post-peak tensile behaviour (dashed lines in Fig. 12) has been approximated in most cases with a flatter slop as input parameter for numerical simulations. To capture the experimental post-peak hardening behaviour, discrete models explicitly accounting for fibre geometry, orientation and distribution, as the one developed by Zhang et al. [62], should be used.

4. Conclusions

This study evaluated the post-cracking flexural behaviour of steel fibre-reinforced alkali-activated slag-based concrete (SFRAASC) and same strength-grade steel fibre-reinforced cement-based concrete (SFRPCC) incorporating single (3D) and multiple (4D and 5D) hooked-end steel fibres in different volume fractions up to 0.75 %. From the experimental Load-CMOD curves, the values of the residual flexural strength f_{R1} and f_{R3} corresponding to CMOD values of 0.5 mm and 2.5 mm, respectively, have been derived. Such values have been then used to verify the applicability to SFRAASC of currently available empirical models developed for SFRPCC to predict the values of the residual strengths f_{R1} and f_{R3} by knowing the properties of the reference concrete matrix and the fibre geometry and volume fraction. Additionally, the values of f_{R1} and f_{R3} have been used to derive tensile stress-crack opening constitutive models for finite element numerical simulations. The concrete damage plasticity (CDP) model available in ABAQUS Software has been used to simulate the post-cracking behaviour of each composite. Based on the experimental and numerical investigations carried out in this study, the following conclusions can be drawn:

- The incorporation of single (3D) and multiple (4D and 5D) hooked-end steel fibres in different volume fractions has a limited effect on the flexural strength corresponding to the limit of proportionality (f_{LOP}) for both SFRAASC and SFRPCC, as it mainly depends on the mechanical behaviour of concrete matrix. However, SFRAASC mixes exhibit higher values of f_{LOP} than SFRPCC for each fibre type and volume fraction, resulting in higher resistance to flexural loading of the alkali-activated slag-based concrete matrix in comparison to a similar strength-grade cement-based concrete.
- The post-peak residual flexural strengths f_{R1} and f_{R3}, corresponding to a CMOD of 0.5 mm and 2.5 mm, respectively, increase with the increase in the fibre volume fraction for each fibre and concrete matrix type. SFRAASC mixes incorporating 3D fibres show higher values of residual flexural strengths in comparison to SFRPCC mixes incorporating the same fibre type and dosage. Although

SFRAASC and SFRPCC mixes incorporating 4D fibres in different volume fractions exhibit similar post-cracking behaviour, SFRPCC mixes incorporating 5D fibres outperform SFRAASC mixes incorporating the same fibres in the same volume fractions.

- The currently available empirical models for SFRPCC predicting the residual flexural strengths f_{R1} and f_{R3} generally overestimate the values of residual flexural strengths of SFRAASC and therefore need to be recalibrated. The empirical equations proposed by Venkateshwaran et al. [11] show the highest accuracy in predicting the residual flexural strengths of SFRAASC, thus, the equations coefficients have been recalibrated using the experimental data generated in this study and new empirical correlations have been proposed.
- The Concrete Damage Plasticity (CDP) model available in ABAQUS Software together with the *fib* Model Code 2020 qualitatively captures the behaviour of SFRAASC and SFRPCC composites incorporating single and multiple hooked-end steel fibres. However, the model proposed by the *fib* Model Code 2020 overestimate the composite peak stress. Additionally, the numerical model underestimates its post-peak behaviour, when fibre volume fractions higher than 0.25 % are used as post-cracking hardening behaviour is not accounted for in the CDP model. In summary, for higher fibre content the numerical model fails to quantitatively capture the experimental results. This is due to inherit theoretical limitation of the CDP model to account for the tensile post-cracking hardening behaviour.

This study is a first step in evaluating and understanding the post-cracking behaviour of steel fibre-reinforced alkali-activated concrete (SFRAASC) highlighting its potential as an alternative to SFRPCC for structural applications. However, further investigations are needed. Single and multiple hooked-end steel fibres should be incorporated in alkali-activated slag-based concretes of different strength grades to evaluate the effect of the concrete matrix properties on the performance of the composite. Furthermore, the fibre-matrix bond interaction should also be investigated to evaluate its effect on the flexural response of the composite. The post-cracking response of the composite, the concrete matrix properties and the fibre-matrix bond strength can then be used as input parameters for numerical simulations. Modelling each steel fibre explicitly can help to alleviate shortcomings of code-based constitutive models, as shown in this study.

CRediT authorship contribution statement

Laura Rossi: Writing – original draft, Validation, Methodology, Investigation, Formal analysis, Conceptualization. **Maria Paula Zappitelli:** Writing – original draft, Visualization, Software, Methodology, Formal analysis, Conceptualization. **Ravi A. Patel:** Writing – review & editing, Supervision, Methodology, Formal analysis, Conceptualization. **Frank Dehn:** Writing – review & editing, Supervision, Resources, Funding acquisition.

Declaration of competing interest

The authors declare that they have no known competing financial interests or personal relationships that could have appeared to influence the work reported in this paper.

Acknowledgements

This project has received funding from the European Union's Horizon 2020 research and innovation programme under grant agreement No 813596 DuRSAAM. The opinions expressed in this document reflect only the author's view and reflect in no way the European Commission's opinions. The European Commission is not responsible for any use that may be made of the information it contains.

Appendix

Numerical inverse analysis

After evaluating the applicability of the tensile constitutive model proposed by the *fib* Model Code 2020 to SFRAASC, inverse analysis was also used to derive a new tensile stress-displacement relationship as input parameter for finite element simulations to improve the accuracy of prediction. A trilinear tensile softening relationship was used for inverse analysis, as shown in Figure A.1.

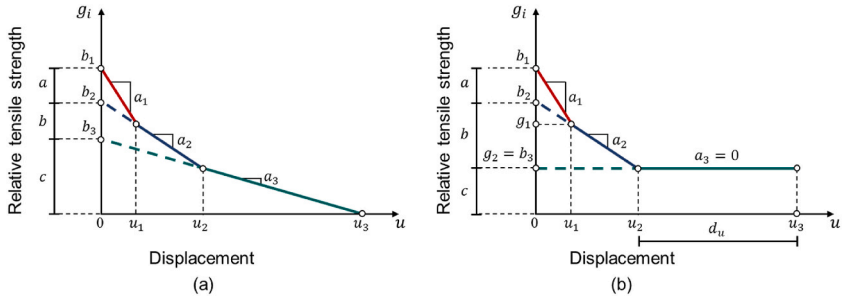

Fig. A.1. Tensile post-cracking trilinear stress-displacement curve used for (a) plain and (b) fibre-reinforced concrete, for both SFRPCC and SFRAASC.

The trilinear softening law is defined by non-dimensional parameters (g_i) obtained by normalising the tensile stress σ with the tensile strength f_t. Each segment of the trilinear curve is defined by two parameters, a_i and b_i, which represent the slope of the segment and its intercept with the y-axis, respectively.

The equations describing each segment are presented in Eq. (A.1) [43,63]:

$$g_i(u) = \frac{\sigma_i(u)}{f_t} = b_i - a_i \cdot u = \begin{cases} 1 - a_1 \cdot u, 0 \le u \le u_1 \\ b_2 - a_2 \cdot u, u_1 \le u \le u_2 \\ b_3 - a_3 \cdot u, u_2 \le u \le u_3 \end{cases} \tag{A.1}$$

The parameters to be optimized are b_i ($i = 2, 3$) and a_i ($i = 1, 2, 3$) for plain concrete. For steel fibre-reinforced concrete, the slope of the third segment is considered zero [68] and the displacement u_3 is increasing to a value d_u. To improve the definition of the bounds in the optimisation, b_i ($i = 2, 3$) parameters are not directly optimized. Instead, the parameters a, b and c (Fig. 2) are introduced. Clearly:

$$a + b + c = 1 \tag{A.2}$$

The number of optimisation parameters can be further reduced by introducing additional parameters α and β, correlating the parameters a, b and c as follows:

$$\alpha = \frac{a}{b}$$

$$\beta = \frac{b}{c} \tag{A.3}$$

Thus, replacing equation (A.2) and (A.3) in (A.1), b_i can be written depending on α and β (Eq. (A.4)):

$$b_2 = 1 - \alpha \cdot \left(\frac{1}{1 + \alpha + \beta}\right)$$

$$b_3 = 1 - (\alpha + \beta) \cdot \left(\frac{1}{1 + \alpha + \beta}\right) \tag{A.4}$$

Only the parameters α, β, a_i ($i = 1, 2, 3$) and d_u need to be optimized through inverse analysis. Global optimisation is performed using a differential evolution algorithm of the SciPy package [69]. The objective function for minimization is the difference between the load-CMOD curve obtained from numerical simulations and experiments. To have meaningful results bounds for the parameters to be optimized are given as follows:

$$a_1 \in [1, 1000],\ a_2 \in [0.1, 10],\ \alpha,\ \beta \in [0.1, 0.95],\ d_u \in [3, 5],\ \text{and}\ f_t \in [2, 4]$$

The experimental three-point bending tests performed for each concrete type (AASC and PCC) incorporating different fibre types (3D, 4D and 5D) at different volume fractions (0 %, 0.25 %, 0.50 % and 0.75 %) are modelled in ABAQUS/Explicit, considering symmetry in the middle of the notched beam. Horizontal and vertical displacements are constrained in the supports at the ends of the beam. The loading is applied as a vertical displacement along the symmetry axis of the beam. The performed analysis was quasi-static, thus, mass scaling was included to accelerate the analysis time. A quadrilateral mesh with CP4SR (four-node bilinear plane stress quadrilateral, reduced integration) elements was used. The element spacing considered was 8 mm, resulting in 662 elements.

Figure A.2 shows the output from inverse analysis and its comparison with the experimental load-CMOD curves obtained for SFRAASC and SFRPCC. The results obtained from inverse analysis are able to qualitatively capture the experimental curves for both the pre-and post-cracking phases. In terms of quantitative evaluation, the model predictions and the experimental results agree well for the reference mix and the mixes incorporating 0.25 % fibre volume fraction for both SFRAASC and SFRPCC. For higher fibre contents, significant differences exist between the numerical model and the experimental load-CMOD curves. This is mainly due to the assumption in the CDP model of a homogeneous material, *i.e.* the steel fibres and the concrete matrix are not modelled separately. Furthermore, continuum damage mechanics suffers from theoretical limitation due to the assumption of monotonically decreasing values for the post-peak tensile stress-displacement function. This is contradictory to the real behaviour of SFRAAC and SFRPCC with

higher fibre volume fractions, for which a post-cracking hardening behaviour can be observed.

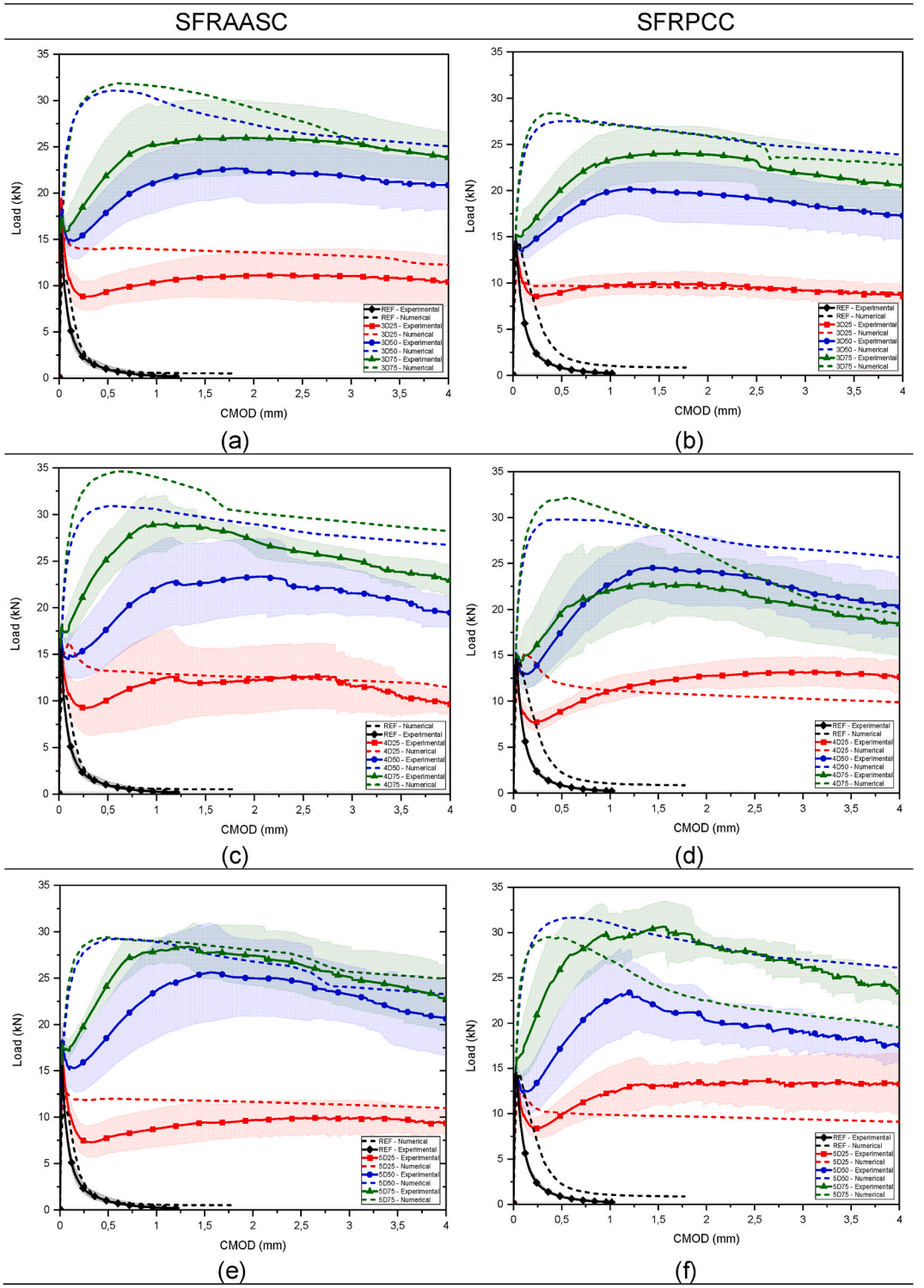

Fig. A.2. Experimental and numerical (dashed lines) load-CMOD curves for SFRAASC and SFRPCC mixes incorporating (a-b) 3D, (c-d) 4D, and (e-f) 5D steel fibres in different volume fractions.

Data availability

Data will be made available on request.

References

[1] A. Adesina, Performance of fibre reinforced alkali-activated composites – a review, Materialia 12 (Jan. 2020) 100782, https://doi.org/10.1016/j.mtla.2020.100782.

[2] G. Chen, D. Gao, H. Zhu, J. Song Yuan, X. Xiao, W. Wang, Effects of novel multiple hooked-end steel fibres on flexural tensile behaviour of notched concrete beams with various strength grades, Structures 33 (Jan. 2021) 3644–3654, https://doi.org/10.1016/j.istruc.2021.06.016.

[3] S. Guler, Z.F. Akbulut, Residual strength and toughness properties of 3D, 4D and 5D steel fiber-reinforced concrete exposed to high temperatures, Construct. Build. Mater. 327 (Jan. 2022) 126945, https://doi.org/10.1016/j.conbuildmat.2022.126945.

[4] D. joo Kim, A.E. Naaman, S. El-Tawil, Comparative flexural behavior of four fiber reinforced cementitious composites, Cem. Concr. Compos. 30 (10) (Jan. 2008) 917–928, https://doi.org/10.1016/j.cemconcomp.2008.08.002.

[5] B. Li, L. Xu, Y. Shi, Y. Chi, Q. Liu, C. Li, Effects of fiber type, volume fraction and aspect ratio on the flexural and acoustic emission behaviors of steel fiber reinforced concrete, Construct. Build. Mater. 181 (Jan. 2018) 474–486, https://doi.org/10.1016/j.conbuildmat.2018.06.065.

[6] A. Enfedaque, M.G. Alberti, J.C. Gálvez, P. Cabanas, Numerical simulation of the fracture behavior of high-performance fiber-reinforced concrete by using a cohesive crack-based inverse analysis, Mater. Basel Switz. 15 (1) (Jan. 2021), https://doi.org/10.3390/ma15010071.

[7] S. Abdallah, M. Fan, X. Zhou, Pull-out behaviour of hooked end steel fibres embedded in ultra-high performance mortar with various W/B ratios, Int. J. Concr. Struct. Mater. 11 (2) (Jan. 2017) 301–313, https://doi.org/10.1007/s40069-017-0193-8.

[8] F.U.A. Shaikh, Y. Shafaei, P.K. Sarker, Effect of nano and micro-silica on bond behaviour of steel and polypropylene fibres in high volume fly ash mortar, Construct. Build. Mater. 115 (Jan. 2016) 690–698, https://doi.org/10.1016/j.conbuildmat.2016.04.090.

[9] S. Abdallah, M. Fan, X. Zhou, S. Le Geyt, Anchorage effects of various steel fibre architectures for concrete reinforcement, Int. J. Concr. Struct. Mater. 10 (3) (Jan. 2016) 325–335, https://doi.org/10.1007/s40069-016-0148-5.

[10] G. Tiberti, F. Germano, A. Mudadu, G.A. Plizzari, An overview of the flexural post-cracking behavior of steel fiber reinforced concrete, Struct. Concr. 19 (3) (Jan. 2018) 695–718, https://doi.org/10.1002/suco.201700068.

[11] A. Venkateshwaran, K.H. Tan, Y. Li, Residual flexural strengths of steel fiber reinforced concrete with multiple hooked-end fibers, Struct. Concr. 19 (2) (Jan. 2018) 352–365, https://doi.org/10.1002/suco.201700030.

[12] M. Amran, et al., Fiber-reinforced alkali-activated concrete: a review, J. Build. Eng. 45 (Jan. 2022) 103638, https://doi.org/10.1016/j.jobe.2021.103638.

[13] Y. Ding, J.-G. Dai, C.-J. Shi, Fracture properties of alkali-activated slag and ordinary Portland cement concrete and mortar, Construct. Build. Mater. 165 (Jan. 2018) 310–320, https://doi.org/10.1016/j.conbuildmat.2017.12.202.

[14] Y. Du, J. Wang, C. Shi, H.-J. Hwang, N. Li, Flexural behavior of alkali-activated slag-based concrete beams, Eng. Struct. 229 (Jan. 2021) 111644, https://doi.org/10.1016/j.engstruct.2020.111644.

[15] H.-J. Lim, C.-G. Cho, J.-Y. You, J.-J. Jeong, Mechanical properties of alkali-activated slag fiber composites varying with fiber volume fractions, Mater. Basel Switz 15 (18) (Jan. 2022), https://doi.org/10.3390/ma15186444.

[16] Ü. Yurt, An experimental study on fracture energy of alkali activated slag composites incorporated different fibers, J. Build. Eng. 32 (Jan. 2020) 101519, https://doi.org/10.1016/j.jobe.2020.101519.

[17] S. Bernal, R. Mejía de Gutiérrez, E. Rodríguez, S. Delvasto, F. Puertas, Mechanical behaviour of steel fibre-reinforced alkali activated slag concrete, Mater. Constr. 59 (293) (Jan. 2009) 53–62, https://doi.org/10.3989/mc.2009.41807.

[18] N. Ranjbar, M. Zhang, Fiber-reinforced geopolymer composites: a review, Cem. Concr. Compos. 107 (Jan. 2020) 103498, https://doi.org/10.1016/j.cemconcomp.2019.103498.

[19] H. El-Hassan, S. Elkholy, Enhancing the performance of Alkali-Activated Slag-Fly ash blended concrete through hybrid steel fiber reinforcement, Construct. Build. Mater. 311 (Jan. 2021) 125313, https://doi.org/10.1016/j.conbuildmat.2021.125313.

[20] A. Adesina, S. Das, Drying shrinkage and permeability properties of fibre reinforced alkali-activated composites, Construct. Build. Mater. 251 (Jan. 2020) 119076, https://doi.org/10.1016/j.conbuildmat.2020.119076.

[21] M.H. Al-Majidi, A. Lampropoulos, A.B. Cundy, Steel fibre reinforced geopolymer concrete (SFRGC) with improved microstructure and enhanced fibre-matrix interfacial properties, Construct. Build. Mater. 139 (Jan. 2017) 286–307, https://doi.org/10.1016/j.conbuildmat.2017.02.045.

[22] N.P. Asrani, et al., A feasibility of enhancing the impact resistance of hybrid fibrous geopolymer composites: experiments and modelling, Construct. Build. Mater. 203 (Jan. 2019) 56–68, https://doi.org/10.1016/j.conbuildmat.2019.01.072.

[23] S. Aydın, B. Baradan, The effect of fiber properties on high performance alkali-activated slag/silica fume mortars, Compos. Part B Eng. 45 (1) (Jan. 2013) 63–69, https://doi.org/10.1016/j.compositesb.2012.09.080.

[24] K. Behfarnia, M. Rostami, Mechanical properties and durability of fiber reinforced alkali activated slag concrete, J. Mater. Civ. Eng. 29 (12) (Jan. 2017) 04017231, https://doi.org/10.1061/(ASCE)MT.1943-5533.0002073.

[25] S. Bernal, R. Gutierrez, S. Delvasto, E. Rodriguez, Performance of an alkali-activated slag concrete reinforced with steel fibers, Construct. Build. Mater. 24 (2) (Jan. 2010) 208–214, https://doi.org/10.1016/j.conbuildmat.2007.10.027.

[26] J.-I. Choi, B.Y. Lee, R. Ranade, V.C. Li, Y. Lee, Ultra-high-ductile behavior of a polyethylene fiber-reinforced alkali-activated slag-based composite, Cem. Concr. Compos. 70 (Jan. 2016) 153–158, https://doi.org/10.1016/j.cemconcomp.2016.04.002.

[27] S.-J. Choi, J.-I. Choi, J.-K. Song, B.Y. Lee, Rheological and mechanical properties of fiber-reinforced alkali-activated composite, Construct. Build. Mater. 96 (Jan. 2015) 112–118, https://doi.org/10.1016/j.conbuildmat.2015.07.182.

[28] H. El-Hassan, S. Elkholy, Performance evaluation and microstructure characterization of steel fiber–reinforced alkali-activated slag concrete incorporating fly ash, J. Mater. Civ. Eng. 31 (10) (Jan. 2019), https://doi.org/10.1061/(ASCE)MT.1943-5533.0002872, 04019223 vols.

[29] K.Z. Farhan, M.A.M. Johari, R. Demirboğa, Impact of fiber reinforcements on properties of geopolymer composites: a review, J. Build. Eng. 44 (Jan. 2021) 102628, https://doi.org/10.1016/j.jobe.2021.102628.

[30] N.A. Farhan, M.N. Sheikh, M.N.S. Hadi, Engineering properties of ambient cured alkali-activated fly ash–slag concrete reinforced with different types of steel fiber, J. Mater. Civ. Eng. 30 (7) (Jan. 2018), https://doi.org/10.1061/(ASCE)MT.1943-5533.0002333, 04018142 vols.

[31] N. Ganesan, R. Abraham, S. Deepa Raj, Durability characteristics of steel fibre reinforced geopolymer concrete, Construct. Build. Mater. 93 (Jan. 2015) 471–476, https://doi.org/10.1016/j.conbuildmat.2015.06.014.

[32] X. Guo, X. Pan, Mechanical properties and mechanisms of fiber reinforced fly ash–steel slag based geopolymer mortar, Construct. Build. Mater. 179 (Jan. 2018) 633–641, https://doi.org/10.1016/j.conbuildmat.2018.05.198.

[33] N. Hammad, A. El-Nemr, H. El-Deen Hasan, The performance of fiber GGBS based alkali-activated concrete, J. Build. Eng. 42 (Jan. 2021) 102464, https://doi.org/10.1016/j.jobe.2021.102464.

[34] A. Koenig, et al., Flexural behaviour of steel and macro-PP fibre reinforced concretes based on alkali-activated binders, Construct. Build. Mater. 211 (Jan. 2019) 583–593, https://doi.org/10.1016/j.conbuildmat.2019.03.227.

[35] C.K. Lau, T.N.S. Htut, J.J. Melling, A. Chegenizadeh, T.S. Ng, Torsional behaviour of steel fibre reinforced alkali activated concrete, Mater. Basel Switz. 13 (15) (Jan. 2020), https://doi.org/10.3390/ma13153423.

[36] Q. Meng, et al., Steel fibre reinforced alkali-activated geopolymer concrete slabs subjected to natural gas explosion in buried utility tunnel, Construct. Build. Mater. 246 (Jan. 2020) 118447, https://doi.org/10.1016/j.conbuildmat.2020.118447.

[37] B. Nematollahi, J. Sanjayan, F.U.A. Shaikh, Matrix design of strain hardening fiber reinforced engineered geopolymer composite, Compos. Part B Eng. 89 (Jan. 2016) 253–265, https://doi.org/10.1016/j.compositesb.2015.11.039.
[38] B. Nematollahi, J. Sanjayan, F.U.A. Shaikh, Comparative deflection hardening behavior of short fiber reinforced geopolymer composites, Construct. Build. Mater. 70 (Jan. 2014) 54–64, https://doi.org/10.1016/j.conbuildmat.2014.07.085.
[39] F.U.A. Shaikh, Review of mechanical properties of short fibre reinforced geopolymer composites, Construct. Build. Mater. 43 (Jan. 2013) 37–49, https://doi.org/10.1016/j.conbuildmat.2013.01.026.
[40] K. Zada Farhan, M. Azmi Megat Johari, R. Demirboğa, Evaluation of properties of steel fiber reinforced GGBFS-based geopolymer composites in aggressive environments, Construct. Build. Mater. 345 (Jan. 2022) 128339, https://doi.org/10.1016/j.conbuildmat.2022.128339.
[41] X. Zhou, Y. Zeng, P. Chen, Z. Jiao, W. Zheng, Mechanical properties of basalt and polypropylene fibre-reinforced alkali-activated slag concrete, Construct. Build. Mater. 269 (Jan. 2021) 121284, https://doi.org/10.1016/j.conbuildmat.2020.121284.
[42] F.U.A. Shaikh, Pullout behavior of hook end steel fibers in geopolymers, J. Mater. Civ. Eng. 31 (6) (Jan. 2019) 04019068, https://doi.org/10.1061/(ASCE)MT.1943-5533.0002722.
[43] D. Gao, C. Ding, Y. Pang, G. Chen, An inverse analysis method for multi-linear tensile stress-crack opening relationship of 3D/4D/5D steel fiber reinforced concrete, Construct. Build. Mater. 309 (Jan. 2021) 125074, https://doi.org/10.1016/j.conbuildmat.2021.125074.
[44] O. Sucharda, M. Pajak, T. Ponikiewski, P. Konecny, Identification of mechanical and fracture properties of self-compacting concrete beams with different types of steel fibres using inverse analysis, Construct. Build. Mater. 138 (Jan. 2017) 263–275, https://doi.org/10.1016/j.conbuildmat.2017.01.077.
[45] S.J. Stephen, B. Raphael, R. Gettu, S. Jose, Determination of the tensile constitutive relations of fiber reinforced concrete using inverse analysis, Construct. Build. Mater. 195 (Jan. 2019) 405–414, https://doi.org/10.1016/j.conbuildmat.2018.11.014.
[46] L.M.P. Matos, J.A.O. Barros, A. Ventura-Gouveia, R.A.B. Calçada, A new inverse analysis approach for predicting the fracture mode I parameters of fibre reinforced concrete, Eng. Fract. Mech. 246 (Jan. 2021) 107613, https://doi.org/10.1016/j.engfracmech.2021.107613.
[47] fib Model Code for Concrete Structures (2020), Version 1. Lausanne: International Federation of Structural Concrete, 2023.
[48] L. Rossi, R.A. Patel, F. Dehn, Compressive behaviour of alkali-activated slag-based concrete and Portland cement concrete incorporating novel multiple hooked-end steel fibres, Mater. Struct. 56 (5) (Jan. 2023), https://doi.org/10.1617/s11527-023-02180-2.
[49] L. Rossi, et al., Future perspectives for alkali-activated materials: from existing standards to structural applications, RILEM Tech. Lett. 7 (Jan. 2022) 159–177, https://doi.org/10.21809/rilemtechlett.2022.160.
[50] S.-J. Lee, D.-Y. Yoo, D.-Y. Moon, Effects of hooked-end steel fiber geometry and volume fraction on the flexural behavior of concrete pedestrian decks, Appl. Sci. 9 (6) (Jan. 2019) 1241, https://doi.org/10.3390/app9061241.
[51] E. Faccin, L. Facconi, F. Minelli, G. Plizzari, Predicting the residual flexural strength of concrete reinforced with hooked-end steel fibers: new empirical equations, in: P. Serna, A. Llano-Torre, J.R. Martí-Vargas, J. Navarro-Gregori (Eds.), Fibre Reinforced Concrete: Improvements and Innovations II, vol. 36, Springer International Publishing, Cham, 2022, pp. 456–468, https://doi.org/10.1007/978-3-030-83719-8_40, in RILEM Bookseries, vol. 36.
[52] B.N. Moraes Neto, J.A.O. Barros, G.S.S.A. Melo, Model to simulate the contribution of fiber reinforcement for the punching resistance of RC slabs, J. Mater. Civ. Eng. 26 (7) (Jul. 2014) 04014020, https://doi.org/10.1061/(ASCE)MT.1943-5533.0000913.
[53] V. Oettel, M. Schulz, M. Haist, Empirical approach for the residual flexural tensile strength of steel fiber-reinforced concrete based on notched three-point bending tests, Struct. Concr. 23 (2) (Apr. 2022) 993–1004, https://doi.org/10.1002/suco.202100565.
[54] M. Di Prisco, M. Colombo, D. Dozio, Fibre-reinforced concrete in fib Model Code 2010: principles, models and test validation, Struct. Concr. 14 (4) (Dec. 2013) 342–361, https://doi.org/10.1002/suco.201300021.
[55] N. Belyakov, O. Smirnova, A. Alekseev, H. Tan, Numerical simulation of the mechanical behavior of fiber-reinforced cement composites subjected dynamic loading, Appl. Sci. 11 (3) (Jan. 2021) 1112, https://doi.org/10.3390/app11031112.
[56] Y. Chi, M. Yu, Le Huang, L. Xu, Finite element modeling of steel-polypropylene hybrid fiber reinforced concrete using modified concrete damaged plasticity, Eng. Struct. 148 (Jan. 2017) 23–35, https://doi.org/10.1016/j.engstruct.2017.06.039.
[57] H. Othman, H. Marzouk, Applicability of damage plasticity constitutive model for ultra-high performance fibre-reinforced concrete under impact loads, Int. J. Impact Eng. 114 (Jan. 2018) 20–31, https://doi.org/10.1016/j.ijimpeng.2017.12.013.
[58] T. Tysmans, M. Wozniak, O. Remy, J. Vantomme, Finite element modelling of the biaxial behaviour of high-performance fibre-reinforced cement composites (HPFRCC) using Concrete Damaged Plasticity, Finite Elem. Anal. Des. 100 (Jan. 2015) 47–53, https://doi.org/10.1016/j.finel.2015.02.004.
[59] T. Jankowiak, T. Łodygowski, Identification of parameters of concrete damage plasticity constitutive model, Found. Civ. Environ. Eng. 6 (Jan. 2005) 53–69.
[60] J. Lee, G.L. Fenves, Plastic-damage model for cyclic loading of concrete structures, J. Eng. Mech. 124 (8) (Jan. 1998) 892–900, https://doi.org/10.1061/(ASCE)0733-9399(1998)124:8(892).
[61] J. Lubliner, J. Oliver, S. Oller, E. Oñate, A plastic-damage model for concrete, Int. J. Solid Struct. 25 (3) (Jan. 1989) 299–326, https://doi.org/10.1016/0020-7683(89)90050-4.
[62] H. Zhang, Y.J. Huang, Z.J. Yang, S.L. Xu, X.W. Chen, A discrete-continuum coupled finite element modelling approach for fibre reinforced concrete, Cement Concr. Res. 106 (Apr. 2018) 130–143, https://doi.org/10.1016/j.cemconres.2018.01.010.
[63] J.F. Olesen, Fictitious crack propagation in fiber-reinforced concrete beams, J. Eng. Mech. 127 (3) (Jan. 2001) 272–280, https://doi.org/10.1061/(ASCE)0733-9399(2001)127:3(272).

Paper 5

Pull-out behaviour of single and multiple hooked-end steel fibres embedded in alkali-activated slag-based concrete and Portland cement concrete

Laura Rossi, Maria Paula Zappitelli, Ravi A. Patel, Frank Dehn

Journal of Building Engineering

(to be submitted)

Final draft

Pull-out behaviour of single and multiple hooked-end steel fibres embedded in alkali-activated slag-based concrete and Portland cement concrete

Laura Rossi [a,b (1)*], Maria Paula Zappitelli[c (2)], Ravi A. Patel [a,b (3)], Frank Dehn [a,b (4)]

[a] Institute of Building Materials and Concrete Structures (IMB), Karlsruhe Institute of Technology (KIT),76131 Karlsruhe, Germany

[b] Materials Testing and Research Institute Karlsruhe (MPA), Karlsruhe Institute of Technology (KIT), 76131 Karlsruhe, Germany

[c] Department of Civil Engineering, Engineering College, National University of La Plata (UNLP), Street 1 and 47, La Plata, Argentina

(1) E-mail: laura.rossi@kit.edu, ORCID: 0000-0002-9669-5796
(2) E-mail: paula.zappitelli@ing.unilp.edu.ar
(3) E-mail: ravi.patel@kit.edu
(4) E-mail: frank.dehn@kit.edu

* Corresponding author

Abstract

This paper evaluates the 7-day and 28-day pull-out behaviour of single (3D), double (4D), and triple hooked-end steel fibres (5D) embedded in alkali-activated slag-based concrete (AASC) and Portland cement-based concrete (PCC). The experimental results show an increase in the maximum pull-out load and average bond strength with the number of bends at the end of the steel fibres in both AASC and PCC, with AASC exhibiting higher values than PCC, indicating a better fibre-matrix interaction. Inverse analysis is conducted using the cohesive zone model (CZM) available in ABAQUS to determine the model parameters for the fibre-matrix interface based on the experimental single-fibre pull-out response of each fibre type in both concrete matrices. Inverse analysis results in a good fit of the pull-out peak load and the post-peak response of 3D, 4D and 5D fibres embedded in AASC, although underestimating the post-peak behaviour for 5D fibres. For PCC, the numerical simulations can match the experimental peak load and the pull-out post-peak descending branch quite accurately only for 4D fibres, whereas for 3D fibres and 5D fibres, an overestimation of the peak load and an underestimation of the post-peak response can be seen, respectively. From the maximum pull-out load, the average fibre-matrix bond strength (τ_{avg}) can be derived, which represents a fundamental parameter to correlate the pull-out performance of a single fibre embedded in a concrete matrix with the post-cracking flexural behaviour of the composite under bending. By knowing τ_{avg} and the number of fibres in the cross-section (N_f) of the notched beams under bending, the residual flexural strength f_{R1} and f_{R3} corresponding to serviceability (CMOD = 0.5 mm) and ultimate (CMOD = 2.5 mm) limit state, respectively, can be derived analytically.

Keywords

Fibre-reinforced alkali-activated concrete; hooked-end steel fibres; pull-out behaviour; FEM; cohesive zone model; inverse analysis

1. Introduction

To overcome concrete brittleness and avoid sudden failure under tension, randomly distributed steel fibres are added to the cementitious matrix, enhancing the composite tensile behaviour and delaying crack formation and propagation [1]. The stress-transferring provided by the fibre-bridging effect at the cracked surfaces is mainly influenced by the characteristics of the matrix, fibres and fibre-matrix interfacial bond strength. A weak fibre-matrix bond provides fibre pull-out at low loading values, nullifying its crack mitigation effect. The same results are given by a too-strong bond, which leads to fibre rupture when tensile load is applied. Thus, the fibre-matrix interface bond needs to be strong enough to allow fibre deformation and stress transfer, avoiding the fibre's sudden slip or rupture [1 – 2]. Among the bonding mechanisms governing the fibre-matrix bond, *i.e.* electrostatic attraction, chemical bonding, and mechanical interlocking, the latter is directly linked to the fibre geometric features, including fibre shape. Compared to straight steel fibres, deformed and hooked-end steel fibres, provide higher fibre-matrix bond strength and pull-out toughness due to the mechanical interlocking contribution given by the fibre shape [1, 3 – 4]. Thus, the introduction of additional bends at both ends of steel fibres represents a possible solution to increase the fibre-matrix bond and the fibre maximum pull-out load under tensile loading [5]. The effect of these novel multiple hooked-end steel fibres, *i.e.* double (4D) and triple (5D) hooked-end steel fibres, on the mechanical performance of Portland cement-based concrete (PCC) and on the fibre-matrix interface have been widely investigated [6 – 10].

To assess the bond characteristics between concrete matrix and steel fibres, single-fibre pull-out tests have been frequently performed [7]. Figure 1 shows a typical pull-out-slip curve of a single hooked-end steel fibre, which can be generally divided into 5 different stages.

The first stage, denoted as Stage I ($\delta < \delta_1$), is the pure elastic stage, during which the fibre is completely bonded to the matrix and adhesion between the fibre and the concrete matrix controls the fibre deformation [3]. The fibre debonding process begins at the end of the linear portion of the curve ($\delta_1 < \delta < \delta_2$) during which the segments of the fibre hooked end bend and plastically deform increasing the pull-out load to its maximum (P_2) and forming two inelastic hinges (H_1 and H_2) [3 – 4]. Once the load reaches its maximum, the straightening process begins. The hinge H_2 vanishes and the pull-out load decreases until the final segment of the fibre end is forced to bend in the opposite direction to its original shape through the second angle of the fibre-matrix interface. This causes a second peak and a subsequent drop in pull-out load $\delta_2 < \delta < \delta_3$). The inelastic hinge H_1 likewise disappears in Stage IV ($\delta_3 < \delta < \delta_4$) and full debonding is achieved at $\delta = \delta_4$ [3].

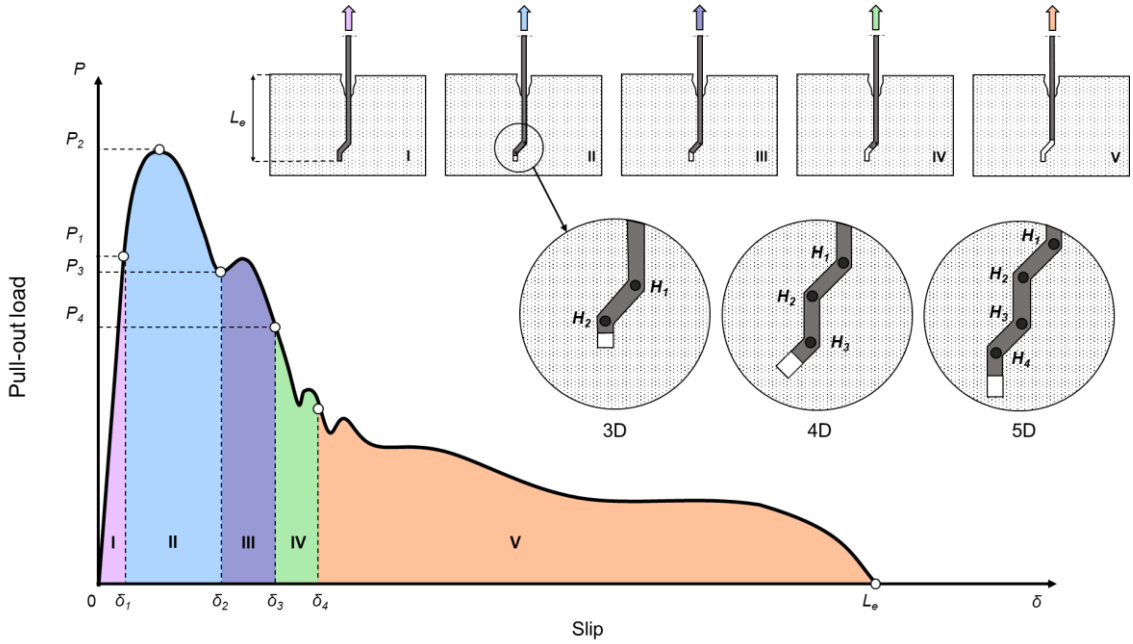

Figure 1: Typical pull-out response of single and multiple hooked-end steel fibres embedded in cement-based concrete (Modified from [3], [4])

In Stage V ($\delta > \delta_4$) the fibre is mainly straight with only frictional sliding preventing fibre pull-out. As soon as the fibre is completely pulled out from the straight channel within the concrete matrix, the pull-out load quickly approaches zero ($\delta = L_e$) [3 – 4]. If the deformed ends of the fibre do not yield, fibre fracture may occur [11].

Although the pull-out behaviour of single hooked-end steel fibres (3D) has been widely investigated, demonstrating that the main factors affecting it are the mechanical deformation of the fibre and the concrete matrix strength [7], the mechanisms associated with the pull-out response of 4D and 5D fibres are not completely understood. Abdallah et al. [7] evaluated the pull-out behaviour of 3D, 4D and 5D fibres in ultra-high-performance cement-based mortar to assess the mechanical anchorage provided by the additional bends at the ends of the fibres. During pull-out, the fibre bends are idealised as two, three and four plastic hinges for 3D, 4D and 5D fibres, respectively. Thus, the mechanical anchorage provided by the additional bends at the ends of the fibres is directly related to the work needed to straighten the fibres during pull-out. Abdallah et al. [8] demonstrated experimentally that the hooked-end of 4D and 5D fibres were only partially deformed and straightened when embedded in a normal strength cement-based concrete, as the concrete matrix strength can improve the pull-out performance of hooked-end steel fibres [12]. Another parameter affecting the pull-out response of single and multiple hooked-end steel fibres is the fibre embedment length, as the maximum pull-out load and pull-out work increase with increased embedded length [13].

Although the pull-out behaviour of 3D, 4D and 5D fibres embedded in cement-based mortar and concrete has been evaluated by several authors [6 – 8, 14 – 15], limited studies evaluating the pull-out response of single and novel multiple hooked-end steel fibres in alternative cement-free binders, such as alkali-activated slag-based concrete (AASC), have been reported. Beglarigale et

al. [16] evaluated the fibre-matrix bond strength of 3D fibres and alkali-activated slag-based mortar and compared it with cement-based ordinary mortar and ultra-high performance cement-based concrete (maximum aggregate size of 4 mm). It was demonstrated that alkali-activated slag-based mortar exhibits higher fibre-matrix bond characteristics than cement-based mortar, showing a higher maximum pull-out load even at lower values of matrix compressive strength than cement-based composites. Shaikh [5] evaluated the pull-out behaviour of 3D, 4D and 5D steel fibres in fly ash-slag blended alkali-activated and cement-based mortars. It was demonstrated that the maximum pull-out load increases with the increase of the number of bends at the fibre end for each type of mortar, with alkali-activated mortars showing higher values than cement mortar. The average fibre-matrix bond strength (τ_{avg}) increases with the fibre bends for alkali-activated mortars, while for cement-based mortar, an increase is observed only from 3D to 4D fibres, with no further increase for 5D fibres. The fibre material utilisation factor (*FMUF*), *i.e.* the ratio between the fibre maximum pull-out load and the fibre tensile strength, increases with the number of bends at the ends of the fibre only for fly ash-slag blended mortar, while for fly ash-based and cement-based mortars, 4D fibres show the highest value of FMUF. However, studies evaluating the pull-out behaviour of single and novel multiple hooked-end steel fibres in alkali-activated slag-based concrete are still limited. Evaluating the pull-out response of single and multiple hooked-end steel fibres embedded in alkali-activated slag-based concrete matrix is fundamental to understand the post-cracking behaviour of the composite under bending. Knowing the fibre-matrix average bond strength (τ_{avg}), which can be derived analytically from the experimental pull-out load-displacement curve, and the number of fibre in the cross-section (N_f) of the notched beams tested under three-point bending tests, it is possible to derive the composite post-cracking residual flexural strengths at serviceability (f_{R1}) and ultimate (f_{R3}) limit states, facilitating the design of novel steel fibre-reinforced cement-free concrete in the absence of dedicated design codes and building regulation.

Several authors [3 – 4, 17 – 26] proposed analytical and numerical models to predict the pull-out behaviour of hooked-end steel fibres embedded in cementitious matrices. Zhan and Meschke [22] proposed an analytical model based on an interface law describing the fibre-matrix frictional behaviour to predict the pull-out response of different configurations of steel fibres. Finite element modelling was also performed to provide supporting information for the analytical model proposed. Isla et al. [27] proposed a new model to predict the pull-out frictional behaviour at the fibre-matrix interface of different hooked-end steel fibres embedded in different mortar and concrete matrices. Storm et al. [28] evaluated the accuracy of three different finite element models to simulate the single-fibre pull-out behaviour: the phase-field approach for fracture, the cohesive zone model (CZM), and the fibre super-element formulation in an overlay mesh. However, due to its simplicity and its acceptable level of accuracy, the cohesive zone model (CZM) has been used in several studies to predict numerically the pull-out response of single fibres embedded in traditional cement-based concrete. Poveda et al. [29] used cohesive elements and contact elements implemented with a rate-dependent frictional law, to capture the bond-slip behaviour and the fibre-matrix frictional contact during pull-out tests, achieving good accuracy. Fantilli and Vallini [30] implemented the cohesive zone model to predict the pull-out response of inclined steel fibres embedded in a cementitious matrix. Abbas et al. [3] developed a finite element model based on cohesive-frictional interactions to simulate the pull-out response of hooked-end steel fibres embedded in cement-based concrete. A modification factor was introduced to account for the 3D

phenomenalistic behaviour simulated by 2D numerical modelling of the fibres during pull-out loading. Zou and Hameed [31] implemented the cohesive zone model with a cohesive energy-related parameter combining the fibre-matrix friction and interface damage. Most of the studies proposing analytical or numerical models to simulate the pull-out response of steel fibres embedded in a cementitious matrix are derived and validated on the fibre-matrix interface properties obtained experimentally or available in the literature. Limited studies derive such properties through inverse analysis. Banholzer et al. [32] proposed an analytical inverse analysis methodology to predict the bond characteristics of the fibre-matrix interface. Kožar et al. [33] proposed a stochastic method to derive the bond-slip parameters from the experimental results using inverse analysis.

Although the single-fibre pull-out behaviour of single and multiple hooked-end steel fibres embedded in a cementitious matrix has been widely investigated experimentally, analytically and numerically, studies focusing on the pull-out response of 3D, 4D and 5D fibres in alkali-activated matrices are still missing. Thus, this study evaluates experimentally the single-fibre pull-out response of 3D, 4D and 5D steel fibres embedded in alkali-activated slag-based concrete and cement-based concrete at the age of 7 and 28 days to evaluate the effect of fibre geometry and concrete matrix properties on the pull-out behaviour. Finally, finite element modelling based on inverse analysis is used to identify the interaction parameters required by the cohesive zone contact model available in ABAQUS to model the fibre-matrix interaction.

2. Experimental programme

2.1. Materials

Ground granulated blast furnace slag (GGBFS) and Portland cement (CEM I 42.5R) supplied by Ecocem Benelux B.V. and Heidelberg Materials, respectively, have been used as binders in this study. Their chemical composition is given in Table 1. Sodium hydroxide (SH) and sodium silicate (SS) have been used together with water to obtain an alkaline solution with a silicate modulus $M_{s(sol)}$ of 0.5 [mol/mol], *i.e.* the molar ratio between SiO_2 and Na_2O, and a total concentration of Na_2O of 5.3 [g/100g GGBFS]. River sand and quartzite gravel have been used as fine and coarse aggregates, respectively.

Table 1: Chemical composition of GGBS and CEM I used in this study

Binder	**CaO [%]**	**SiO_2 [%]**	**Al_2O_3 [%]**	**Fe_2O_3 [%]**	**MgO [%]**	**P_2O_5 [%]**	**K_2O [%]**	**Na_2O [%]**
GGBFS	41.84	35.91	10.74	0.39	6.99	0.47	0.40	0.31
CEM I	60.80	19.60	5.25	2.38	1.53	0.13	0.80	0.10

Single and multiple hooked-end steel fibres supplied by NV Bekaert SA with a length of 60 mm and a diameter of 0.90 mm have been used in this study. The three different fibre types investigated, *i.e.* single (Dramix® 3D 65/60 BG), double (Dramix® 4D 65/60 BG) and triple (Dramix® 5D 65/60 BG) hooked-end steel fibres, differ from each other for the number of bends at the end

of the fibre and the tensile strength of the wire. Table 2 summarises the properties of the different fibres.

Table 2: Hooked-end steel fibres properties

Fibre type	Length (l_f) [mm]	Diameter (d_f) [mm]	Aspect ratio (l_f/d_f)	Hook length [mm][a]	Fibre tensile strength (σ_{tf}) [MPa]	Strain at ultimate strength [%]
3D 65/60 BG	60	0.90	65	4.76	1160	0.8
4D 65/60 BG	60	0.90	65	7.55	1600	0.8
5D 65/60 BG	60	0.90	65	10.24	2300	6.0

[a] Calculated from [13]

2.2. Mix proportions

Table 3 shows the mix proportions used for both alkali-activated slag-based concrete (AASC) and Portland cement-based concrete (PCC). The same binder content, aggregate type and content have been used for both mixtures to achieve a similar slump flow class (F4) and 28-day mean cubic compressive strength (CS).

Table 3: Mix proportions for AASC and PCC in kg/m3. The values in the brackets are the standard deviation from the mean value of compressive strength

Mix	GGBS	CEM I	SH	SS	Water	Sand (0-2 mm)	Fine aggregates (2-8 mm)	Coarse aggregates (8-16 mm)	7-day CS [MPa]	28-day CS [MPa]
AASC	425	-	50	36	154	660	495	495	36.6 (0.38)	50.2 (0.44)
PCC	-	425	-	-	229	660	495	495	41.3 (0.78)	49.5 (0.79)

2.3. Specimen preparation

A prismatic steel mould of dimensions 500 mm x 80 mm x 50 mm able to allocate six single fibres at a regular distance has been used. The fibres were positioned in the mould before casting to guarantee a fibre embedded length of 15 mm. After demoulding, each beam was sawed and six samples of dimensions 80 mm x 80 mm x 50 mm were obtained, as shown in Figure 2. The samples were demoulded after one day and stored up to an age of 7 and 28 days wrapped in foil at (20 ± 2) °C to avoid corrosion of the exposed fibre. Additionally, 12 cubes of dimensions 150 mm x 150 mm x 150 mm were cast to evaluate the compressive strength of AASC and PCC according to EN 12390-3 both at an age of 7 and 28 days.

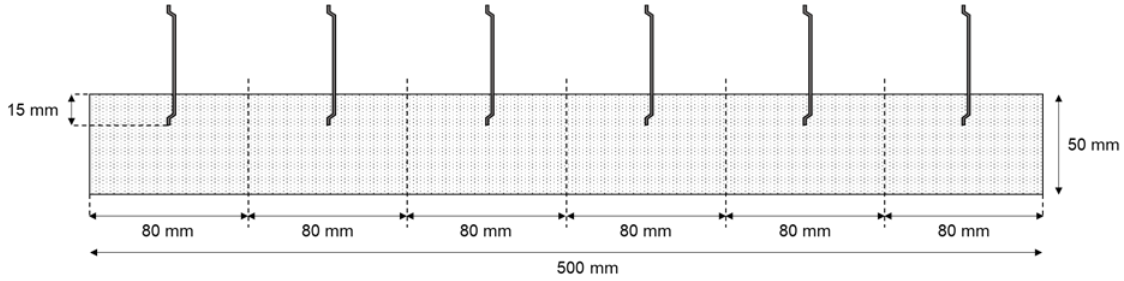

Figure 2: Schematic representation of the single-fibre pull-out samples. The dashed lines represents the sawing locations

2.4. Test setup

A total of 72 samples, six for each fibre geometry, concrete matrix and age, have been tested according to the setup shown in Figure 3.

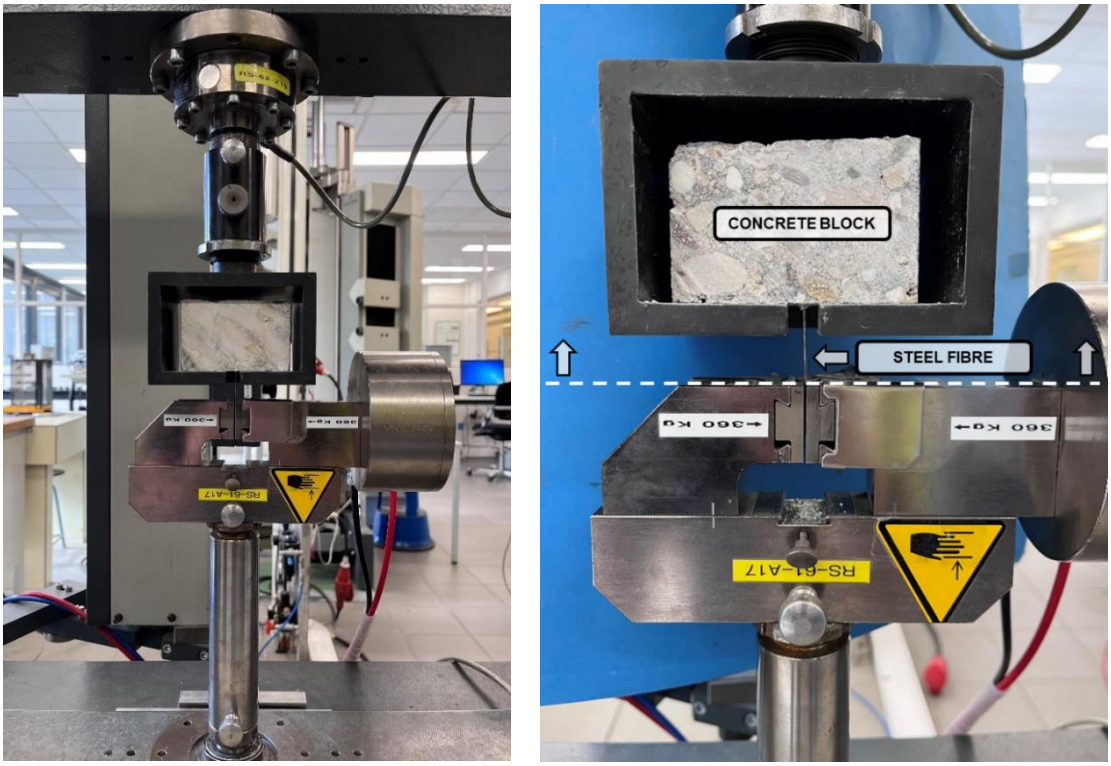

(a) (b)

Figure 3: Single fibre pull-out test setup

The test is displacement controlled with a loading rate of 10 mm/min and a preload of 5N. The elastic elongation of the fibre during the test was neglected. From each load-displacement (slip) curve, the maximum pull-out load and the corresponding displacement can be calculated. In addition, the average bond strength (τ_{avg}), the equivalent bond strength (τ_{eqv}) and the fibre material utilisation factor ($FMUF$) can be derived according to Shaikh [5] as follows:

$$\tau_{avg} = \frac{P_{max}}{\pi d_f L_e} \quad (1)$$

$$\tau_{eqv} = \frac{2W_p}{\pi d_f L_e^2} \quad (2)$$

$$FMUF = \frac{\sigma_{t,max}}{\sigma_{tf}} \quad (3)$$

where P_{max} is the maximum pull-out load, d_f is the fibre diameter, L_e is the embedded length of the fibre (15 mm in this study), W_p is the pull-out work, *i.e.* the area under the pull-out load-displacement curve, $\sigma_{t,max}$ is the tensile stress induced in the steel fibre at the maximum pull-out load, and σ_{tf} is the tensile strength of the single fibre as given in Table 2.

2.5. Three-point bending test and number of fibres at the cross-section

Three-point bending tests on notched beams of dimensions 150 mm x 150 mm x 550 mm have been performed for each concrete matrix and fibre type at different dosages (20 kg/m^3, 40 kg/m^3, and 60 kg/m^3) according to EN 14651. The experimental load-CMOD (crack mouth opening displacement) curves and the values of the residual flexural strengths f_{R1} and f_{R3}, corresponding to a CMOD value of 0.5 mm and 2.5 mm, respectively, have been published by the authors in a previous paper [34]. After each bending test, the tested beams have been completely broken in half to count the number of fibres (N_f) in the cross-section above the notch (Figure 4).

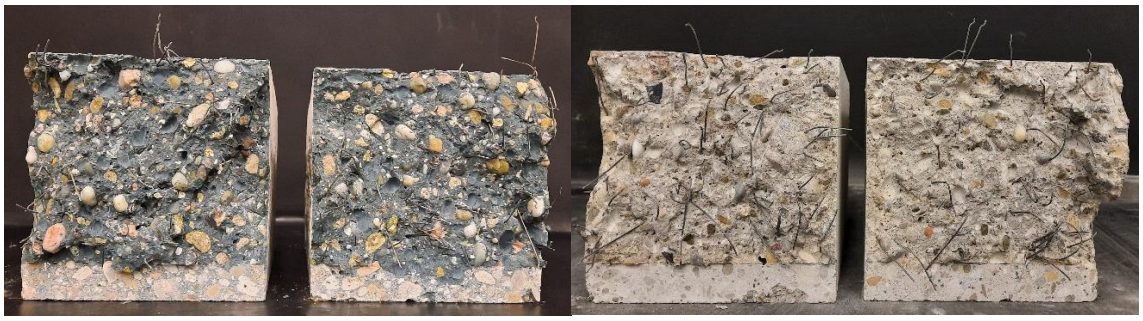

(a) (b)

Figure 4: Example of broken tested beams for the mixes (a) AASC-3D75 and (b) PCC-3D75 used to count the number of fibres at the cross-section

Although the fibre embedded length in the concrete matrix and its orientation have not been considered in determining the value of N_f, which represents only the number of visible fibres, the value of N_f is coherent with the theoretical values obtained using the analytical formula proposed by Dupont and Vandewalle [35]:

$$N_f = \frac{G \cdot \alpha}{\left(\frac{\pi \cdot d_f^2}{4}\right) \cdot \rho_s} \cdot b \cdot h_{sp} \quad (4)$$

Where G is the fibre dosage [kg/m^3], α is the orientation coefficient (assumed 0.58 in this study from Dupon and Vandewalle [35]), b is the width of the beam (150 mm), h_{sp} is the distance from

the top of the notch to the top of the beam (125 mm), d_f is the fibre diameter (0.90 mm) and ρ_s is the density of the steel of the fibres (7850 kg/m^3).

Using Eq. (4), the number of fibre at the cross-section can be calculated and compared with the experimental values obtained from the beams tested in a previous study [34]. The values of f_{R1} and f_{R3}, and N_f, both experimental and predicted, together with the fibre type and dosage, are summarised in Table 4. The values in the brackets represent the standard deviation from the mean value.

Table 4: Values of N_f (experimental and predicted), f_{R1} and f_{R3} for each concrete matrix and fibre type

Matrix type	Fibre type	Fibre dosage [kg/m^3]	N_f Experimental	N_f Predicted	Ratio predicted/ experimental	f_{R1} [MPa]	f_{R3} [MPa]
AASC	3D	20	56 (9.8)	44	0.786	2.93	3.45
		40	115 (12.4)	87	0.757	5.66	6.93
		60	151 (25.0)	131	0.866	6.88	8.03
	4D	20	50 (10.2)	44	0.880	3.15	3.91
		40	86 (15.6)	87	1.012	5.55	6.91
		60	152 (21.4)	131	0.862	7.86	8.05
	5D	20	39 (9.2)	44	1.128	2.44	3.07
		40	99 (18.3)	87	0.879	6.23	7.88
		60	152 (22.2)	131	0.862	7.66	8.30
PCC	3D	20	42 (7.3)	44	1.048	2.88	3.05
		40	87 (23.1)	87	1.000	5.41	6.07
		60	122 (22.5)	131	1.074	6.34	7.28
	4D	20	44 (8.5)	44	1.000	2.81	4.14
		40	76 (11.7)	87	1.145	5.53	7.05
		60	105 (20.6)	131	1.248	6.16	6.66
	5D	20	42 (6.8)	44	1.048	3.11	4.27
		40	96 (15.5)	87	0.906	5.10	5.98
		60	91 (10.4)	131	1.440	8.23	8.73

2.6. Numerical simulations

The concrete matrix and the single, double and triple hooked-end steel fibres have been modelled in the finite element ABAQUS Software as 2D geometry (ABAQUS/Standard). The schematic representation of the model geometry, boundary conditions and loading configuration are shown in Figure 5a. Displacement was restricted at the bottom and at the sides of the concrete block, while a displacement of 14 mm was applied at the reference point (RP) coupled to the fibre end. To simulate the properties of the different elements in model, *i.e.* the concrete matrix, the steel fibre and the fibre-matrix interface bond, different constitutive models have been used.

For the concrete matrix, a linear elastic behaviour is considered, *i.e.* the modulus of elasticity and Poisson's ratio (obtained by previous investigation of the authors [36]) is the only input parameter required. For the steel fibres, elasto-plastic behaviour is considered, *i.e.* a strain-hardening behaviour under uniaxial tension, as shown in Figure 5b.

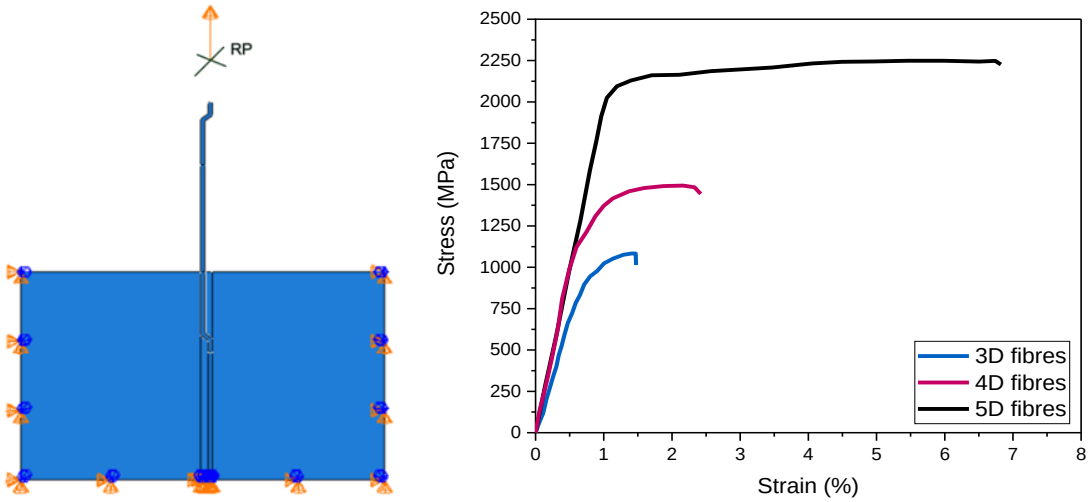

Figure 5: Schematic representation of the model geometry, boundary conditions and loading configurations (a) and the elastoplastic behaviour of 3D, 4D and 5D fibres under uniaxial tension used as input parameter in the model

The critical point in the numerical simulation of the singe-fibre pull-out response is the definition of the fibre-matrix interface properties. In this study, a cohesive zone model (CZM) implemented in ABAQUS cohesive surfaces is used. In this model, the interaction force between two interfaces is considered as the cohesive force existing in a fictitious crack preventing its propagation [37 – 38]. The traction-separation law is used to describe the evolution of the cohesive stress with displacement continuity [39]. This traction-separation law considers an initial linear elastic behaviour followed by damage initiation and evolution [39 – 40]. The equation describing the elastic response is given as follows:

$$t = \begin{bmatrix} t_n \\ t_s \\ t_t \end{bmatrix} = \begin{bmatrix} K_{nn} & K_{ns} & K_{nt} \\ K_{sn} & K_{ss} & K_{st} \\ K_{nt} & K_{ts} & K_{tt} \end{bmatrix} = \begin{bmatrix} \delta_n \\ \delta_s \\ \delta_s \end{bmatrix} = K\delta \tag{5}$$

where t is the nominal traction stress vector and t_n, t_s, and t_t are the components of such vector in the normal (t_n) and shear directions (t_s, t_t), δ_n, δ_s, and δ_t are the corresponding separations, and K represents the stiffness matrix. For the single-fibre pull-out, in plane-share is considered [39, 41], thus, $K_{ns} = K_{sn} = K_{nt} = K_{nt} = K_{st} = K_{tt} = 0$ and K_{nn} is assumed equal to K_{ss} [3]. For the damage initiation, consider as the degradation of the cohesive response at a contact point [40], a quadratic stress criterion is assumed in this study, which is defined as:

$$\left\{\frac{\langle t_n \rangle}{t_n^0}\right\}^2 + \left\{\frac{t_s}{t_s^0}\right\}^2 + \left\{\frac{t_t}{t_t^0}\right\}^2 = 1 \tag{6}$$

where t_n^0, t_s^0 and t_t^0 are the peak values of the contact stress when the separation is either purely normal to the interface (t_n^0) or purely in the first or second shear direction (t_s^0, t_t^0), respectively [40]. As previously, $t_t^0 = 0$. Also, t_n^0 is considered 10 times t_s^0, due to the assumption in this study of interfacial shear slip dominating the debonding process [41]. Finally, the damage evolution criterion indicates the rate of degradation of the cohesive stiffness after the damage initiation criterion is reached [3, 40]. The damage at a contact point is represented by a scalar damage variable (D). The value of this variable evolves monotonically from 0, corresponding to no damage, to 1, representing complete damage. The contact stress components are affected by the damage as follows:

$$t_n = \begin{cases} (1-D)t_{n,}^- & t_n^- > 0 \\ t_n^- & t_n^- \leq 0 \end{cases} \tag{7}$$

$$t_s = (1-D)t_s^- \tag{8}$$

where t_n^- and t_s^- are the contact stress components predicted by the elastic traction-separation law without considering damage. Different kind of laws can be adopted for defining the damage variable. In this paper, the linear damage law proposed in Eq. (9) was used [31]:

$$D = \frac{\delta_s^f(\delta_s - \delta_s^0)}{\delta_s(\delta_s^f - \delta_s^0)} \tag{9}$$

where δ_s^f is the separation at complete failure and δ_s^0 is the separation at damage initiation. The CZM is further implemented in this study through cohesive surfaces. Thus, normal and tangential surface interaction properties need to be defined. To avoid surface interpenetration, hard contact was considered. The tangential property consists in a Coulomb friction model defined as follows:

$$\tau_{crit} = \mu * p \tag{10}$$

where τ_{crit} is the critical shear stress at which sliding of the surfaces starts, μ is the friction coefficient, and p is the contact pressure between the surfaces. Modelling the fibre-matrix interface through cohesive surfaces allows the representation of all the stages governing the pull-out process (Figure 1): Stages I to IV are governed by cohesive behaviour, while Stage V is governed by the Coulomb friction model, once complete fibre-matrix debonding is achieved.

To determine the values of the input parameters K_s, t_s^0 and δ_s^f required by the CZM, and the friction coefficient (μ) required by the Coulomb friction model, a numerical inverse analysis was performed. This analysis consists in a Global optimisation using a differential evolution algorithm of the SciPy package [42]. The objective function for minimization is the difference between the load-displacement curve obtained from numerical simulations and experiments. The bounds for the parameters to be optimized are considered as follows:

$K \in$ [0.5 N/mm, 20 N/mm], $t_s^0 \in$ [0.1 MPa, 5 MPa], $\delta_s \in$ [1 mm, 3 mm] and $\mu \in [1e^{-5}, 0.5]$ [3, 31, 41].

3. Results

3.1. Effect of the concrete matrix type and strength

The experimental pull-out curves obtained for AASC and PCC incorporating 3D, 4D and 5D fibres after 7 and 28 days are shown in Figure 6 and Figure 7, respectively. The shape of the pull-out load-slip curve for 3D, 4D and 5D fibres is similar in both alkali-activated and cement-based concrete matrices at both ages. Up to the maximum pull-out peak load, debonding of the fibre from the concrete matrix initiates. Once the fibre-matrix debonding is complete, the bends of the fibre undergo plastic deformation, resulting in several load peaks till pull-out load decreases till complete slippage of the fibre. Rupture of the fibres can also be seen for AASC incorporating 4D fibres at 28 days due to the higher maximum pull-out load.

For both AASC and PCC, the variability of the results increases with the increase in the number of bends at the end of the fibre (5D > 4D > 3D). This can be related to the hook geometry and its variations [43] and to micro-defects and variability in porosity around the fibres with more complicated geometries. All the fibres embedded in the alkali-activated slag-based concrete matrix generally show higher values of maximum and residual pull-out load at 7 and 28 days than the ones embedded in PCC. This could be related to the higher shrinkage of alkali-activated slag-based concrete matrices, which results in compressive hydrostatic pressure around the fibres and improved fibre-matrix interface bond [16]. Additionally, alkali-activated slag-based concretes generally exhibits a denser fibre-matrix interfacial transition zone (ITZ) and a more compact microstructure due to lower porosity than the one observed in cement-based concrete [5].

Figure 7 shows a direct comparison between 3D, 4D and 5D fibres in both AASC and PCC at 7 and 28 days. As shown in Figure 7a and 7b, each fibre shows a similar pull-out behaviour in AASC at 7 and 28 days of age, with 5D fibres outperforming 4D and 3D fibres (5D > 4D > 3D). Although the compressive strength of AASC increases of 37.2% from 7 to 28 days, its effect on the pull-out maximum load and post-peak response is quite limited. The same can be concluded for PCC. Although the compressive strength increases of 19.9% from 7 to 28 days, the single-fibre pull-out response is similar at both ages for each fibre type with 5D fibres outperforming 4D and 3D fibres, despite showing the highest variability in the experimental results. Thus, the compressive strength of the concrete matrix has a limited effect on the pull-out response of single and multiple hooked-end steel fibres in both AASC and PCC.

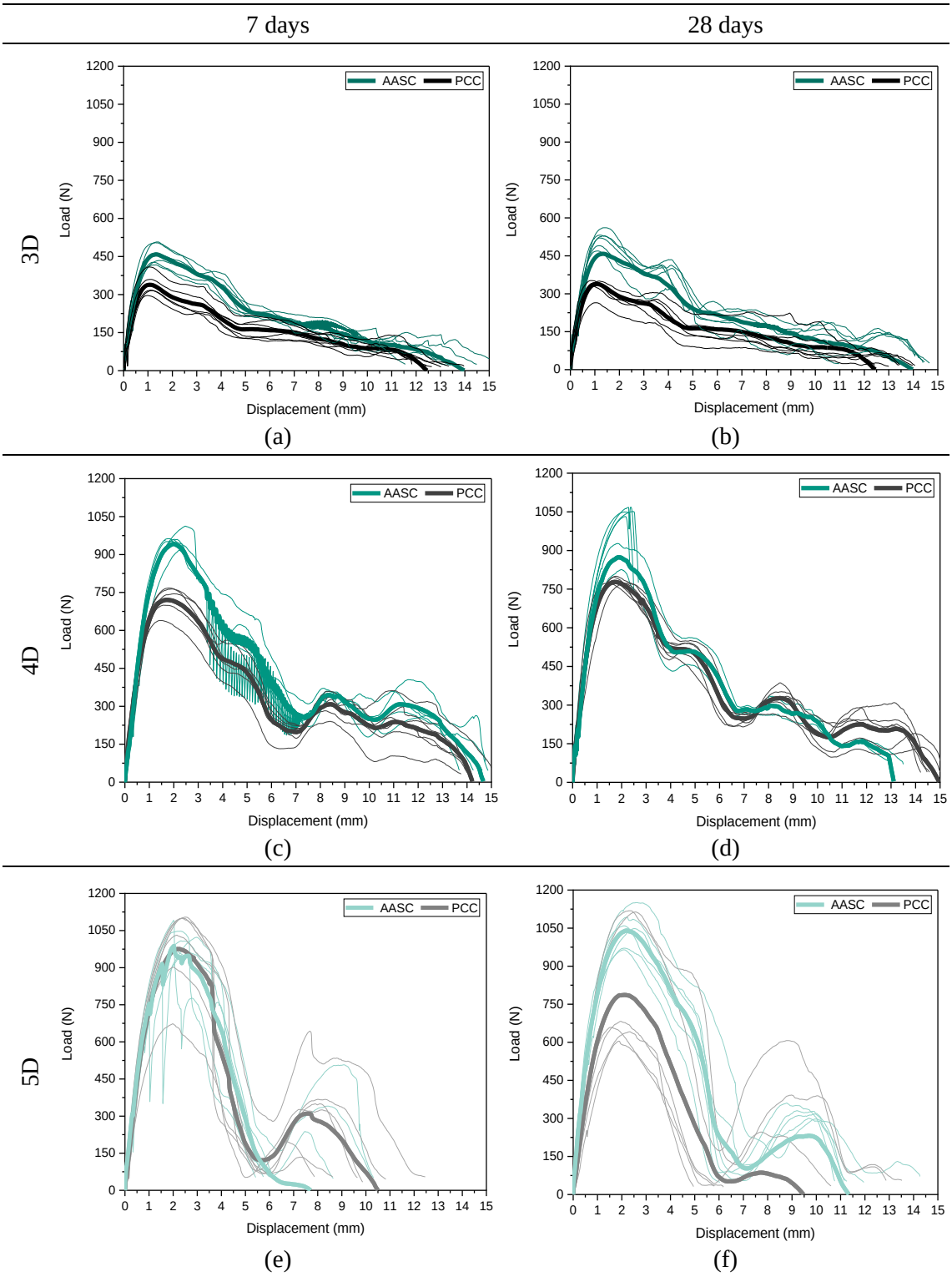

Figure 6: Experimental pull-out curves for AASC and PCC incorporating (a, b) 3D, (c, d) 4D and (e, f) 5D fibres at an age of 7 and 28 days

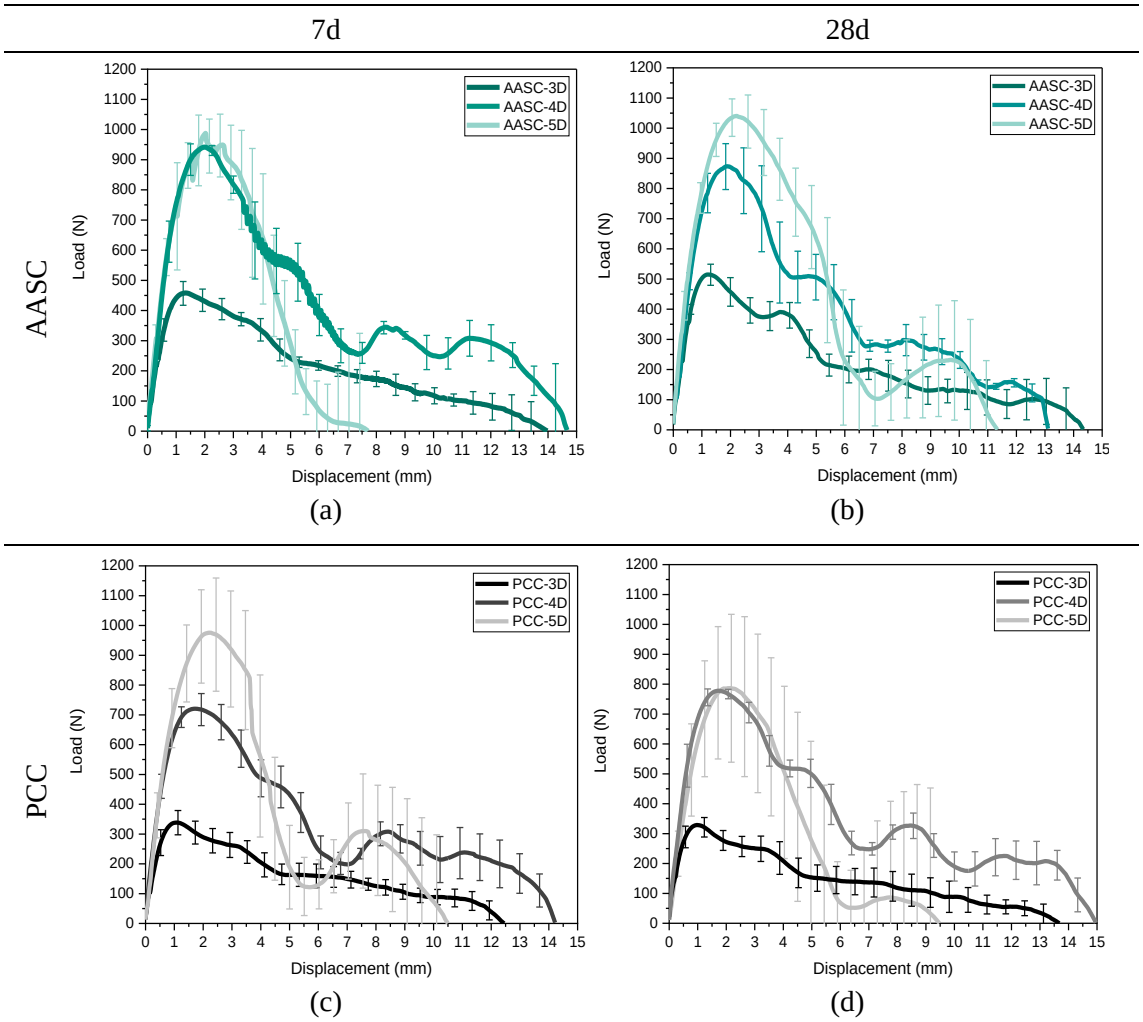

Figure 7. Experimental pull-out curves for (a, b) AASC and (c, d) PCC incorporating 3D, 4D and 5D fibres at an age of 7 and 28 days

3.2. Effect of the fibre geometry

As shown in Figure 6 and 7, the maximum pull-out load increases with the increase in the number of bends at the fibre ends for both AASC and PCC at both 7 and 28 days. The area under the curves represents the energy absorbed during fibre debonding and pull-out. Significant energy is absorbed during debonding and plastic deformation of the fibre hooks due to the mechanical anchorage provided by the additional bends in the hooked end, thus, it increases with the increase in the number of bends (5D > 4D > 3D). After achieving the maximum peak value, the pull-out load drops more abruptly for 5D fibres than 3D and 4D in both AASC and PCC, although AASC shows higher energy absorption.

Table 5 and Table 6 show the values of the maximum pull-out load (P_{max}), the average and equivalent bond strength (τ_{avg} and τ_{eqv}, respectively) and the fibre material utilisation factor ($FMUF$) for each fibre and concrete matrix type at 7 and 28 days. As observed in Figure 8a – 8d, for both AASC and PCC, the maximum pull-out load and the average bond strength increase with the

increase in the number of bends at the ends of the steel fibres, with 5D fibres achieving the highest values of each parameter, although showing the highest variability for PCC mixes. For both AASC and PCC, 4D fibres show the highest values of equivalent bond strength (Figure 8e – 8f), which correlates directly to their $FMUF$ almost close to 1 (Figure 8g – 8h).

Table 5: Values of P_{max}, τ_{avg}, τ_{eqv}, and FMUF for AASC and PCC at 7 days. The values in the parentheses indicate the standard deviation

Fibre type	**Maximum pull-out load [N]**		τ_{avg} **[MPa]**		τ_{eqv} **[MPa]**		$FMUF$	
	AASC	PCC	AASC	PCC	AASC	PCC	AASC	PCC
3D 65/60 BG	459.0 (39.6)	339.1 (40.3)	10.8 (0.9)	8.0 (0.9)	9.45 (0.93)	6.58 (1.13)	0.62 (0.05)	0.46 (0.05)
4D 65/60 BG	958.7 (30.9)	723.1 (48.3)	22.6 (0.7)	17.1 (1.0)	19.65 (1.72)	15.54 (2.32)	0.94 (0.03)	0.71 (0.05)
5D 65/60 BG	1017.4 (48.1)	985.0 (171.4)	24.0 (1.0)	23.3 (3.7)	12.90 (2.96)	14.21 (4.22)	0.70 (0.03)	0.67 (0.12)

Table 6: Values of P_{max}, τ_{avg}, τ_{eqv}, and FMUF for AASC and PCC at 28 days. The values in the parentheses indicate the standard deviation

Fibre type	**Maximum pull-out load [N]**		τ_{avg} **[MPa]**		τ_{eqv} **[MPa]**		$FMUF$	
	AASC	PCC	AASC	PCC	AASC	PCC	AASC	PCC
3D 65/60 BG	517.1 (32.7)	330.3 (33.2)	12.2 (0.7)	7.8 (0.7)	10.11 (1.82)	6.54 (1.65)	0.70 (0.04)	0.45 (0.04)
4D 65/60 BG	992.4 (96.0)	782.9 (12.4)	23.4 (2.1)	18.5 (0.27)	10.31 (5.85)	17.15 (1.33)	0.97 (0.09)	0.77 (0.01)
5D 65/60 BG	1048.1 (71.6)	803.3 (243.7)	24.7 (1.5)	18.9 (5.2)	17.35 (3.81)	12.45 (8.05)	0.72 (0.05)	0.55 (0.17)

Similar behaviour was observed by Shaikh [5], with the values of P_{max}, τ_{avg}, τ_{eqv} and $FMUF$ generally increasing with the increase in the number of bends at the fibre ends for each type of mortar matrix investigated, *i.e.* fly ash-based alkali-activated mortar, fly ash-slag alkali-activated mortar and cement-based mortar. Additionally, the $FMUF$ achieved by Shaikh [5] shows its higher value for 4D fibres in fly ash-based mortars and cement-based mortar, as also obtained in this study for AASC and PCC. The pull-out performance of hooked-end steel fibres embedded in a concrete matrix depends on the properties of the matrix, of the fibre and on their bond strength, thus, a fibre can perform at its maximum potential only when embedded in a concrete matrix with appropriate characteristics, *i.e.* microstructure and strength, to develop the best fibre-matrix bond.

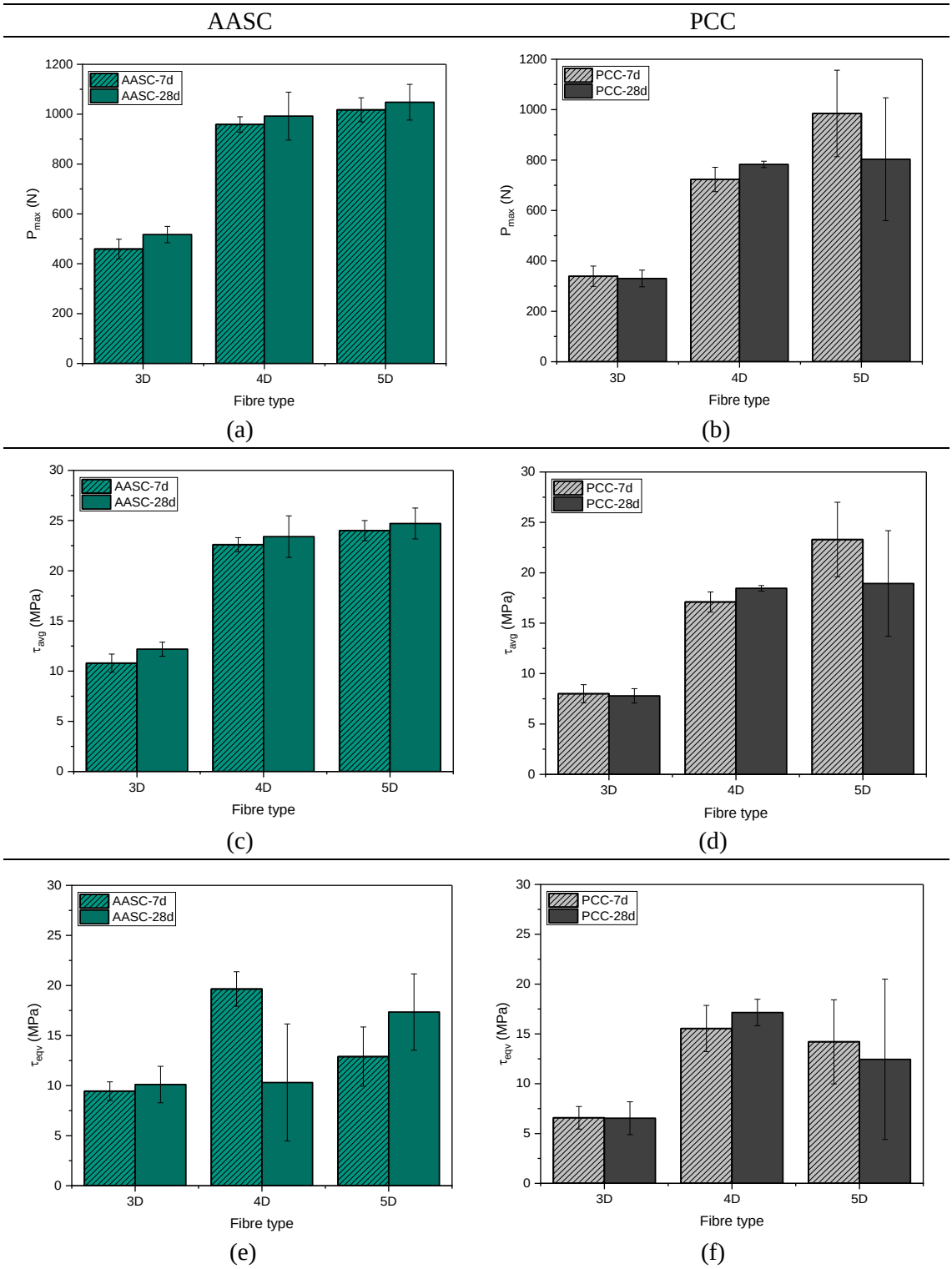

Figure 8: Comparison between the values of (a, b) F_{max}, (c, d) τ_{avg}, (e, f) τ_{eqv}, and (g, h) *FMUF* for AASC and PCC at 7 and 28 days, respectively

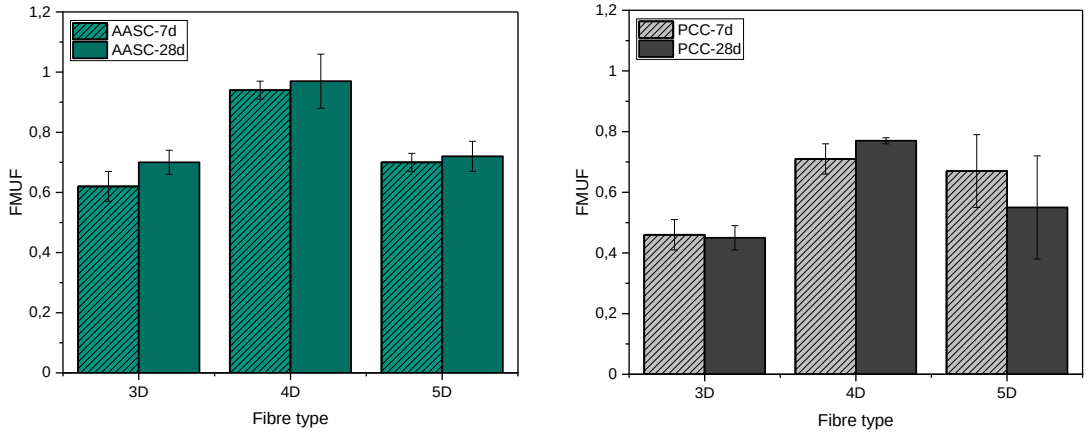

(g) (h)

Figure 8: (continued) Comparison between the values of (a, b) F_{max}, (c, d) τ_{avg}, (e, f) τ_{eqv}, and (g, h) *FMUF* for AASC and PCC at 7 and 28 days, respectively

3.3. Numerical modelling

Figure 9 and Figure 10 show the 7-day and the 28-day experimental and numerical load-displacement curves obtained through inverse analysis for AASC and PCC for each fibre type. At both ages, for AASC, the numerical results can accurately capture the experimental pull-out behaviour for each fibre type. For 3D and 4D fibres, the numerical peak load and the post-peak descending branch are within the range of the experimental results, while for 5D fibres, more discrepancies can be observed (Figure 9e and Figure 10e). For PCC, the numerical curves are in the range of the experimental results for each fibre type, although for 3D fibres, an overestimation of the peak load can be observed at both ages (Figure 9b and Figure 10b). This could be attributed to the inability of the model to account for micro-scale heterogeneities at fibre-matrix interface which plays pivotal role in pull-out response.

Table 7 summarises the values of the fibre-matrix interface parameters (K_{ss} [N/mm], t_{ss} [MPa], δ_s^f [mm], and μ) obtained through inverse analysis for both concrete matrices and for each fibre type at 7 and 28 days.

Table 7: Values of the fibre-matrix interface parameters obtained through inverse analysis at 7 and 28 days

Parameter	AASC						PCC					
	3D		4D		5D		3D		4D		5D	
	7d	28d	7d	28d	7d	28d	7d	28d	7d	28d	7d	28d
K_{ss}	3.01	3.11	17.07	17.05	5.01	1.75	0.51	0.50	14.19	14.04	0.71	0.66
t_{ss}	0.79	0.76	3.87	3.93	1.07	0.11	0.44	0.50	1.27	1.71	0.40	0.50
δ_s^f	2.83	2.63	1.51	1.86	1.01	1.00	2.06	2.98	1.69	1.12	1.27	2.10
μ	0.30	0.30	0.11	0.11	$9.9e^{-4}$	$4.54e^{-5}$	0.11	0.10	0.12	0.10	$1.27e^{-5}$	$2.43e^{-5}$

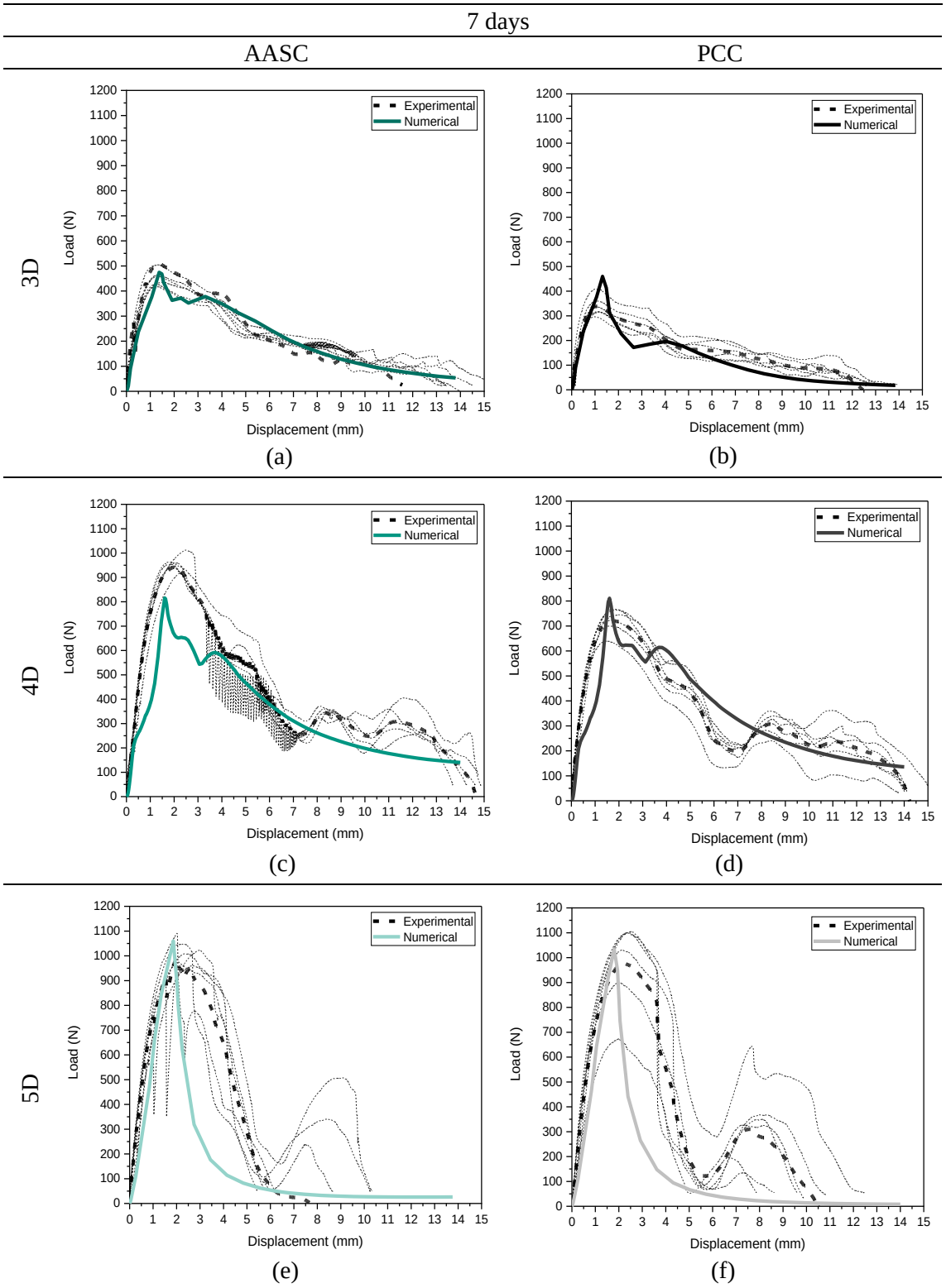

Figure 9: Experimental and numerical pull-out load-displacement curves for AASC and PCC incorporating (a, b) 3D, (c, d) 4D, and (e, f) 5D fibres at 7 days

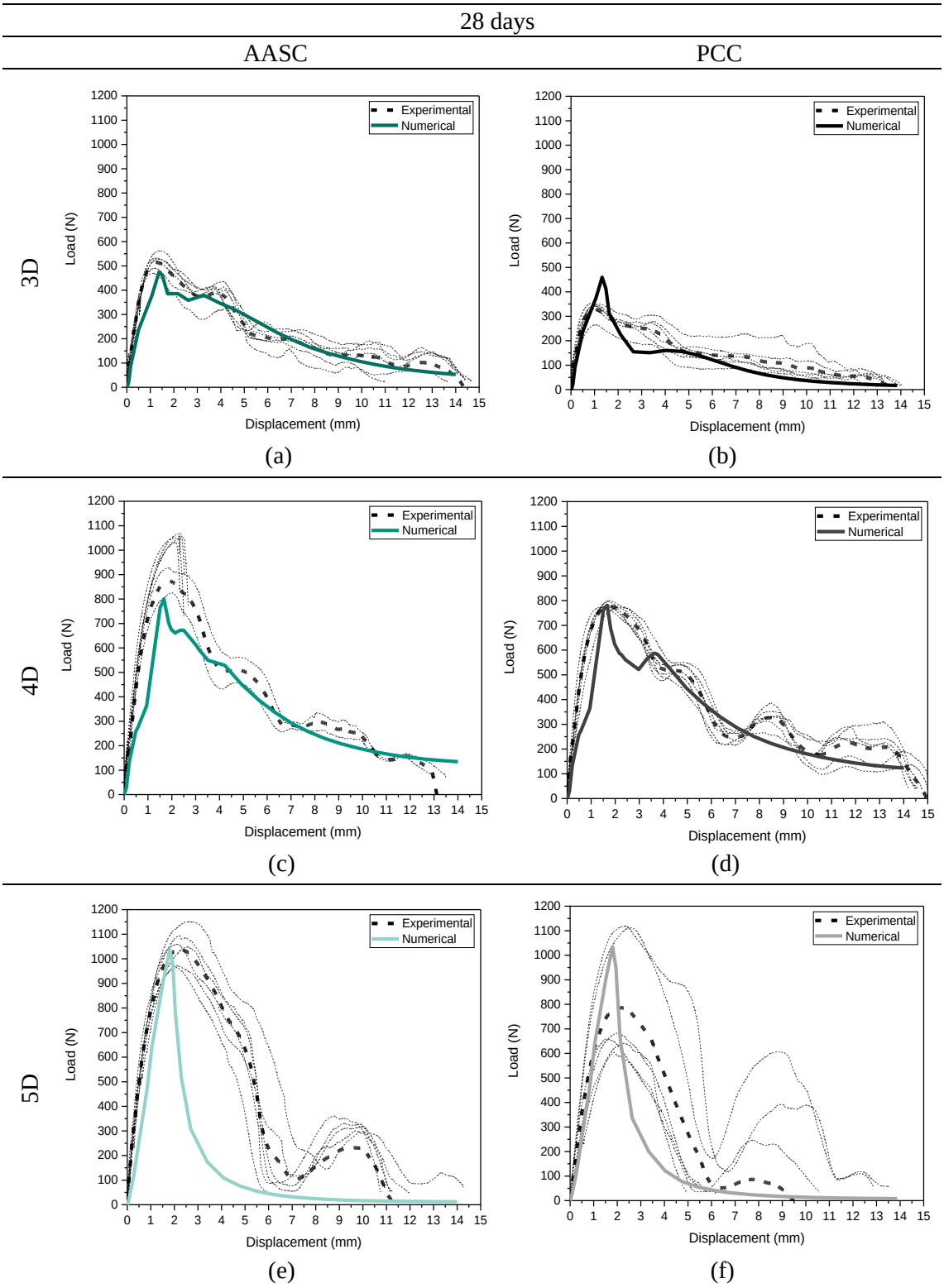

Figure 10: Experimental and numerical pull-out load-displacement curves for AASC and PCC incorporating (a, b) 3D, (c, d) 4D, and (e, f) 5D fibres at 28 days

As shown in Table 7, AASC generally shows higher values of the fibre-matrix interface parameters than PCC. The parameters K_{ss} and t_{ss} are directly correlated to the initial slop of the pull-out load-displacement curve and its peak value. Thus, higher values of these parameters for AASC can represent a higher fibre-matrix bond strength and a higher maximum pull-out load than PCC. The highest values of K_{ss} and t_{ss} are observed for 4D fibres embedded in AASC and it could result from the highest fibre material utilisation factor obtained for this fibre type in this study.

For both AASC and PCC, a reduction of the friction coefficient μ with the increase of the number of bends at the end of the fibre can be seen. This could be related to the increased mechanical anchorage provided by the additional bends in 4D and 5D fibres during the pull-out mechanism, resulting in the formation of additional plastic hinges in comparison to 3D fibres. Thus, the frictional contribution of 4D and 5D fibres is lower than 3D fibres. From the model parameters, the fracture energy G_F can be derived as the area under the $t_{ss} - \delta_s^f$ curve. The values of the fracture energy for both AASC and PCC, for each fibre type at 7 and 28 days are shown in Table 8.

Table 8: Values of the fracture energy G_F [Nmm/mm^2] at 7 and 28 days

AASC						PCC					
3D		4D		5D		3D		4D		5D	
7d	28d	7d	28d	7d	28d	7d	28d	7d	28d	7d	28d
1.12	1.00	2.92	3.65	0.54	0.06	0.45	0.75	1.07	0.96	0.25	0.53

In both concrete matrices, the highest values of fracture energy are obtained for 4D fibres, which can be related to the highest fibre material utilization factor obtained for this fibre type.

3.4. Correlation between pull-out response and flexural behaviour

Once the number of fibres at the cross-section of each beam (N_f) and the fibre-matrix bond strength (τ_{avg}) for each fibre type and concrete matrix are known, it is possible to derive a correlation between the pull-out response and the residual flexural strengths (f_{R1} and f_{R3}), as shown in Figure 11.

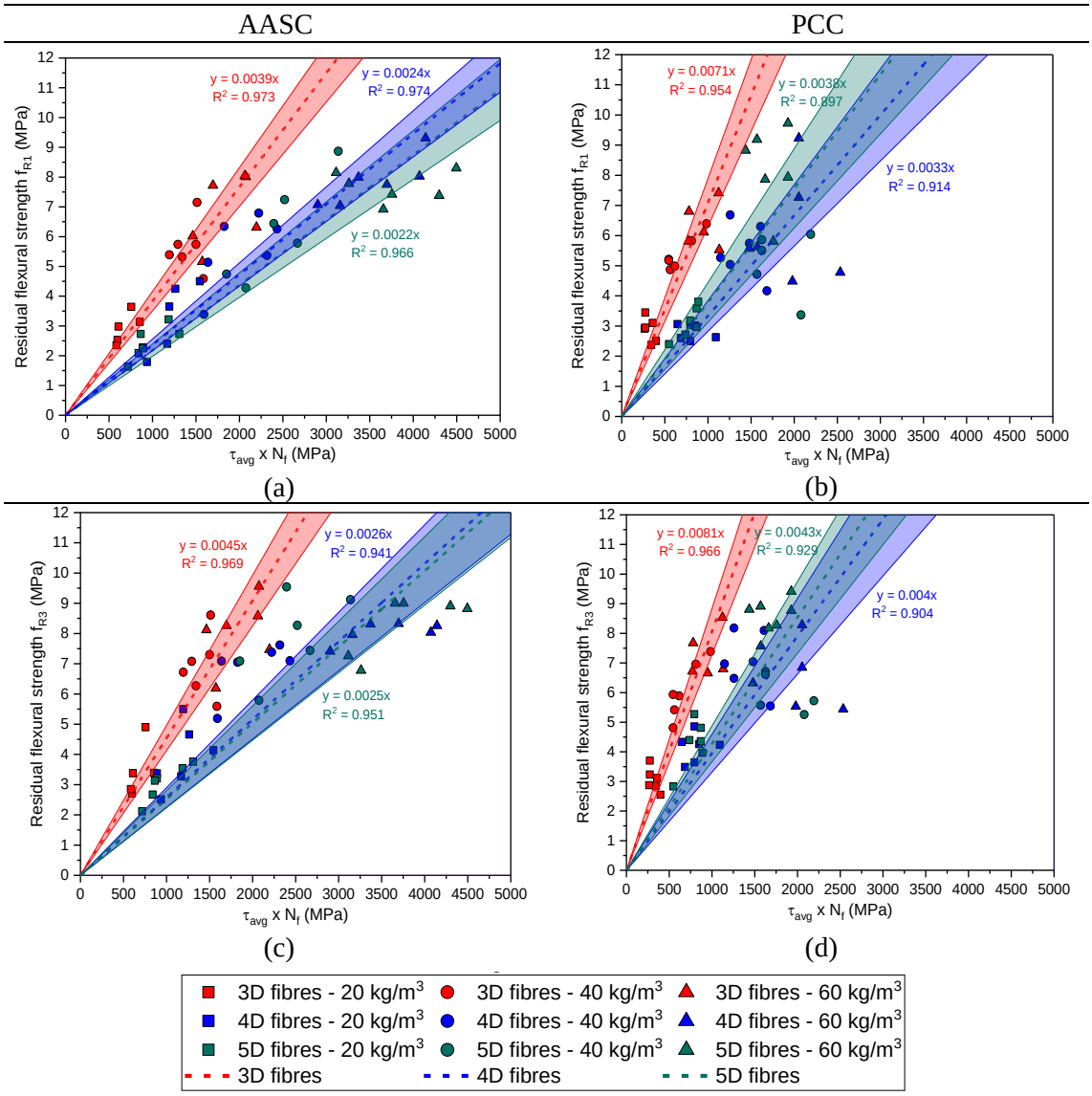

Figure 11: Correlation between the number of fibre and the fibre-matrix bond strength and the residual flexural strength (a, b) f_{R1} and (c, d) f_{R3} for AASC and PCC mixes

Linear fitting for each fibre and concrete matrix type has been performed and the coefficient A of the general formula $y = A \cdot x$, where y represents the residual flexural strengths f_{R1} and f_{R3} and $x = \tau_{avg} \cdot N_f$, and the R^2 values are summarised in Table 9 and Table 10.

Table 9: Values of the coefficient A and R^2 for f_{R1} for each fibre and concrete matrix type

	f_{R1}					
	AASC			PCC		
	3D	4D	5D	3D	4D	5D
A	0.0039	0.0024	0.0022	0.0071	0.0033	0.0038
R^2	0.973	0.974	0.966	0.954	0.914	0.897

Table 10: Values of the coefficient A and R^2 for f_{R3} for each fibre and concrete matrix type

	f_{R3}					
	AASC			PCC		
	3D	4D	5D	3D	4D	5D
A	0.0045	0.0026	0.0025	0.0081	0.0040	0.0043
R^2	0.969	0.941	0.951	0.966	0.904	0.929

As shown in Figure 11, 4D and 5D fibres show a similar behaviour in both AASC and PCC, while 3D fibres show the highest values of the coefficient A and therefore a steeper inclination of the line representing the linear fitting. As a result, as the value of τ_{avg} increases with the increase of the number of bends at the end of the fibres (5D > 4D > 3D) a higher number of 3D fibres than 4D and 5D fibres is needed to achieve the same value of residual flexural strength f_{R1} or f_{R3}. Thus, higher dosages of 3D fibres are needed to achieve the same performance observed for composites incorporating 4D and 5D fibres. The similar behaviour of 4D and 5D fibres in both AASC and PCC can be due to the incompatibility between the enhanced performance of the fibre and the concrete matrix compressive strength, resulting in 5D fibres underperforming compared to their expected potential.

4. Conclusions

This study evaluates experimentally the single-fibre pull-out response of single and multiple hooked-end steel fibres (3D, 4D and 5D) embedded in different concrete matrices, *i.e.* alkali-activated slag-based concrete (AASC) and Portland cement-based concrete (PCC). Finite element modelling based on inverse analysis has been used obtain the parameters describing the fibre-matrix interface required as input parameters in the Cohesive Zone Model (CZM). From the experimental investigations and inverse analysis, the following conclusions can be drawn:

- The concrete matrix compressive strength has a marginal effect on the pull-out maximum load and post-peak response for each fibre type for both AASC and PCC. However, all the fibres embedded in AASC exhibit higher values of maximum pull-out load than PCC due to the better fibre-matrix interface bond given by higher shrinkage of alkali-activated slag-based concrete than traditional cement-based concrete.

- The fibre geometry, *i.e.* the number of bends at the end of the fibre, has a more significant effect on the maximum pull-out load and post-peak behaviour. The maximum pull-out load increases with the increase in the fibre bends for both AASC and PCC, with 5D fibres outperforming 3D and 4D fibres in both AASC and PCC (5D > 4D > 3D).

- The fibre-matrix average bond strength (τ_{avg}) increases with the increase in the number of bends at the fibre end (5D > 4D > 3D). Correlating this value with the number of fibres in the cross-section of beams tested under three-point bending tests (N_f), the post-cracking residual flexural tensile strengths f_{R1} and f_{R3} can be predicted. From the linear correlation between $\tau_{avg} \cdot N_f$ and f_{R1} or f_{R3}, similar behaviour of all fibre types in the different concrete matrices can be seen, with 3D fibres differing from 4D and 5D. Although exhibiting lower

values of τ_{avg}, 3D fibres have the highest values of N_f compared to 4D and 5D fibres, resulting in higher values of the post-cracking residual flexural strengths for the same value of $\tau_{avg} \cdot N_f$. Thus, to achieve the same values of f_{R1} and f_{R3}, a higher amount of 3D fibres compared to 4D and 5D fibres will be needed.

- The parameters obtained through inverse analysis directly correlates to the different stages of the pull-out load-displacement curve. The parameters K_{ss} and t_{ss} govern the debonding stage, represented by the initial slope of the curve up to the maximum pull-out load. Higher values of K_{ss} and t_{ss} for AASC than PCC reflect the experimental results, as fibres embedded in AASC show higher maximum pull-out loads than PCC. For both AASC and PCC, the highest values of the friction coefficient μ are observed for 3D fibres. This can be related to the higher mechanical anchorage provided by the additional bends at the fibre ends in 4D and 5D fibres and a resulting lower frictional resistance. 4D fibres embedded in AASC and PCC show the highest values of the fracture energy, due to the highest fibre material utilisation factor observed for this fibre type in both concrete matrices.

Acknowledgements

This project has received funding from the European Union's Horizon 2020 research and innovation programme under grant agreement No 813596 DuRSAAM. The opinions expressed in this document reflect only the author's view and reflect in no way the European Commission's opinions. The European Commission is not responsible for any use that may be made of the information it contains.

Author contribution: CRediT

Laura Rossi: Conceptualization, Formal analysis, Investigation, Methodology, Validation, Writing – Original Draft

Maria Paula Zappitelli: Conceptualization, Formal analysis, Methodology, Software, Visualization, Writing – Original Draft

Ravi A. Patel: Conceptualization, Formal analysis, Methodology, Supervision, Writing – Review & Editing

Frank Dehn: Funding acquisition, Resources, Supervision, Writing – Review & Editing

References

[1] C. Lin, T. Kanstad, S. Jacobsen, and G. Ji, 'Bonding property between fiber and cementitious matrix: A critical review', Constr. Build. Mater., vol. 378, p. 131169, May 2023, doi: 10.1016/j.conbuildmat.2023.131169.

[2] S. Abdallah, M. Fan, and D. W. A. Rees, 'Predicting pull-out behaviour of 4D/5D hooked end fibres embedded in normal-high strength concrete', Eng. Struct., vol. 172, pp. 967–980, Oct. 2018, doi: 10.1016/j.engstruct.2018.06.066.

[3] Y. M. Abbas, 'Microscale Cohesive-Friction-Based Finite Element Model for the Crack Opening Mechanism of Hooked-End Steel Fiber-Reinforced Concrete', Materials, vol. 14, no. 3, p. 669, Feb. 2021, doi: 10.3390/ma14030669.

[4] F. Deng, X. Ding, Y. Chi, L. Xu, and L. Wang, 'The pull-out behavior of straight and hooked-end steel fiber from hybrid fiber reinforced cementitious composite: Experimental study and analytical modelling', Compos. Struct., vol. 206, pp. 693–712, Dec. 2018, doi: 10.1016/j.compstruct.2018.08.066.

[5] F. U. A. Shaikh, 'Pullout Behavior of Hook End Steel Fibers in Geopolymers', J. Mater. Civ. Eng., vol. 31, 04019068 vols, no. 6, Jan. 2019, doi: 10.1061/(ASCE)MT.1943-5533.0002722.

[6] S. Abdallah, D. W. A. Rees, S. H. Ghaffar, and M. Fan, 'Understanding the effects of hooked-end steel fibre geometry on the uniaxial tensile behaviour of self-compacting concrete', Constr. Build. Mater., vol. 178, pp. 484–494, Jan. 2018, doi: 10.1016/j.conbuildmat.2018.05.191.

[7] S. Abdallah, M. Fan, and D. W. A. Rees, 'Analysis and modelling of mechanical anchorage of 4D/5D hooked end steel fibres', Mater. Des., vol. 112, pp. 539–552, Jan. 2016, doi: 10.1016/j.matdes.2016.09.107.

[8] S. Abdallah, M. Fan, X. Zhou, and S. Le Geyt, 'Anchorage Effects of Various Steel Fibre Architectures for Concrete Reinforcement', Int. J. Concr. Struct. Mater., vol. 10, no. 3, pp. 325–335, Jan. 2016, doi: 10.1007/s40069-016-0148-5.

[9] S. Abdallah and D. W. A. Rees, 'Comparisons Between Pull-Out Behaviour of Various Hooked-End Fibres in Normal–High Strength Concretes', Int. J. Concr. Struct. Mater., vol. 13, no. 1, p. 27, Apr. 2019, doi: 10.1186/s40069-019-0337-0.

[10] G. Chen, D. Gao, H. Zhu, J. Song Yuan, X. Xiao, and W. Wang, 'Effects of novel multiple hooked-end steel fibres on flexural tensile behaviour of notched concrete beams with various strength grades', Structures, vol. 33, pp. 3644–3654, Jan. 2021, doi: 10.1016/j.istruc.2021.06.016.

[11] I. Löfgren, Fibre-reinforced concrete for industrial construction: A fracture mechanics approach to material testing and structural analysis, vol. N.S., 2378. in Doktorsavhandlingar

vid Chalmers Tekniska Högskola, vol. N.S., 2378. Göteborg: Chalmers Univ. of Technology, 2005.

[12] D.-Y. Yoo, J.-J. Park, and S.-W. Kim, 'Fiber pullout behavior of HPFRCC: Effects of matrix strength and fiber type', Compos. Struct., vol. 174, pp. 263–276, Aug. 2017, doi: 10.1016/j.compstruct.2017.04.064.

[13] S. Abdallah, Fan, Mizi, and Zhou, Xiangming, 'Effect Of Hooked-End Steel Fibres Geometry On Pull-Out Behaviour Of Ultra-High Performance Concrete', Nov. 2016, doi: 10.5281/ZENODO.1128020.

[14] S. Abdallah, M. Fan, and X. Zhou, 'Pull-Out Behaviour of Hooked End Steel Fibres Embedded in Ultra-high Performance Mortar with Various W/B Ratios', Int. J. Concr. Struct. Mater., vol. 11, no. 2, pp. 301–313, Jan. 2017, doi: 10.1007/s40069-017-0193-8.

[15] F. U. A. Shaikh, Y. Shafaei, and P. K. Sarker, 'Effect of nano and micro-silica on bond behaviour of steel and polypropylene fibres in high volume fly ash mortar', Constr. Build. Mater., vol. 115, pp. 690–698, Jan. 2016, doi: 10.1016/j.conbuildmat.2016.04.090.

[16] A. Beglarigale, S. Aydın, and C. Kızılırmak, 'Fiber-Matrix Bond Characteristics of Alkali-Activated Slag Cement–Based Composites', J. Mater. Civ. Eng., vol. 28, no. 11, p. 04016133, Nov. 2016, doi: 10.1061/(ASCE)MT.1943-5533.0001642.

[17] F. Laranjeira, C. Molins, and A. Aguado, 'Predicting the pullout response of inclined hooked steel fibers', Cem. Concr. Res., vol. 40, no. 10, pp. 1471–1487, Oct. 2010, doi: 10.1016/j.cemconres.2010.05.005.

[18] K. Georgiadi-Stefanidi, E. Mistakidis, D. Pantousa, and M. Zygomalas, 'Numerical modelling of the pull-out of hooked steel fibres from high-strength cementitious matrix, supplemented by experimental results', Constr. Build. Mater., vol. 24, no. 12, pp. 2489–2506, Dec. 2010, doi: 10.1016/j.conbuildmat.2010.06.007.

[19] T. Soetens, A. Van Gysel, S. Matthys, and L. Taerwe, 'A semi-analytical model to predict the pull-out behaviour of inclined hooked-end steel fibres', Constr. Build. Mater., vol. 43, pp. 253–265, Jun. 2013, doi: 10.1016/j.conbuildmat.2013.01.034.

[20] R. Breitenbücher, G. Meschke, F. Song, and Y. Zhan, 'Experimental, analytical and numerical analysis of the pullout behaviour of steel fibres considering different fibre types, inclinations and concrete strengths', Struct. Concr., vol. 15, no. 2, pp. 126–135, Jan. 2014, doi: 10.1002/suco.201300058.

[21] J. Feng, W. W. Sun, X. M. Wang, and X. Y. Shi, 'Mechanical analyses of hooked fiber pullout performance in ultra-high-performance concrete', Constr. Build. Mater., vol. 69, pp. 403–410, Oct. 2014, doi: 10.1016/j.conbuildmat.2014.07.049.

[22] Y. Zhan and G. Meschke, 'Analytical Model for the Pullout Behavior of Straight and Hooked-End Steel Fibers', J. Eng. Mech., vol. 140, 04014091 vols, no. 12, Jan. 2014, doi: 10.1061/(ASCE)EM.1943-7889.0000800.

[23] S. Abdallah, M. Fan, and D. W. A. Rees, ‘Bonding Mechanisms and Strength of Steel Fiber–Reinforced Cementitious Composites: Overview’, J. Mater. Civ. Eng., vol. 30, 04018001 vols, no. 3, Jan. 2018, doi: 10.1061/(ASCE)MT.1943-5533.0002154.

[24] L. Chen, W. Sun, B. Chen, Z. Shi, J. Lai, and J. Feng, ‘Multiscale study of fibre orientation effect on pullout and tensile behavior of steel fibre reinforced concrete’, Constr. Build. Mater., vol. 283, p. 122506, May 2021, doi: 10.1016/j.conbuildmat.2021.122506.

[25] V. M. C. F. Cunha, J. A. O. Barros, and J. M. Sena-Cruz, ‘Pullout Behavior of Steel Fibers in Self-Compacting Concrete’, J. Mater. Civ. Eng., vol. 22, no. 1, pp. 1–9, Jan. 2010, doi: 10.1061/(ASCE)MT.1943-5533.0000001.

[26] A. Hemmatian, M. Jalali, H. Naderpour, and M. L. Nehdi, ‘Machine learning prediction of fiber pull-out and bond-slip in fiber-reinforced cementitious composites’, J. Build. Eng., vol. 63, p. 105474, Jan. 2023, doi: 10.1016/j.jobe.2022.105474.

[27] F. Isla, P. Argañaraz, and B. Luccioni, ‘Numerical modelling of steel fibers pull-out from cementitious matrixes’, Constr. Build. Mater., vol. 332, p. 127373, May 2022, doi: 10.1016/j.conbuildmat.2022.127373.

[28] J. Storm, M. Pise, D. Brands, J. Schröder, and M. Kaliske, ‘A comparative study of micro-mechanical models for fiber pullout behavior of reinforced high performance concrete’, Eng. Fract. Mech., vol. 243, p. 107506, Feb. 2021, doi: 10.1016/j.engfrac-mech.2020.107506.

[29] E. Poveda, R. C. Yu, M. Tarifa, G. Ruiz, V. M. C. F. Cunha, and J. A. O. Barros, ‘Rate effect in inclined fibre pull-out for smooth and hooked-end fibres: a numerical study’, Int. J. Fract., vol. 223, no. 1–2, pp. 135–149, May 2020, doi: 10.1007/s10704-019-00404-7.

[30] A. P. Fantilli and P. Vallini, ‘A Cohesive Interface Model for the Pullout of Inclined Steel Fibers in Cementitious Matrixes’, J. Adv. Concr. Technol., vol. 5, no. 2, pp. 247–258, 2007, doi: 10.3151/jact.5.247.

[31] Z. Zou and M. Hameed, ‘Combining interface damage and friction in cohesive interface models using an energy based approach’, Compos. Part Appl. Sci. Manuf., vol. 112, pp. 290–298, Sep. 2018, doi: 10.1016/j.compositesa.2018.06.017.

[32] B. Banholzer, W. Brameshuber, and W. Jung, ‘Analytical evaluation of pull-out tests—The inverse problem’, Cem. Concr. Compos., vol. 28, no. 6, pp. 564–571, Jul. 2006, doi: 10.1016/j.cemconcomp.2006.02.015.

[33] I. Kožar, N. Torić Malić, D. Simonetti, and Ž. Smolčić, ‘Bond-slip parameter estimation in fiber reinforced concrete at failure using inverse stochastic model’, Eng. Fail. Anal., vol. 104, pp. 84–95, Oct. 2019, doi: 10.1016/j.engfailanal.2019.05.019.

[34] L. Rossi, M. P. Zappitelli, R. A. Patel, and F. Dehn, ‘Flexural tensile behaviour of alkali-activated slag-based concrete and Portland cement-based concrete incorporating single and

multiple hooked-end steel fibres', J. Build. Eng., vol. 98, p. 111090, Dec. 2024, doi: 10.1016/j.jobe.2024.111090.

[35] D. Dupont and L. Vandewalle, 'Distribution of steel fibres in rectangular sections', Cem. Concr. Compos., vol. 27, no. 3, pp. 391–398, Mar. 2005, doi: 10.1016/j.cemconcomp.2004.03.005.

[36] L. Rossi, R. A. Patel, and F. Dehn, 'Compressive behaviour of alkali-activated slag-based concrete and Portland cement concrete incorporating novel multiple hooked-end steel fibres', Mater. Struct., vol. 56, no. 5, Jan. 2023, doi: 10.1617/s11527-023-02180-2.

[37] D. S. Dugdale, 'Yielding of steel sheets containing slits', J. Mech. Phys. Solids, vol. 8, no. 2, pp. 100–104, May 1960, doi: 10.1016/0022-5096(60)90013-2.

[38] G. I. Barenblatt, 'The Mathematical Theory of Equilibrium Cracks in Brittle Fracture', in Advances in Applied Mechanics, vol. 7, Elsevier, 1962, pp. 55–129. doi: 10.1016/S0065-2156(08)70121-2.

[39] A. Rolland, P. Argoul, K. Benzarti, M. Quiertant, S. Chataigner, and A. Khadour, 'Analytical and numerical modeling of the bond behavior between FRP reinforcing bars and concrete', Constr. Build. Mater., vol. 231, p. 117160, Jan. 2020, doi: 10.1016/j.conbuildmat.2019.117160.

[40] M. Smith, ABAQUS/Standard User's Manual, Version 6.9. Providence, RI: Simulia.

[41] H. Zhang, Y. J. Huang, Z. J. Yang, S. L. Xu, and X. W. Chen, 'A discrete-continuum coupled finite element modelling approach for fibre reinforced concrete', Cem. Concr. Res., vol. 106, pp. 130–143, Apr. 2018, doi: 10.1016/j.cemconres.2018.01.010.

[42] R. Storn and K. Price, 'Differential evolution - A simple and efficient heuristic for global optimisation over continuous spaces', J. Glob. Optim., vol. 11, no. 4, pp. 341–359, Jan. 1997, doi: 10.1023/A:1008202821328.

[43] F. Isla, G. Ruano, and B. Luccioni, 'Analysis of steel fibers pull-out. Experimental study', Constr. Build. Mater., vol. 100, pp. 183–193, Dec. 2015, doi: 10.1016/j.conbuildmat.2015.09.034.